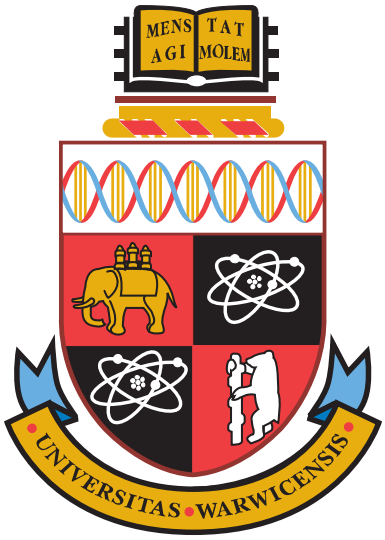

Single point defect imaging studies in diamond

by

Philip L. Diggle

Thesis

Submitted to the University of Warwick

for the degree of

Doctor of Philosophy

Department of Physics

May 2019

Contents

List of Tables

List of Figures

Acknowledgments

You can't go back and change the beginning, but you can start where you are and change the ending.

- C. S. Lewis

Whilst, at times, completing this doctoral work has felt like the ultimate challenge, there are inevitably many people that I'd like to express my gratitude for.

Firstly a thank you to Prof. Mark Newton, for supervision, support and guidance throughout my PhD. Also to Dr. Chris Welbourn and Dr. Ben Green, for insightful comments on synthetic diamond growth, and the variety of defects, which has shaped some of the considerations given here. Equally, aspects of this work wouldn't have been possible without Dr. Ben Breeze providing guidance on taming the spectrometers, even when, occasionally, I've felt like a muppet myself.

Likewise, I am grateful to the Gemological Institute of America (GIA) for funding such an interesting topic, as well as making available some very unique samples. In particular I'd like to thank Dr. Wuyi Wang and Dr. Ulrika D'Haenens-Johansson for their support throughout. Mid-way through my PhD, I was fortunate enough to spend a short time working at the New York lab, and came away feeling as though I'd learnt so much! To this, I also thank Dr. Karen Smit, Dr. Evan Smith and many others of the GIA research staff for making me feel so welcome.

The Diamond Science and Technology Centre for Doctoral Training (DST CDT) has opened up a large avenue of research and industry contacts. This has provided generous support in understanding diamond, not only as a material, but as a technology platform. The DST CDT will undoubtedly provide many great scientists, to which I feel humbled to have been a part of.

There are too many people to mention, past and present, of the Warwick Diamond and EPR group; so collectively I say a huge thanks for not only showing me the ropes but for ensuring there was never a shortage of coffee for too long!

To the League; thank you for the belief that I could!

Finally, it goes without saying that one can draw the greatest strength from their loved ones, and it is to them that I dedicate this thesis. Dad I know you would have been proud to see me finally leave university and "*get a real job*"! To Mum, words aren't enough to say thank you for always being there through thick and thin. My better half, Lucy, thank you for being the light in my life that continues to shine no matter what - I Love You So Much.

Declaration and published work

I declare that the work presented in this thesis is my own except where stated otherwise, and was carried out entirely at the University of Warwick, during the period of October 2015 to May 2019, under the supervision of Prof. Mark Newton. The research reported here has not been submitted, either wholly or in part, in this or any other academic institution for admission to a higher degree.

Some parts of the work reported and other work not reported in this thesis have been published, as listed below. It is anticipated that further parts of this work will be submitted for publication in due course.

Published papers

1. D. Howell, A. Collins, L. Loudin, P. Diggle, U. D'Haenens-Johansson, K. Smit, A. Katrusha, J. Butler, F. Nestola, *Diamond and Related Materials* **96**, 207–215 (2019)

2. C. J. Stephen, B. L. Green, Y. N. D. Lekhai, L. Weng, P. Hill, S. Johnson, A. C. Frangeskou, P. L. Diggle, M. J. Strain, E. Gu, M. E. Newton, J. M. Smith, P. S. Salter, G. W. Morley, *arXiv:1807.03643*, 2–9 (2018)

3. E. Fraczek, V. G. Savitski, M. Dale, B. G. Breeze, P. Diggle, M. Markham, A. Bennett, H. Dhillon, M. E. Newton, A. J. Kemp, *Optical Materials Express* **7**, 2571 (2017)

Papers in preparation

1. P. L. Diggle, U. F. S. D'Haenens-Johansson, B. L. Green, C. M. Welbourn, T. N. T. Thi, A. Katrusha, W. Wang, M. E. Newton *Decoration of growth sector boundaries with single nitrogen vacancy centres in as-grown single crystal HPHT synthetic diamond*

2. P. L. Diggle, B. L. Green, M. E. Newton *On the suitability of high purity*

HPHT synthetic diamond for quantum processing

3. P. L. Diggle, B. L. Green, M. L. Markham, D. J. Twitchen, M. E. Newton *Dislocation facilitated incorporation of single point defects in single crystal boron doped CVD diamond*

Conference presentations

1. The GIA Symposium, Carlsbad, California. Oral presentation 'Diamond at the diffraction limit: optical characterisation of synthetic diamond'
2. De Beers 69th Diamond Conference, The University of Warwick. Oral presentation 'Spectroscopic characterisation of single point defects in single-crystal boron doped CVD diamond'
3. De Beers 69th Diamond Conference, The University of Warwick. Poster presentation 'Decoration of growth sector boundaries with single nitrogen vacancy centres in as-grown single crystal HPHT diamond'
4. New Diamond and Nano Carbon Conference, Flagstaff, Arizona. Oral presentation 'Spectroscopic characterisation of single point defects in single-crystal boron doped CVD diamond'
5. New Diamond and Nano Carbon Conference, Flagstaff, Arizona. Poster presentation 'Decoration of growth sector boundaries with single nitrogen vacancy centres in as-grown single crystal HPHT diamond'
6. The Rank Prize Funds Symposium on Diamond Photonics: Sources and Sensors, Grasmere, UK. 'Spectroscopic characterisation of single point defects in single-crystal boron doped CVD diamond'
7. De Beers 68th Diamond Conference, The University of Warwick. Oral presentation 'Decoration of Growth Sector Boundaries with Single Nitrogen Vacancy Centres in As-Grown Single Crystal HPHT Synthetic Diamond'
8. De Beers 68th Diamond Conference, The University of Warwick. Poster presentation 'Investigating the Nitrogen Vacancy Charge State in a Boron / Nitrogen Co-Doped Single Crystal Synthetic Diamond'

9. New Diamond and Nano Carbon Conference, Cairns, Australia. Oral presentation 'Decoration of Growth Sector Boundaries with Single Nitrogen Vacancy Centres in As-Grown Single Crystal HPHT Synthetic Diamond'

10. New Diamond and Nano Carbon Conference, Carins, Australia. Poster presentation 'Investigating the Nitrogen Vacancy Charge State in a Boron / Nitrogen Co-Doped Single Crystal Synthetic Diamond'

11. De Beers 67$^{\text{th}}$ Diamond Conference, The University of Warwick. Poster presentation 'Investigating the Nitrogen Vacancy Charge State in a Boron / Nitrogen Co-Doped Single Crystal Synthetic Diamond'

12. SBDD XXI - Hasselt Diamond Workshop. Poster presentation 'Investigating the Nitrogen Vacancy Charge State in a Boron / Nitrogen Co-Doped Single Crystal Synthetic Diamond'

Abstract

This thesis considers the recent advances in synthetic diamond growth. To enable this, it has been necessary to construct a custom confocal photoluminescence scanning microscope to interrogate single point defects in diamond, where detection is constrained by the diffraction limit of light. Complementary techniques have been used to support the understanding of bulk diamond material such as, electron paramagnetic resonance (EPR), absorption spectroscopies in the ultraviolet-visible (UV-vis) and infrared (IR) range, cathodoluminescence (CL) spectroscopy, and X-ray topography (XRT).

For boron doped diamond, the inclusion of point defects is not so well understood. Here, a diamond synthesised via chemical vapour deposition (CVD) contained distinct regions of boron doping. Confocal microscopy with 532 nm excitation found single point defects could be identified in these regions. Spectroscopy revealed two dominant classes of zero phonon line (ZPL) emission, centred on 580 ± 10 nm and 612 ± 18 nm. Polarisation measurements on these defects strongly suggest a defect of $\mathscr{D}_{2\mathrm{d}}$ or $\mathscr{C}_{2\mathrm{v}}$ symmetry with the optical transition occurring from a ground A state to an excited A state. In addition, the incorporation of these defects follow linear structures, and may therefore imply a decoration of a dislocation in the boron doped region.

The remainder of the thesis concentrates on the synthesis of diamond from the high pressure, high temperature (HPHT) method. In high purity, type IIa, HPHT diamond it was found that the growth sector interface between {1 1 1} and {1 1 3} are decorated with single negatively charged nitrogen vacancy (NV^-) defects with no preferential orientation. In the bulk {1 1 1} growth sectors it could be found that single and small ensemble negatively charged silicon vacancy (SiV^-) defects also do not grow in preferentially orientated, whilst a nickel related defect does.

The growth sector dependence of nitrogen and boron incorporation was investigated and found to agree with the Kanda model. Here CL measurements demonstrate a good way to obtain the boron concentration per growth sector, whilst it was necessary to electron irradiate and anneal to understand the growth sector dependence of nitrogen. Furthermore, it was found that both substitutional nitrogen and boron decrease significantly following electron irradiation and annealing to 800 °C. The mechanism for the reduction in boron is not well understood and requires further investigation.

Finally, the suitability of HPHT diamond was assessed for quantum applications where the spin decoherence lifetime (T_2) was used as a figure of merit. It was found that the NV^- centre is sensitive to the local boron concentration. It has been possible to measure the T_2 lifetime to be limited by ^{13}C in the as-grown NV^- defects for a boron concentration < 50 ppb. An implantation study also revealed the growth sector dependence of the T_2 lifetime where the ^{13}C limit is approached in the {0 0 1} growth sector.

Abbreviations

Definitions

[X]	Concentration of X
CL	Cathodoluminescence
cps	Counts per second
ct	Carat
CVD	Chemical vapour deposition
CW-EPR	Continuous wave electron paramagnetic resonance
EM	Electromagnetic
EPR	Electron paramagnetic resonance
fcc	Face centred cubic
FTIR	Fourier transform infrared
FFT	Fast Fourier transform
FWHM	Full width at half maximum
$g^{(2)}(\tau)$	Second-order correlation function
HBT	Hanbury Brown-Twiss
HPHT	High pressure high temperature
ISC	Intersystem crossing
IR	Infrared
kcps	Kilo-counts per second
λ	Wavelength of light
LVM	Local vibrational mode
MPCVD	Microwave plasma CVD
ODMR	Optically detected magnetic resonance
PBC	Periodic bond chain
PL	Photoluminescence

POI	Point of interest
ppb	Parts per billion atomic density
ppm	Parts per million atomic density
ppt	Parts per trillion atomic density
PSF	Point spread function
RP-EPR	Rapid passage electron paramagnetic resonance
SIMS	Secondary ion mass spectrometry
T_2	Spin decoherence lifetime
UV-Vis	Ultraviolet-visible
XRT	X-ray topography
ZPL	Zero-phonon line

Crystallographic notation

$[h\,k\,l]$	a specific hkl direction
$\langle h\,k\,l \rangle$	a general hkl direction
$(h\,k\,l)$	a specific hkl plane
$\{h\,k\,l\}$	a general hkl plane

1

Introduction

Diamonds are for everything

- DST CDT

Adamas, the Greek word for unconquerable, and the origin from which the word diamond is derived. There exists many historical accounts associated with diamond, including being adorned upon the body in the belief that the bearer would behold an air of invincibility as it was said to be indestructible [1].

Diamond can be seen as a symbol of status with notable exhibits including the Cullinan and the Koh-i-Noor in the British Crown Jewels, or perhaps the more eccentric diamond lenses in the Halqeh-ye-nur [2]. Today, diamond is perhaps notoriously associated with the precious gemstone, crafted to an item of jewellery, and given as a token of affection to loved ones. The significance and value in all these diamonds is, in part, commensurate of the origin; diamond growth over millions of years within the mantle of the Earth (natural diamond).

However, from the advent of diamond synthesis in the lab, and through its development, today it is also possible to purchase synthetic lab-grown gem-quality diamond. Furthermore, over the last 60 years of research in synthesis techniques, along with the many superlative material properties, diamond is now being utilised in a wide range of applications from oil and gas retrieval [3–5] to quantum information processing [6, 7].

1.1 Diamond synopsis

1.1.1 Crystalline structure

Carbon is the fourth most abundant element in our solar system [8], it is the fundamental building block for life on Earth, and the foundation for all organic chemistry. Diamond is just one of the many allotropes formed by carbon [9], but is unique due to the type of bonding each carbon atom shares with its neighbour.

As the lightest element in Group IV of the periodic table, carbon contains six electrons with a ground state orbital configuration of $1s^2 2s^2 2p^2$, and therefore has four valence electrons all of which take part in atomic bonding. Of these four electrons, two occupy the $2s$ orbital whilst the other two occupy a $2p_x$ and $2p_y$ orbital each. By the promotion of an electron from the $2s$ orbital, a third $2p$ orbital is created as $2p_z$ and allows hybrid orbitals to form. The fashion in which the $2s$ and $2p$ orbitals hybridise determines the allotrope of carbon.

For four of the three electrons occupying three equivalent hybridised orbitals of $2s$ and $2p_x$, $2p_y$, with the fourth electron in the $2p_z$ orbital unhybridised, this constitutes an sp^2 hybridisation. This sp^2 arrangement generates a planar geometry with an angle of 120° between orbitals, with the $2p_z$ perpendicular in a π orbital. sp^2 orbitals create strong σ bonds where a one dimensional sheet constitutes as graphene, and layers of graphene weakly bound by the π bond through a van der Waals force is known as graphite.

If, however, the remaining $2s$ orbital forms a hybridisation with all three $2p$ orbitals, an sp^3 hybridisation occurs, resulting in a tetrahedral geometry with an angle of 109.5° between orbitals. With adjacent carbon atoms, the sp^3 hybridisation allows for a strong C-C σ bond resulting in one carbon atom covalently bonded to four neighbouring carbon atoms in a tetrahedral structure, shown in figure 1-1, and is the atomic structure of the diamond crystal.

The unit cell of diamond consists of 8 carbon atoms, in a face centred cubic (fcc) Bravais lattice with a two point basis at $(0, 0, 0)$ and $(\frac{1}{4}, \frac{1}{4}, \frac{1}{4})$. The unit cell

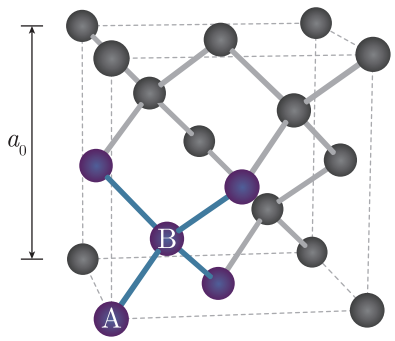

Figure 1-1 The unit cell of diamond with cell length $a_0 = 0.357$ nm and the C-C bond length is 0.154 nm. Two point basis of the fcc Bravais lattice denoted by position $(0, 0, 0)$ for atom A, and $(\frac{1}{4}, \frac{1}{4}, \frac{1}{4})$ for atom B. The tetrahedral structure is highlighted by the four carbon atoms in represented in blue.

length (a_0) is 0.357 nm with a C-C bond length of 0.154 nm. Carbon in this close packing arrangement of the diamond lattice provides an atomic density of $8/a_0^3 = 1.76 \times 10^{23}$ cm^{-3}, and from this it is possible to define a point defect concentration of 1 part per billion carbon atoms (ppb) as 1.76×10^{14} point defects cm^{-3}.

1.1.2 Diamond type, properties, and applications

Aside from carbon, diamond can also contain atomic impurities of which the most dominant is nitrogen [10, 11]. Type I diamond is differentiated from type II diamond by the concentration of nitrogen, where the former contains an appreciable concentration and is detectable in infrared (IR) absorption. Type I diamonds are therefore sub categorised based on the aggregation form of nitrogen, and type II diamonds are sub-categorised based on whether they contain boron or not. The route to "*type classification*" is outlined in figure 1-2.

Diamond has many physical properties which far exceeds that of other materials. A summary of these properties can be found in table 1-1 which have shown importance for enabling several technological applications. For instance the extreme hardness of diamond makes it suitable for cutting, drilling and mining [3–5] or utilised as anvils to probe new states of elements, such as metallic hydrogen [18]. The high thermal conductivity makes it ideal for integration into devices to take heat away from components [19–21]. The large band gap results in the material being

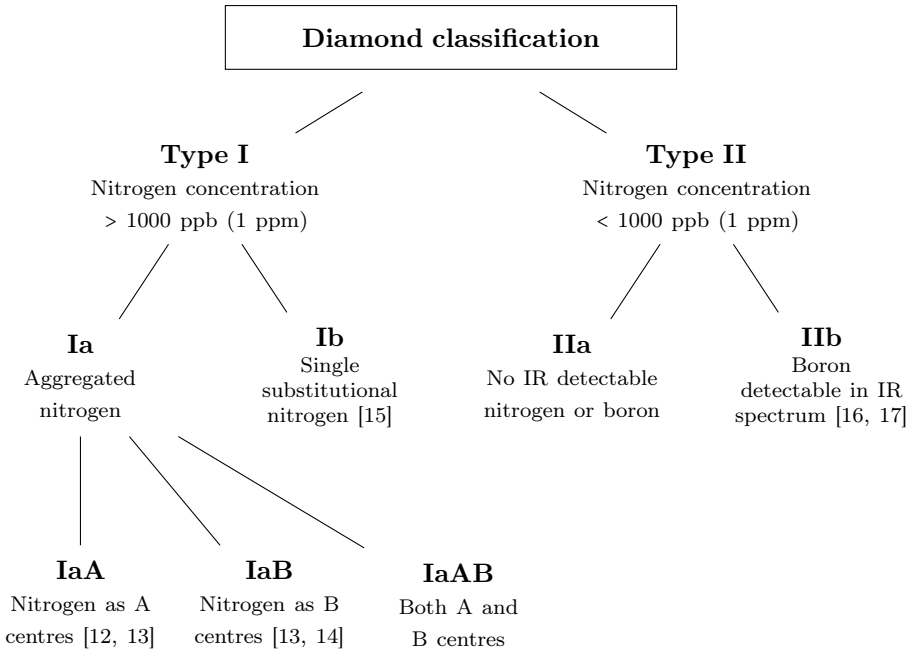

Figure 1-2 Diamond type classifications of diamond based on their detection IR absorption spectra.

transparent across a wide wavelength range and so optical windows and lenses can be fabricated [22–24]. Furthermore the crystal can also wavelength-shift light by a Stokes shift enabling new wavelengths of lasers to be developed [25–27]. From the biological compatibility, there are also medical uses for diamond where artificial joints can be coated to improve wear resistance [28, 29], or provide very sharp clean cuts in ophthalmic surgery [30].

1.1.3 Defects in diamond

A defect is defined as an interruption to the perfect carbon tetrahedral lattice, described as either a point or extended defect. The distinction is implied by the nomenclature; a point defect restricts the imperfection within the unit cell, whereas an extended defect applies to the bulk crystal across many unit cells of diamond. Whilst this thesis concentrates predominately on the characterisation of point defects, it is necessary to consider extended defects to complete the picture of defect incorporation and migration. An extensive catalogue of defects and their optical properties can be found in reference [37]. Chapter 2 will review the current understanding on diamond growth and defects.

Property		Reference
Bandgap (indirect)	5.48 eV	[31]
Bandgap (direct)	7.30 eV	[31]
Electrical insulator	10^{13} Ω cm	[32]
Breakdown field	20 MV cm^{-1}	[33]
Electron mobility	4500 cm^2 V^{-1} s^{-1}	[33]
Hole mobility	3800 cm^2 V^{-1} s^{-1}	[33]
Low coefficient of friction	0.1	[32]
High thermal conductivity (at 20 °C)	2×10^3 W m^{-1} K^{-1}	[32]
Low linear thermal expansion	0.8×10^{-6} K	[34]
Low dn/dT	$9.8 - 11.4 \times 10^{-6}$ K^{-1}	[35]
Highest Young's modulus	1223 GPa	[36]
Highest material hardness	Mohs 10	[34]
Fastest isotropic sound propagation velocity	17.5 km s^{-1}	[32]
Biologically compatible and chemically inert		[32]

Table 1-1 A summary of material properties associated with diamond.

Generally, point defects involve one, or a combination, of the following:

- Interstitials; a carbon atom not located at a regular lattice site
- Impurities; a non-carbon atom occupying either a regular or non-regular lattice site
- Vacancies; a lattice site which is missing a carbon atom

The introduction of a different element (or impurity atom) is known as doping, which can produce many interesting properties and can be exploited for applications. Heavily boron doped diamond produces electrically conductive diamond which can then treat contaminated water [38] or act as a pH sensor [39]. Diamond is also proving its worth in the quantum realm, with the negatively charged nitrogen vacancy centre (single substitutional nitrogen next to a vacancy, NV^-) where magnetometry has been amply demonstrated [40, 41], as well as being a platform for quantum information processing [42, 43].

The incorporation of defects in a sufficient concentration will also result in the colour of a diamond; a significant consideration for the gemmological market. For

example, blue colouration is caused by substitutional boron, green from the H3 defect (two substitutional nitrogens surrounding a vacancy, N_2V^0), or pink/red from the NV defect. An overview of common defects that result in the colour (or equally, the lack of colour) can be found in the reference chart by Shigley and Breeding [44]. It is also known that the colour of the diamond can be modified by subsequent processing (or treatment) of the material: for instance, brown colouration in natural diamond can be removed by high pressure, high temperature (HPHT) annealing [45] which may therefore alter the market value of the diamond.

1.2 Motivation for study

Given the incorporation of diamond into a plethora of applications it is clear that the evolution and improvement of diamond synthesis, has in part, been driven by the expanding industrial and technological markets. Furthermore, there is a direct feedback of this synthesis and defect knowledge in to the gemmological market, for which the synthesis of (large) synthetic gem-quality diamonds is now commercially viable [46–49]. Hence there is an opportunity to investigate synthetic diamond and learn more about the growth through the defect incorporation. This in turn will provide a further insight for both areas of diamond usage.

1.2.1 Gemmology

For 2017, the natural diamond jewellery market was valued at ~US$ 82 billion [50, 51], but the market value for synthetic diamond jewellery is currently unknown. For the consumer, synthetic diamond can be cheaper to purchase than an equivalent natural diamond[a]. Equally, it is possible to treat diamond to improve its colour, and therefore value, for both natural and synthetic types. The interplay between point defect incorporation and migration, as well as any knowledge on extended defects go a long way to provide information on the origin and treatment history of the diamond.

[a] As of Sept. 2018 Lightbox Jewelry sells chemical vapour deposition (CVD) synthetic diamond at US$ 800 per carat `www.lightboxjewelry.com`

The identification between natural and synthetic, in most cases, is clear. A simple picture of the diamond taken with UV light can reveal the interior morphology [52], where synthetics can show structures indicative to the growth method used. For instance, cubo-octahedral growth sectors are present in HPHT synthetic diamond and striations are typical in CVD synthetic diamond, both of which are not typically seen in natural diamond. This distinction will be reviewed in Chapter 2.

Further to UV imaging, the presence/absence of defects in diamond are equally essential to make the distinction between between natural and synthetic diamond, and whether they are treated or untreated. Published lab notes by the Gemological Institute of America (GIA) highlight that synthetic diamonds, on rare occasions, have been inscribed with identification markers relating to natural diamond [53, 54]. Another article highlights one case of fraudulence on a natural diamond which was described as untreated, but analysis revealed this had been HPHT treated which likely improved its colour and value [55]. Whilst these articles describe fraudulence as rare, it does however highlight the importance of this discrimination by correlating imagery to defect identification to identify the genesis and history of a particular diamond.

1.2.2 Quantum engineering

The NV^- centre has firmly rooted diamond as a viable material for many quantum based applications. This is owed to the ability to optically initialise and read out the quantum spin state at room temperature with a stable photon count rate [56]. Despite this, the defect only weakly emits coherent photons in to the zero phonon line (around 3% at 300 K) which requires an element of engineering to overcome. Cryogenic cooling can increase emission into the zero phonon line [57], whilst nanophotonic structures can help overcome the high refractive index of diamond increasing the detectable photon count rate [58, 59].

There are hundreds of point defects identified in diamond, of which NV^- is just one, and there is now a push to realise new defects in diamond that "*tick the boxes*" where the NV^- cannot. Therefore, not only is a refined understanding of diamond synthesis required but also further knowledge on defect incorporation, migration,

and interactions along with their quantum properties. A review of the common defects investigated for quantum applications will be collated in Chapter 2.

1.2.3 Defect incorporation in low concentrations

Owing to the improvement in diamond synthesis, it not unreasonable to speculate that advances of it will continue to be made and will be of significant importance both for the gemmological and quantum markets. However there is still more to be understood from refined growth processes by investigating the role, and any correlation thereof, for point and extended defects.

In order to realise this, it is necessary to consider synthetic diamond which contains a low enough point defect concentration that single, individual defects can be examined. Typically, bulk characterisation of point defects in diamond requires them to be present in a substantial concentration to facilitate detection (usually > 1 ppb). Therefore, there is motivation to study diamond on an optical system where the limiting factor is the diffraction limit of light and not the concentration of defects. This can be achieved in a scanning confocal photoluminescence microscope, and will therefore be heavily employed in the work of this thesis. Not only will this facilitate the detection of isolated single defects at sub-ppb concentrations, but can also be used to interrogate the emission statistics and spin properties of the defect. Further routine bulk characterisation techniques will also be supplemented and will be outlined later in this thesis.

1.3 Thesis outline

An outline of the remainder of this thesis is as follows:

- Chapter 2 reviews diamond synthesis techniques, extended and point defects, and in particular reviews the challenges of defect identification and newly discovered defects with interesting properties.
- Chapter 3 provides the theory required for the interpretation of the results of the experimental studies.
- Chapter 4 sets out the experimental techniques relevant to this thesis.
- Chapter 5 examines a multi-layered, chemical vapour deposition (CVD), grown diamond with an emphasis on defects found in boron doped regions.
- Chapter 6 analyses two synthetic diamonds grown by the high pressure, high temperature (HPHT) method by different suppliers and shows defect incorporations which are sector dependent.
- Chapter 7 explores defect migration in these HPHT samples and what this means for the synthesis of diamond and defect incorporation.
- Chapter 8 employs spin coherence measurements to NV^- centres in HPHT diamond for both as-grown defects and implanted defects, where the local defect concentration is shown to have a significant impact on the decoherence lifetimes.
- Chapter 9 concludes this thesis with an overview of the results and their impact.

References

1. S. Tolansky, *The history and use of diamond* (Methuen, 1962).
2. C. Atkinson et al., *Philosophical Transactions of the Royal Society A: Mathematical, Physical and Engineering Sciences* **373**, 20140270–20140270 (2015).
3. D. Belnap, A. Griffo, *Diamond and Related Materials* **13**, 1914–1922 (2004).
4. V. Kanyanta et al., *International Journal of Refractory Metals and Hard Materials* **46**, 145–151 (2014).
5. M. Yahiaoui et al., *International Journal of Refractory Metals and Hard Materials* **56**, 87–95 (2016).
6. I. Aharonovich et al., *Reports on Progress in Physics* **74**, 076501 (2011).
7. M. Markham et al., *Diamond and Related Materials* **20**, 134–139 (2011).
8. K. Lodders, H. Palme, H.-P. Gail, in *Solar System*, ed. by J. Trümper (Springer Berlin Heidelberg, Berlin, Heidelberg, 2009), vol. 4B, pp. 712–770.
9. A. Hirsch, *Nature Materials* **9**, 868–871 (2010).
10. R. M. Chrenko, R. E. Tuft, H. M. Strong, *Nature* **270**, 141–144 (1977).
11. A. T. Collins, *Physica B: Physics of Condensed Matter* **185**, 284–296 (1993).
12. G. Davies, *Journal of Physics C: Solid State Physics* **9**, L537–L542 (1976).
13. R. Jones, P. R. Briddon, S. Öberg, *Philosophical Magazine Letters* **66**, 67–74 (1992).
14. A. Mainwood, *Physical Review B* **49**, 7934–7940 (1994).
15. R. M. Chrenko, H. M. Strong, R. E. Tuft, *Philosophical Magazine* **23**, 313–318 (1971).
16. A. T. Collins, A. W. S. Williams, *Journal of Physics C: Solid State Physics* **4**, 1789–1800 (1971).
17. R. M. Chrenko, *Physical Review B* **7**, 4560–4567 (1973).
18. R. P. Dias, I. F. Silvera, *Science* **355**, 715–718 (2017).
19. P. H. Chen et al., *IEEE Photonics Technology Letters* **20**, 845–847 (2008).
20. P. Millar, A. J. Kemp, D. Burns, *Optics Letters* **34**, 782 (2009).
21. Y. Han et al., *IEEE Transactions on Components, Packaging and Manufacturing Technology* **4**, 983–990 (2014).

22. T. P. Mollart et al., presented at the Proceedings of SPIE, ed. by R. W. Tustison, vol. 4375, pp. 180–198.
23. E. Woerner et al., *Diamond and Related Materials* **10**, 557–560 (2001).
24. E6, *Enable extreme performance photonics*, 2014, `https://e6cvd.com/media/catalog/category/Element_Six_Optical.pdf` (Retrieved 23/06/2018).
25. R. P. Mildren et al., *Osa Cleo Qels*, 573–574 (2010).
26. D. C. Parrotta et al., *Optics Express* **19**, 24165 (2011).
27. S. Reilly et al., *Optics Letters* **40**, 930 (2015).
28. M. D. Fries, Y. K. Vohra, *Journal of Physics D: Applied Physics* **35**, L105–L107 (2002).
29. R. Lappalainen et al., *Journal of Biomedical Materials Research* **66B**, 410–413 (2003).
30. S. Al-Swailem, A. Behrens, A. Al Mahmood, *Middle East African Journal of Ophthalmology* **21**, 25 (2014).
31. W. Saslow, T. K. Bergstresser, M. L. Cohen, *Physical Review Letters* **16**, 354–356 (1966).
32. J. E. Field, *The Properties of Natural and Synthetic Diamond* (Academic Press, 1992).
33. S. Hadlington, *IEE Review* **51**, 30–33 (2005).
34. I. Sunagawa, in *Crystals* (Cambridge University Press, Cambridge), pp. 167–197.
35. G. N. Ramachandran, *Proceedings of the Indian Academy of Sciences - Section A* **25**, 266 (1947).
36. S.-F. Wang et al., *Materials Chemistry and Physics* **85**, 432–437 (2004).
37. A. M. Zaitsev, *Optical Properties of Diamond* (Springer Berlin Heidelberg, Berlin, Heidelberg, 2001).
38. V. Schmalz et al., *Water Research* **43**, 5260–5266 (2009).
39. S. Fierro et al., *Scientific Reports* **3**, 3257 (2013).
40. L. Rondin et al., *Rep Prog Phys* **77**, 56503 (2014).
41. J. F. Barry et al., arXiv: `1903.08176` (2019).
42. B. Hensen et al., *Nature* **526**, 682–686 (2015).
43. P. C. Humphreys et al., *Nature* **558**, 268–273 (2018).

44. J. Shigley, C. Breeding, *Gems & Gemology* **49**, 107–111 (2013).
45. D. Fisher, *Lithos* **112**, 619–624 (2009).
46. U. F. D'Haenens-Johansson et al., *Gems & Gemology* **51**, 260–279 (2015).
47. B. Deljanin et al., *Contributions to Gemology* **15**, 1–7 (2015).
48. B. Law, W. Wang, *Gems and Gemology* **52**, 414–416 (2016).
49. I. V. Klepikov, A. V. Koliadin, E. A. Vasilev, *IOP Conference Series: Materials Science and Engineering* **286**, 012035 (2017).
50. Bain & Company, *The Global Diamond Industry 2018*, Technical Report, 2018, `https://www.bain.com/contentassets/a53a9fa8bf5247a3b7bb0b10561510c2/bain_diamond_report_2018.pdf` (Retrieved 22/12/2018).
51. De Beers Group, *The Diamond Insight Report 2018*, Technical Report, 2018, `https://www.debeersgroup.com/~/media/Files/D/De-Beers-Group/documents/reports/insights/the-diamond-insight-report-2018.pdf` (Retrieved 22/12/2018).
52. C. M. Welbourn, M. Cooper, P. M. Spear, *Gems & Gemology* **32**, 156–169 (1996).
53. B. Law, *Gems and Gemology* **53**, 235–236 (2017).
54. C. M. Breeding, T. Ardon, *Gems and Gemology* **53**, 366 (2017).
55. B. Law, *Gems and Gemology* **54**, 57–58 (2018).
56. M. W. Doherty et al., *Physics Reports* **528**, 1–45 (2013).
57. F. Jelezko, J. Wrachtrup, *physica status solidi (a)* **203**, 3207–3225 (2006).
58. L. Li et al., *Nano Letters* **15**, 1493–1497 (2015).
59. B. J. M. Hausmann et al., *Nano Letters* **13**, 5791–5796 (2013).

2

The synthesis of diamond and incorporated defects: A review

Knowledge is like a garden: if it is not cultivated, it cannot be harvested

- African Proverb

In order to realise the potential of diamond across the span of diverse applications one must understand the growth and incorporated defects. Due to the significant expansion of diamond science and technology in the last several decades, an attempt to review the entirety of this field is beyond the scope of this thesis. Consequently, this chapter reviews the relevant background of diamond growth, defect identification and the new generation of defects that continue to be characterised.

2.1 Diamond synthesis; from inception to today

The phase diagram of carbon is well known for different pressures and temperatures where the Berman-Simon line marks the transition between diamond- and graphite-stable regions [1, 2] as shown in figure 2-1. Consequently, at room temperature and normal atmospheric pressure, graphite is the thermodynamically stable phase. Temperature and pressure within the Earth's mantle varies with depth, according to the geothermal gradient, and a portion of this resides within the diamond stable region (figure 2-1) where the majority of natural diamonds are formed [3].

Since the 1950s diamond has been synthesised in the laboratory by one of two methods, high-pressure, high temperature (HPHT), or chemical vapour deposition

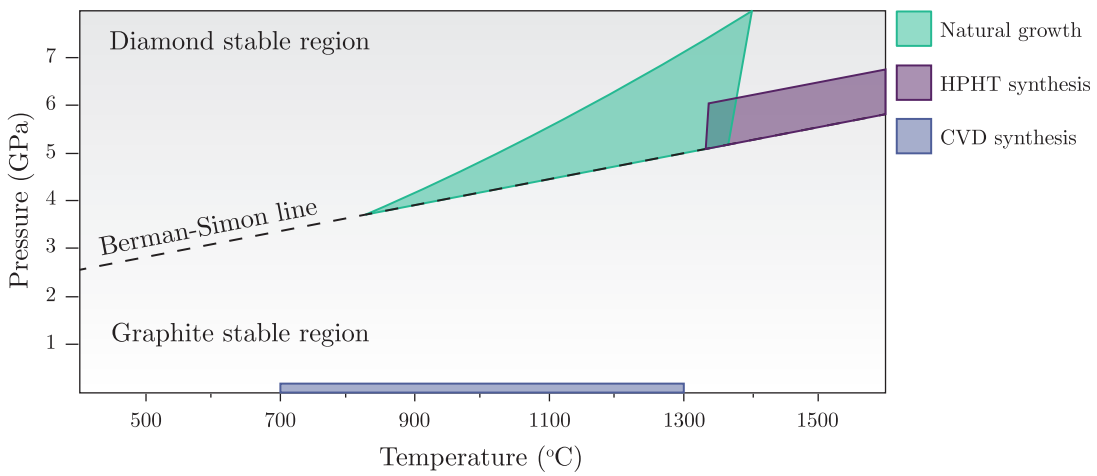

Figure 2-1 A portion of the phase diagram for carbon, showing only the graphite and diamond stable regions of carbon, adapted from [3, 4]. Purple and blue areas denote the typical temperature and pressures harnessed in catalytic HPHT and CVD synthesis respectively, where the vertical scale of CVD synthesis has been inflated for clarity. The transition line between graphite and diamond is known as the Berman-Simon line.

(CVD) where the typical pressures and temperatures of these two methods are also indicated in figure 2-1. Evidently then, these two methods rely on very different conditions to be successful, namely thermodynamics and chemical kinetics respectively. Finally, nanodiamond particles can be produced either by CVD or by detonation where high pressures and temperatures are created in a fraction of second [5]. However, since nanodiamond is not the focus of this thesis, it will not be further discussed.

2.1.1 High Pressure, High Temperature

2.1.1.1 The advent of HPHT synthesis

HPHT synthesis is directly derived from the processes that occur naturally in the Earth, where carbon is subject to high pressures at elevated temperatures for growth to occur in the diamond stable region. The realisation that diamond could indeed be synthesised this way was born from competition between two large electricity suppliers; General Electric (GE) and Allmänna Svenska Elektriska Aktiebolaget (ASEA) [6].

Bundy *et al* [7] at GE are accredited with the first successful synthesis of diamond by the HPHT technique in 1955. This built upon the previous work of Bridgman whose attempts to grow by HPHT always tended towards failure since it was not possible to sustain high pressures or temperatures for any period of time, leading him to suggest that a solvent/catalyst chemistry may be required [8]. However, Bundy and his team were able to develop a belt press capable of pressures up to 10 GPa at a sustained temperature of 2000 °C, which was not previously possible, and through this they were able to successfully synthesize diamonds ranging from 0.1 mm to 1 mm in size.

In a controversial move, ASEA claimed they produced synthetic diamond by the same method the year before GE announced their success [9], but failed to publish their results at the time.

2.1.1.2 Catalytic HPHT synthesis and growth by the temperature gradient method

The direct conversion of graphite to diamond can be inefficient owing to the extreme temperatures and pressures needed. However, it is now commonplace that HPHT synthesis is aided by carbon transport in a solvent/catalyst or by a temperature gradient within the growth capsule.

For the growth of diamond in a solvent/catalyst, it was once more the work of Bundy and colleagues [10] that realised this and used a transition metal to reduce the conditions necessary for homoepitaxial growth on a diamond seed. Carbon has a good solubility in transition metals, where typically iron is used as the solvent medium, with additional metals being used to further reduce the eutectic point [11, 12]. Commonly, these additional metals will be either cobalt or nickel, resulting in a growth environment described as Co-Fe-C or Ni-Fe-C respectively [13]. This melt then acts as a medium for the carbon to transport from the carbon/graphitic source to the diamond seed. Consequently, a typical P-T parameter space usually falls within 1200 - 1500 °C, between 5 and 6 GPa [13, 14].

The press design can also facilitate a temperature gradient across the growth capsule,

whereby a 20 - 50 °C gradient provides a driving force for crystallisation [13]. Here, crystallisation is facilitated by concentration gradients and convection, and is said to result in higher purity single crystal diamond [15–19].

An overview of various mutli-anvil high pressure presses can be found at reference [20]. However, in all presses, HPHT synthesis usually occurs within a growth capsule, shown in figure 2-2, containing multiple repeated layers whereby a carbon source is typically at the top, a metallic solvent in the middle and diamond seeds at the bottom. This package is then housed within a pressure transport medium and a graphitic heater, such that under the required pressures and temperatures carbon undergoes mass transport forming diamond on top of the diamond seed via homoepitaxial growth [15].

Inclusions can often be present in natural diamond, which are typically mineral based or metallic [3, 21]. During HPHT synthesis it can be possible for large metallic deposits to be included into the forming diamond matrix [19, 22, 23]. Therefore it

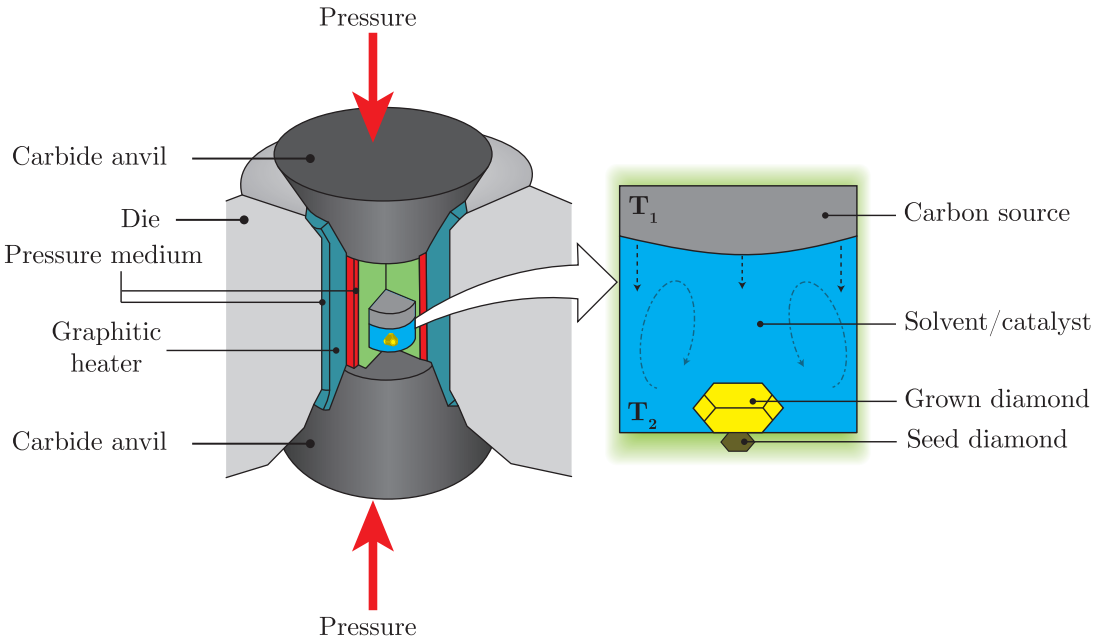

Figure 2-2 Left: Cut away of a belt-type press showing the location of the growth capsule relative to the anvil, die and heater. Right: Layered growth capsule where the carbon source is at the top, solvent/catalyst in the middle and the seed and grown diamond at the bottom. For the temperature gradient method, $T_1 > T_2$ where the difference is 20 - 50 °C. Circular dashed arrows represent convection currents in the melt whilst the vertical dashed lines represent the carbon mass transport. Figure adapted from [15].

is useful to test a diamond, with a clearly visible inclusion, by introducing a small permanent magnet nearby and if it the diamond is attracted to it then this would suggest the diamond is synthetic [24, 25].

Further to a large metallic inclusion, the metallic element itself can also incorporate into the diamond lattice as an atomic impurity where, for instance, nickel is readily incorporated and gives rise to many point defects [26, 27]. Further discussion on these types of defects are included later in this chapter.

Without any further addition of material to the growth capsule, HPHT synthetics are typically yellow to brown in colour, characteristic of nitrogen incorporation. This occurs since the growth cell incorporates air from the room, which itself is 78% nitrogen, or from impurities in the carbon source/packing capsule [28]. By adding an additional element to the capsule, known as a nitrogen getter, stable nitrides can be formed in the melt, thus restricting nitrogen incorporation in to the diamond lattice [13, 29]. Typical nitride forming elements include titanium, aluminium or zirconium, however there is a trade-off such that these elements can also form carbides at various temperatures, or facilitate inclusions, and so the choice of getter must be considered for the temperature of growth [29].

Alternative metals can be used for the growth of HPHT diamond. Kupriyanov *et al* [30] investigated the growth of diamond in a copper system where carbon's solubility in copper is 3 orders of magnitude lower than in nickel. Growth in such a medium was thought to be a potential route to limit impurity incorporation, but this was not realised.

It is also possible to grow with a solvent/catalyst by means of a non-transition metal solvent which can restrict the incorporation of nitrogen. For instance, using magnesium as the solvent medium has yielded an increased growth rate of synthetic diamond of up to 10 mm/hr, but eliminates the need for any nitrogen getter since magnesium is effective as a nitrogen getter [31].

2.1.1.3 HPHT morphology

Natural diamond exhibits octahedral morphology in agreement with the periodic bond chain (PBC) theory, however HPHT synthesis of diamond will tend to result in a cubo-octahedral crystal morphology [32].

The temperature and pressure at which a HPHT diamond grows will have a direct influence on the presence of growth sectors of different crystallographic planes. HPHT diamond can grow with mainly {0 0 1} (cubic) faces, mainly {1 1 1} (octahedral), or with both {0 0 1} and {1 1 1} (cubo-octahedral) faces [32, 33]. By looking at the effect of the solvent metal on the morphology of HPHT grown diamond, Kanda *et al* [34] also showed that {1 1 1} faces are the most stable and least susceptible to fluctuations during growth. In addition, for a decrease in growth rate, minor planes such as {1 1 0} and {1 1 3} will develop [17].

Aside from variations in the pressure and temperature conditions, impurity uptake can also influence the morphology of HPHT diamond. In type Ib HPHT diamond, the role of nitrogen can act to stabilise octahedral growth sectors when the growth rate is reduced [35]. For type IIb diamond, boron can promote growth of {1 1 5} sectors [36] or aid development of {1 1 1} sectors [37].

Equally, the growth of diamond in a metallic solvent will also influence the final morphology where adsorption in the metallic nitride can result in developed {1 1 0} and {1 1 3} faces [34]. Non-traditional melts can also promote the growth of higher order planes, where Palyanov *et al* found trapezohedron growth sectors in diamond grown in a sulfur-carbon [38] and phosphorus-carbon systems [39].

Whether the diamond is fashioned into a gemstone or sliced into plates, the morphology of HPHT diamond can be distinguished by above band gap excitation and optical imaging, such as UV excitation [40], or by imaging with high energy electrons in the scanning electron microscope (SEM) fitted with a cathodoluminescence (CL) detector [41]. This is, in part, due to the growth sector dependence on impurity uptake, which ultimately affects the luminescence as detected either by UV excitation or electron excitation. More on the growth sector dependence of impurities will be discussed later on in this chapter.

2.1.1.4 Recent advances in HPHT growth

Historically HPHT synthetic diamond tend to be grown as small, micron-sized particles for abrasive applications (otherwise termed as diamond grit), where the diamond retains its yellow/brown colouration to help reduce the cost of the diamond with high growth rates. Large yellow Ib diamond has also long been produced [35, 42], but it had always remained challenging to produce large IIa diamond by HPHT whilst retaining good crystalline quality.

In 2015, D'Haenens-Johansson *et al* [43] reported on a large type IIa HPHT diamond, grown by New Diamond Technology Ltd (NDT), cut to a gemstone at 5 ct in mass (1 ct = 0.2 g), highlighting very good clarity (no inclusions) and good colouration (implies little to no nitrogen or boron incorporation). Deljanin *et al* [44] also reported on a 10 ct type IIb HPHT diamond grown too by NDT. In the same year, Sumiya *et al* [45] independently demonstrated the growth of high purity type IIa HPHT diamond, where the final crystal size was over 10 mm in diameter and up to 10 ct in mass with low dislocation densities.

More recently, a 15 ct HPHT synthetic diamond (gem cut) was also investigated by the GIA grading laboratory [46], again grown by NDT. Although this diamond contained several instances of inclusions, it does signify that the size of diamond grown by HPHT is now increasing.

Not only is the size of HPHT diamond increasing, but the quality of the diamond is also improving. From white beam X-ray topography, high purity HPHT diamond can exhibit very low dislocation densities [47] which is a desirable trait for applications that material with high crystalline perfection such that X-ray optics are improved [48–50], offering several superlative material properties over silicon.

2.1.2 Chemical Vapour Deposition

2.1.2.1 Diamond growth in the graphite stable region

Whilst growth of diamond by the HPHT mechanism is intuitive with regards to the carbon phase diagram, chemical kinetics can be harnessed to enable the growth

of diamond where graphite is the thermodynamically stable phase of carbon (see figure 2-1).

Within a reaction chamber, diamond growth is facilitated by the dissociation of a carbonaceous gas, such as methane (CH_4), along with hydrogen gas (H_2) whereby hydrocarbon and atomic hydrogen radicals are created (activation). Dissociation typically occurs either by heat or microwave plasma, and growth (by carbon deposition) happens at the bottom of the chamber on a substrate containing either non-diamond or single crystal diamond for hetero- or homoepitaxial growth respectively.

Chemical vapour deposition (CVD) was first realised by Eversole throughout the 1950s and later patented in 1962 [51, 52]. It is said that Eversole's first successful attempt at synthesising diamond came in 1952 [6] thus predating the advent of HPHT synthesis. CVD growth was then independently demonstrated by Angus *et al* [53] and Derjaguin *et al* [54] in 1968. A breakthrough in the CVD growth of diamond came from the National Institute for Research in Inorganic Materials (NIRIM) in Japan throughout the 1970s and 1980s. Teams at NIRIM were able to demonstrate improvements in the growth rate of diamond from both hot filament and plasma activation methods, resulting in the design and commercial sale of CVD reactors [55–58].

Today, there are a multitude of different reactor architectures, where Schwander and Partes [59] have provided an in-depth review of these. From the heating of a hot filament (usually tungsten) which has a limited power input, particulates are often sputtered on to the growing diamond region [60, 61], thus the highest purity diamond is born from a microwave plasma CVD (MPCVD) approach [62, 63]. An example of an MPCVD reactor is shown in figure 2-3 along with the chemical processes that occur during synthesis.

Regardless of the reactor, the mechanism for diamond growth remains the same by a series of events following the dissociation process. Very simplistically, the process of diamond growth can be broken down to this sequence [67]:

1. A free H radical abstracts a surface bonded H, leaving behind a reactive site

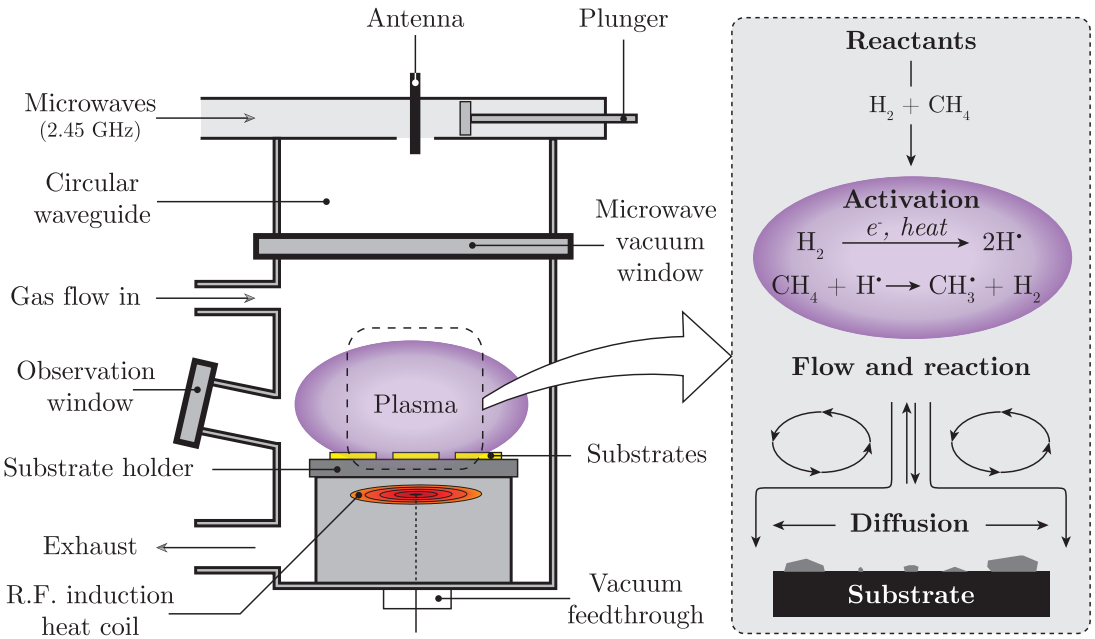

Figure 2-3 Left: A schematic of one type of chemical vapour deposition (CVD) where diamond growth occurs on top of the substrate by the activation of carbonaceous gas via a microwave plasma. Right: The chemical processes that occur for carbon deposition on the substrate. Figures adapted from [64–66].

2. A methyl radical collides with the reactive site, leaving CH_3 surface bonded
3. The neighbouring surface bonded H is abstracted by another free H radical, and step 2 then occurs again
4. The two neighbouring surface bonded CH_3 groups, each have a bonded H abstracted by reacting with free H radicals
5. Neighbouring CH_2 groups reconstruct to complete the carbon ring resulting in a hydrogen terminated diamond surface.

Pertinent to CVD growth therefore is a sufficient quantity of hydrogen in the reactants to drive the abstraction process and prevent graphitisation [68]. The chemical ratio of carbon to hydrogen, along with oxygen, required for CVD synthesis is summarised by the Bachmann triangle where diamond growth tends to occur close to the C-O line [69].

In reality there are many other factors to consider for CVD growth of diamond. For the substrate alone, one must consider the influence of the starting material,

temperature, and distance from the activation zone with regards to the growth of diamond itself [70–74]. Many other parameters such as plasma shape, density, temperature, gas purity, pressure and reactants all play a vital role in MPCVD growth resulting in a large parameter space to operate within [75].

MPCVD synthesis has achieved growth rates as high as 150 µm h^{-1} [76] where it has also been demonstrated that good quality, low absorption diamond can be produced at a synthesis rate of up to 100 µm h^{-1} [77].

2.1.2.2 CVD diamond morphology and impurity control

With homoepitaxial growth of CVD diamond, the choice of substrate orientation will directly influence the synthesised diamond quality and defect incorporation. As the {0 0 1} crystallographic plane is the easiest to mechanically polish with a good flatness [78], this tends to be the plane presented for CVD synthesis. Growth in this orientation facilitates high quality controlled growth yielding good quality material, although care must be taken at the substrate to limit dislocations that propagate in a ⟨0 0 1⟩ direction [79, 80].

It is not surprising that diamond can be grown on on {1 1 1}, {1 1 3}, and {1 1 0} orientated substrates, but doing so can cause some complications with the diamond lattice. For the case of {1 1 1} substrates, the synthesised diamond is prone to twinning [81, 82] and microfaceting can be observed from {1 1 0} growth [83]. Usually growth on either three of these orientations provides a route for defects to be grown in with a preferential orientation [84–88].

The final morphology of the CVD grown diamond is characterised by the relative growth speeds of {1 1 1}, {1 1 0}, and {1 1 3} normalised to the {0 0 1} plane, and results in three parameters known as α, β, and γ respectively describing the steady state morphology which can be adequately modelled [89–91]. For various applications of diamond, the morphology and crystallinity needs to be considered, where material properties can be affected. Nitrogen incorporation is known to modify the morphology as well as increasing the growth rate [63, 92].

The presence of sufficiently high nitrogen concentration in the gas phase results in

a step-flow growth model for CVD synthesis, such that steps and risers form in the material giving rise to striations throughout the material [79]. This can be seen by an increased production of the nitrogen vacancy defect and will be discussed later in this chapter. Step-flow growth in this way can also act to cause a deflection in the propagation direction of dislocations, from [0 0 1] to [1 0 1], for CVD grown on (0 0 1) substrates [93].

With the reduction of nitrogen from the source gas, the mechanism for growth alters such that step-flow growth is no longer dominant. Inhibiting the incorporation of nitrogen can be achieved by an increase in the substrate temperature, as well as the addition of oxygen [94, 95]. It has been reported that a nitrogen concentration below 0.2 parts per billion (ppb) can be achieved, as limited by the detection sensitivity [92]. In a review by Butler *et al* [96], the kinetic Monte Carlo models of CVD growth without nitrogen suggests that on a {0 0 1} surface, the layers are built by a process similar to island-type growth. On the other hand, it has been suggested that growth with oxygen may promote lateral growth with reduced nitrogen incorporation [97].

2.1.2.3 Novel uses of CVD grown diamond

The CVD synthesis method lends itself to create geometries of diamond that would not otherwise be possible without significant post-growth processing. In all cases where a non-diamond template is used, the diamond deposited is polycrystalline in nature due to the lattice mismatch on heteroepitaxial growth substrates.

Tweeter domes are a key component within loudspeakers, where the function is to radiate high frequency sound with minimal distortion. As the geometry of this component is hemispherical it must be made from stiff and durable material [98], and thus often manufactured from plastics or lightweight metals. In preshaping an appropriate growth substrate (such as silicon) to a hemispherical geometry, polycrystalline diamond is grown directly in the tweeter dome shape without the need for significant post-growth machining. Using diamond this way yields an acoustic cone break up frequency over 3x higher than the upper limit of the human-audible range, providing very high fidelity across the acoustic spectrum [4,

99], and is now a viable commercial product.[a]

Several other areas of hemispherical diamond have also been reported such as hip joint implants [100, 101], jaw implants [102, 103] and military applications [104]. However in most cases the material deposited is diamond-like carbon or tetrahedrally bonded (sp^3) amorphous carbon rather than true (poly)crystalline diamond.

2.1.2.4 Advances and challenges owing to CVD growth

Clearly then, there is a wealth of history and expansion in the capabilities of CVD diamond. There are, however several limitations associated with this technique.

There are several material properties of diamond that make it an attractive material for the power electronics market, such as the high thermal conductivity, high breakdown field and low dielectric constant [105]. Whilst large scale wafers of diamond are not currently routinely produced by CVD, Yamada *et al* has proven it is possible to grow a larger crystal, approximately 50 mm in width, by a mosaic approach [106, 107]. This process relies on cloning a HPHT substrate and tiling them for CVD overgrowth, although dislocations tend to be introduced at the substrate boundaries.

Heteroepitaxial growth on non-diamond is starting to show promise for large area single crystal diamond. In growing on an iridium based substrate a large (92 ct) wafer was recently synthesised with a maximum lateral diameter of 92 mm and a thickness of 1.6 mm [108]. However, heteroepitaxy on iridium based substrates results in a diamond that contains a substantial concentration of dislocations, due to a lattice mismatch, which degrades crystalline quality and may therefore impinge on the suitability for certain applications [105, 109].

The size of single crystal homoepitaxially grown CVD diamond does, however, appear to be increasing. Recently the GIA research laboratory characterised a CVD diamond over 5 ct in mass [110]. Here, this lab note states that the polished

[a]At time of writing; Bowers & Wilkins 800 Series Diamond home audio (Queens Award for Enterprise in Innovation), Bowers & Wilkins Diamond Surround Sound System for BMW 5, 6 and 7 series GT

gemstone dimensions were $10.04 \times 9.44 \times 6.18$ mm, implying that the grown rough had substantial thickness, as well as lateral width, in order to remove material by cutting and polishing resulting in this gemstone.

It is known that CVD grown diamonds contain a higher number of dislocations in the material compared to HPHT grown diamond, as influenced by the choice of substrate [80, 111]. There are several ways to help reduce dislocations in CVD growth which involve careful substrate choice and preparation. There are two well demonstrated techniques for this:

- the reduction of the surface roughness for a $\{0\,0\,1\}$-orientated substrate by oxygen etching [112] or chemical mechanical polishing [113]
- the selection of a growth substrate that is high purity and low dislocation density HPHT diamond [114]

Whilst the purity of CVD diamond can be controlled with a semiconductor-like precision, some impurities are persistent and often silicon tends to be incorporated into the diamond, and is considered to be due to the etching of the quartz windows on the reactor [79, 115]. Quantum based applications require extreme control of material growth to reduce unwanted impurity incorporation (such as silicon and nitrogen), so that defects can be introduced post-growth without becoming compromised. Strides are being made to reduce this in CVD diamond, by careful consideration of the source gas and use of purifiers so that impurity incorporation is minimised [116], where it is possible to purchase CVD with incredibly low impurity concentrations[b].

2.2 Defects in diamond

As described in chapter 1, diamond is not typically just a perfect and pure carbon lattice but can contain impurities, or defects, that either extend beyond the unit cell or are contained within it which are termed extended and point defects respectively. Fundamentally, this gives rise to many defects within diamond, which can be

[b] "*Quantum Grade*" CVD: `www.e6cvd.com`

characterised through a plethora of techniques. Irrespective of diamond for the gemmological or industrial markets, one must be aware of defects (both extended and point) and how they impact on the properties of the diamond itself.

2.2.1 Extended defects

The three main types of extended defects in single crystal diamond are twinning, stacking faults and dislocations.

Twinning can be seen in natural and synthetic diamond [81, 82, 117–120]. Fundamentally, a twin is the mirror image of the diamond crystal joined to itself, often seen as a rotation in the lattice by 180° about the ⟨1 1 1⟩ crystallographic axis (the C-C bond axis). The perfect fcc diamond lattice can be represented in terms of layers as *ABCABCACB* (figure 2-4a), where twinning changes this to *ABCABACBA* for the mirror plane, *B* (figure 2-4b). In CVD diamond, it is thought that twinning is caused by re-entrant corners which can also act to increase the growth rate [119]. Whereas in HPHT synthesis, it is suggested that either plastic deformation during growth [120] or a large concentration of nitrogen incorporation [35] can give rise to twinning. Twinning can also occur by a 109.5° rotation about the ⟨0 1 1⟩ axis during CVD synthesis on a {0 0 1} orientated substrate [121].

Conversely, a stacking fault is considered as a perturbation to the layers whereby the layer order is out of sequence either by the exclusion of layer (*ABCACABC*, figure 2-4c) or inclusion of an extra layer (*AB**A**CABCABC*). These are most prevalent in {1 1 1} sectors of HPHT material, as well as natural material, and are easily observed by x-ray topography (XRT) by different crystallographic reflections [122]. It is sometimes possible to remove a stacking fault by high pressure, high temperature annealing, where the stacking fault may dissociate into dislocations [80].

Whether natural or synthetic, dislocations present discontinuities in the diamond lattice that follow a particular crystallographic direction. Here, dislocations tend to be mainly restricted to {1 1 1} glide planes [123, 124]. Since the majority of CVD grown diamond can be controlled by their α, β, and γ parameters, twinning and stacking faults (which are often seen in the {1 1 1} crystallographic plane) can

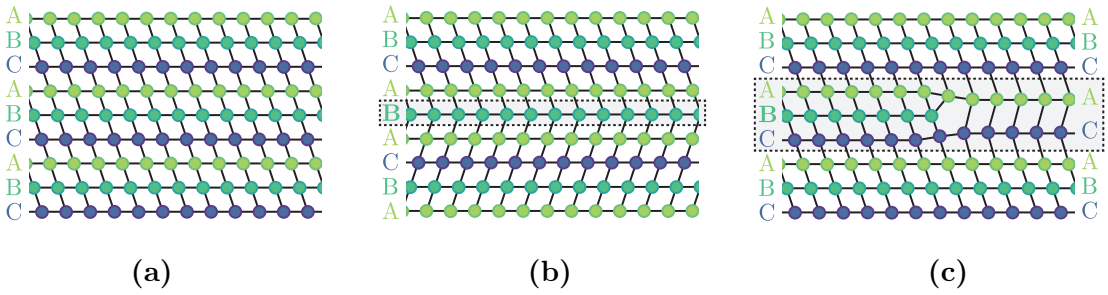

Figure 2-4 (a) Normal representation of diamond with layers *ABCAB-CACB*. (b) A twinned diamond lattice where *B* is the mirror plane responsible for twinning. (c) An intrinsic stacking fault by the removal of atoms in the highlighted *B* layer.

be limited and so the most discussed extended defect usually concerns dislocations.

Dislocations in diamond have many types and are defined by their Burgers vector, $\boldsymbol{b}$, relative to the dislocation line, $\boldsymbol{l}$. Classifications of dislocations are made where $\boldsymbol{b} \perp \boldsymbol{l}$ is an edge dislocation, $\boldsymbol{b} \parallel \boldsymbol{l}$ is a screw dislocation, and a mixed dislocation when $\boldsymbol{b} \measuredangle \boldsymbol{l}$ (i.e. mixed 60°). They are often characterised through XRT and/or by transmission electron microscopy (TEM). Blumenau *et al* [125] have provided a theoretical study of 12 different dislocation structures in the $\{1\,1\,1\}\langle 1\,1\,0\rangle$ slip system, as is relevant for a fcc crystal. For CVD grown on a $\{0\,0\,1\}$ substrate threading dislocations are also seen to propagate in a $\langle 0\,0\,1\rangle$ direction on a $\{0\,1\,1\}$ plane [126, 127].

Sumiya and Tamasaku [128] show dislocation densities in the HPHT synthesised diamond are directly influenced by the diamond seed choice, with very low dislocation and high purity material being synthesised by the temperature gradient method from very low dislocation diamond seeds. Khokhryakov *et al* [42] investigated the role of nitrogen in HPHT synthesis and saw that as the concentration of nitrogen increases, so does the dislocation density since the C-N bond is 30% longer than the C-C bond, and, thus introduces local strain to form dislocations.

Dislocations in CVD material also tend to reflect the quality of the growth substrate used. Martineau *et al* [79] found that in homoepitaxial growth on HPHT diamond, dislocations begin at the interface with the substrate and propagate through the material. Recently, Tallaire *et al* [114] have demonstrated that it is possible to grow very low dislocation density CVD diamond by homoepitaxial growth on very

low dislocation HPHT diamond.

Conversely, heteroepitaxial growth of CVD diamond often results in highly dislocated material where the dislocation density is higher than that homoepitaxially grown. However, dislocations in this material will be greater at the substrate side compared to later in the growth as the dislocations will evolve either by annihilation, addition or scattering [109].

The strain field induced by dislocations gives rise to a birefringence pattern observable under cross-polarisation imaging, where analysis of the birefringence can lead to an estimate of the stress caused by a number of dislocations [129]. Quantitative birefringence measurements, as taken on a Metripol system, can also reveal the nature of dislocations and stacking faults in diamond [122]. Dislocations can also be revealed by selective etching revealing pits at the surface of the diamond where the angle of inclination changes depending on the dislocation type [130].

Broad emission between 420 - 440 nm (2.8 - 2.9 eV) is referred to as Band A emission, which can be seen in CL imaging and spectroscopy and is correlated with the presence of dislocations in the material. The mechanism for this emission isn't yet fully understood; a long standing proposal from Dean [131] suggests the emission is from donor-acceptor recombination at the dislocation. However Band A emission can be seen in diamonds with no boron included (an electron acceptor) [132] and in studying diamond films, it is suggested the Band A emission may arise from sp^2 networks in the sp^3 matrix [133].

2.2.2 Point defects

Work within this thesis concerns the characterisation of diamond material through their point defects. Whilst the consideration of extended defects enables diamond to be utilised in several applications, an understanding of the point defect inclusion also enables many other technologies. A point defect presents a quantum system, where technologies are facilitated either by the exploitation of the properties of this system or the removal of certain (parasitic) point defects. A menagerie of point defects have already been identified in diamond, many catalogued by Zaitsev [134],

but new defects continue to be discovered and characterised.

On the simplest level, a point defect in diamond can be the substitution of a carbon atom with another element, such as nitrogen or boron, which are similar atomic size to a carbon atom. The (intentional) inclusion of another atomic element is referred to as doping. The next step up is the generation of Frenkel defects by the creation of a vacancy and interstitial, upon which many other more complex defects are formed by migration. What follows is an overview of common and new point defects found in diamond, with an emphasis on their optical signatures.

2.2.2.1 Carbon interstitials and vacancies

With sufficient energy, radiation either by electrons, neutrons or ions, are able to displace carbon atoms in the diamond lattice. Frenkel defects are formed as a consequence, and if the energy is high enough, cascade damage is possible. Subsequently radiation damage has revealed a variety of intrinsic point defects.

EPR experiments in 1962 showed that in electron irradiated type IIa diamond, two new spectra could be obtained which were subsequently assigned as R1 and R2 [135]. Later it was confirmed that R1 is the di-$\langle 0\,0\,1\rangle$-split interstitial defect with $\mathscr{C}_{1h}$ symmetry [136] and R2 the neutral $\langle 0\,0\,1\rangle$-split self interstitial ($C^0_{I_{001}}$) with $\mathscr{D}_{2d}$ symmetry [137]. A series of optical lines are associated with the R2 defect at 666.9 nm (1.859 eV) and 735.8 nm (1.685 eV), with the latter being a forbidden transition by mixing of states with the 666.9 nm line [138, 139]. No optical lines have been attributed to the R1 defect, and many other self-interstitial related defects may exist yielding many possibilities for optical lines or EPR signals.

Within diamond, the vacancy itself is one of the best understood defects and observed in the vast majority of irradiated diamond [140, 141]. GR1 dominates irradiated diamond with a zero phonon line (ZPL) doublet at 741.1 nm and 744.6 nm (1.673 eV and 1.665 eV), along with the vibronic absorption band. The strength of GR1 is directly correlated with the irradiation dose [140] and is assigned as the neutral charge state, V^0. An additional set of peaks in absorption between 430.5 nm and 411.9 nm (2.880 eV and 3.010 eV) are said to be electronic transitions

of V^0 and are assigned as GR2 - 8. ND1 can also be seen after irradiation with a ZPL at 393.7 nm (3.149 eV) with associated vibronic absorption band. In reviewing irradiation data, Davies suggested that by the irradiation of nitrogen rich diamond, ND1 must be the negative charge state of the vacancy, V^- [142].

Both charge states of the vacancy exhibit $\mathscr{T}_d$ symmetry [143, 144], where the doublet for GR1 arises from a transition between the ^1E ground state and $^1T_2$ excited state. The ground state of V^0 is diamagnetic (S = 0) and cannot be measured by EPR, although it has been possible to measure an excited state ($^5A_2$) by EPR and electron double nuclear double resonance with optical excitation [145]. The ground state of V^-, and symmetry, were confirmed through EPR by Isoya *et al* [146], showing that the ground state is paramagnetic at $S = \frac{3}{2}$.

Through a series of isothermal anneals, both charge states of the vacancy are shown to have the same migration energy (2.3 eV) [141]. A slight decrease in GR1 absorption at an activation energy of 1.6 eV - 1.7 eV is thought to correspond to vacancies combining with local interstitials [147, 148], which can also result in a narrowing of the linewidth of the ZPL [149]. The vacancy is immobile at room temperature, but becomes highly mobile with temperature and anneals out ~ 600 °C, forming vacancy-complexes with impurities or with additional vacancies. Long lifetimes in positron annihilation studies give evidence for vacancy clusters in brown coloured natural diamond, which can be removed upon HPHT annealing [124, 150].

2.2.2.2 Substitutional and interstitial nitrogen in diamond

Given nitrogen is readily soluble in both natural and synthetic diamond, there is a wealth of knowledge on nitrogen related defects. Clearly, the significance of nitrogen in diamond is noted by the classification of the diamond type by the inclusion or exclusion of nitrogen in the diamond lattice (see figure 1-2).

EPR measurements taken on natural diamond in 1959 correctly identified the neutral substitutional nitrogen defect, N_S^0 (sometimes referred to as P1), as bonded to four nearest-neighbour carbon atoms, where the unpaired electron occupies an

antibonding orbital between the nitrogen atom and one of the nearest neighbour carbon atoms [151]. Since then, N_S^0 has been readily identified not only in EPR but through absorption spectroscopy. A quantification of the N_S^0 concentration can be made by EPR, but also by the maximum in infrared absorption at 1130 cm^{-1} [152, 153]. This defect also provides a sharp peak at 1344 cm^{-1} which is associated with a local vibrational mode [154].

Since N_S^0 is a deep donor in diamond, electrons are readily donated to nearby defects in the lattice leaving behind N_S^+ which is not EPR-active (non-paramagnetic) but can be seen in infrared absorption with peaks at 950 cm^{-1}, 1046 cm^{-1} and 1332 cm^{-1} [155]. Again, a quantitive measurement of the concentration of N_S^+ can be made by the 1332 cm^{-1} peak, although care must be taken with this assignment since there is a high density of phonon states at this position and so all three features must be present [155]. Ultrafast spectroscopy has also suggested the negative charge, N_S^-, may exist whereby the electron liberated from N_S^0 into the conduction band will readily recombine with another N_S^0, and is thought to give rise to an absorption peak at 1349 cm^{-1} [156].

Typically the representation of charge transfer is given by equation (2-1) whereby X can be any defect and the relative charge states can be manipulated either by applying heat or UV illumination.

$$N_S^0 + X^0 \underset{\text{Light}}{\overset{\text{Heat}}{\rightleftharpoons}} N_S^+ + X^- \tag{2-1}$$

The presence of nitrogen during growth can directly influence the morphology and increases the growth rate for both HPHT and CVD synthesis [157, 158], but it is known that the nitrogen concentration in diamond directly depends upon the crystallographic plane. A study by Kanda, and later updated by Burns *et al*, resulted in the (modified) Kanda diagram which describes the growth sector dependence for the uptake of substitutional nitrogen, and boron, which is strongly seen in HPHT synthetic diamond [159]. Thus, nitrogen uptake typically decreases based on this sector ordering: $\{1\,1\,1\} > \{1\,0\,0\} > \{1\,1\,3\} > \{1\,1\,0\}$.

Relative to self-interstitials and their complexes, less is known for nitrogen related interstitials, however it is reasonable to speculate there can be many permutations

either as a lone interstitial, interstitial aggregates or complexes with other point defects. In type I diamond, one such interstitial related defect is the di-nitrogen ⟨0 0 1⟩-split interstitial [160, 161], where uniaxial stress and isotopic substitution has shown that this defect has a local vibrational mode at 1450 cm^{-1} in absorption (known as H1a) [162, 163]. A ZPL at 594 nm (sometimes reported as 595 nm) is also created in radiation damage, nitrogen containing diamond. Whilst there has been no unambiguous assignment of this defect, annealing studies suggest it is correlated with the production of two new zero phonon lines at 1934 nm and 2024 nm (0.612 eV and 0.641 eV) known as H1b and H1c respectively, and thought that the 594 nm centre migrates before becoming trapped at A-centres (N_{2S}) and B-centres (N_4V) [164].

2.2.2.3 The nitrogen vacancy defect

A suite of complexes can also form with substitutional nitrogen which tend to involve a vacancy, and depending on the material, hydrogen. An overview of these complexes is presented in figure 2-5a. Of these, the NV centre (figure 2-5b) is perhaps the most heavily studied due to facilitating optically detected magnetic resonance (ODMR) in the negative charge state, which is pertinent to applications in quantum sensing and processing [165, 166].

The first observation of the NV centre was reported by du Preez in 1965 in type Ib diamond that had been irradiated and annealed, where temperatures above 900 K resulted in absorption with a peak around 637 nm (1.945 eV) [168]. Subsequent work by Davies and Hamer revealed this ZPL belongs to a trigonal defect with a transition occurring between the ground A state and excited E state [169]. Loubser and van Wyk [170] concluded the presence of an NV centre by conducting EPR on samples that had been irradiated and annealed. At 900 K, an $S = 1$ defect with trigonal ($\mathscr{C}_{3v}$) symmetry and zero field splitting of 2.88 GHz was observed, where the hyperfine structure indicated the defect has a single nucleus of $I = 1$ with ~100% abundance indicating nitrogen was present. Reddy *et al* and Redman *et al* [171, 172] then demonstrated that the 637 nm ZPL was associated with this EPR defect and confirmed the transition. The ZPL transition is now known to occur

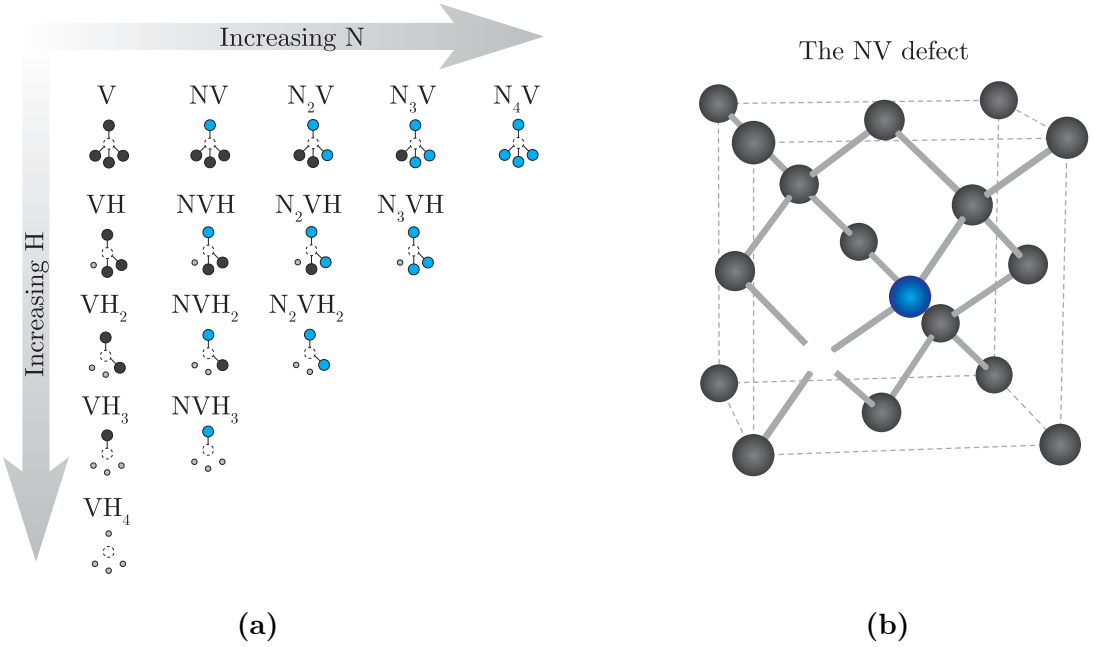

Figure 2-5 (a) With just one vacancy in the lattice, there are a multitude of nitrogen vacancy and nitrogen vacancy decorated with hydrogen defects in diamond. A depiction of the 5 atom basis of each defect is given where blue indicates nitrogen, grey indicates hydrogen and dashed outline as the vacancy. (b) The nitrogen vacancy (NV) centre in diamond is the most heavily studied defect in diamond, where the blue atom represents nitrogen next to a missing carbon atom. Figure adapted from [167]

between the $^3A_2 \rightarrow {}^3E$ states (figure 2-6a), and is reported to have a fluorescence lifetime between 10 and 12 ns [173].

With high enough nitrogen concentrations, both charge states of the NV centre can be observed simultaneously [174]. The neutral charge state, NV^0 has also been characterised as having $\mathscr{C}_{3v}$ symmetry with a ground state of $S = \frac{1}{2}$, where a 575 nm (2.156 eV) ZPL transition occurs between the $^2E \rightarrow {}^2A$ states [175] (figure 2-6b), and a fluorescence lifetime between 13 and 21 ns [176–178]. Despite being paramagnetic, it is not possible to detect NV^0 in the ground state due to the Jahn-Teller effect, however Felton *et al* [179] successfully detected NV^0 by EPR by the excited $^4A_2$ state.

In addition to the charge state manipulation in equation (2-1), the relative charge states can be described by the processes in equations (2-2). Clearly if there is a surplus of N_S^0 relative to the NV centres, then the majority of the NV centres will favour the negative charge state until there is a critical point when N_S^0 is no longer

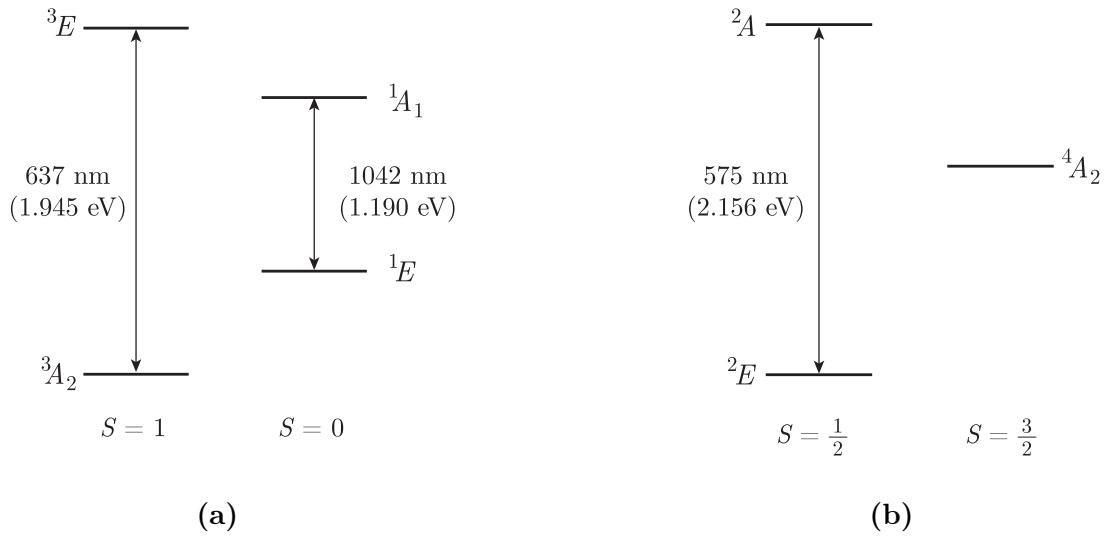

Figure 2-6 The energy levels for the nitrogen vacancy centre in the (a) negative charge state, NV^- and (b) neutral charge state, NV^0. The arrows represent the ZPL transition for each defect, and the associated spin state is listed underneath. Figure adapted from [173]

involved in the charge dynamics and the neutral charge state will become present.

$$N_S^0 + V^0 \rightarrow NV^0 \tag{2-2a}$$

$$NV^0 + N_S^0 \rightarrow NV^- + N_S^+ \tag{2-2b}$$

It is thought the positive charge state, NV^+, is stable in diamond, but to date has not been unambiguously spectrally characterised. Density functional theory (DFT) indicates the Fermi level of the defect is ~1.0 eV above the valence band [180]. Steeds *et al* [181] reported a new ZPL at 517.6 nm by the annealing of electron irradiated HPHT diamond containing boron, but has not since been replicated or confirmed to be NV^+. Pfender *et al* [182] were able to demonstrate a 4-fold increase in the nuclear spin coherence time by electrically biasing NV^0 into a state devoid of luminescence, thought to be NV^+.

As CVD diamond growth relies on chemical kinetics, preferential alignment of the NV centre has been observed for diamond grown on substrates with a non-{0 0 1} surface, where it is thought that the NV centre grows in as a unit [86–88]. Less is known about the incorporation of NV in HPHT and natural diamond.

ODMR on the NV^- centre is carried out in photoluminescence measurements, with the supply of microwaves to the diamond at the zero field splitting (~2.88 GHz),

such that up to a 30% reduction in contrast of the fluorescence is observed by the intersystem crossing to the singlet S = 0 state [183]. The relaxation in the singlet state yields a ZPL at 1042 nm [173] (figure 2-6a). Excitation of NV^- and relaxation through the intersystem crossing pathway leads to a spin polarisation into the $m_s = 0$ state.

The spin Hamiltonian of the NV^- centre (see section 3.2.3) shows that the NV^- centre is directly affected by the electric, magnetic and strain field vectors. The ODMR spectrum can be a powerful tool for magnetometry since an external magnetic field lifts the degeneracy of the $m_s = \pm 1$ levels. As the NV^- principle symmetry axis lies along $\langle 1\,1\,1 \rangle$ it can take one of four orientations in the crystal. When an external magnetic field is co-linear with one of the $\langle 1\,1\,1 \rangle$ directions of NV^-, the magnitude of separation between the resonances is greatest and is linearly dependent upon the strength of the magnetic field. It is for this reason that it has been possible to use NV^- centres in the reading of hard drive discs [184] and even provide high spatial resolution maps of living cells [185]. Electric field and strain vectors have also shown similar affects [186, 187].

Single NV^- centres present an environment where a single electron can be optically manipulated and readout at room temperature. This very nature of the defect has enabled the first loophole free (no contradiction to local realism) violation of the Bell inequality, by the quantum entanglement of two individual NV^- centres separated by a distance of 1.3 km [188] which is an important step forwards for secure quantum communications.

A typical figure of merit for quantum computation however is the decoherence lifetime (T_2) of the system, where a long decoherence lifetime will facilitate many operations before the system needs to be reinitialised. In high purity CVD material, it can be seen that the T_2 time of the NV^- can approach a temporal length that is ^{13}C limited at ~650 µs, even at room temperature, whilst a ^{12}C enrichment can yield nearly a 3 fold increase in the decoherence time [116, 189].

More on the physics of the NV^- centre will be presented in section 3.2.3, however a comprehensive review of the characterisation of this defect and its applications can be found in the review paper by Doherty *et al* [173].

To aid the incorporation of NV^- into quantum technology, techniques have been developed for the deterministic creation of single centres at specific locations, which is another requirement for scalable quantum computation. One technique relies on the implantation of nitrogen, either by a focussed beam [190] or masking methods [191], typically into CVD diamond (with [N] $<$ 5 ppb), and then upon annealing NV^- centres with long decoherence lifetimes can be made [189]. An alternative, recent development has been the laser writing of NV^- centres in low N_S^0 concentration diamond, and is facilitated by a series of ultrafast laser pulses to create vacancies through a multi-photon process which are then captured by nearby N_S^0 defect [192]. This negates the need for pattern masking and ion implantation, enabling the fabrication of 3D arrays, with near unity yield [193], of single NV^- centres exhibiting ^{13}C limited decoherence lifetimes [194].

Given the prominence of NV centres in research, as well as the nature of hydrogen in CVD growth, the NV : H defect has also been identified. This defect gives rise to the 3123 cm^{-1} peak in IR absorption which was originally thought to be the negative charge state but later reassigned to the neutral charge state $NV : H^0$ [79, 195]. $NV : H^-$ can be detected and quantified through EPR but does not have any associated IR absorption peaks [86, 195, 196]. Khan *et al* [195] also investigated the correlation of a 520 nm absorption band relative to the intensity of the 3123 cm^{-1} peak by charge transfer and annealing, and whilst there was a direct correlation between the two features, it wasn't clear if they are the same as the acceptor level of NV : H is lower in energy than the 520 nm band.

Following on from the pathway setout in figure 2-5a other notable nitrogen-vacancy related defects with optical signatures are:

- N_2V^0 (H3 defect) with ZPL at 503 nm (2.463 eV) and N_2V^- (H2 defect) with ZPL at 986 nm (1.257 eV). These defects are $\mathscr{C}_{2v}$ in symmetry [169, 197] and are known to be highly photochromic [198]. The assignment of H2 to N_2V^- was made possible by the EPR signal of the $S = \frac{1}{2}$ ground state in ^{15}N enriched diamond [199]. To date, no conclusive optical identification of N_2V decorated with hydrogen has been observed, however a new EPR signal highlighted by Hartland [200] indicated the defect involved hydrogen and

two nitrogen atoms and thus may be a stable defect in diamond.

- N_3V (N3 defect) with ZPL at 415 nm (2.985 eV) and has the $\mathscr{C}_{3v}$ point group [201]. This defect is synonymous with natural diamonds and is only formed in synthetic diamond through HPHT treatment [202]. The $N_3V:H$ centre has been observed in IR absorption with a strong 3107 cm^{-1} absorption peak, accompanied by a bend mode at 1405 cm^{-1}. Uniaxial stress measurements concluded $N_3V:H$ also belongs to the $\mathscr{C}_{3v}$ point group, and that the 3107 cm^{-1} peak is the result of an $A \rightarrow A$ transition [203, 204].
- N_4V (H4 defect) with ZPL at 496 nm (2.499 eV), as well as a broad IR absorption in the one-phonon region [205], with tetrahedral ($\mathscr{T}_d$) symmetry. Through a series of annealing studies by Collins [202], it was determined that this defect is less stable than the H3 defect which potentially explains why H4 detection in natural diamond is rare despite the presence of B centres in the absorption spectroscopy.

2.2.2.4 Boron related defects

Of similar atomic size to carbon, boron can be incorporated as a substitutional atom in the diamond lattice. As an electron acceptor, boron doped diamond is readily seen in applications where electrically conductive material is required in harsh or demanding environments, such as electrochemical sensors [206, 207], water cleanup [208] or high power electronics [209, 210].

As highlighted in section 2.2.2.2, the modified Kanda diagram reveals the sector dependence of nitrogen and boron [159]. From this, the boron uptake typically decreases based on this sector ordering: $\{111\} > \{110\} > \{113\} > \{100\}$.

Boron quantification in diamond has seen a multitude of research take place with quantitative analysis of the concentration by secondary ion mass spectrometry (SIMS) [211], Raman spectroscopy [212, 213], infrared (IR) absorption [214, 215], Hall effect measurements [214, 216] and CL spectroscopy [217, 218]. The quantification of the boron concentration will be further discussed in chapters 3 and 4.

The calibration constants for B_S^0 in IR absorption were devised by Collins [215] in extension to the work carried out by Collins and Williams [214] which determined a calibration between the IR absorption at 2802 cm^{-1} against the Hall effect measurement which measures the difference between acceptors and donors.

Kawarada *et al* [217], and later Barjon *et al* [218], have also provided calibration constants for the determination of boron by the ratios of bound exciton (due to boron, 237.8 nm, 5.214 eV) against the free exciton (235.2 nm, 5.272 eV) which is thought to measure the total content of boron [219, 220].

Following the annealing of diamond in the graphite stable region (up to 2650 °C at 7.0 - 7.5 GPa), Kupriyanov *et al* [221] were able to extract diamond fragments and showed that the IR absorption features did not change, despite the considerable graphitisation. During the annealing, a broad CL emission peak at 2.85 eV was produced, known to be related to dislocations in diamond and thought to have arisen from plastic deformation during annealing. This indicates that boron is a very stable point defect in diamond lattice with a different annealing behaviour relative to nitrogen, and in agreement with the high migration energies predicted from theory [222].

Through electron energy loss spectroscopy (EELS) on heteroepitaxially grown CVD diamond, Turner *et al* [223] found the boron concentration to be greater around dislocations, which is thought to be facilitated by the tensile strain field around edge-type dislocations. Etching at a dislocation during homoepitaxial CVD growth has also revealed preferential incorporation of boron on (1 1 3) facets around these etch pits [224]. It is also thought that the number of dislocations is likely to increase from boron doping [225], and in high boron concentrations boron dimers can generate dislocations [226, 227].

Very little is reported about photoluminescence from boron related point defects in diamond. Green [228] correlated a feature in type IIb diamond at 648 nm (1.913 eV) by an irradiation and annealing study. By observing the defect annealing out at the same time as V^0, after 700 °C, it was proposed the defect was a boron interstitial as supported by careful analysis of the uniaxial stress and dipole absorption measurements.

2.2.2.5 New emerging point defects

Whilst the NV^- centre has shown some novel applications, the defect suffers from just ~4% coherent photons in the ZPL at room temperature, with the remainder being the phonon side band extending up to ~850 nm, and so does not lend itself well to applications requiring indistinguishable photons. Hence, there are efforts to investigate other defects that are single photon sources for their use within quantum applications which show a good degree of coherent photons in the ZPL relative to the emission window of the defect. Aharonovich and Neu [229] have provided an overview of this, where figure 2-7 shows the spectral window of recently found single photon sources and those that have so far demonstrated single spin manipulation, and has been updated to reflect more recent literature.

From figure 2-7, it is evident that defects involving Group IV elements are good candidates for single photon sources with a narrow emission window and exhibiting the capability of single defect spin manipulation. In light of the expanding interest of the Group IV-vacancy defects, Thiering and Gali [233] have provided an *ab initio* study of the magneto optical spectrum for these Group IV-vacancy defects

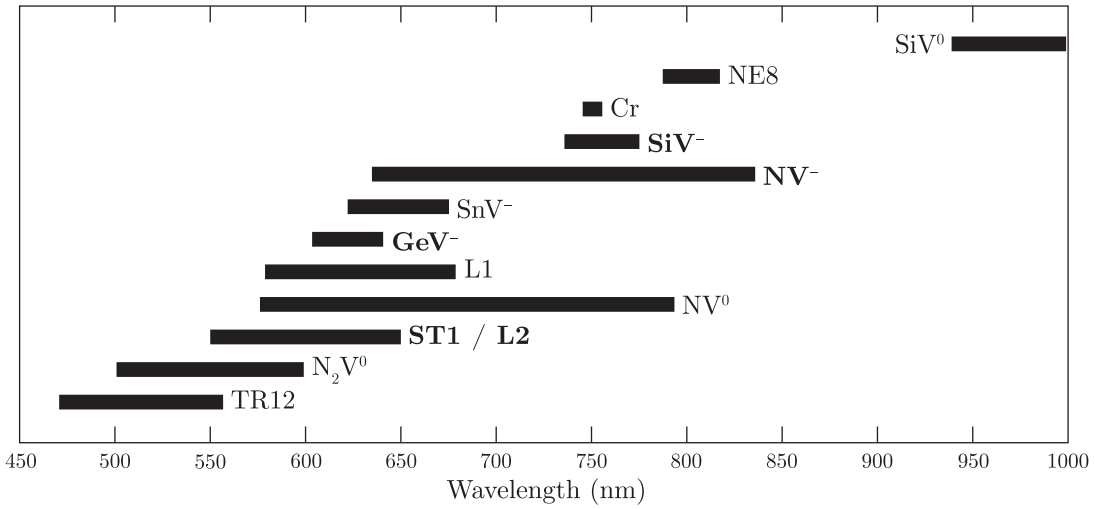

Figure 2-7 The spectral window of recently discovered single photon sources in diamond (along with the NV centre) where the length of the bar indicates the spectral window the centre emits over (ZPL + phonon side band). Defect names in bold represent centres that have shown spin manipulation in single centres. Figure adapted from [229] with added data points from references [230–232]

and implies this group of defects should exhibit desirable properties for quantum applications, in line with the so far obtained experimental results [231, 234–236]. Three common features to these defects resides in the following:

- The Group IV atom incorporates in a bond-centre location with a $\langle 1\,1\,1 \rangle$ split vacancy configuration
- Their ZPL emission is narrow with a large percentage of the total defect emission contained within it
- The ground state splitting of each Group IV-vacancy defect increases in accordance with the size of the substitutional atom, and it is suggested that the increase in splitting may enable long spin coherence times without the need for careful cryogenic cooling

As the oldest known out of the Group IV-vacancy centres, the understanding of the silicon vacancy (SiV) is now well developed and known to exist in two stable charge states, SiV^- and SiV^0 with ZPL transitions at 737 nm and 946 nm (1.68 eV and 1.31 eV) respectively. SiV^- exhibits inversion symmetry ($\mathscr{D}_{3d}$ point group), a principle symmetry axis along $\langle 1\,1\,1 \rangle$, with approximately 70% of the defect emission occurring as coherent photons in the ZPL, where at temperatures ≤4 K the ZPL is resolvable as 4 transitions, revealing the electronic fine structure [234, 237]. An all-optical spin manipulation process is feasible for SiV^-, however the system is hampered by the spin-orbit interaction and phononic coupling and, without decoupling techniques, requires temperatures below 100 mK to achieve a spin decoherence time < 200 ns [238–241]. In contrast, SiV^0, exhibits a longer spin decoherence lifetime (approximately 1 ms at T = 4 K [242]), whilst being nearer to the IR communications band, which is a requirement for implementing quantum communication into existing fibre networks without significant conversion.

Doping studies by Siyushev *et al* [231] have shown that single germanium-vacancy centres (GeV, ZPL at 602 nm (2.06 eV)) can be optically addressed for single shot spin readout. Equally, transform limited photons have very recently been demonstrated in single tin-vacancy (SnV, ZPL at 619 nm (2.00 eV)) centres which is promising for the applicability of this defect for quantum applications [235].

Trusheim *et al* [236] also characterised single lead-vacancy (PbV, ZPL at 520 nm (2.38 eV)) centres created by ion implantation.

The implantation of ions in to diamond tends to result in known defects, but occasionally it can generate previously unseen defects with interesting properties. For instance, after vertical nanowire fabrication in high purity HPHT diamond, Lee *et al* [243] found a defect (designated ST1) with a ZPL at 550 nm (2.25 eV) capable of coherent control of a single spin and ODMR, although it is unclear how this defect was generated or the constituent ion introduced. Independently, John *et al* [232] found that following an implantation run with 27 amu ions, new defects had been generated, here designated L1 and L2, where upon further consideration L2 shared several similar optical properties to ST1.

Whilst this is a very small snapshot of recently characterised point defects, with a bias on quantum based applications, it does however highlight the continuing advances not only of point defect characterisation but also material growth, enabling single defect incorporation at specification.

References

1. R. Berman, F. Simon, *Zeitschrift für Elektrochemie* **59**, 333–338 (1955).
2. F. P. Bundy et al., *The Journal of Chemical Physics* **35**, 383–391 (1961).
3. S. B. Shirey, J. E. Shigley, *Gems & Gemology* **49** (2013).
4. R. S. Balmer et al., *Journal of Physics: Condensed Matter* **21**, 364221 (2009).
5. K. Turcheniuk, V. N. Mochalin, *Nanotechnology* **28**, 252001 (2017).
6. R. Hazen, *The Diamond Makers* (Cambridge University Press, 1999).
7. F. P. Bundy et al., *Nature* **176**, 51–55 (1955).
8. P. W. Bridgman, *The Journal of Chemical Physics* **15**, 92–98 (1947).
9. H. T. Hall, *Journal of Chemical Education* **38**, 484 (1961).
10. H. P. Bovenkerk et al., *Nature* **184**, 1094–1098 (1959).
11. A. A. Giardini, J. E. Tydings, *American Mineralogist* **47**, 1393 (1962).
12. H. M. Strong, *American Journal of Physics* **57**, 794–802 (1989).
13. Y. N. Palyanov et al., in *Handbook of Crystal Growth* (Elsevier, 2015), pp. 671–713.
14. H. Kanda, T. Sekine, in *Properties, Growth and Applications of Diamond*, ed. by M. H. Nazaré, A. J. Neves, chap. B1.1, pp. 247–255.
15. H. Sumiya, S. Satoh, *Diamond and Related Materials* **5**, 1359–1365 (1996).
16. H. Sumiya et al., *Journal of Crystal Growth* **178**, 485–494 (1997).
17. Y. N. Palyanov et al., *Russian Geology and Geophysics* **38**, 920–945 (1997).
18. Y. Pal'yanov et al., *Diamond and Related Materials* **7**, 916–918 (1998).
19. M.-H. Hu et al., *Chinese Physics B* **21**, 098101 (2012).
20. E. Ito, in *Treatise on Geophysics (Second Edition)*, ed. by G. Schubert (Elsevier, Oxford, Second Editiondi, 2015), chap. 2.10, pp. 233–261.
21. E. M. Smith et al., *Science* **354**, 1403–1405 (2016).
22. L.-W. Yin et al., *Applied Physics A: Materials Science & Processing* **71**, 473–476 (2000).
23. A. Yelisseyev et al., *Diamond and Related Materials* **11**, 22–37 (2002).
24. K. Feral, *Gems & Gemology* **48**, 262–272 (2012).
25. U. F. D'Haenens-Johansson et al., *Gems & Gemology* **50**, 30–45 (2014).
26. A. Collins, *Diamond and Related Materials* **9**, 417–423 (2000).

27. V. Nadolinny, A. Komarovskikh, Y. Palyanov, *Crystals* **7**, 237 (2017).
28. C. V. H. Strömann et al., *Synthesis of diamond*, WO 2006/061672 A1, 2006.
29. R. Burns et al., *Diamond and Related Materials* **8**, 1433–1437 (1999).
30. I. N. Kupriyanov et al., *Diamond and Related Materials* **69**, 198–206 (2016).
31. Y. N. Palyanov et al., *CrystEngComm* **17**, 4928–4936 (2015).
32. I. Sunagawa, *Journal of Crystal Growth* **99**, 1156–1161 (1990).
33. I. Sunagawa, *The Journal of Gemmology* **24**, 485–499 (1995).
34. H. Kanda et al., *Journal of Crystal Growth* **94**, 115–124 (1989).
35. Y. N. Palyanov et al., *Crystal Growth & Design* **10**, 3169–3175 (2010).
36. M.-L. T. Rooney, *Journal of Crystal Growth* **116**, 15–21 (1992).
37. J. H. Gong et al., *Materials Research Innovations* **19**, S9–32–S9–36 (2015).
38. Y. Pal'yanov et al., *Diamond and Related Materials* **10**, 2145–2152 (2001).
39. Y. N. Palyanov et al., *Crystal Growth & Design* **11**, 2599–2605 (2011).
40. C. M. Welbourn, M. Cooper, P. M. Spear, *Gems & Gemology* **32**, 156–169 (1996).
41. A. R. Lang, G. M. Meaden, *Journal of Crystal Growth* **108**, 53–62 (1991).
42. A. F. Khokhryakov et al., *Journal of Crystal Growth* **386**, 162–167 (2014).
43. U. F. D'Haenens-Johansson et al., *Gems & Gemology* **51**, 260–279 (2015).
44. B. Deljanin et al., *Contributions to Gemology* **15**, 1–7 (2015).
45. H. Sumiya, K. Harano, K. Tamasaku, *Diamond and Related Materials* **58**, 221–225 (2015).
46. T. Ardon, S. Eaton-Magaña, *Gems and Gemology* **54**, 217–218 (2018).
47. T. N. T. Thi et al., *Journal of Applied Crystallography* **50**, 561–569 (2017).
48. Y. V. Shvyd'ko et al., *Nature Physics* **6**, 196–199 (2010).
49. S. Stoupin et al., *Journal of Synchrotron Radiation* **23**, 1118–1123 (2016).
50. Y. Shvyd'ko, V. Blank, S. Terentyev, *MRS Bulletin* **42**, 437–444 (2017).
51. W. G. Eversole, *Synthesis of diamond*, US3030187A, 1962.
52. W. G. Eversole, *Synthesis of diamond*, US3030188A, 1962.
53. J. Angus, H. Will, W. Stanko, *Journal of Crystal Growth* **3-4**, 172 (1968).
54. B. Derjaguin et al., *Journal of Crystal Growth* **2**, 380–384 (1968).
55. S. Matsumoto et al., *Japanese Journal of Applied Physics* **21**, L183–L185 (1982).

56. M. Kamo et al., *Journal of Crystal Growth* **62**, 642–644 (1983).
57. M. Kamo, H. Yurimoto, Y. Sato, *Applied Surface Science* **33-34**, 553–560 (1988).
58. E. Sevillano, in *Low-Pressure Synthetic Diamond* (Springer Berlin Heidelberg, Berlin, Heidelberg, 1998), pp. 11–39.
59. M. Schwander, K. Partes, *Diamond and Related Materials* **20**, 1287–1301 (2011).
60. L. H. Robins et al., *Physical Review B* **39**, 13367–13377 (1989).
61. P. Mehta Menon et al., *Diamond and Related Materials* **8**, 101–109 (1999).
62. H. Okushi, *Diamond and Related Materials* **10**, 281–288 (2001).
63. J. Achard et al., *Journal of Physics D: Applied Physics* **40**, 6175–6188 (2007).
64. P. K. Bachmann, *Physics World* **4**, 32–38 (1991).
65. S. Eaton-Magaña, J. E. Shigley, *Gems & Gemology* **52** (2016).
66. J. E. Butler, R. L. Woodin, *Philosophical Transactions of the Royal Society of London. Series A: Physical and Engineering Sciences* **342**, 209–224 (1993).
67. P. W. May, *Phil. Trans. R. Soc. Lond. A* **358**, 473–495 (2000).
68. J. Lander, J. Morrison, *Surface Science* **4**, 241–246 (1966).
69. P. K. Bachmann, D. Leers, H. Lydtin, *Diamond and Related Materials* **1**, 1–12 (1991).
70. H. Liu, D. S. Dandy, *Diamond and Related Materials* **4**, 1173–1188 (1995).
71. G. S. Ristić et al., *Materials Chemistry and Physics* **80**, 529–536 (2003).
72. E. J. Corat, D. G. Goodwin, *Journal of Applied Physics* **74**, 2021–2029 (1993).
73. K. Hemawan et al., *Diamond and Related Materials* **19**, 1446–1452 (2010).
74. J. Lu et al., *Diamond and Related Materials* **37**, 17–28 (2013).
75. A. Tallaire et al., *Comptes Rendus Physique* **14**, 169–184 (2013).
76. C.-s. Yan et al., *Proceedings of the National Academy of Sciences* **99**, 12523–12525 (2002).
77. Q. Liang et al., *Diamond and Related Materials* **18**, 698–703 (2009).
78. M. S. Couto, W. J. P. van Enckevort, M. Seal, *Philosophical Magazine B* **69**, 621–641 (1994).
79. P. M. Martineau et al., *Gems & Gemology* **40**, 2–25 (2004).

80. P. Martineau et al., *Journal of Physics: Condensed Matter* **21**, 364205 (2009).
81. R. Zhang, S. Lee, Y. Lam, *Diamond and Related Materials* **5**, 1288–1294 (1996).
82. J. E. Butler, I. Oleynik, *Philosophical Transactions of the Royal Society A: Mathematical, Physical and Engineering Sciences* **366**, 295–311 (2008).
83. W. van Enckevort et al., *Diamond and Related Materials* **2**, 997–1003 (1993).
84. U. F. S. D'Haenens-Johansson et al., *Physical Review B* **82**, 155205 (2010).
85. U. F. S. D'Haenens-Johansson et al., *Physical Review B* **84**, 245208 (2011).
86. A. M. Edmonds et al., *Physical Review B* **86**, 035201 (2012).
87. J. Michl et al., *Applied Physics Letters* **104**, 102407 (2014).
88. M. Lesik et al., *Diamond and Related Materials* **56**, 47–53 (2015).
89. F. Silva et al., *Journal of Crystal Growth* **310**, 187–203 (2008).
90. F. Silva et al., *Diamond and Related Materials* **18**, 683–697 (2009).
91. F. Silva et al., *Diamond and Related Materials* **17**, 1067–1075 (2008).
92. A. Tallaire et al., *Diamond and Related Materials* **15**, 1700–1707 (2006).
93. P. M. Martineau et al., *Physica Status Solidi (C) Current Topics in Solid State Physics* **6**, 1953–1957 (2009).
94. G. A. Scarsbrook, D. J. Twitchen, M. L. Markham, *Solid state material*, WO2010010344A1, 2010.
95. G. A. Scarsbrook, D. J. Twitchen, M. L. Markham, *Diamond material*, WO2010010352A1, 2010.
96. J. E. Butler et al., *Journal of Physics: Condensed Matter* **21**, 364201 (2009).
97. T. Teraji et al., *physica status solidi (a)* **212**, 2365–2384 (2015).
98. J. Borwick, *Loudspeaker and Headphone Handbook* (Focal Press, 2001).
99. E. Wörner et al., *Advances in Science and Technology* **48**, 142–150 (2006).
100. S. Affatato, M. Frigo, A. Toni, *Journal of Biomedical Materials Research* **53**, 221–226 (2000).
101. B. Pope et al., *Prosthetic hip joint having sintered polycrystalline diamond compact articulation surfaces*, US6290726B1, 2001.
102. M. D. Fries, Y. K. Vohra, *Journal of Physics D: Applied Physics* **35** (2002).
103. M. J. Papo et al., *Journal of Materials Science: Materials in Medicine* **15**, 773–777 (2004).

104. T. P. Mollart et al., presented at the Proceedings of SPIE, ed. by R. W. Tustison, vol. 4375, pp. 180–198.
105. S. Shikata, *Diamond and Related Materials* **65**, 168–175 (2016).
106. H. Yamada et al., *Applied Physics Express* **3**, 051301 (2010).
107. H. Yamada et al., *Applied Physics Letters* **104**, 102110 (2014).
108. M. Schreck et al., *Scientific Reports* **7**, 44462 (2017).
109. M. Schreck et al., *physica status solidi (a)* **213**, 2028–2035 (2016).
110. B. Law, W. Wang, *Gems and Gemology* **52**, 414–416 (2016).
111. A. Secroun et al., *physica status solidi (a)* **204**, 4298–4304 (2007).
112. A. Tallaire et al., *physica status solidi (a)* **201**, 2419–2424 (2004).
113. J. Achard et al., *physica status solidi (a)* **211**, 2264–2267 (2014).
114. A. Tallaire et al., *Diamond and Related Materials* **77**, 146–152 (2017).
115. W. Wang et al., *Gems & Gemology* **48**, 80–97 (2012).
116. G. Balasubramanian et al., *Nature materials* **8**, 383–7 (2009).
117. A. Yacoot, M. Moore, W. G. Machado, *Journal of Applied Crystallography* **31**, 767–776 (1998).
118. W. G. Machado, M. Moore, A. Yacoot, *Journal of Applied Crystallography* **31**, 777–782 (1998).
119. J. C. Angus et al., *Journal of Materials Research* **7**, 3001–3009 (1992).
120. E. L. Tomlinson et al., *Diamond and Related Materials* **20**, 11–17 (2011).
121. C.-S. Yan, Y. K. Vohra, *Diamond and Related Materials* **8**, 2022–2031 (1999).
122. M. Moore, S. Nailer, W. Wierzchowski, *Crystals* **6**, 71 (2016).
123. B. Willems et al., *physica status solidi (a)* **203**, 3076–3080 (2006).
124. D. Fisher, *Lithos* **112**, 619–624 (2009).
125. A. T. Blumenau et al., *Physical Review B* **65**, 205205 (2002).
126. M. Gaukroger et al., *Diamond and Related Materials* **17**, 262–269 (2008).
127. A. Tallaire et al., *Crystal Growth & Design* **16**, 2741–2746 (2016).
128. H. Sumiya, K. Tamasaku, *Japanese Journal of Applied Physics* **51**, 090102 (2012).
129. H. Pinto, R. Jones, *Journal of Physics: Condensed Matter* **21**, 364220 (2009).
130. A. F. Khokhryakov, Y. N. Palyanov, *Journal of Crystal Growth* **306**, 458–464 (2007).

131. P. J. Dean, *Physical Review* **139** (1965).

132. J. Ruan, K. Kobashi, W. J. Choyke, *Applied Physics Letters* **60**, 3138–3140 (1992).

133. D. Takeuchi et al., *Physical Review B* **63**, 245328 (2001).

134. A. M. Zaitsev, *Optical Properties of Diamond* (Springer Berlin Heidelberg, Berlin, Heidelberg, 2001).

135. E. A. Faulkner, J. N. Lomer, *Philosophical Magazine* **7**, 1995–2002 (1962).

136. D. J. Twitchen et al., *Physical Review B* **54**, 6988–6998 (1996).

137. D. C. Hunt et al., *Physical Review B* **61**, 3863–3876 (2000).

138. J. Walker, *Journal of Physics C: Solid State Physics* **10**, 3867–3876 (1977).

139. J. Goss et al., *physica status solidi (a)* **186**, 215–220 (2001).

140. C. D. Clark, R. W. Ditchburn, H. B. Dyer, *Proceedings of the Royal Society A: Mathematical, Physical and Engineering Sciences* **234**, 363–381 (1956).

141. G. Davies et al., *Physical Review B* **46**, 13157–13170 (1992).

142. G. Davies, *Nature* **269**, 498–500 (1977).

143. G. Davies, E. C. Lightowlers, *Journal of Physics C: Solid State Physics* **3**, 638–650 (1970).

144. C. D. Clark, J. Walker, *Proceedings of the Royal Society A: Mathematical, Physical and Engineering Sciences* **334**, 241–257 (1973).

145. J. A. van Wyk et al., *Physical Review B* **52**, 12657–12667 (1995).

146. J. Isoya et al., *Physical Review B* **45**, 1436–1439 (1992).

147. L. Allers, A. T. Collins, J. Hiscock, *Diamond and Related Materials* **7**, 228–232 (1998).

148. M. Newton et al., *Diamond and Related Materials* **11**, 618–622 (2002).

149. K. Iakoubovskii et al., *Physica B: Condensed Matter* **340-342**, 67–75 (2003).

150. R. Jones, *Diamond and Related Materials* **18**, 820–826 (2009).

151. W. V. Smith et al., *Physical Review* **115**, 1546–1552 (1959).

152. R. M. Chrenko, H. M. Strong, R. E. Tuft, *Philosophical Magazine* **23**, 313–318 (1971).

153. G. S. Woods, J. A. Van Wyk, A. T. Collins, *Philosophical Magazine B* **62**, 589–595 (1990).

154. A. T. Collins, M. Stanley, G. S. Woods, *Journal of Physics D: Applied Physics* **20**, 969–974 (1987).

155. S. C. Lawson et al., *Journal of Physics: Condensed Matter* **10**, 6171–6180 (1998).

156. R. Ulbricht et al., *Physical Review B* **84**, 165202 (2011).

157. Y. Babich et al., *Diamond and Related Materials* **9**, 893–896 (2000).

158. A. Tallaire et al., *Diamond and Related Materials* **14**, 249–254 (2005).

159. R. Burns et al., *Journal of Crystal Growth* **104**, 257–279 (1990).

160. G. S. Woods, *Philosophical Magazine B* **50**, 673–688 (1984).

161. S. Liggins et al., *Physical Review B* **81**, 085214 (2010).

162. G. S. Woods, A. T. Collins, *Journal of Physics C: Solid State Physics* **15**, L949–L952 (1982).

163. A. T. Collins et al., *Journal of Physics C: Solid State Physics* **21**, 1363–1376 (1988).

164. A. T. Collins, G. Davies, G. S. Woods, *Journal of Physics C: Solid State Physics* **19**, 3933–3944 (1986).

165. A. Gruber, *Science* **276**, 2012–2014 (1997).

166. F. Jelezko et al., *Physical Review Letters* **92**, 076401 (2004).

167. C. V. Peaker, PhD thesis, Newcastle University, 2018.

168. L. du Preez, PhD thesis, University of the Witwatersrand, 1965.

169. G. Davies, M. F. Hamer, *Proceedings of the Royal Society A: Mathematical, Physical and Engineering Sciences* **348**, 285–298 (1976).

170. J. H. N. Loubser, J. A. van Wyk, *Reports on Progress in Physics* **41**, 1201–1248 (1978).

171. N. Reddy, N. Manson, E. Krausz, *Journal of Luminescence* **38**, 46–47 (1987).

172. D. A. Redman et al., *Physical Review Letters* **67**, 3420–3423 (1991).

173. M. W. Doherty et al., *Physics Reports* **528**, 1–45 (2013).

174. A. T. Collins, *Journal of Physics: Condensed Matter* **14**, 3743–3750 (2002).

175. N. B. Manson et al., *Physical Review B - Condensed Matter and Materials Physics* **87**, 2–6 (2013).

176. N. Mizuochi et al., *Nature Photonics* **6**, 299–303 (2012).

177. K. Beha et al., *Physical Review Letters* **109**, 1–5 (2012).

178. E. Fraczek et al., *Optical Materials Express* **7**, 2571 (2017).

179. S. Felton et al., *Physical Review B - Condensed Matter and Materials Physics* **77**, 1–4 (2008).

180. P. Deák et al., *Physical Review B* **89**, 075203 (2014).

181. J. Steeds, S. Kohn, *Diamond and Related Materials* **50**, 110–122 (2014).

182. M. Pfender et al., *Nano Letters* **17**, 5931–5937 (2017).

183. F. Jelezko, J. Wrachtrup, *physica status solidi (a)* **203**, 3207–3225 (2006).

184. D. A. Simpson et al., *Sci Rep* **6**, 22797 (2016).

185. D. Le Sage et al., *Nature* **496**, 486–489 (2013).

186. F. Dolde et al., *Nature Physics* **7**, 459–463 (2011).

187. P. Neumann et al., *Nano Letters* **13**, 2738–2742 (2013).

188. B. Hensen et al., *Nature* **526**, 682–686 (2015).

189. M. Markham et al., *Diamond and Related Materials* **20**, 134–139 (2011).

190. J. Meijer et al., *Applied Physics Letters* **87**, 1–3 (2005).

191. J. L. O'Brien, A. Furusawa, J. Vučković, 1–11 (2009).

192. Y.-c. Chen et al., *Nature Photonics* **11**, 77–80 (2016).

193. Y.-C. Chen et al., *Optica* **6**, 662 (2019).

194. C. J. Stephen et al., *arXiv:1807.03643*, 2–9 (2018).

195. R. U. A. Khan et al., *Journal of Physics: Condensed Matter* **21**, 364214 (2009).

196. C. Glover et al., *Physical Review Letters* **90**, 185507 (2003).

197. S. C. Lawson et al., *Journal of Physics: Condensed Matter* **4**, 3439–3452 (1992).

198. Y. Mita et al., *Journal of Physics: Condensed Matter* **2**, 8567–8574 (1999).

199. B. L. Green et al., *Physical Review B* **92**, 165204 (2015).

200. C. B. Hartland, PhD thesis, University of Warwick, 2014.

201. M. F. Thomaz, G. Davies, *Proceedings of the Royal Society A: Mathematical, Physical and Engineering Sciences* **362**, 405–419 (1978).

202. A. T. Collins et al., *Journal of Applied Physics* **97**, 083517 (2005).

203. R. J. Cruddace, PhD thesis, University of Warwick, 2007.

204. S. Liggins, PhD thesis, University of Warwick, 2010.

205. E. S. D. Sa, G. Davies, *Proceedings of the Royal Society A: Mathematical, Physical and Engineering Sciences* **357**, 231–251 (1977).

206. J. V. Macpherson, *Physical Chemistry Chemical Physics* **17**, 2935–2949 (2015).

207. S. J. Cobb, Z. J. Ayres, J. V. Macpherson, *Annual Review of Analytical Chemistry* **11**, annurev–anchem–061417–010107 (2018).

208. V. Schmalz et al., *Water Research* **43**, 5260–5266 (2009).

209. J. Achard et al., *Diamond and Related Materials* **20**, 145–152 (2011).

210. R. Edgington et al., *Biosensors and Bioelectronics* **33**, 152–157 (2012).

211. E. Gaillou et al., *American Mineralogist* **97**, 1–18 (2012).

212. M. Bernard, A. Deneuville, P. Muret, *Diamond and Related Materials* **13**, 282–286 (2004).

213. V. Mortet et al., *Carbon* **115**, 279–284 (2017).

214. A. T. Collins, A. W. S. Williams, *Journal of Physics C: Solid State Physics* **4**, 1789–1800 (1971).

215. A. T. Collins, presented at the De Beers 61st Diamond Conference.

216. N. Fujimori, H. Nakahata, T. Imai, *Japanese Journal of Applied Physics* **29**, 824–827 (1990).

217. H. Kawarada et al., *Physical Review B* **47**, 3633–3637 (1993).

218. J. Barjon et al., *Physical Review B* **83**, 073201 (2011).

219. F. Omnès et al., *Diamond and Related Materials* **20**, 912–916 (2011).

220. J. Barjon, *Physica Status Solidi (A) Applications and Materials Science* **1700402**, 1–10 (2017).

221. I. Kupriyanov et al., *Diamond and Related Materials* **17**, 1203–1206 (2008).

222. J. P. Goss, P. R. Briddon, *Physical Review B - Condensed Matter and Materials Physics* **73**, 1–8 (2006).

223. S. Turner et al., *Nanoscale* **8**, 2212–2218 (2016).

224. A. Tallaire et al., *Diamond and Related Materials* **20**, 875–881 (2011).

225. R. J. Graham et al., *Applied Physics Letters* **65**, 292–294 (1994).

226. M. P. Alegre et al., *Applied Physics Letters* **105**, 173103 (2014).

227. F. Lloret et al., *Nanomaterials* **8**, 480 (2018).

228. B. L. Green, PhD thesis, University of Warwick, 2013.

229. I. Aharonovich, E. Neu, *Advanced Optical Materials* **2**, 911–928 (2014).

230. B. L. Green et al., *Physical Review Letters* **119**, 096402 (2017).

231. P. Siyushev et al., *Physical Review B* **96**, 1–5 (2017).

232. R. John et al., *New Journal of Physics* **19**, 053008 (2017).

233. G. Thiering, A. Gali, *Physical Review X* **8**, 021063 (2018).

234. L. J. Rogers et al., *Physical Review B* **89**, 235101 (2014).

235. M. E. Trusheim et al., 1–6 (2018).

236. M. E. Trusheim et al., presented at the Conference on Lasers and Electro-Optics, FTu4H.2, arXiv: 1805.12202.

237. A. T. Collins et al., *Diamond and Related Materials* **3**, 932–935 (1994).

238. L. J. Rogers et al., *Physical Review Letters* **113**, 263602 (2014).

239. J. N. Becker et al., *Nature Communications* **7**, 13512 (2016).

240. D. D. Sukachev et al., *Physical Review Letters* **119**, 223602 (2017).

241. J. N. Becker et al., *Physical Review Letters* **120**, 053603 (2018).

242. B. C. Rose et al., *Science* **361**, 60–63 (2018).

243. S.-Y. Lee et al., *Nature Nanotechnology* **8**, 487–492 (2013).

3

Theory

All of physics is either impossible or trivial. It is impossible until you understand it, and then it becomes trivial.

- Ernest Rutherford

3.1 Diamond bulk characterisation

Throughout this thesis, several characterisation techniques have been employed in order to characterise the diamond samples studied. Here, the underlying theoretical principles of bulk characterisation are presented to link the experimental results presented later in this thesis.

3.1.1 Electron paramagnetic resonance (EPR)

The theory of electron paramagnetic resonance (EPR) has been well covered by several authors [1–3], and so only a brief narrative will be presented here.

As the name implies, EPR detection requires a system to be paramagnetic, that is to say there are one or more unpaired electrons such that the net electron spin is non-zero ($S \neq 0$). EPR measurements have provided a great deal of information about the constituent atoms, energy levels, structure and environment for paramagnetic point defects. Furthermore, the concentration of the point defect can be extracted from the signal since the intensity is directly proportional to the number of spins and hence quantity of the defect present.

Equation (3-1) is the spin Hamiltonian which completely describes unpaired electrons, and is a convolution of different interactions that modify the electron energy.

$$\hat{\mathscr{H}} = \underbrace{\mu_B \boldsymbol{B}^T \cdot \boldsymbol{g} \cdot \hat{\boldsymbol{S}}}_{\text{Zeeman}} + \underbrace{\hat{\boldsymbol{S}}^T \cdot \boldsymbol{D} \cdot \hat{\boldsymbol{S}}}_{\text{zero field}} + \sum_i^n \Big[\underbrace{-\mu_N g_{n_i} \boldsymbol{B}^T \cdot \hat{\boldsymbol{I}}_i}_{\text{nuclear Zeeman}} + \underbrace{\hat{\boldsymbol{S}}^T \cdot \boldsymbol{A}_i \cdot \hat{\boldsymbol{I}}_i}_{\text{hyperfine}} + \underbrace{\hat{\boldsymbol{I}}_i^T \cdot \boldsymbol{P}_i \cdot \hat{\boldsymbol{I}}_i}_{\text{quadrupole}} \Big] \tag{3-1}$$

From this, each interaction can then be discussed.

3.1.1.1 Electronic Zeeman interaction

For an unpaired electron in a magnetic field $\boldsymbol{B}$, the Zeeman interaction is

$$E = -\boldsymbol{\mu} \cdot \boldsymbol{B} \tag{3-2}$$

where the magnetic dipole $\hat{\boldsymbol{\mu}}$ of an electron is the contribution of its orbital angular momentum $\hat{\boldsymbol{L}}$ and intrinsic angular momentum (spin) $\hat{\boldsymbol{S}}$ such that

$$\hat{\boldsymbol{\mu}} = -\mu_B (\hat{\boldsymbol{L}} + g_e \hat{\boldsymbol{S}}) \tag{3-3}$$

With μ_B as the Bohr magneton, defined as $\mu_B = {}^{e\hbar}/_{2m}$ and the electron g-factor g_e which is a well defined, dimensionless constant [4]. In applying a magnetic field along the z axis where $\boldsymbol{B}^T = (0, 0, B_0)$, and assuming an isotropic g-factor, the electron energy is then given by

$$\hat{\mathscr{H}}_{eZ} = -\boldsymbol{B}^T \cdot \hat{\boldsymbol{\mu}} = g\mu_B \boldsymbol{B}^T \cdot \hat{\boldsymbol{S}} = g\mu_B B_0 \hat{S}_z \tag{3-4}$$

By quantum mechanics, the spin of a particle is quantised along z where it has spin quantum number $m_s = S, S-1, \cdots -S$ for a spin multiplicity $2S+1$ and spin S. By this, an electron has a spin quantum number $m_s = \pm {}^1/_2$. Thus, in an applied magnetic field the spin states are no longer degenerate, and the energy difference between the two states is given as

$$\Delta E = \pm \frac{1}{2} g_e \mu_B B_0 \tag{3-5}$$

Finally, a resonance condition is met when a high energy photon is incident with a frequency that matches ΔE, shown schematically in figure 3-1, whereby

$$\Delta E = h\nu = g_e \mu_B B_0 \tag{3-6}$$

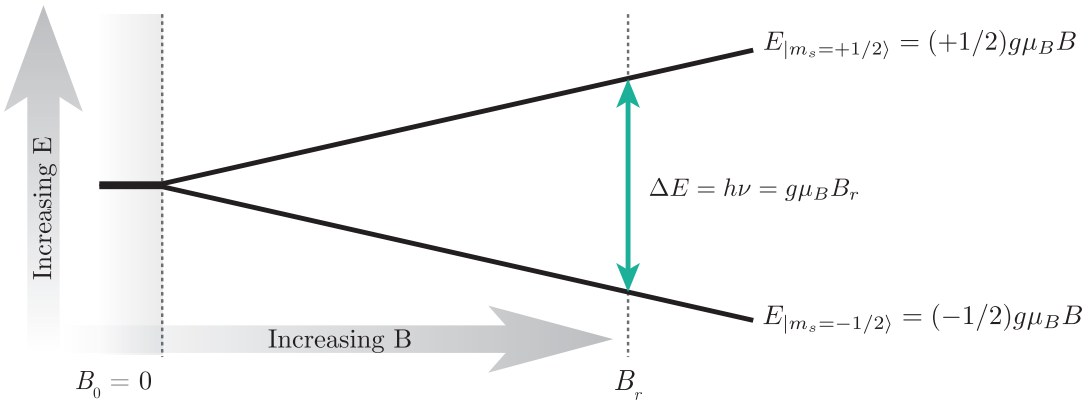

Figure 3-1 Electronic Zeeman effect for an electron with a net spin of $S = 1/2$. The application of the magnetic field lifts the degeneracy so that the energy difference between the spin-up and spin-down component has a linear dependence, where a resonant transition can be driven by the absorption of a high energy photon of energy $h\nu$.

3.1.1.2 Zero field interaction

The interaction between two or more unpaired electrons ($S \geq 1$) gives rise to a splitting in the energy levels. As such, an overlap in electron wavefunction, spin orbit and dipole-dipole interactions lifts the $(2S+1)$ degeneracy of the spin states when no external magnetic field is present. The zero field interaction involves the traceless $\underline{\boldsymbol{D}}$ tensor which contains contributions of both spin-orbit and dipolar interactions such that the Hamiltonian is

$$\hat{\mathscr{H}}_{zf} = \hat{\boldsymbol{S}}^T \cdot \underline{\boldsymbol{D}} \cdot \hat{\boldsymbol{S}} \tag{3-7}$$

Often, the $\underline{\boldsymbol{D}}$ tensor is rewritten based on the Cartesian coordinate system as

$$D = \frac{3D_z}{2}, \qquad E = \frac{D_x - D_y}{2} \tag{3-8}$$

Therefore, the zero field Hamiltonian can be rewritten as

$$\hat{\mathscr{H}}_{zf} = D(S_z^2 - \frac{1}{3}S(S+1)) + E(S_x^2 - S_y^2) \tag{3-9}$$

Since E represents the rhombicity of system, those with cubic ($\mathscr{T}_\mathrm{d}$) symmetry yield $D = E = 0$, whilst axially symmetric systems tend to follow $D \neq 0$, $E = 0$. Lower symmetry systems results in a non-zero E term. Hence, the zero field interaction can be significant in understanding the constituent atoms, structure and symmetry of the system.

3.1.1.3 Hyperfine interaction

A non-zero nuclear spin, I, can couple to an unpaired electron as the hyperfine interaction and presents itself as a further splitting in the EPR spectrum. Hyperfine interactions have been a powerful source of data extracted from an EPR spectrum which reveals the local environment, symmetry and spin localisation of the unpaired election relative to the host material. Typical contributions to the nuclear g-factor, and hence hyperfine interactions in diamond, arise from ^{1}H, ^{13}C, ^{14}N, and ^{15}N.

The hyperfine interaction comprises of two components, one isotropic and one anisotropic:

- The Fermi contact interaction, which is the result of the non-zero unpaired electron probability density at the nucleus. This is an isotropic interaction as only $s-$shell electrons contribute which are spherically symmetric.
- Dipole-dipole coupling between electron and nucleus facilitating a change in energy levels.

Since this thesis does not further consider hyperfine interactions, the derivation of the associated Hamiltonian has been omitted for brevity.

3.1.1.4 Nuclear Zeeman interaction

Similar to the electron Zeeman interaction, the nuclear Zeeman corresponds to interactions due to a non-zero nuclear magnetic moment in a magnetic field ($I > 0,\ \boldsymbol{B}^T \neq 0$). The Hamiltonian is familiar with equation (3-4) where g and μ_B are replaced by g_N and μ_N respectively.

$$\hat{\mathscr{H}}_{NZ} = -\sum_i \mu_N g_{N_i} \boldsymbol{B}^T \cdot \hat{\boldsymbol{I}}_i \tag{3-10}$$

Given the nuclear mass is significantly higher than the electron mass, it follows that $\mu_N \ll \mu_e$. If the strength of the hyperfine interaction is much greater than the nuclear Zeeman, then this provides little contribution to the EPR spectrum.

3.1.1.5 Quadrupole interaction

Non-spherical charge distributions inside a nucleus of spin $I \geq 1$ causes an interaction from the field gradient and the nuclear quadrupole moment. This interaction causes a small shift in lines of the EPR spectrum, and can also facilitate state mixing between m_s and m_I allowing transitions that break selection rules (forbidden transitions) to be observed. As this interaction is small, it is not considered in the EPR analysis within this thesis (see section 4.1.1), and thus the quadrupole interaction will not be further discussed.

3.1.2 Absorption and optical transitions

The attenuation of an electromagnetic (EM) wave propagating through a material is caused by scattering and absorption mechanisms. In semiconductors, the band gap dictates the transparency window. Optical transitions in diamond are therefore due to the interaction of an EM wave with the lattice, where intrinsic absorption is due to the pure carbon lattice, whilst extrinsic absorption involves defects.

Energy levels within the band gap of the diamond caused by defects can reveal several interesting properties of that system, such as the symmetry and preferential orientation, either by their absorption and/or luminescence characteristics. There is an extensive list of literature that concerns the optical properties of defects in diamond, such as that by Walker [5] and Davies [6], or the notable book by Fox [7] for a more generalistic view on optical systems in solids. The following, therefore, is a short overview on the relevant optical theory applicable to the work of this thesis, and further expanded in section 3.2 to detail photoluminescence with single defect centres in diamond.

The range of optical absorption can be broadly split in to three regions: ultraviolet (UV) for wavelengths < 400 nm, visible (Vis) for wavelengths between 400 nm and 700 nm and the infrared (IR) for wavelengths > 700 nm.

The Beer-Lambert law describes the absorption of light in a medium which is dependent upon the initial intensity, thickness of the medium t and the absorption

coefficient α which is the fraction absorbed per unit length. The change in intensity is thereby given as

$$\mathrm{d}I = -\alpha I(t)\ \mathrm{d}z \tag{3-11}$$

Thus by the integration of equation (3-11), for an EM wave of angular frequency ω, travelling in one dimension z, the intensity I of that wave for a given position yields the Beer-Lambert law

$$I(z,\omega) = I_{(0,\omega)}e^{-\alpha(\omega)z} \tag{3-12}$$

where $I_{0,\omega}$ is the intensity at $z = 0$, and $\alpha(\omega)$ is the absorption coefficient within the medium. Experimentally then, the final intensity recorded I_t depends upon the thickness t of the material passed through such that absorbance $A(\omega)$ is given by

$$A(\omega) = -\log_{10}\left(\frac{I_t(\omega)}{I_{(0,\omega)}}\right) \tag{3-13}$$

Finally, it is possible to relate absorption coefficient to absorbance by the linear dependence

$$\alpha(\omega) = \frac{\ln(10)}{t}A(\omega) \tag{3-14}$$

Owing to the thickness and refractive index of the material, etaloning can cause periodic interference in the absorption spectrum where multiple reflections of light occur at each surface. For a material of refractive index n, the total transmission of light at a given wavenumber k is

$$T = \frac{(1-R)^2e^{-\alpha t}}{1+R^2e^{-2\alpha t}-2Re^{-\alpha t}\cos(2knt)} \tag{3-15}$$

where R is the Fresnel reflection at the material-air interface. For diamond this value is approximately 17% in the visible region and for multiple reflections the maximum attainable transmission of light in diamond is approximately 71%.

3.1.2.1 Intrinsic absorption

Intrinsic diamond is transparent over a wide spectral range since it has a large indirect band gap of 5.47 eV [8]. The zero-momentum optical phonon in diamond carries a frequency of 1332 cm^{-1} and is known as the Raman frequency, hence multi-phonon absorption occurs at integer multiples of 1332 cm^{-1}.

Inversion symmetry of the intrinsic diamond structure prohibits absorption in the one-phonon region, and whilst transparent to wavelengths longer than 227 nm, multiphonon absorption occurs between 2.6 - 6.2 µm where the absorption at a given frequency is proportional to the number of pairs of phonon modes created [9].

Absorption of energy that is equal to, or above, the band gap is also facilitated in diamond where a hole (h^+) is subsequently generated in the valence band by the promotion of an electron (e^-) to the conduction band. Phonon-assisted relaxations lead to the recombination of the e^--h^+ pair, releasing an exciton. Here, non-zero momentum is applied to thermalised electrons in the conduction band and thus a recombination at the energy of the band gap of diamond is forbidden. Hence, exciton emission can only occur with the involvement of transverse optical (TO), longitudinal optical (LO), transverse acoustic (TA) and longitudinal acoustic (LA) phonon modes of energy $\hbar\omega$. This underlies the principle of cathodoluminescence and will be discussed further in § 3.1.2.4.

3.1.2.2 Extrinsic absorption

Absorption can also be extrinsic to the material. Extended and point defects break local symmetry and present themselves as energy states within the band gap. The introduction of a non-carbon atom therefore upsets the *status quo* and provides a pertubation as a vibration through the lattice when excited.

These vibrations can be described by a simple diatomical model synonymous with the mass on a spring concept [10]. Here, the impurity of mass m and the carbon atom of mass M can be separated by a spring constant k such that the frequency of vibration ω is given by

$$\omega = \sqrt{\frac{k}{\chi M + m}} \tag{3-16}$$

where χ is an empirical constant of which considers host atom vibrations [10].

For an impurity heavier than carbon, such as nitrogen, vibrations occur at a frequency lower than that of the Raman frequency. Hence, single nitrogen and nitrogen aggregates show strong absorption features in the one phonon region [5]. On the other hand, defects which involve a lighter impurity can show up in the two

and three phonon region. For instance, the C-H stretch band in diamond occurs between 2700 cm^{-1} and 3400 cm^{-1} [11].

The Franck-Condon principle states that, as electrons are much smaller than the nucleus, an electronic transition will happen on a time scale much quicker than the nuclear motion, whereby phonons will allow the nucleus to realign to the new electronic configuration. This picture is represented in figure 3-2a.

The pure electronic transition between the ground and excited state is observed as a sharp spectral feature known as the zero phonon line (ZPL). Electron-phonon coupling facilitates mixed transitions, in addition to the ZPL, known as the phonon sideband (PSB). The emission of coherent photons into the ZPL intensity is quantified by the Debye-Waller factor (DWF) such that

$$\mathrm{DWF} = e^{-S} = \frac{I_{\mathrm{ZPL}}}{I_{\mathrm{ZPL}} + I_{\mathrm{PSB}}} \tag{3-17}$$

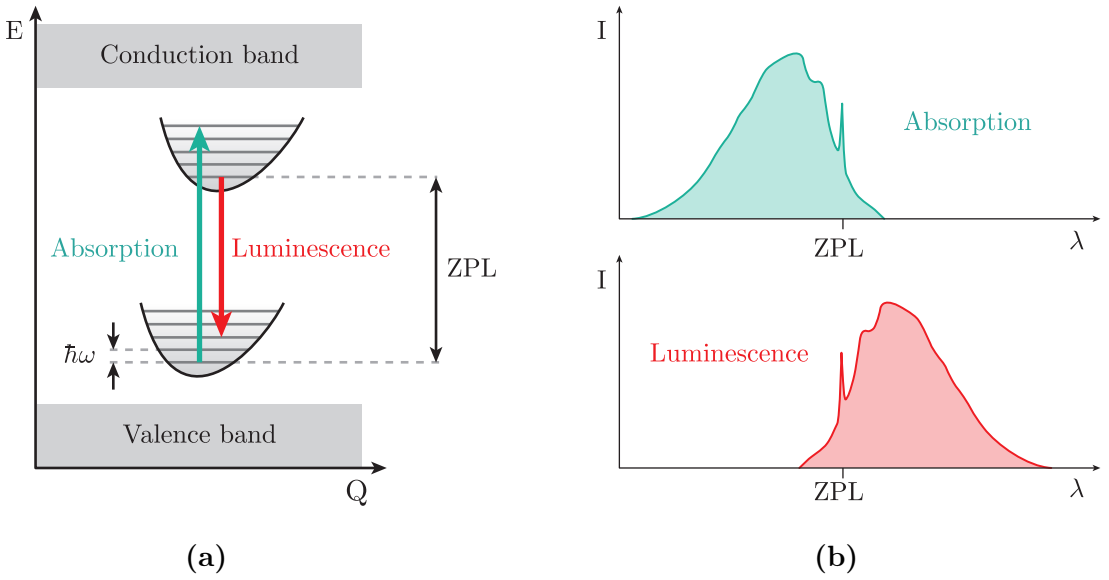

Figure 3-2 (a) The ground and excited states of a defect within the band gap of diamond, where each manifold contains several vibrational energy states (solid horizontal lines) separated by $\hbar\omega$. Energy (E) and configuration coordinate (Q) of the system are indicated accordingly. The Franck-Condon principle depicted here highlights optical transitions that occur by the vertical arrows with a fixed Q. The transition from lowest vibrational state in the excited state manifold from/to the lowest vibrational state in the ground state manifold is termed the zero phonon line (ZPL) (b) Typical spectroscopic shape of absorption and luminescence from a defect within the band gap where the intensity (I) and wavelength (λ) are shown for guidance. Figure adapted from Fox [7].

where I_{ZPL} and I_{PSB} are the integrated areas of the ZPL and PSB respectively. The electron-phonon coupling strength is described by the Huang-Rhys factor S where $S < 1$ is said to be weakly coupled ($I_{\mathrm{PSB}} \to 0,\ I_{\mathrm{ZPL}} \to 1$), and $S > 1$ is strongly coupled ($I_{\mathrm{PSB}} \gg I_{\mathrm{ZPL}},\ I_{\mathrm{ZPL}} \to 0$).

Absorption requires a photon much higher in energy than the ZPL transition leading to an excited vibrational mode. The PSB is therefore seen in the spectrum at higher energies than the ZPL transition, figure 3-2b. Conversely, the luminescence spectrum shows the emitted energy of the ZPL transition and the difference in energy between the ZPL transition and vibrational modes in the ground electronic state such that the PSB is lower in energy than the ZPL.

In cases where the vibrational motion is higher than the Raman frequency, the vibration is localised to the point defect since it cannot propagate through the lattice. As a consequence it is possible to observe a smaller transition in the absorption/emission spectra in the PSB at an energy separation > 165 meV, which is known as a local vibrational mode (LVM).

By measuring an absorption spectrum due to a defect, the resultant absorption coefficient will be directly proportional to the density (and hence concentration) of a defect. Therefore absorption measurements are considered to be a powerful quantitive technique for not only understanding the defect present but also the amount of defect within the material.

3.1.2.3 Photoluminescence (PL)

The absorption of a photon will cause states lying in the band gap to become excited, as already discussed. If that energy is below the band gap, an electron is promoted from the ground into the excited state. Then, after some time, the electron relaxes and releases energy, minus the deficit in initially raising to the excited state, in a process known as photoluminescence (PL). Kasha's rule states that luminescence will occur from the lowest vibrational level of the excited state to a vibrational level in the ground state [12], where a ZPL and PSB is shown in figure 3-2b, and leads to the mirror symmetry between absorption and luminescence.

However, unlike absorption spectra, PL is complicated by radiative and non-radiative relaxation pathways, and from this it is not considered quantitative for determining defect concentrations directly. On the other hand, PL spectra can be readily acquired and where the defect concentration is low (below 1 ppb) it is possible to detect single defect centres, as will be discussed in section 3.2, which can lead to an estimation of the defect concentration.

At room temperature, the Boltzmann distribution leads to higher vibrational states being populated, allowing the PSB to be prominent. In reducing the temperature by cryogenic cooling, the higher vibrational states are no longer accessible and the PSB reduces and increases the amount of photons increased in the ZPL. Furthermore, since the thermalisation energy at room temperature ($k_BT \approx 25$ meV) is reduced, in defect systems which exhibit Jahn-Teller and spin-splitting effects from their symmetry, the ZPL will become multiple, spectrometer-limited, narrow lines.

The width, and subsequently the intensity, of the ZPL is governed by the lifetime of the excited state [13]. However, in practice this tends to be broadened by perturbations to the lattice, such as strain, which impact on the energy levels of the system. For this reason, the NV^- centre has shown to be a sensitive defect to heat, strain, electric and magnetic fields by changes in the ZPL [14–17].

Each point defect will have an absorption dipole with a crystallographic orientation determined by the symmetry of the defect which can be deduced by group theory [18]. For a linearly polarised excitation source, the absorption dipole at a given orientation will depend upon the crystallographic viewing direction. NV^- is known to have absorption dipoles perpendicular to the symmetry axis of $\{1\,1\,1\}$, hence figure 3-3 shows a simulation of the polarisation plot for NV^- along each four possible $\{1\,1\,1\}$ orientations, relative to the crystallographic viewing direction.

As the relaxation pathway of the defect in the band gap is unique to a particular chemistry, the PL spectrum can be a powerful resource to understanding how the material was made, in a non-destructive characterisation technique. Care should be taken however as the range of optically active defects in diamond range from UV and into the IR, and so a full assay of defects will require a large spectrum of excitation sources to probe a large energy range. For example, the N_3V defect (N3

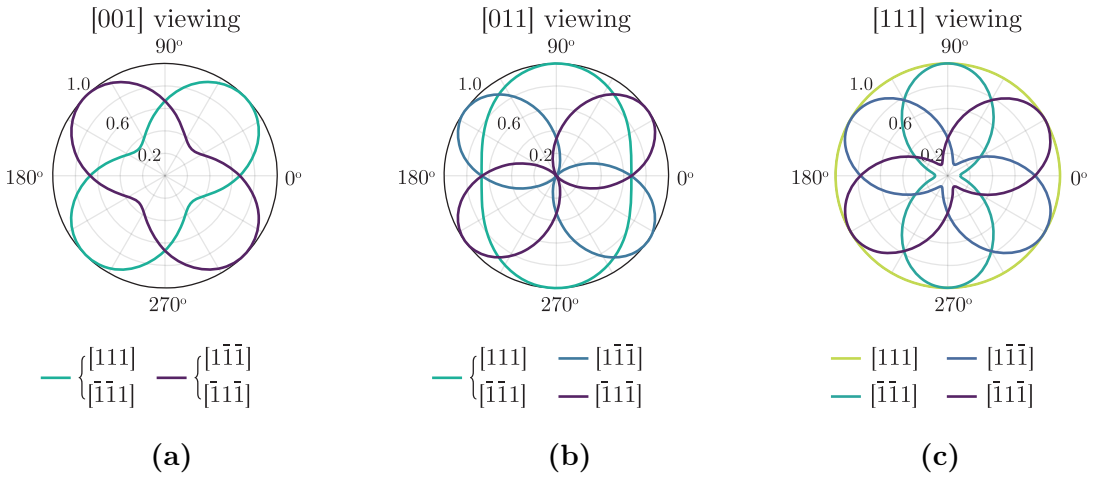

Figure 3-3 A simulation of the absorption dipoles as a function of linear polarisation angle for NV^- based on (a) [0 0 1], (b) [0 1 1], and (c) [1 1 1] viewing directions.

centre) in diamond has a ZPL at 415 nm (2.987 eV), where as the N_2V^- defect (H2 centre) has a ZPL at 986 nm (1.257 eV) and so appropriate laser sources higher in energy of the ZPL must be used to excite the defect.

Furthermore, the stability of point defect emission is reliant on two factors, a suitable excitation wavelength, and, a charge stable environment. In the former case, an excitation energy this is too high can photoionise defects, whilst in the latter the defect may already be subject to charge dynamics where the defect is readily ionised by a stochastic process. Both cases can be seen in the NV centre, where an excitation < 500 nm can remove NV^- emission with an increase in NV^0 [19], or NV^- centres close to the surface can become unstable (known as blinking) by localised charges at the surface [20].

3.1.2.4 Cathodoluminescence (CL)

Cathodoluminescence (CL) can be considered as the reverse of the photoelectric effect, such that the emission of light is caused by incident electrons. Recording a CL spectrum from material can be achieved by one of two methods, a series of optics connected to a scanning electron microscope (SEM) or by an electron gun coupled to an optical microscope. For CL studies in this thesis, it is only CL collected by SEM that will be considered.

The displacement threshold for diamond is quoted as 38 eV in the [0 0 1] direction [21], and hence electrons of energy above 180 keV will result in the creation of Frenkel defects. For electron energies lower than this, both elastic and inelastic scattering events occur such that the electron changes its direction or reduces its kinetic energy respectively. The interaction of the electron beam with the material generates an interaction volume. Figure 3-4 schematically shows where backscattered electrons from elastic scattering events originate with respect to the inelastic scattering events, which also include Auger and secondary electrons, X-rays, phonons, CL emission and plasmons.

It is possible to employ Monte Carlo simulations [23][a] for understanding the electron trajectories in diamond, and the profile from which the electron energy is absorbed generating CL emission (figure 3-5). Typically these simulations do not consider the structure of the material, only the density, hence we assume this model to be *amorphous* carbon with the density of diamond (3.51 g cm^{-3}). Figure 3-5a and 3-5b relate to the electron trajectories in diamond from SEM microscopes where the electron source is from a field effect gun (FEG) and lanthanum hexaboride (LaB_6) source respectively. Here, typical values have been entered to the simulation where the FEG SEM operates with an accelerating voltage of 10 keV and focussed electron spot size of 5 nm, whereas the LaB_6 SEM parameters are 15 keV and 100 nm

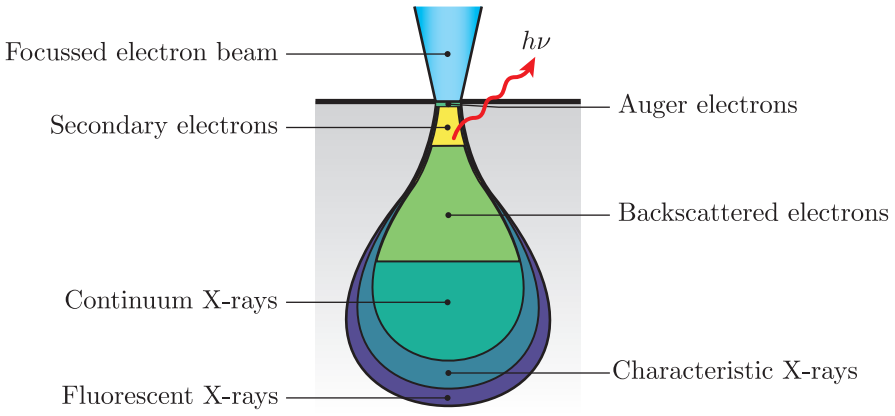

Figure 3-4 The interaction volume generated by the incidence of an electron beam at the surface of a material. Figure adapted from [22]

[a]Monte Carlo Simulation of Electron Trajectories in Solids (CASINO): `http://www.gel.usherbrooke.ca/casino/index.html`

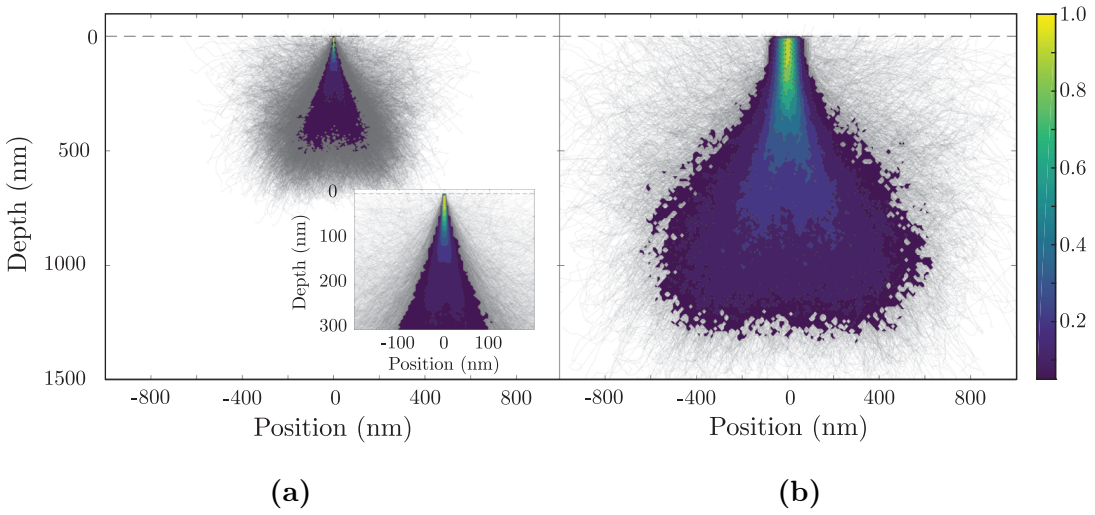

Figure 3-5 A Monte Carlo simulation for (a) 10 keV and (b) 15 keV electron accelerating voltages with spot sizes 5 nm and 100 nm respectively where the grey lines indicate the trajectories of the electrons in either scenario. The dashed line at 0 nm depth represents the surface between air and diamond and shown on the inset of (a) is a closer view at the surface of incidence for the 10 keV model. The colour contour map represents the energy deposited by the electrons in diamond and subsequently the origin of the CL intensity where the colour bar is normalised against the maximum.

respectively. Therefore the spatial resolution, and CL intensity, is convolved as the spot size and accelerating voltage with the exciton diffusion length in diamond, which is reported to be up to 7.9 µm [24].

For diamond, CL is driven by the energy of the electron (e^-) source which is several orders of magnitude higher than the band gap of the material, such that a hole (h^+) is generated in the valence band from the promotion of e^- to the conduction band. Free exciton emission is then generated by the recombination of the e^--h^+ pair. However, this emission can be modified by the inclusion of either a shallow donor or acceptor state in the band gap, resulting in a bound exciton.

Similar to electron relaxation in PL, phonon assisted relaxations also take place within the CL mechanism. Non-zero momentum is applied to thermalised electrons in the conduction band and hence a direct transition at the energy of the band gap of diamond is forbidden. Therefore CL optical transitions will also involve a phonon of energy $\hbar\omega$. The free exciton emission of diamond results in a maximum at 5.272 eV (235.2 nm) with the optical transition involving the transverse optical (TO) phonon, with other phonon modes (transverse acoustic (TA), longitudinal

optical and acoustic (LO, LA)) as less intense features.

Emission due to excitons bound to shallow acceptor/donor states in the band gap are shifted in energy by a deficit known as the localisation energy E_{loc}. By charge conservation arguments, capture of a free exciton X by such a state creates a complex with four components; $B_S^0 X = (B^+,\ 2e^-,\ h^+) \rightarrow B_S^0 + X$ where here B_S^0 is the boron acceptor in diamond, but holds true also for phosphorous and arsenic [25].

For boron in diamond, the bound exciton maxima also involves the TO phonon, with emission peaking at 5.217 eV (237.7 nm) and hence suggests $E_{loc} = 55$ meV.

Consequently excitonic emission is considered as a three level system [25] where the populations of free excitons n_F and bound excitons n_B are described by simple rate equations where by

$$\frac{dn_F}{dt} = G - \frac{n_F}{\tau_F^r} - \sigma \nu_{th} N n_F \tag{3-18a}$$

$$\frac{dn_B}{dt} = -\frac{n_F}{\tau_B} + \sigma \nu_{th} N n_F \tag{3-18b}$$

where τ_F^r and τ_B represent the radiative lifetime of the free exciton and total bound exciton lifetime respectively, with ν_{th} as the average thermal velocity of the free exciton, G as the generation rate of the exciton and finally the capture process is bound by the capture cross section σ and impurity concentration N.

From this, the intensities of free and bound exciton emission are governed by their radiative lifetime as dictated by quantum mechanical optical transition rules as

$$I_F = \frac{n_F}{\tau_F^r} \tag{3-19a}$$

$$I_B = \frac{n_B}{\tau_B^r} \tag{3-19b}$$

Under continuous excitation and within the steady state regime, with equa-

tion (3-18b) one can write the ratio of bound over free exciton to directly

$$R = \frac{I_{\mathrm{B}}}{I_{\mathrm{F}}} \tag{3-20a}$$

$$= \tau_{\mathrm{F}}^{\mathrm{rad}} \frac{\tau_{\mathrm{B}}}{\tau_{\mathrm{B}}^{\mathrm{rad}}} \sigma \nu_{\mathrm{th}} N \tag{3-20b}$$

$$= sN \tag{3-20c}$$

Hence in taking R it is possible to directly know the donor (or acceptor) concentration since s is independent of G and not influenced by populations of other impurities. This very nature has been developed in many semiconductor materials, and in diamond both Kawarada [26] and Barjon [27] have realised a calibration constant relating R to the concentration of substitutional boron $[\mathrm{B_S}]$ as

$$[\mathrm{B_S}] = 1.26 \times 10^{17} R \ [\mathrm{cm^{-3}}] \tag{3-21a}$$

$$= 7.16 \times 10^{2} R \ [\mathrm{ppb}] \tag{3-21b}$$

In this, one can assume that the concentration is determined irrespective of charge state since it is neutralised by the injection of carriers [28]. Thus, it has been experimentally proven to obtain a concentration of boron in diamond with a detection limit of 0.05 ppb [25].

3.1.3 X-ray topography (XRT)

In 1912 Paul Peter Ewald and Max von Laue discovered that crystalline material could be used as a diffraction grating for X-rays. Three years later, father and son physicists William Henry Bragg and William Lawrence Bragg won the Nobel Prize for Physics from their work of X-ray diffraction for crystallographic properties. From this, Bragg's law was born which describes diffraction not just of crystallographic material, but diffraction in general as

$$n\lambda = 2d \sin(\theta) \tag{3-22}$$

where n is the diffraction order, λ is the wavelength of the EM wave, d is the atomic spacing and θ is the half angle for which the EM wave is diffracted.

In the crystallographic sense, the collision of X-rays with atoms and their electrons results in the deflection of the X-ray away from the original direction of travel. For elastic scattering (otherwise known as Thompson scattering) the X-ray wavelength does not change and only results in a change of momentum and hence the detection of this change reveals information about the electron distribution in the material.

Diamond has long been the subject of X-ray diffraction studies [29], where the reader is directed to Moore's review for a compendium of imaging diamond with X-rays [30].

Characterisation of the diamond crystalline quality is therefore assessed by means of X-ray topography (XRT). For a perfect diamond lattice, the X-ray will not deviate resulting in topograph free of contrast. Hence extended defects that cause deviation to the X-ray beam are readily understood. This can be done either in a reflection or transmission geometry, where the former only reveals surface information and the latter is useful when the crystal is of good quality.

With synchrotron based techniques, a white-beam X-ray source is incident upon the diamond. If the diamond is smaller than the beam diameter then multiple Bragg diffraction spots are created simultaneously. Due to the low divergence of the beam, each spot generated contains a wealth of information about extended defects in the lattice (such as dislocations or stacking faults) by the intensity variations and diffraction distribution. In transmission, the images projected are the integrated intensities of diffraction and hence depth information is lost.

Care must be taken with the XRT with respect to the crystallographic direction of reflection. For example, the $\langle 2\,2\,2 \rangle$ reflection is forbidden since $\langle 1\,1\,1 \rangle$ is a $\lambda/2$ harmonic of Bragg diffraction and hence produces weak diffraction. Equally, the Burgers vector $\boldsymbol{b}$ describes the direction upon which the defect is orientated throughout the lattice. For a given diffraction vector $\boldsymbol{g}$, the invisibility criterion is satisfied when

$$\boldsymbol{g} \cdot \boldsymbol{b} = 0 \tag{3-23}$$

and hence when the extended defect lies in a plane parallel to the diffraction, the defect cannot be seen.

3.2 Point defect characterisation

With respect to the identification of single point defects in diamond, the purity of the diamond must be inherently high. Here the theory is presented for how one is able to image the photoluminescence from point defects with diffraction-limited optical resolution. Further theory is also included on the physics of the negative nitrogen vacancy, NV^-, centre.

3.2.1 Scanning confocal microscopy

For PL measurements it is standard practice to collect light through an optical microscope where the excitation source (often a laser) is directed to the sample, by a dichroic, and the generated fluorescence from the sample is either incident upon a spectrometer or imaging system. With a simple design, most microscopes are coined as *widefield* microscopes since they collect light/PL from everywhere. It is possible to image down to the diffraction limit of light by optical sectioning in a *confocal* microscope, through a means of rejecting out-of-focus light by integrating a simple pinhole (see section 4.2 for implementation).

The imaging resolution of an optical microscope is defined by the point spread function (PSF) as the image produced by the imaging system for an infinitely small point object. This PSF is then convolved with the intensity of the object as the image intensity (I) recorded as

$$I(x,y,z,t) = o(x,y,z,t) \otimes \mathrm{PSF}(x,y,z,t) \tag{3-24}$$

where x, y, z, t describe the dimensions of space-time, o is the object, and $\otimes$ is the convolution operator. For a perfect diffraction limited optical system, the image intensity can be described by the Airy disk pattern [31] where the intensity for the lateral $I(\nu)$ and axial $I(u)$ intensities are

$$I(\nu) = \left(\frac{2J_1(\nu)}{\nu}\right)^2 \tag{3-25a}$$

$$I(u) = \left(\frac{\sin(u/4)}{u/4}\right)^2 \tag{3-25b}$$

for normalised (dimensionless) image coordinates ν and u, and where J_1 is the Bessel function of the first kind. From this, it is possible to directly image the PSF of a microscope by imaging an object that is smaller than the diffraction limit of light (a point source). The theoretical PSF for both widefield and confocal microscopes are represented in figure 3-6 (a)-(d).

Therefore, the spatial resolution of a microscope both laterally (Δr_{FWHM}) and axially (Δz_{FWHM}) is bound by the ability to image the PSF. For a widefield microscope, the optical resolution of the PSF for a point object is given as

$$\Delta r_{\mathrm{FWHM}} = \frac{0.51\lambda}{\mathrm{NA}} \tag{3-26a}$$

$$\Delta z_{\mathrm{FWHM}} = \frac{1.77\lambda n}{\mathrm{NA}^2} \tag{3-26b}$$

where λ is the wavelength of light, n is the refractive index of the medium between sample and microscope objective, and NA is the numerical aperture. If one were to implement an infinitely small pinhole into a confocal microscope on the detection, the act is to effectively square the PSF [32] (equation (3-25)) whereby the optical resolution of the PSF is given as

$$\Delta r_{\mathrm{FWHM}} = \frac{0.37\lambda}{\mathrm{NA}} \tag{3-27a}$$

$$\Delta z_{\mathrm{FWHM}} = \frac{1.28\lambda n}{\mathrm{NA}^2} \tag{3-27b}$$

for an approximately $\sqrt{2}$ improvement in the lateral and axial resolution as highlighted in figure 3-6 (e) and (f).

In the 19th Century, Ernst Abbe theorised that the optical resolution of a microscope can be limited by the diffraction of light (c.f. equation (3-22)) where the optical resolution follows

$$d = \frac{\lambda}{2\mathrm{NA}} \tag{3-28}$$

where d is the lateral resolution, λ is the wavelength of light, and NA is the numerical aperture which is a dimensionless number defining the solid angle in which light rays are collected such that $\mathrm{NA} = n \sin \alpha$. Hence the lateral resolution limit can be approximated to half the wavelength of excitation light.

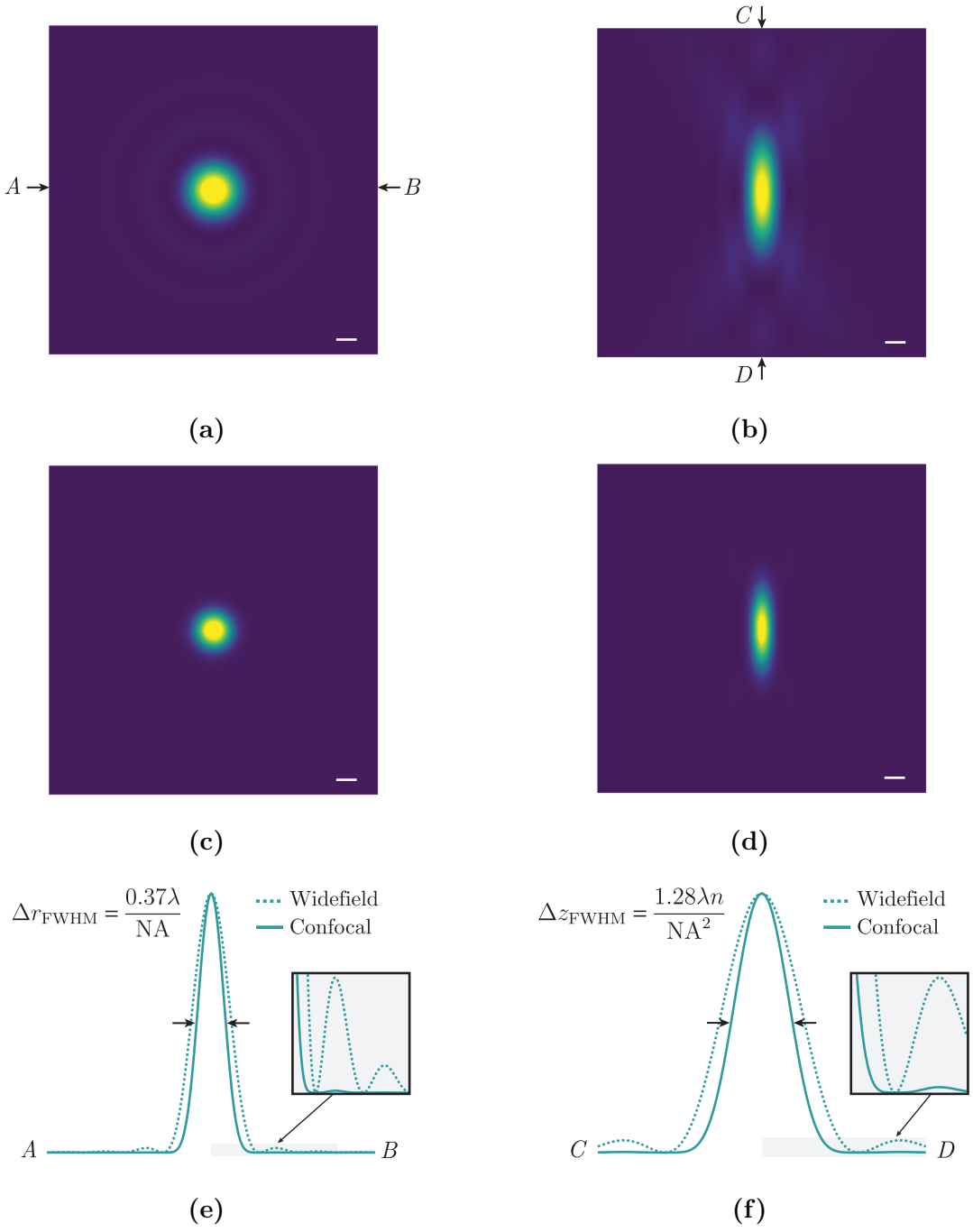

Figure 3-6 The theoretical PSF where the lateral and axial components are shown for widefield (a), (b) and confocal (c),(d) respectively. The line trace *A*-*B* and *C*-*D* show the airy pattern in each case and the improvement on the PSF for the confocal case (e),(f) respectively. Scale bar = 1 optical coordinate.

Subsequently, 50 years after the death of Abbe the confocal microscope was developed by Marvin Minsky and later patented [33]. Minsky's memoir [34] recalls the problems he faced when trying to take microscope images of nerve cells: one cell could only be imaged at a time since staining a collection resulted in too little signal compared to the noise. After completing his doctoral thesis, he returned to this problem and realised that both the excitation and detection should consider the image of a point source. Minsky therefore put a pinhole in front of both the excitation source and detector such that light outside of the focal plane was rejected. In doing so it was possible to image one point at a time, hence the sample needed to be scanned to build up a picture, and Minsky was finally able to resolve points closer than 1 µm apart.

There also exists two further definitions for the ability to resolve two point sources in the same axial plane:

- Rayleigh's criterion: two objects are resolvable when the minima of one Airy disk coincides with the maximum of the second object where

$$\Delta r_{\text{Rayleigh}} = \frac{0.61\lambda}{\text{NA}} \tag{3-29}$$

- Sparrow's criterion: two objects are resolvable when a saddle point can be seen between two maxima where

$$\Delta r_{\text{Sparrow}} = \frac{0.47\lambda}{\text{NA}} \tag{3-30}$$

  and is closer to Abbe's formula (equation (3-28))

Since the confocal microscope offers a $\sqrt{2}$ improvement in resolution, Abbe's formula holds true and the resolvable objects meet Sparrow's criterion (figure 3-7).

Practically, the choice of the pinhole for the detection is chosen to achieve a good level of rejection whilst not losing too much signal. It is therefore necessary to consider the energy distribution $E(\nu)$ contained within the diffraction pattern and is done so by integrating equation (3-25) where

$$E(\nu) = \int_0^{\nu} \left(\frac{2J_1(\nu)}{\nu} \right)^2 \, \mathrm{d}\nu \tag{3-31a}$$

$$= 2 \int_0^{\nu} \frac{J_1^2(\nu)}{\nu} \, \mathrm{d}\nu \tag{3-31b}$$

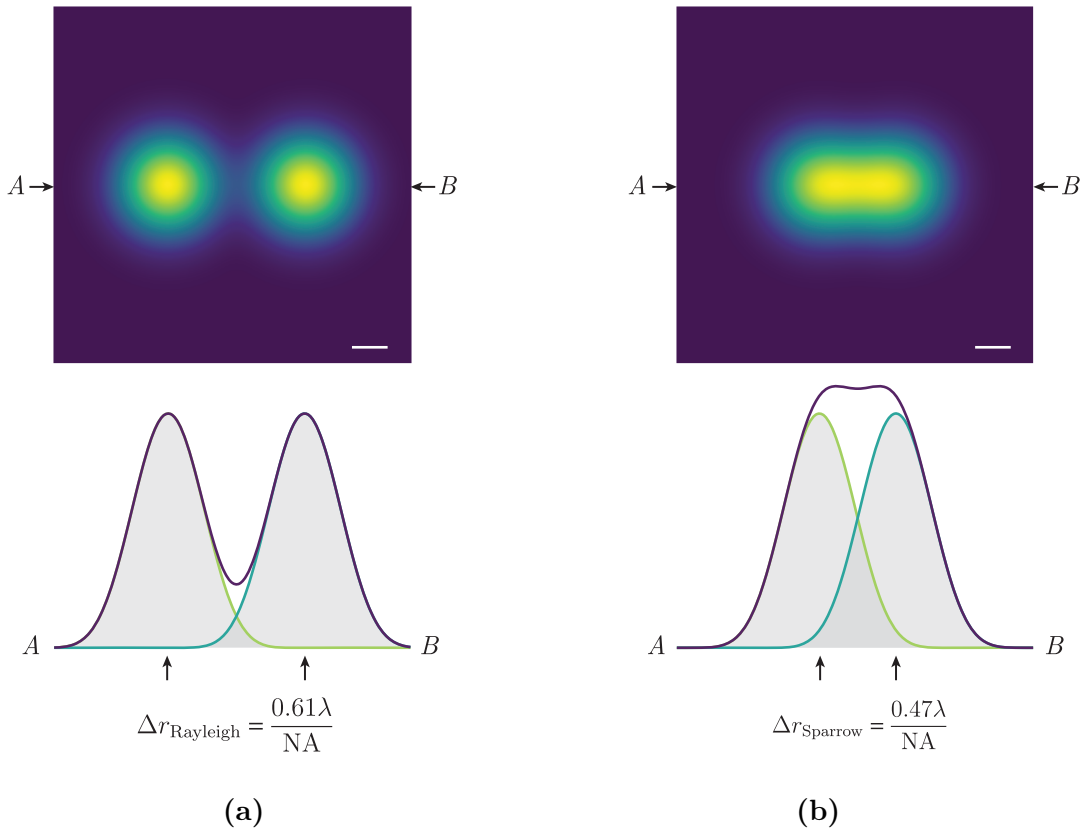

Figure 3-7 Demonstration of resolving two confocal Airy disks based on (a) Rayleigh's criterion, and (b) Sparrow's criterion

By the recurrance relation

$$\frac{\mathrm{d}}{\mathrm{d}x}(x^{n+1}J_{n+1}(x)) = x^{n+1}J_n(x) \tag{3-32}$$

the integrand in equation (3-31b) becomes

$$\frac{J_1^2(\nu)}{\nu} = J_0(\nu)J_1(\nu) - \frac{\mathrm{d}J_1(\nu)}{\mathrm{d}\nu}J_1(\nu) \tag{3-33a}$$

$$= -\frac{1}{2}\frac{\mathrm{d}}{\mathrm{d}x}(J_0^2(\nu) + J_1^2(\nu)) \tag{3-33b}$$

since $J_0(0) = 1$ and $J_1(0) = 0$ we arrive at

$$E(\nu) = 1 - J_0^2(\nu) - J_1^2(\nu) \tag{3-34}$$

The result of this is plotted in figure 3-8 and it can be seen that the pinhole for the system should be chosen such that $\nu_P = 2.5$ to allow a theoretical collection efficiency of around 75% by retaining good axial resolution without significant

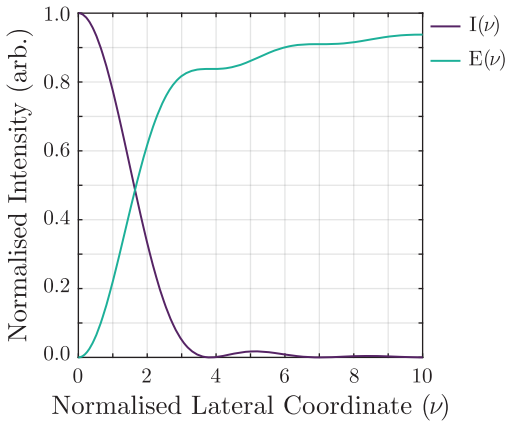

Figure 3-8 The normalised Airy diffraction intensity (I(ν)) and energy (E(ν)) distribution plot as a function of the normalised lateral coordinate ν

compromise to the lateral resolution. If $\nu_P \geq 4$ the microscope can be considered as a widefield microscope.

Finally, the knowledge of diffraction theory and pinhole size can be reduced, such that the level of confocality can be decided on the following criteria [32]

$$\frac{M}{\mathrm{NA}} \geq \frac{\pi d_0}{\nu_{P_{\max}} \lambda} \tag{3-35}$$

where M and NA are the magnification and numerical aperture of the microscope objective, d_0 is the pinhole diameter at the detector and $\nu_{P_{\max}}$ is the maximum desired lateral optical coordinate for the system (see [32] for details).

Since point defects in diamond emit photons at a point source, the ability to resolve point objects allows one to count emitters and approximate the defect concentration within the diamond, if they are homogeneously distributed, by the following relation

$$\xi \approx V[X] \tag{3-36}$$

where ξ is the number of defects counted, V is the volume sampled and $[X]$ is the concentration of the defect. For example, if a confocal image is taken in the XY plane with an area of 100 µm^2, and assuming an axial resolution of 1 µm, if 18 separately resolvable objects are counted (also assuming each is a single point defect) this would approximate to a concentration of 0.001 ppb, or 1 part per trillion (ppt). However, care must be taken for polarisation effects and defect ionisation during imaging such that equation (3-36) can only ever be an approximation.

3.2.2 Single photon emission

The identification of a single photon source is readily verified by the second-order correlation function $g^{(2)}(\tau)$. For classical behaviour of light, $g^{(2)}(\tau)$ has a lower bound of unity. However with a quantum mechanical approach a single photon source $g^{(2)}(\tau)$ will equal zero for $\tau = 0$. This nature of photons is characterised by means of the Hanbury Brown Twiss (HBT) interferometer which correlates the emission of light with arrival times on two detectors for coherently created photons [35].

In classical theory, the second order correlation function is defined as [36]

$$g^{(2)}(\tau) = \frac{\langle I(t) + I(t+\tau)\rangle}{\langle I(t)\rangle^2} \tag{3-37}$$

for a time dependent intensity $I(t)$ and where $\langle \ldots \rangle$ is the average over long intervals.

Since $g^{(2)}(\tau)$ considers the temporal coherence we consider the case when $\tau \gg \tau_c$, where τ_c is the coherence time of the source. From this the intensity fluctuations will be completely uncorrelated with each other. In defining $I(t) = \langle I\rangle + \Delta I(t)$ it then follows that

$$\langle I(t) + I(t+\tau)\rangle_{\tau \gg \tau_c} = \langle (\langle I\rangle + \Delta I(t))\,\langle I\rangle + \Delta I(t+\tau))\rangle \tag{3-38a}$$

$$= \langle I\rangle^2 \tag{3-38b}$$

Hence we arrive at

$$g^{(2)}(\tau \gg \tau_c) = \frac{\langle I(t)I(t+\tau)\rangle}{\langle I(t)\rangle^2} = \frac{\langle I\rangle^2}{\langle I\rangle^2} = 1 \tag{3-39}$$

If $\tau \ll \tau_c$ then there will be correlations between intensities at the two times where for $\tau = 0$

$$g^{(2)}(0) = \frac{\langle I(t)^2\rangle}{\langle I(t)\rangle^2} \tag{3-40}$$

Thus for any classical time dependent intensity the two relations are found

$$g^{(2)}(0) \geq 1 \tag{3-41a}$$

$$g^{(2)}(0) \geq g^{(2)}(\tau) \tag{3-41b}$$

In the quantum mechanical picture, the quantisation of the electromagnetic field enables one to define photon number states $|n\rangle$ by

$$\hat{H}|n\rangle = \hbar\omega\left(\hat{a}^\dagger\hat{a} + \frac{1}{2}\right)|n\rangle = \left(n + \frac{1}{2}\right)\hbar\omega|n\rangle \tag{3-42}$$

for non-negative integers n where photons have angular frequency ω and $\hat{H}$ represents the energy operator. The operators $\hat{a}^\dagger$ and $\hat{a}$ are the creation and destruction operators respectively whereby

$$\hat{a}^\dagger|n\rangle = \sqrt{n+1}|n+1\rangle \tag{3-43a}$$

$$\hat{a}|n\rangle = \sqrt{n}|n-1\rangle \tag{3-43b}$$

Which are commutable as

$$[\hat{a}, \hat{a}^\dagger] = \hat{a}\hat{a}^\dagger - \hat{a}^\dagger\hat{a} = 1 \tag{3-44}$$

The number operator $\hat{n}$ can also be defined as

$$\hat{n} = \hat{a}^\dagger\hat{a} \tag{3-45}$$

where $\hat{n}|n\rangle = n|n\rangle$.

Conducting a HBT experiment requires the use of two single photon detectors, D1 and D2, where the stream of photons are split by a 50:50 beamsplitter such that each detector has a 50% probability of encountering a photon at each arrival time. Since the detector count rate is proportional to the number of photons it is possible to represent the second-order correlation function as

$$g^{(2)}(\tau) = \frac{\langle n_1(t)n_2(t+\tau)\rangle}{\langle n_1(t)\rangle\langle n_2(t+\tau)\rangle} \tag{3-46}$$

where n_i is the photon count rate at detector i for a time t.

Consequently, through the quantum theory of light and description of the time dependent electromagnetic field, it is possible to reproduce equation (3-46) in terms of the creation and destruction operators [37] as

$$g^{(2)}(\tau) = \frac{\langle\hat{a}^\dagger\hat{a}^\dagger\hat{a}\hat{a}\rangle}{\langle\hat{a}^\dagger\hat{a}\rangle^2} \tag{3-47}$$

Since the order of commutation is important this can be rewritten as

$$g^{(2)}(\tau) = \frac{\langle \hat{a}^\dagger(\hat{a}\hat{a}^\dagger - 1)\hat{a}\rangle}{\langle \hat{a}^\dagger\hat{a}\rangle^2} \tag{3-48a}$$

$$= \frac{\langle (\hat{a}^\dagger\hat{a})^2\rangle - \langle \hat{a}^\dagger\hat{a}\rangle}{\langle \hat{a}^\dagger\hat{a}\rangle^2} \tag{3-48b}$$

$$= \frac{\langle n\rangle^2 - \langle n\rangle}{\langle n\rangle^2} \tag{3-48c}$$

The correlation between the two detectors therefore follows that of equation (3-48) and hence describes the simultaneous probability of counting photons on D2 at $t = 0$, given a detection event on D1 also at $t = 0$. For a single photon source then, it is impossible to have an event on D2 at $t = 0$ if D1 records an event at $t = 0$ and therefore

$$g^{(2)}(0) = 0 \tag{3-49}$$

Furthermore the consequence of equation (3-48c) results in boundaries for the number of emitters observed which are summarised in table 3-1.

n	Boundary condition
1	$0 < g^{(2)}(0) < 0.50$
2	$0.5 \leq g^{(2)}(0) < 0.67$
3	$0.67 \leq g^{(2)}(0) < 0.75$
4	$0.75 \leq g^{(2)}(0) < 0.80$
5	$0.80 \leq g^{(2)}(0) < 0.83$

Table 3-1 The boundary condition on $g^{(2)}(0)$ for a number of photon sources n measured.

The nature of the photon stream can be described as coherent (random), bunched or anti-bunched based on the value of $g^{(2)}(0)$ where

$$g^{(2)}(0) \begin{cases} > 1, & \text{for bunched} \\ = 1, & \text{for random} \\ < 1, & \text{for antibunched} \end{cases} \tag{3-50}$$

Antibunched light therefore is considered non-classically and must only be present in the quantum mechanical picture.

For a point defect in diamond it has already been discussed how PL is generated. Put into Dirac notation, the defect ground state will be $|1\rangle$ where absorption of laser causes excitation into state $|2\rangle$. The relaxation from $|2\rangle$ to $|1\rangle$ is hence the PL of the system. The relaxation of the system from $|2\rangle$ can also enter a third state $|3\rangle$ before relaxing back to $|1\rangle$. Here, $|3\rangle$ is of a different spin multiplicity, and the non-radiative transition into and out of this branch is known as intersystem crossing (ISC).

The relative population dynamics can therefore be described by the rate equations [38]

$$\begin{pmatrix} \dot{n_1} \\ \dot{n_2} \\ \dot{n_3} \end{pmatrix} = \begin{pmatrix} -r_{12} & r_{21} & r_{31} \\ r_{12} & -r_{21} - r_{23} & 0 \\ 0 & r_{23} & -r_{31} \end{pmatrix} \cdot \begin{pmatrix} n_1 \\ n_2 \\ n_3 \end{pmatrix} \tag{3-51}$$

where $\dot{n_i}$ is the level population of state n with a transition rate r_{ij} for $i, j = 1, 2, 3$. Equation (3-51) can be modified for a 2-level system where $n_3,\ \dot{n_3},\ r_{31},\ r_{23} = 0$. Finally, by solving equation (3-51) for the ground state condition the analytical expression for the second order correlation of a 2-level and 3-level system become respectively

$$g^{(2)}(\tau) = 1 - e^{-\lambda_1 \tau} \tag{3-52a}$$

$$g^{(2)}(\tau) = 1 - (1 + a)e^{-\lambda_1 \tau} + ae^{-\lambda_2 \tau} \tag{3-52b}$$

where $\lambda_1 = r_{12} + r_{21}$, $\lambda_2 = r_{31} + r_{23}r_{12}/\lambda_1$ and $a = r_{12}r_{23}/(\lambda_1 r_{31})$. A representation of both a 2-level and 3-level function is ploted in figure 3-9. From this, it is possible to extract the fluorescence lifetime of the defect by $1/\lambda_1$ for antibunching, and a second lifetime in the 3-level system relating to the shelving state as $1/\lambda_2$.

The efficiency of a single emitting dipole governs the strength of the emission seen. By first considering the 2-level system it is possible to explain the pumping rate r_{12} with a linear dependence on the excitation power P_e as

$$r_{12} = kP_e \tag{3-53}$$

where k is a constant of proportionality. Under equilibrium conditions from equation (3-51) we see that the population of state $|2\rangle$ can be expressed as

$$n_2 = \frac{r_{12}}{r_{12} + r_{21}} \tag{3-54}$$

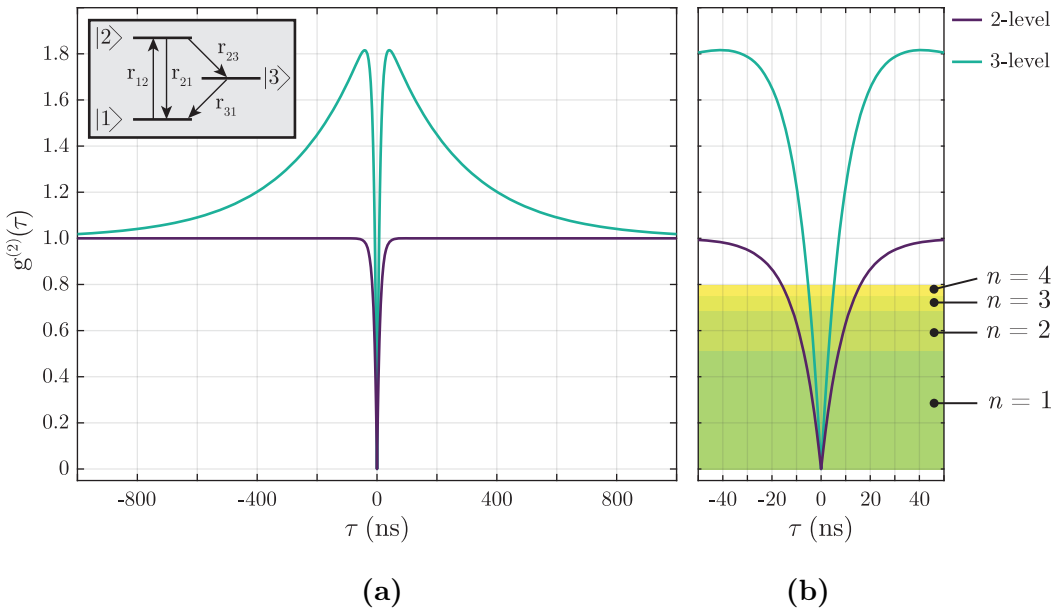

Figure 3-9 The theoretical second-order correlation function of a single emitter where (a) at long τ the 2-level system tends to 1 whilst the 3-level system (defined on the inset schematic) shows $g^{(2)}(\tau) > 1$ for the shelving third level before tending to 1 at long τ. (b) shows the fluorescence lifetime can be seen in the antibunching region where $\tau_1 = 10$ ns for both plots. The boundary regions have been highlighted for the minima to be contained within for the number of photon emitters n between 1 and 4.

As the photon emission rate $R = r_{21}n_2$, from equations (3-53) and (3-54) R can be defined in terms of the excitation power

$$R = \frac{r_{21}P_e}{P_e + r_{21}/k} = \frac{r_{21}P_e}{P_e + P_{\text{sat}}} \tag{3-55}$$

where P_{sat} corresponds to a saturation power and as $P_e \gg P_{\text{sat}}$, R approaches r_{21}.

By now considering the 3-level system, the rate equations modify the equilibrium population of $|2\rangle$ such that

$$n_2 = \frac{r_{12}}{(1 + \frac{r_{23}}{r_{31}})r_{12} + r_{21} + r_{23}} \tag{3-56}$$

And in doing so, the photon emission rate is therefore modified to include the dependence on the third level as

$$R = \Omega \frac{r_{21}P_e}{P_e + P_{\text{sat}}} \tag{3-57}$$

where

$$\Omega = \frac{1}{1 + \frac{r_{23}}{r_{31}}} \tag{3-58}$$

For a given value of R, it is clear to see the effect of increasing the excitation power where $P > P_{\text{sat}}$ results in an increase of the ratio of r_{23}/r_{31}. Thus, the $g^{(2)}(\tau)$ value increases above unity and indicates correlated emission (figure 3-9). As $P \gg P_{\text{sat}}$ the second decay lifetime becomes shorter still and the maximum value of $g^{(2)}(\tau)$ continues to increase.

3.2.3 Optically detected magnetic resonance (ODMR)

Optically detected magnetic resonance (ODMR) is the ability to initialise and readout out a spin state by means of optical detection. This is complementary to the techniques of EPR which measures a magnetic resonance of an unpaired electron and records an absorption in energy for spin transitions. For this thesis, ODMR will be restricted only to that of the NV^- centre. The electron energy structure for NV^- can be seen in figure 3-10a where the characteristic 637 nm ZPL is the relaxation from the excited ^3E state down to the $^3A_2$ state.

As NV^- exhibits a triplet spin multiplicity, the electron can take spin angular momentum of either $|m_s = 0\rangle$ or the degenerate $|m_s = \pm 1\rangle$ state. These states are separated by an amount of energy as described by the zero field interaction (§ 3.1.1.2). Hence the zero field Hamiltonian can be given by equation (3-9), where the zero field splitting for NV^- is $D = 2.87$ GHz. Equally, under a magnetic field, the electronic Zeeman interaction lifts the degeneracy of $|m_s = \pm 1\rangle$ states (figure 3-10b) where two resonance conditions are then possible at $D - \delta$ and $D + \delta$, where $\delta = g\mu_B B_0$ (c.f. equation (3-6))

Furthermore, during relaxation the excited electron has a 30% chance of entering the $S = 0$ manifold by ISC [39]. In this pathway no fluorescence at 637 nm is seen and consequently the electron preferentially relaxes into the $m_s = 0$ state of the $^3A_2$ level. Hence, the excitation and relaxation with $S = 1$ is known as the bright state, and relaxation by ISC known as the dark state.

With all of this, ODMR is therefore driven by simultaneously exciting with a frequency-swept microwave source whilst monitoring the fluorescence intensity. As the microwave energy becomes equal to the zero field splitting, the resonance

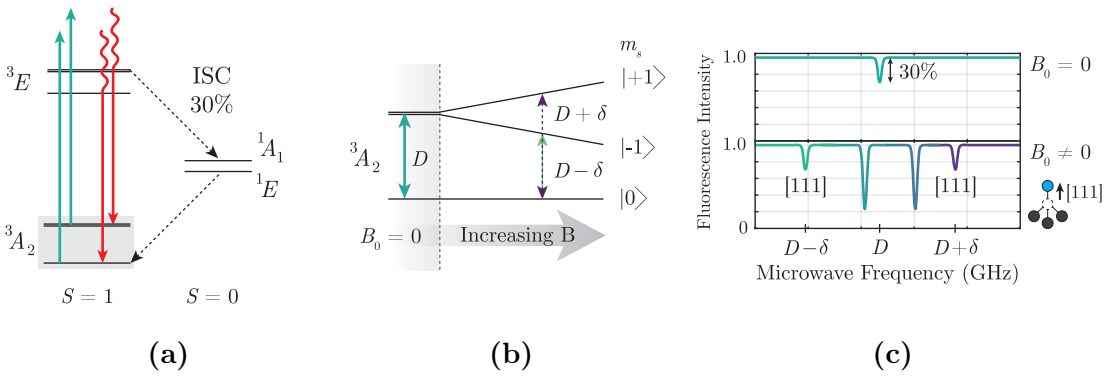

Figure 3-10 (a) Energy level diagram of the NV⁻ centre where excitation and emission is illustrated by the green and red arrows respectively where a 30% chance of intersystem crossing (ISC) into the $S = 0$ manifold can occur. (b) Zeeman effect on the ground $^3A_2$ state where the zero field splitting is $D = 2.87$GHz and resonance locations with an external magnetic field are denoted by $D \pm \delta$. (c) ODMR simulations showing a 30% fluorescence contrast without external field (top) as caused by the ISC pathway and resonance locations in ensemble ODMR with a 100 Gauss field aligned to [1 1 1].

condition yields a maximum 30% reduction in fluorescence intensity for NV⁻ due to ISC (figure 3-10c). Given the Zeeman interaction, this change in fluorescence can then occur at multiple frequencies, where the separation between resonance is linearly dependent upon the magnetic field strength aligned with the direction of the defect.

NV⁻ has the principle symmetry axis of ⟨1 1 1⟩, and as such can be aligned any of the four ⟨1 1 1⟩ directions. In an ODMR spectrum of multiple NV⁻ defects in one excitation spot (ensemble) it is possible to observe a set of four resonances for a field aligned to [1 1 1] where the outer most resonances correspond to NV⁻||[1 1 1] and the other three orientations all make a 109.5° angle to the field resulting in another two resonance positions with a contrast approximately 3 times greater (figure 3-10c).

In knowing the resonance location of a specific electron transition, it is possible to perform quantum operations on it. The quantum state of the electron can be represented by the Bloch sphere (figure 3-11a) where the poles represent the pure states and everywhere else on the surface is a superposition state. By applying a microwave pulse the magnetisation vector of the electron begins to change and thus moves around the Bloch sphere. The spin state is then readout by another laser

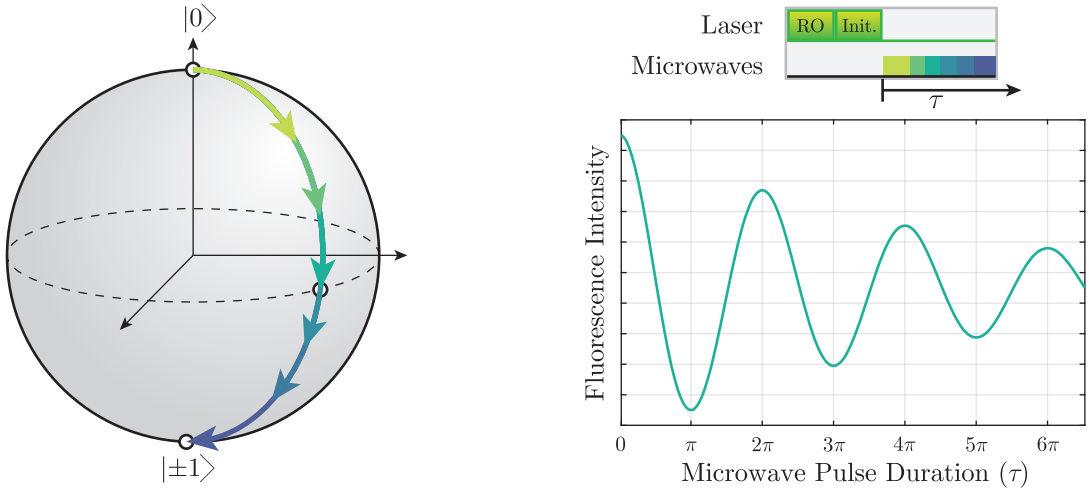

(a) **(b)**

Figure 3-11 (a) Bloch sphere representation of quantum states where the arrows represent a change in the spin state as caused by varying lengths of microwave pulses. (b) The pulse sequence for a Rabi measurement where the spin state is readout (RO) and then initialised (Init.) into the $|m_s = 0\rangle$ state. In each iteration the microwave pulse becomes longer before the next RO.

pulse which then re-initialises the system into the $|m_s = 0\rangle$ state. As illustrated in figure 3-11b, plotting the fluorescence intensity as a function of microwave pulse duration (τ) the experiment can be described by a damped cosine function

$$I(\tau) = Ae^{-\lambda\tau}\cos(-\omega\tau) \tag{3-59}$$

where A is a constant, λ is the damping coefficient due to the relaxation during long microwave pulse lengths and ω is the angular frequency of the oscillation. From this it becomes possible to know the microwave pulse length needed to transform the $|m_s = 0\rangle$ state into $|m_s = 1\rangle$, where the pulse length is known as a π-pulse.

Finally, the coherence properties of the defect system can be known from employing a Hahn echo sequence. In the same Bloch sphere representation, if an electron is manipulated onto the equator of the sphere ($+x$ axis) by a $\pi/2$-pulse the spin state begins dephase at an evolution time τ. By applying a π-pulse the evolution is inverted, and the spin state is refocused in the $-x$ axis. From an additional $\pi/2$-pulse the spin state is brought back to the pole of the sphere (figure 3-12a), and the spin state is read out by the laser.

This pulse sequence is analogous to the Hahn echo sequence often employed in EPR

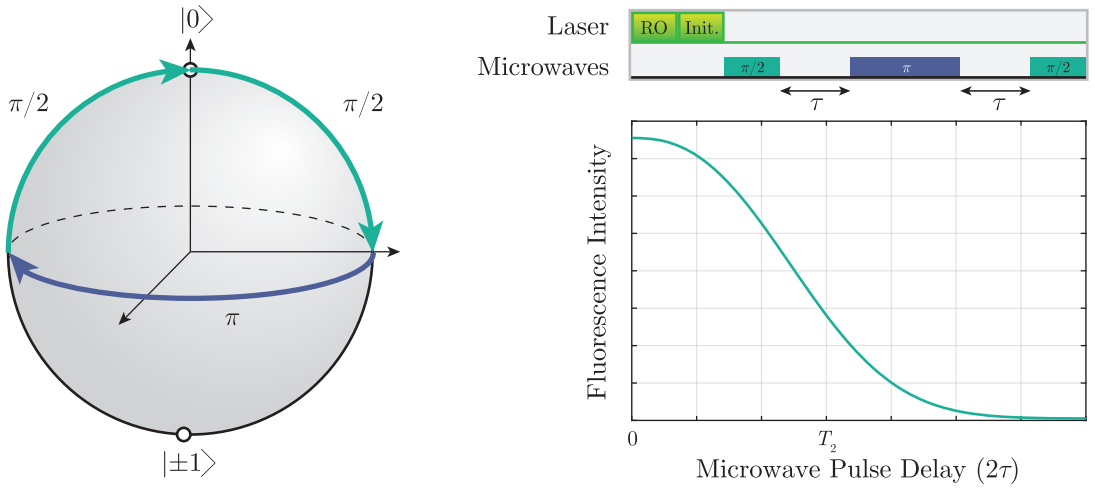

(a) **(b)**

Figure 3-12 (a) Bloch sphere representation of quantum states where the arrows represent a change in the spin state as caused by the $\pi/2$- and π-pulses. (b) The pulse sequence for a Hahn echo measurement where the laser reads out (RO) and initialises (Init.) the system into the $|m_s = 0\rangle$ state and for each iteration the temporal separation between microwave pulses becomes longer, the fluorescence intensity is then plotted against the microwave pulse separation with a characteristic decay time T_2.

experiments where the final $\pi/2$ pulse is omitted since the refocusing of the spin state produces a spin echo absorption. In the fluorescence picture, the intensity of fluorescence is determined by the efficiency of the state being projected back to $|m_s = 0\rangle$ on the final $\pi/2$-pulse. The characteristic decay time for the fluorescence intensity I of the Hahn echo is known as the decoherence time T_2 and follows a stretched exponential decay

$$I(\tau) = Ae^{-(\tau/T_2)^n} \tag{3-60}$$

where A is a constant, T_2 is the decoherence time and n is the exponent for a stretched exponential decay which can be seen in figure 3-12b.

For quantum computation a long T_2 time is desirable as this facilitates many quantum operations before the state is no longer coherent. In diamond, for a lattice free of significant spin-noise (i.e. low impurity and extended defect concentrations) the T_2 can be limited by the natural abundance of carbon-13 in the lattice, which can be extended either through decoupling techniques [40] or isotopic engineering of the diamond lattice [41].

References

1. J. A. Weil, J. R. Bolton, *Electron Paramagnetic Resonance* (John Wiley & Sons inc., Hoboken, NJ., 2nd, 2007).
2. A. Abragam, B. Bleaney, *Electron Paramagnetic Resonance of Transition Ions* (Oxford University Press, Oxford, 1980).
3. G. R. Eaton et al., *Quantitative EPR* (SpringerWienNewYork, New York, NY, 2010).
4. B. Odom et al., *Physical Review Letters* **97**, 030801 (2006).
5. J. Walker, *Reports on Progress in Physics* **42**, 1605–1659 (1979).
6. G. Davies, in *Identification of Defects in Semiconductors*, ed. by M. Stavola (Academic Press, 1999), chap. 1, pp. 1–92.
7. M. Fox, *Optical Properties of Solids* (Oxford University Press, Oxford, ed. 2, 2010).
8. C. D. Clark, P. J. Dean, P. V. Harris, *Proceedings of the Royal Society of London. Series A. Mathematical and Physical Sciences* **277**, 312–329 (1964).
9. R. Mildren, J. Rabeau, *Optical Engineering of Diamond* (Wiley, 2013).
10. M. D. McCluskey, *Journal of Applied Physics* **87**, 3593–3617 (2000).
11. R. J. Cruddace, PhD thesis, University of Warwick, 2007.
12. M. Kasha, *Discussions of the Faraday Society* **9**, 14 (1950).
13. M. Sauer, J. Hofkens, J. Enderlein, *Handbook of Fluorescence Spectroscopy and Imaging* (Wiley-VCH Verlag GmbH & Co. KGaA, Weinheim, Germany, 2011).
14. P. Neumann et al., *Nano Letters* **13**, 2738–2742 (2013).
15. M. W. Doherty et al., *Physical Review Letters* **112**, 047601 (2014).
16. F. Dolde et al., *Nature Physics* **7**, 459–463 (2011).
17. P. Maletinsky et al., *Nature Nanotechnology* **7**, 320–324 (2012).
18. B. L. Green, PhD thesis, University of Warwick, 2013.
19. N. Aslam et al., *New Journal of Physics* **15**, 013064 (2013).
20. C. Bradac et al., *Nature Nanotechnology* **5**, 345–349 (2010).
21. J. Koike, D. M. Parkin, T. E. Mitchell, *Applied Physics Letters* **60**, 1450–1452 (1992).

22. L. J. Brillson, in *Surfaces and Interfaces of Electronic Materials* (Wiley-VCH Verlag GmbH & Co. KGaA, Weinheim, Germany, 2012), pp. 279–304.
23. D. Drouin et al., *Scanning* **29**, 92–101 (2007).
24. J. Barjon et al., *Applied Physics Letters* **100**, 122107 (2012).
25. J. Barjon, *Physica Status Solidi (A) Applications and Materials Science* **1700402**, 1–10 (2017).
26. H. Kawarada et al., *Physical Review B* **47**, 3633–3637 (1993).
27. J. Barjon et al., *Physical Review B* **83**, 073201 (2011).
28. J. Barjon et al., *physica status solidi (a)* **204**, 2965–2970 (2007).
29. A. Lang, *Journal of Crystal Growth* **24-25**, 108–115 (1974).
30. M. Moore, *Journal of Physics: Condensed Matter* **21**, 364217 (2009).
31. M. Born, E. Wolf, *Principles of Optics* (Pergamon Press, ed. 4, 1970), pp. 370–458.
32. O. Hollricher, W. Ibach, in *Confocal Raman Microscopy*, ed. by T. Dieing, O. Hollricher, J. Toporski (Springer Berlin Heidelberg, 2010), chap. 1, pp. 1–20.
33. M. Minsky, *Microscopy apparatus*, US3013467A, 1961.
34. M. Minsky, *Scanning* **10**, 128–138 (1988).
35. R. Q. Twiss, A. G. Little, R. Hanbury Brown, *Nature* **180**, 324–326 (1957).
36. M. Fox, *Quantum Optics: An introduction* (Oxford University Press, Oxford, 2006).
37. R. Loudon, *The Quantum Theory of Light* (Oxford University Press, Oxford, ed. 3, 2000).
38. I. Aharonovich et al., *Physical Review A* **81**, 043813 (2010).
39. M. W. Doherty et al., *Physics Reports* **528**, 1–45 (2013).
40. N. Bar-Gill et al., *Nature Communications* **3**, 858 (2012).
41. G. Balasubramanian et al., *Nature materials* **8**, 383–7 (2009).

4

Experimental Details

Science is simply the word we use to describe a method of organising our curiosity

- Tim Minchin

Before studying single point defects in diamond it is necessary to first understand the bulk of the material. Therefore this chapter contains two major branches of experimental method, namely the techniques used to understand the morphology and defect incorporation within diamond, followed by further investigation of the diamond samples by *confocal* microscopy.

4.1 Bulk diamond characterisation

4.1.1 Quantitative EPR

Quantitative electron paramagnetic resonance (EPR) has long been demonstrated to be a powerful tool in determining defect concentrations in diamond. This area has been discussed in the previous chapters, and for this work EPR has been employed for the determination of the neutral substitutional nitrogen N_S^0 concentration ($[N_S^0]$).

Continuous wave (CW) EPR is typically carried out in a 'slow passage' regime, where the time scale of the experiment is much longer than the spin relaxation times (i.e. T_1 and T_2) of the defect under investigation. However, it is possible to modify the operating parameters of an EPR experiment, for example the power sweep rate and modulation, such that the rate of change in the magnetic field is greater

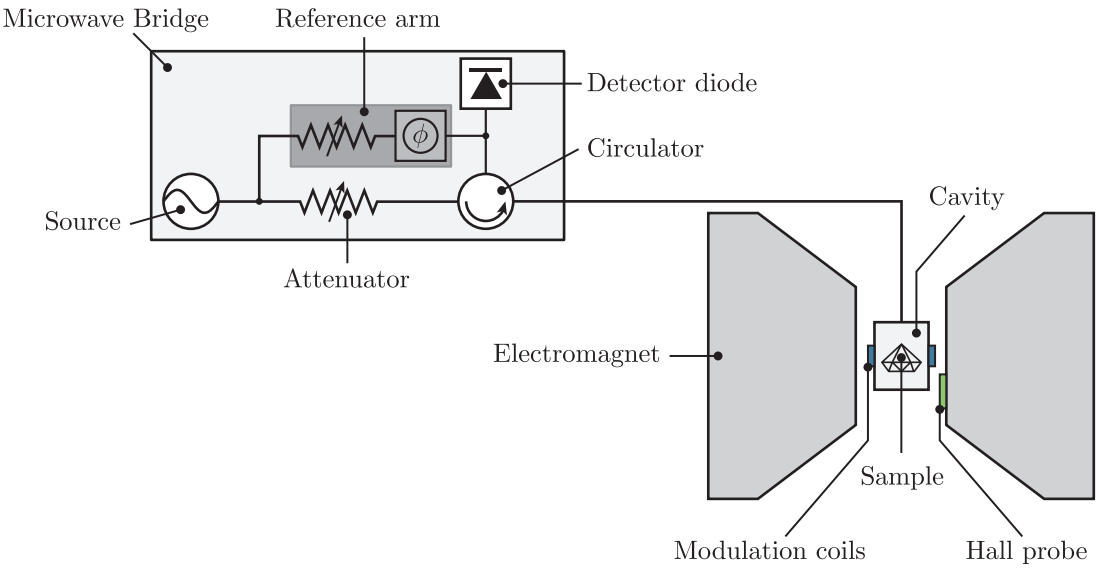

Figure 4-1 The key components of an EPR spectrometer, where the computer, console and magnet power supply have been omitted for simplicity. Figure adapted from [2].

than the spin relaxation time of the paramagnetic system. This creates a larger tip angle for the net magnetisation vector of the defect. When operating within this parameter space, the technique is known as rapid passage EPR (RP-EPR) as the magnetisation is not in a steady state, and becomes closer to a pulsed EPR measurement. This produces a higher signal-to-noise ratio compared to CW EPR and is able to produce quantitative measurements for $[N_S^0]$ below 1 ppm [1].

Shown in figure 4-1 is the simplified illustration of an EPR spectrometer and is largely comprised of a microwave bridge, large electromagnets and a resonance cavity. Microwaves from the bridge are delivered to the cavity via a waveguide. Upon loading a sample into the cavity, a central magnetic field is initialised and the cavity is tuned to match the impedance with the waveguide. Once the impedance of the waveguide and loaded resonator are matched at all microwave attenuations, the system is then critically coupled. A Hall probe acts as feedback instrumentation to ensure accurate knowledge of the field, and modulation coils provide lock-in detection.

All EPR spectra are obtained at room temperature on a Bruker EMX-E, combined with a Bruker ER041X (60 dB attenuation) X-band microwave bridge. Samples were loaded into a Bruker ER 4122SHQ spherical cavity which supports the TE011

mode. For RP-EPR, the experiment is conducted with a swept magnetic field and the microwave absorbance is recorded as a function of field strength, with acquisition parameters in accordance to those defined by Cann, and later developed by Breeze [1, 3].

If $[N_S^0]$ is sufficiently high, it is possible to align the diamond to a particular crystallographic direction by the interactive control of the EPR spectrometer, where a $\{0\,0\,1\}$ alignment produces 3 lines of equal intensity with a 3.3 mT separation [4]. However in the cases where the $[N_S^0]$ is low, the sample is left in an undetermined crystallographic orientation and the EPR spectrum is fitted to a simulation afterwards to determine the orientation [5].

Under identical acquisition parameters, the EPR intensity should scale according to the number of spins in the system, hence in taking a RP-EPR scan of a reference sample with a known $[N_S^0]$, the concentration in the sample can be found [1, 5]. By knowing the acquisition parameters, the sample $[N_S^0]$ can be given by

$$[N_S^0]_s = [N_S^0]_r \frac{I_s c_s}{I_r c_r} \tag{4-1}$$

here the subscripts denote sample and reference, for I as the EPR intensity of the spectrum and where c is related to experimental parameters which can be determined by

$$\frac{1}{c} = \sqrt{P} \cdot B_{\mathrm{mod}} \cdot Q \cdot \underbrace{[G \cdot N \cdot t]}_{\text{scan}} \cdot \underbrace{\left[g^2 \cdot S(S+1) \cdot m\right]}_{\text{sample}} \tag{4-2}$$

where P is the microwave power, B_{mod} is the modulation amplitude of the magnetic field, Q is the cavity Q-factor (coupling efficiency), G is the detector gain, N is the number of scans taken, t is the acquisition time, g is the electron g-factor, S is the total effective spin, and m is the mass of diamond.

All EPR spectra taken are loaded in to EPRsimulator [5], where a simulation of N_S^0 is fitted to the spectrum. All non-sample specific parameters (equation (4-2)) are stored within the EPR spectrum file generated by the Bruker software to which EPRsimulator extracts. For the reference data, the sample mass and concentration is entered and EPRsimulator then generates a reference file containing knowledge of $[N_S^0]_r$, I_r, and c_r. The sample data is then loaded, and again fitted with a

simulation of N_S^0. The sample mass is then inputted to the *quantify* section and the reference data also loaded. The *Calculate* button then solves equations (4-1) and (4-2) to return $[N_S^0]_s$.

4.1.2 Optical imaging

4.1.2.1 UV excitation imaging

Imaging with UV excitation allows one to gain an insight as to the growth morphology of the diamond, as both fluorescence and phosphorescence emission is generated. De Beers Technology Center (now De Beers Technologies UK) first introduced their product DiamondView™ in the late 1990s [6]. This instrument contains a UV source where the excitation wavelength is shorter than 230 nm, in other words very close to the band gap of diamond. By UV excitation of this wavelength, all diamond samples will generate fluorescence at the surface which is then picked up by a CCD camera to give the operator a 2D image.

The sample is loaded into DiamondView™ by the front sample chamber, and is held in place by a vacuum pad. Once loaded the sample is manipulated into the focus of the camera and orientated by rotating the external dials until the sample is flat relative to the camera. A fluorescence image can be taken by short UV exposure and simultaneously recording the image on the CCD, or phosphorescence can be taken by first exposing the sample to UV and then triggering the camera once the exposure has finished. For phosphorescence imaging, the UV exposure time and triggering delay time can be controlled.

4.1.2.2 Birefringence microscopy

Owing to extended defects in the material, the refractive index of diamond changes very slightly throughout the lattice. For a perfect, strain free diamond lattice, the transmission of light through the material will be unaffected, such that illuminating with one polarisation of light and placing an orthogonal polariser in front of the detector will yield a black image as the two polarisations cancel. However, if strain

is present the refractive index varies and produces birefringence. Consequently, the polarisation of light is changed slightly as it passes through and is not cancelled out by the orthogonal polariser. This process of imaging is known as cross-polarisation imaging, or birefringence microscopy.

Birefringence microscopy was facilitated by a Leica DMI4000B optical microscope, equipped with several air objectives and orthogonal polarisers. Typically, a low magnification 10x objective (NA = 0.25), is used and the birefringence image is recorded on a Leica DFC310FX CCD camera, controlled by Leica Application Suite X (LAS X). On capture, the white balance is auto-adjusted in LAS X to ensure optimal contrast is displayed. For samples larger than the field of view of the objective, the sample is manually translated, and a series of images are recorded, ensuring some overlap between regions. These images are then post-processed in Adobe Photoshop using the *Photomerge* automation wizard. In cases where the automation fails, images are manually stitched together to ensure no loss of information is encountered.

4.1.2.3 Synchrotron XRT

To reveal further information about extended defects in the diamond samples investigated, X-ray topography (XRT) images were obtained at the European Synchrotron Radiation Facility (ESRF) in Grenoble, on bending magnet beamline BM05.

The X-ray beam itself is approximately 'white' with a continuum of energy between 10 - 120 keV, which is collimated to 5 × 6 mm. XRT images were recorded in transmission mode (figure 4-2) using X-ray films (Agfa Structurix D3-SC, 130 mm × 180 mm) with an average sample-to-film distance of 300 mm. Following exposure, the X-ray films are then exposed in a dark room and digitised by a low magnification optical microscope. For a $\{0\,0\,1\}$ surface orientated diamond sample, typical strong XRT have diffraction vectors pointing along $\langle 2\,2\,0\rangle$ and $\langle 4\,0\,0\rangle$ directions.

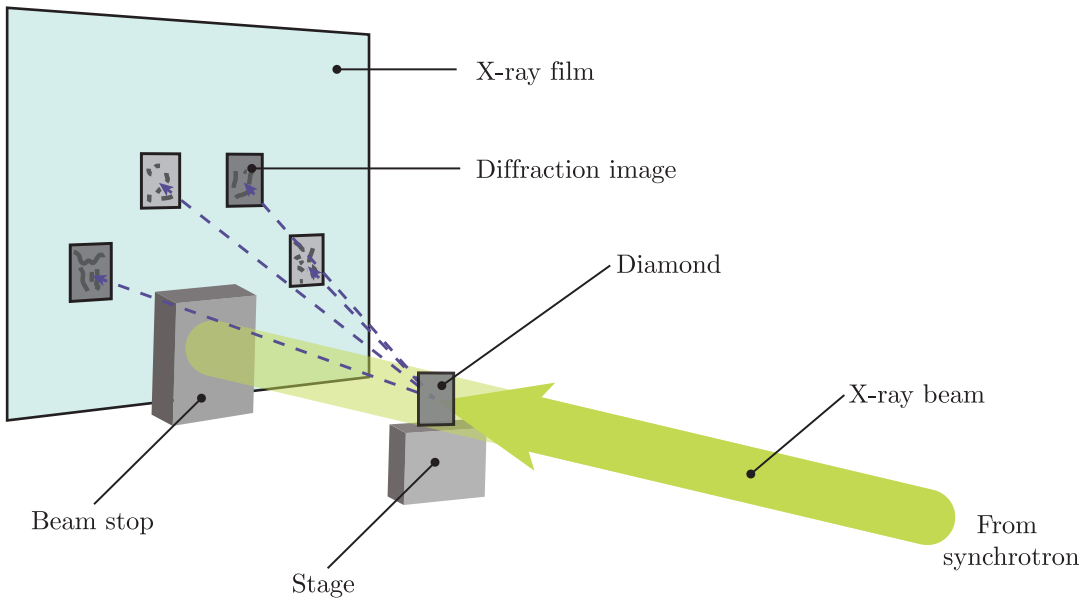

Figure 4-2 Setup of transmission XRT at ESRF.

4.1.3 Optical absorption spectroscopy

4.1.3.1 FTIR

Fourier transform infrared (FTIR) spectroscopy is the method of creating an interferogram of a broadband source and recording the absorption due to material in front of the detector. Typically the interferogram is generated by a Michelson interferometer, as shown in figure 4-3a, where a light source is split in two by a beamsplitter: one half of the beam then reflects from a stationary mirror whilst the other half reflects from a moving mirror. In doing so, the two beams combine on the detection pathway and are subject to constructive and destructive interference, producing an interferogram. By placing a material, here diamond, in the detection pathway the interferogram is modified by the absorption through the sample. The recorded signal is then Fourier transformed, and then background subtracted, to give an absorption spectrum in the frequency domain (figure 4-3b).

Coupled with a broadband excitation source, a FTIR spectrometer offers three key advantages over a dispersive spectrometer

- Multiplex/Fellget advantage: Rapid collection of a complete spectrum as all source wavelengths are simultaneously measured.

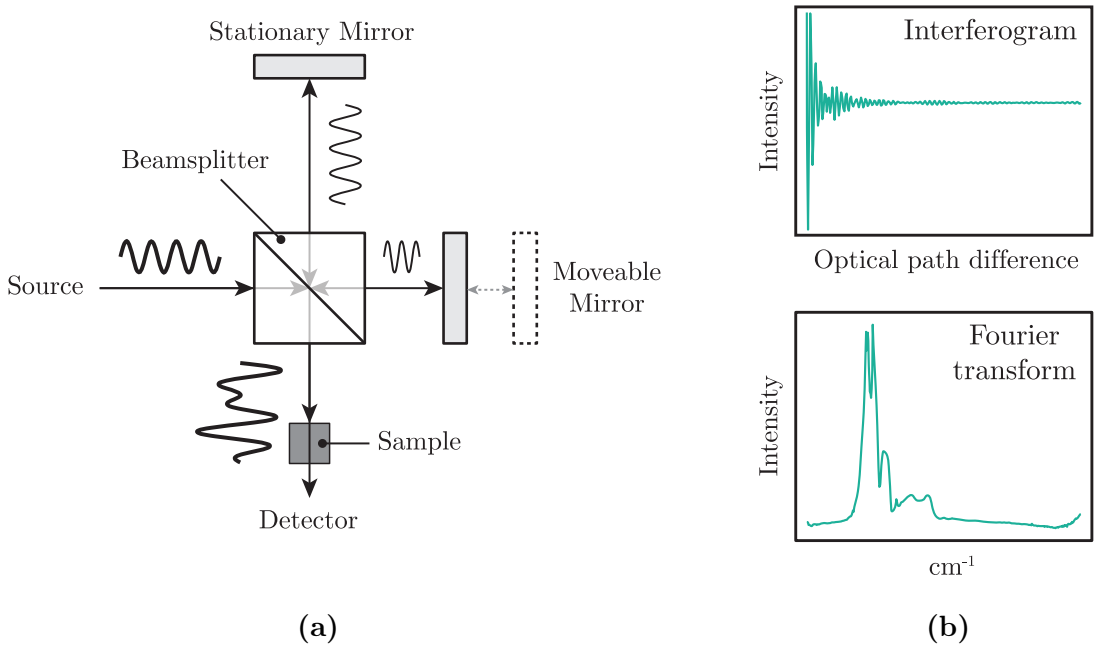

Figure 4-3 (a) The Michelson interferometer setup. (b) an example background corrected interferogram (top) which reveals the absorption in wavenumbers upon taking the Fourier transform (bottom).

- Throughput/Jacquinot advantage: The ability to achieve the same signal-to-noise ratio as a dispersive spectrometer in a much shorter time frame as the energy throughput is higher.
- Connes advantage: Accurate internal calibration of the wavenumber scale which is derived from a HeNe laser for each scan.

Unless otherwise stated, all FTIR measurements within this thesis were obtained with a PerkinElmer Spectrum GX FTIR spectrometer at room temperature. Mid-IR (MIR) measurements were made between the range 370 - 7800 cm^{-1} at a resolution of 1 cm^{-1}. Within the sample chamber, the excitation source is subject to a 5× beam condenser generating a spot size approximately 1 mm in diameter, and simultaneously provided a vertical translation of the beam which enabled samples to be mounted horizontally on top of a brass aperture. The sample chamber itself was maintained with a flow of dry N_2 gas to reduce absorption from CO_2 and atmospheric particulates. Absorption from the diamond was then recorded by the transmitted light on to the TGS detector.

Once data had been recorded, the spectra are post-processed by SpectrumManipu-

lator [5]. From this, the absorption data is normalised to that of a standard (defect free) type IIa diamond absorption where the absorption coefficient is 12.3 cm^{-1} at 2000 cm^{-1}, and in doing so enabled in-house defect references to be fitted for a quantitative analysis of defect concentration.

4.1.3.2 UV-vis absorption

Unlike FTIR, the ultraviolet-visible (UV-vis) absorption measurement is undertaken in a dispersive spectrometer. As a result, the spectrum is built by incrementally rotating a grating such that the point detector records an intensity as a function of wavelength. Whilst this achieves high resolution and sensitivity, the measurement itself can be time-consuming.

Here UV-vis measurements were facilitated by a PerkinElmer Lambda 1050 spectrometer. The excitation range is broad and covered by two lamps, a deuterium lamp for the UV range and a tungsten filament halogen lamp for the NIR-visible range. The excitation source is monochromated and depolarised where the light is directed into two pathways by a rotating mirror. The sample chamber therefore has two light pathways, one used for the sample to be measured and the second as the reference arm. Finally light from both the reference and sample arm are focused onto the detectors, where a photomultiplier tube (PMT) records the UV-vis range and a Peltier cooled InGaAs detector records NIR wavelengths. Prior to any absorption measurement, the spectrometer was calibrated for the background over the measurement range and then subtracted from the absorption data when the samples are measured.

Quantitative UV-vis absorption spectra were collected at liquid nitrogen temperature (77 K) in order to increase the emission into the ZPL. The sample was mounted in an indium aperture held at the end of a cold finger, which was then placed inside an exchange gas Oxford Instruments continuous flow cryostat. The temperature throughout the measurement was maintained by an Oxford Instruments intelligent temperature controller (ITC).

After the measurement completed, the background and absorption measurements

were exported to an ASCII file format and imported into MATLAB for numerical analysis. For the work in this thesis it has been necessary to determine the concentration of the neutral vacancy ($[V^0]$) only by UV-vis absorption. Once the data is converted to absorption coefficient, $[V^0]$ (cm^{-3}) is determined by [7]

$$[V^0] = \frac{A_{V^0}}{1.2 \times 10^{-16}} \tag{4-3}$$

where A_{V^0} is the area under the ZPL for V^0 in meV cm^{-1}.

4.1.4 Cathodoluminescence imaging and spectroscopy

As described in section 3.1.2.4, cathodoluminescence (CL) imaging and spectroscopy is the study of light which has been generated by an incident electron beam. To do this, a scanning electron microscope (SEM) can be retrofitted with a retractable parabolic mirror (schematically shown in figure 4-4) and an additional detection arm. The retractable parabolic mirror contains a central hole to enable the focussed electron beam to pass through. Divergent CL emission from the sample is then collected by the parabolic mirror and collimated towards the detection arm. Typically, the detection comprises of a monochromator and grating to perform spectroscopy where these can also be by-passed to take a panchromatic image on the camera (either CCD or PMT).

For the work of this thesis, CL is facilitated by the use of an SEM (Zeiss EVO 50) where the electron beam is from a lanthanum hexaboride (LaB_6) source. The accelerating voltage of the beam is set to 15 keV with a probe current between 100 and 200 nA. The focussed electron beam spot size is approximately 100 nm. This technique will henceforth be referred to as SEM-CL.

Since diamond is an insulating material, a build up of charge can occur at the surface under a focussed electron beam. Therefore in order to passivate this and observe a CL signal, the diamond surface is sputtered with a thin layer of gold atoms. The diamond was then mounted onto a 5-axis cryogenic cooling stage (Gatan C1002) either by double-sided copper tape or mounted in an indium aperture. Once the SEM chamber is pumped to vacuum, the stage is cooled to 77 K by liquid nitrogen. The SEM-CL system is retrofitted with a Gatan MonoCL3 detection arm where

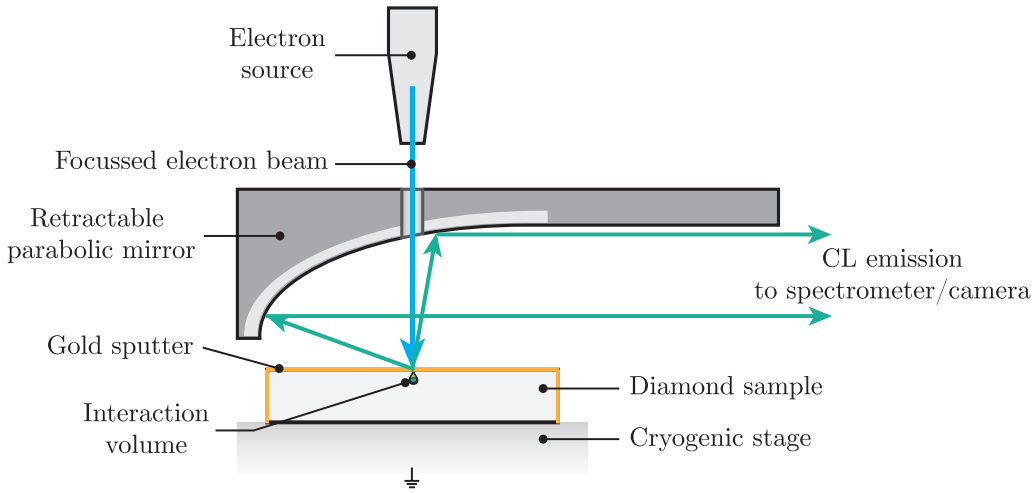

Figure 4-4 Schematic of the SEM-CL configuration where the retractable parabolic mirror has a central hole to allow the focussed electron beam to pass. The CL emission is then collected and collimated towards the detection arm.

the UV spectral data is acquired with a 1800 l/mm grating, blazed at 240 nm, on a Hamamatsu R943 water-cooled PMT detector. For spectroscopy in the visible region, a 1200 l/mm grating blazed at 500 nm is employed.

One draw back to the parabolic mirror is the limited field of view of the sample for imaging. Since the sample needs to be at the focus of the mirror, images tend to suffer from a *hotspot* where the CL intensity is bright. Hence the SEM-CL system is equipped with a bespoke imaging system from Oxford Instruments where CL light is collected from the SEM chamber without the parabolic mirror, and a low magnification image recorded on a Hamamatsu R374 PMT.

The use of CL spectroscopy in the UV region allows for the boron concentration to be determined. Therefore the spectral data is exported to ASCII format and analysed in MATLAB. The ratio of the boron bound exciton peak height (237.8 nm) against free exciton peak height (235.2 nm) is taken, and converted to a boron concentration by equation (3-21b).

4.1.5 Photoluminescence

Since it is possible for defects to emit over a broad range of wavelengths, it is necessary to assay diamond by a wide range of laser excitation wavelengths. Hence,

a suite of *widefield* photoluminescence (PL) measurements were conducted across several different Raman microscopes, able to conduct PL acquisitions, which are summarised in table 4-1.

All microscopes were equipped with a motorised XYZ stage which allows for quick sample positioning and automated mapping. Visible PL measurements taken on the Renishaw systems were obtained with a 50× air objective (NA = 0.75) at room temperature and a 50× long working distance air objective (NA = 0.50) for cryogenic measurements. For excitation with 325 nm, a 15× UV air objective (NA = 0.32) is used. Room temperature PL measurements on the Horiba system were conducted with a 100× air objective (NA = 0.90).

Where cryogenic measurements are necessary, samples were mounted in a Linkham TMS600 stage. To maintain thermal contact, samples were adhered to the stage with silver thermal paste. The stage is first heated to 110 °C for 5 minutes in order to bake out any residual water, and then cooled to 77 K by liquid nitrogen.

Raman Microscope	Available Laser Excitations (nm))
Horiba LabRam HR Evolution	488$^{\diamond}$, 660*
Renishaw inVia Raman Microscope	514*, 785*
Renishaw inVia Reflex Raman Microscope	325†, 442†, 633‡
Renishaw inVia Reflex Raman Microscope	532*

Table 4-1 The suite of microscopes used for *widefield* PL measurements and their excitation wavelengths, all of which are continuous wave. $\diamond$ = optically pumped semiconductor laser (OPSL) $\star$ = diode pumped solid state (DPSS), † = helium-cadmium (HeCd) laser, ‡ = helium-neon (HeNe) laser.

4.1.6 Defect generation

It is possible to introduce point defects into diamond by several different methods, where two of the more common approaches are electron irradiation to generate vacancies, and ion implantation for specific point defect creation. The final step to defect creation from either method, is then a subsequent annealing process.

4.1.6.1 Electron irradiation

The irradiation with high energy electrons to the diamond lattice follows conventional momentum transfer principles and as such tend to be modelled by the classic colliding billiard balls ideology. By considering the relativistic effects of electron motion, for an electron of mass m_e accelerated to energy E, the maximum recoil energy of a particle with mass M is given by

$$T_{\max} = \frac{2m_e E}{M}\left(\frac{E}{m_e c^2} + 2\right) \tag{4-4}$$

For a 4.5 MeV electron incident upon a stationary carbon atom, it can be calculated that the maximum recoil energy of carbon will be 4.4 keV. Since the displacement threshold energy T_d for diamond is quoted as 38 eV in the [0 0 1] direction [8], providing the incident particle has sufficient energy, the carbon atom will be ejected from the lattice site with a kinetic energy equal to $T - T_d$. By modelling the interaction of electrons in diamond, Campbell and Mainwood have given the maximum penetration depth of electrons in diamond as a function of accelerating energy, where it can be approximated that the penetration depth is 1.5 mm MeV^{-1} and roughly corresponds to 2 vacancies per electron at 4.5 MeV irradiation [9].

Electron irradiation in this study (Chapter 7) was conducted by a sterilisation company in England, UK, where the linear accelerator provides a 4.5 MeV electron beam with a 20 mA current. To avoid significant heating during irradiation, samples are placed in direct contact with a water-cooled stainless steel table with the sample placed centrally for the electron beam to raster over.

4.1.6.2 Ion implantation

Ion implantation is often employed for deterministic creation of single centres, and typically with high purity diamond. Unlike electron irradiation, ion implantation generates an appreciable wake of secondary damage due to the ion mass. Once again this interaction can be modelled, and in considering a molecular dynamics approach, where channelling effects are considered, it is shown that the stopping range of the ion depends both upon the implantation energy and crystallographic direction [10].

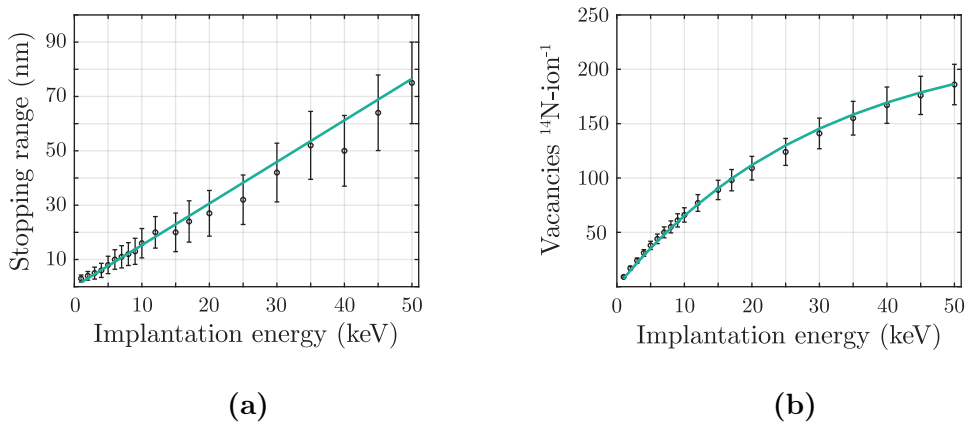

Figure 4-5 (a) The stopping range of the ^{14}N-ion implantation as a function of energy (keV). The line of best fit implies a stopping range of 1.5 nm keV^{-1} (b) The vacancy generation rate per ^{14}N-ion implant.

Ion implantation undertaken in this thesis was conducted at the Ion Beam Centre at the University of Surrey, UK. In the study of implant-generated NV$^-$ centres (chapter 8), nitrogen-14 (^{14}N) was chosen as the implant species with an energy of 20 keV at a nominal dose rate of 1×10^9 cm^{-2}. Figure 4-5a shows the stopping ranges as a function of acceleration energy, as calculated using SRIM[a]. The simulated data shows that the stopping range of ^{14}N is approximately 1.5 nm keV^{-1}. From the simulations, a 20 keV implantation corresponds to a depth of 28 ± 9 nm creating 109 ± 10 vacancies per ^{14}N-ion (figure 4-5b).

4.1.6.3 Annealing

In most defect generation cases, it becomes necessary to subject the diamond lattice to heat in a process known as annealing. At a temperature above 600 °C, vacancies begin to migrate and either recombine with interstitial carbon or become trapped at impurities.

Annealing was performed in-house in an Elite Thermal Systems horizontal tube furnace, where the sample chamber is held just above atmospheric pressure by a continuous purge of nitrogen gas producing a non-oxidising atmosphere. Heat transfer from the heating elements is facilitated by an alumina tube. The diamond is then loaded into this tube by placing it into an alumina boat which is then

[a]Stopping and Range of Ions in Matter: `http://www.srim.org/`

slowly pushed into the middle of the furnace tube. To retain heat in the tube, alumina radiation shields are inserted at either end. In cases where the annealing temperature is above 600 °C, the diamond sample is buried in sacrificial diamond grit to avoid significant etching of the diamond surface. During retrieval of the diamond, the boat is slowly pulled from the centre of the tube to avoid thermal shock, and then acid cleaned to remove any graphitic material (see section 4.2.5).

4.2 Confocal imaging and spectroscopy

Confocal microscopy within this work was conducted on a purpose-built system. The following is a breakdown of the components implemented, achieved resolution, hardware control, and detail on sample preparation.

4.2.1 Optical design

Prior to this project, an iteration of this confocal microscope had been built. However, it was established that the count rate for a single NV^- defect at saturation, with a 1.4 NA oil-immersion objective, was < 40 kcps. This proved to be at least a factor of three lower than that demonstrated by other research groups [11, 12]. Consequently, this led to the rebuild of the microscope during this project, with the purchase of newer optics and higher sensitivity detectors.

The optical architecture of the *confocal* microscope can be found in figure 4-6, where two primary continuous wave (CW) excitation wavelengths are implemented:

- λ_{exc} = 488 nm. Argon ion (Ar^+) laser line from Modu-Laser Stellar Pro Select 150 (40 mW maximum output)
- λ_{exc} = 532 nm. LaserQuantum gem532 (100 mW maximum output, DPSS)

In order to enable optically detected magnetic resonance studies (ODMR) with the NV^- centre, the 532 nm laser source was focused first into an acousto-optic modulator (AOM, Isomet 1250C). By setting up an acoustic wave inside a quartz crystal, the light was diffracted, with the highest power in the first order of

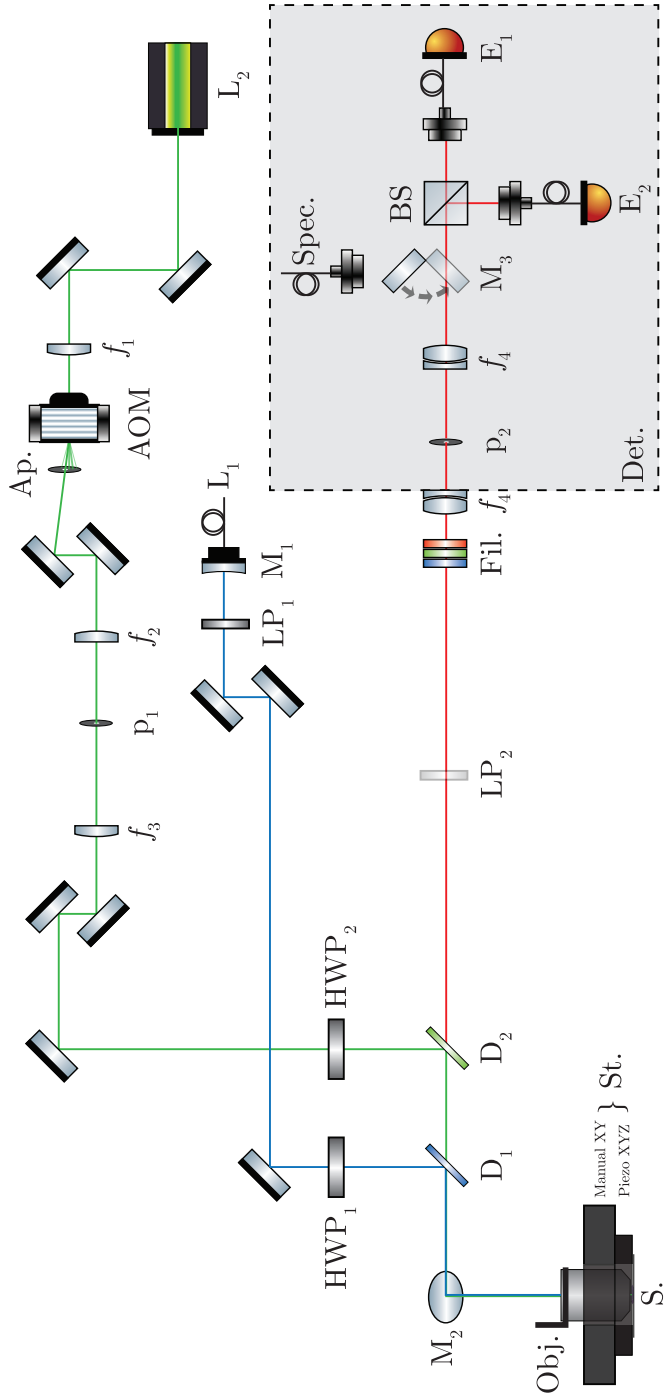

Figure 4-6 Illustration of the optical design for the purpose-built *confocal* microscope. L_1 = 488 nm laser source, L_2 = 532 nm laser source, f_1 = 40 mm, f_2 = 75 mm, f_3 = 150 mm, f_4 = 100 mm vis-NIR coated achromatic, M_1 = parabolic collimator, M_2 = periscope mirror, M_3 = flip mirror, p_1 = 30 µm pinhole, p_2 = 25 µm pinhole, AOM = acousto-optic modulator, Ap. = iris to select first diffraction order, HWP_1 = 488 nm half waveplate, HWP_2 = 532 nm half waveplate, D_1 = Semrock 488 nm longpass dichroic, D_2 = Semrock 532 nm longpass dichroic, LP_1 = linear polariser, LP_2 = optional linear polariser Obj. = Microscope objective (air or oil) mounted on manual Z translation stage, St. = Manual translation stage and PI P-562 300 µm piezoelectric stage, S. = Diamond sample mounting, Fil. = Various Semrock filters, BS = 50:50 beamsplitter, E_1 = Excelitas single photon counting module 1, E_2 = Excelitas single photon counting module 2, Spec. = Fibre coupling port for Andor spectrometer, Det. = black out box for detection optics.

diffraction. Consequently, an iris was placed after the AOM so that this first order diffraction was selected. When the acoustic wave is removed, no laser power is sent through the system, a requirement to run pulsed measurements. The characteristic rise time of the AOM was measured to be 30 ns.

Once the first order diffraction was selected, the light is directed by two steering mirrors into a 2× magnification telescope arrangement. Unfortunately, as the AOM introduces unwanted distortion, the Gaussian profile of the TEM_{00} laser beam is removed. Hence a 30 µm pinhole was placed at the focal point of the first telescope lens. This generates a typical Gaussian beam profile in the middle of an Airy disc. The divergent light is then collimated by the second lens in the telescope to produce a beam diameter of approximately 6 mm; sufficient to fill the back aperture of a microscope objective. Further steering mirrors then direct the green excitation towards the microscope objective.

Since the Ar^+ laser requires significant air-cooling to produce stable wavelengths, the laser body and external fan source were mounted on an isolated frame underneath the optical bench. By doing so, mechanical vibrations were not introduced to the optical bench. In order to bring the excitation wavelength on to the optical bench, it was necessary to couple the light into a single mode fibre by two alignment mirrors, which was achieved with 50% efficiency. The collimation of the 488 nm laser source on the optical bench was facilitated by a fibre coupled parabolic mirror. This produced a collimated beam diameter of 8.5 mm, and was not subjected to an AOM. Due to the fibre coupling into a single mode fibre, the original linear polarisation was lost and the output depolarised. This was subsequently corrected by the addition of a linear polariser.

Thus, as both laser sources are linearly polarised towards the microscope objective, the orientation of polarisation can be rotated by an appropriate polymer zero-order half waveplate to enable optical polarisation measurements. Two long pass dichroic mirrors were used for the corresponding laser wavelength (488 nm: Semrock 488 nm RazorEdge, 532 nm: Semrock 552 nm edge LaserMUX) to reflect the laser light towards the microscope objective, but allow longer wavelengths of photoluminescence to pass through towards the detectors. Both dichroics were

mounted on to high repeatability magnetic kinematic bases (Thorlabs SB1/M), such that either one could be removed when not in use to avoid any interference. Indeed it was found that the removal and replacement of each dichroic did not introduce any significant misalignment to either the excitation or detection pathways, confirming a high degree of repeatability.

The arrangement of the confocal microscope is such that a periscope mirror provided a vertical translation of the excitation source, which enabled the study sample to be mounted horizontally and flat. The sample is typically mounted on to a glass slide, which in turn is housed on to a Physik Instrumente (PI) P-562 piezoelectric XYZ stage, capable of 300 µm travel in XYZ with 0.4 nm precision. This stage itself was mounted on a manual XY linear stage (Newport M-406) for the rough positioning of the sample over the microscope objective. Here, a choice of either air (Olympus MPLAPON 100× NA = 0.95) or oil-immersion (Zeiss Plan Apochromat 100× NA = 1.40) microscope objective could be installed. A manual Z stage was used to introduce the chosen microscope objective towards the sample until the laser is focussed at the surface. To ensure the sample was at the focus of the microscope objective, a piece of white paper was used to inspect the back reflection of excitation light from the sample, and once this appeared collimated over ~ 30 cm the objective was left in position.

As the imaging system does not depend upon the spectral dispersion of light, it was necessary to intervene with fluorescence filters. The spectral transmission properties of the filters used in this work are found in figure 4-7a, and since these filters are targeted for specific defects in diamond, table 4-2 assigns a filter to a defect. Since the diamond Raman line appears at 521.9 nm under 488 nm excitation, it was not possible to purchase a very narrow notch filter at this wavelength. Therefore in rotating a 532 nm laser notch filter by 15° the notch is effectively blueshifted to cover the Raman emission (figure 4-7b). This rotation was particularly useful for imaging the photoluminescence of N_2V^0 (H3) defects.

Confocal sectioning is facilitated by a 25 µm pinhole within the light tight detection box, placed at the focal point of a $f = 100$ mm achromatic doublet lens. By placing a second $f = 100$ mm achromatic doublet lens at a distance of $2f$ from the

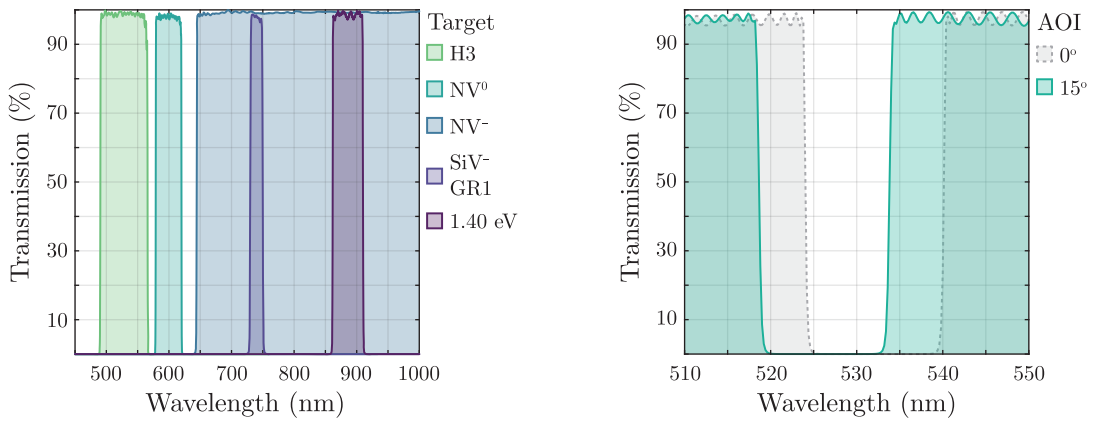

Figure 4-7 (a) The transmission windows of filters employed in *confocal* microscopy imaging where each is targeted for a specific emission window of a defect in diamond. (b) The theoretical notch rejection of a Semrock 532 nm StopLine® filter both for a 0° angle of incidence (AOI) and 15°.

Target defect	Filter type
N_2V^0 (H3)	Semrock BrightLine® 527/70 nm bandpass (FF01-527/70-25)
NV^0	Semrock BrightLine® 600/52 nm bandpass (FF01-600/52-25)
NV^-	Semrock EdgeBasic® 633 nm longpass (BLP01-633R-25)
SiV^- or V^0 (GR1)	Semrock BrightLine® 740/13 nm bandpass (FF01-740/13-25)
1.40 eV	Semrock BrightLine® 889/42 nm bandpass (FF01-889/42-25)

Table 4-2 List of fluorescence filters used in this study.

pinhole, the divergent light was brought back to a focus. In this focussing path, a 50:50 beamsplitter was installed for the Hanbury Brown Twiss arrangement, thus creating two foci. At each foci, a 3-axis flexure stage was placed with a 105 µm core multimode fibre, each connected to a single photon counting module (SPCM, Excelitas SPCM-AQRH-14-FC). On initial installation, the position of each fibre was optimised by monitoring the photon count rate due to the surface reflection of a glass slide, where the reflected power was very low (< 10 µW), until the count rate was maximal. For spectroscopy, the filters are removed from the detection box and a mirror is flipped into the pathway, after the final lens and before the

beamsplitter, such that the light is then focussed onto another 105 µm multimode fibre connected to a spectrometer (Andor SR-303i-B).

4.2.2 Achieved resolution and count rate

To assess the optical resolution of the microscope, a diamond containing a low density of shallow NV^- centres (< 100 nm) as created by ion implantation and annealing was imaged without, and with, the 25 µm pinhole in the detection pathway. This can be seen in figure 4-8, where it is shown that the system agrees with the theory for a $\sqrt{2}$ improvement on the lateral and axial resolution when confocality is achieved. Therefore, this resolution achievement implies a detection limit of one single point defect in a volume of 341,120 carbon atoms.

By taking the background-subtracted average of the photon count rate detected from the NV^- centres in both *widefield* and *confocal* images, the pinhole accounts for a ~39% reduction in detected fluorescence intensity. From the energy distribution plot in figure 3-8, this equates the 25 µm pinhole to 1.9 normalised lateral coordinates and therefore satisfies the condition in equation (3-35).

Finally, the achieved saturation count rate for a single NV^- centre, with the oil-immersion objective, was typically ~ 110 kcps and comparable to other research groups [11, 12]. The power required to reach saturation was measured as ~ 0.2 mW at the back aperture of the microscope objective.

4.2.3 Microwave delivery and magnetic field alignment

For the experiments in which ODMR is conducted, the sample mounting is altered. Instead, the diamond is glued to a small piece of glass coverslip, which itself is then glued on to a co-planar waveguide. The co-planar waveguide is manufactured from FR-4 grade printed circuit board (PCB), where the ground strips are designed to match the impedance at approximately 50 Ω. To direct the microwaves across the surface of the sample, the centre line is broken by a central aperture and a 20 µm wire is then stretched over the top of the diamond and soldered to the PCB (figure 4-9).

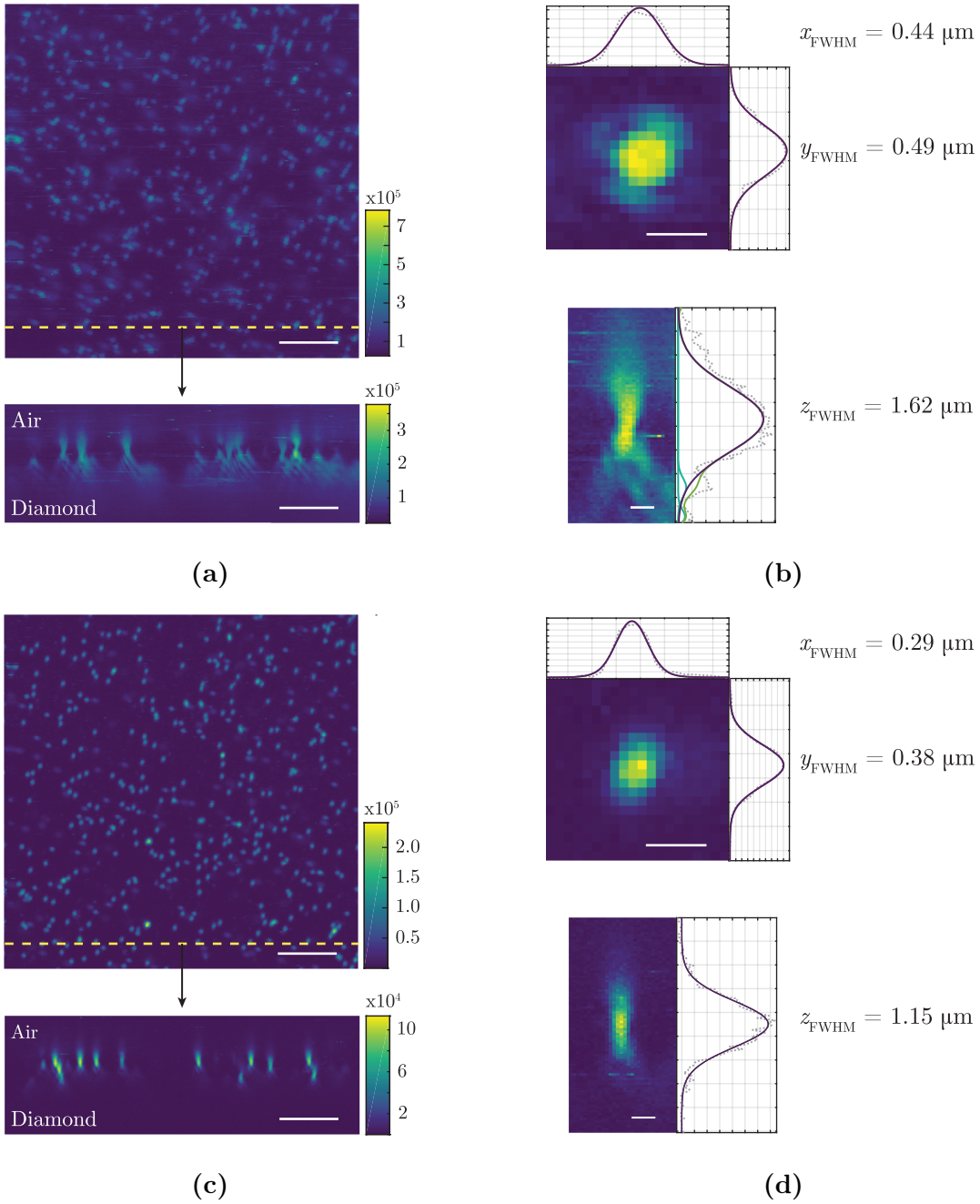

Figure 4-8 Measured point spread functions of implanted NV^- centres in diamond. (a) reveals the 30×30 µm XY and 30×10 µm XZ scan without a pinhole on the detection side and slight spherical aberration from refractive index mismatch. (b) shows that whilst a single NV^- centre can be imaged due to the low density of defects, the optical resolution is not diffraction limited. (c) Same region of interest as (a) but with a 25 µm pinhole in the detection arm, where (d) shows a diffraction limited system by the $\sqrt{2}$ lateral and axial improvement. Scale bars (a) and (c) = 5 µm, (b) and (d) = 0.5 µm. Photoluminescence intensity scale bar represents the photon count rate per second (cps).

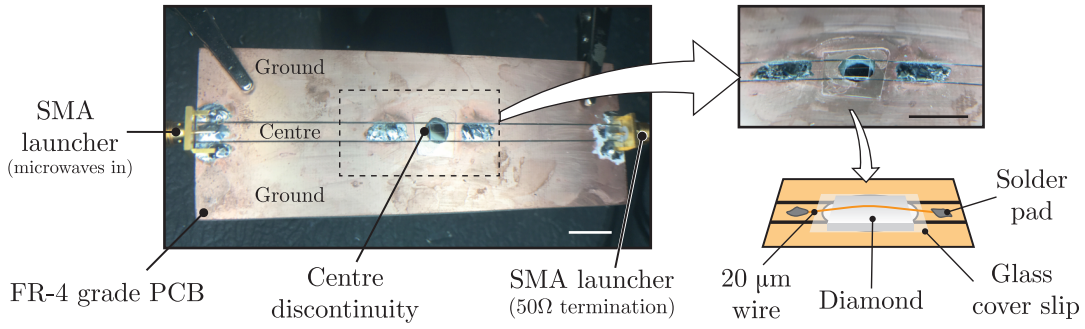

Figure 4-9 The co-planar waveguide mounting of a diamond. The waveguide consists of FR-4 grade PCB with SMA launchers soldered at either end. The centre line contains a discontinuity which is bridged by soldering a 20 µm thick wire over the diamond sample. Scale bar = 10 mm.

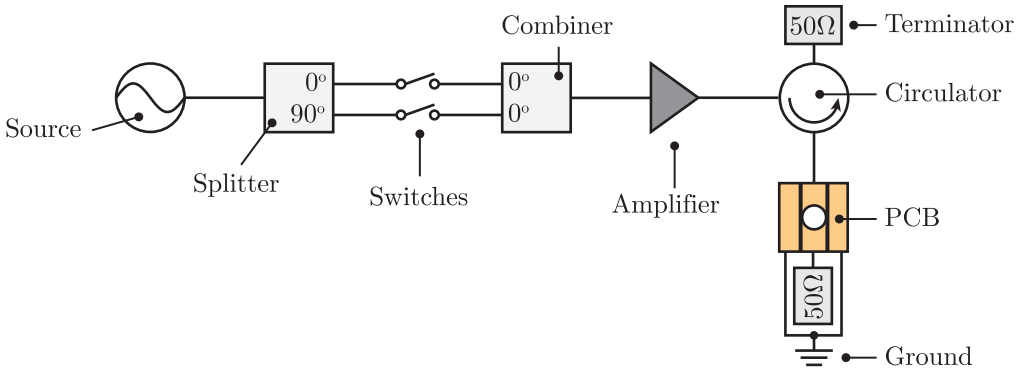

Figure 4-10 Schematic of the microwave generation and delivery pathway to enable ODMR measurements.

A schematic for the microwave generation and delivery is given in figure 4-10. Microwaves are generated by a radio frequency (RF) vector signal generator (Keysight N5172B) and directed to a 90° splitter (MiniCircuits ZAPDQ-4-S) to create two arms with a relative phase difference of 90°. Both paths are then separately switched (2× MiniCircuits ZASW-2-50-DR+) and triggered by an arbitrary waveform generator (Swabian Instruments Pulse Streamer 8/2). A 0° combiner (MiniCircuits ZN2PD2-50-S+) joins both pathways and is amplified by a 45 dB gain amplifier (MiniCircuits ZHL-16W-43+). Before delivering the microwaves to the co-planar waveguide, the microwaves finally pass through a circulator (AT11B-E212-AF) to eliminate reflections back through the system. The output of the circulator is connected by coaxial cable to the co-planar waveguide by an SMA connection. The other side of the co-planar waveguide is terminated with a 50 Ω terminator to absorb the microwaves and minimise reflections.

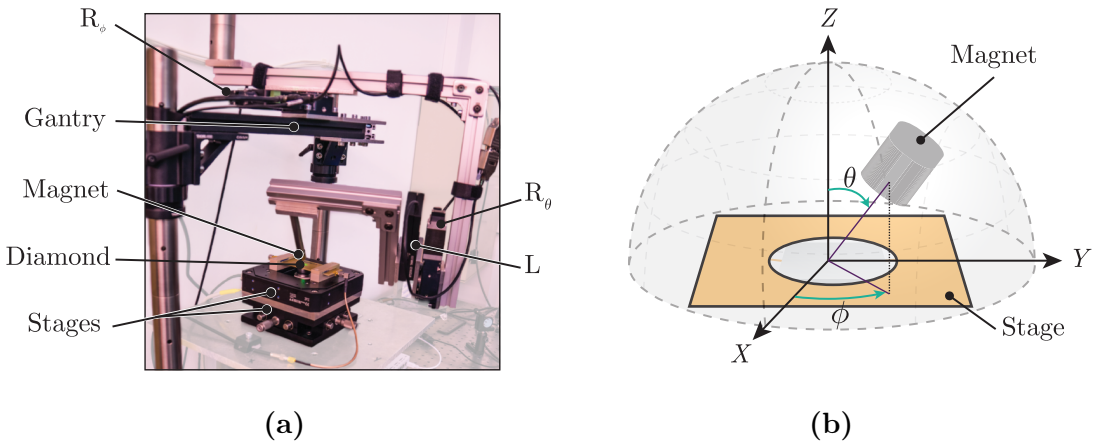

(a) **(b)**

Figure 4-11 (a) Photograph of installed magnetic field alignment setup where R_θ and R_ϕ denote the rotation stages and L denotes the linear translation stage. The magnetic field is provided by a permanent magnet. (b) Illustration of the hemisphere over the diamond where θ and ϕ correspond to the motion of the rotation stages.

For the magnetic field alignment, a permanent magnet (NdFeB) is manipulated about a hemispherical space above the sample (figure 4-11). This is facilitated by two piezoelectric rotation stages (Zaber X-RSW60C) and a piezoelectric linear translation stage (Thorlabs MTS25). The two rotation stages provide full θ and ϕ control whilst the linear stage provides a means to increase/decrease the field strength at the sample.

4.2.4 Hardware control

All of the hardware control for the mechanical components on the confocal microscope were controlled via the open source software *Qudi*, developed by the University of Ulm using the Python language platform [13]. This provides an intuitive graphical user interface (GUI) to allow experiments to be conducted. Qudi also enables the user to utilise the interactive Python (iPython) environment to make live modifications to the experiment, or *Jupyter* notebooks to perform custom experiments. Some additional modifications were made to enable control of different hardware, as well as the provision of new logic for experimental methods[b].

[b] A working copy of Qudi, as modified at The University of Warwick, can be found on the WarwickEPR github account: `https://github.com/WarwickEPR/qudi`

Aside from providing the mapping capabilities, one key feature of Qudi employed here is the use of autofocus, and the point of interest (POI) manager. To conduct an experiment (i.e. ODMR or pulsed measurements as described in chapter 3) on a single centre, a POI is set to the defect of interest containing the current *xyz* coordinates. Then, at periodic intervals, Qudi interrupts the experiment to optimise the count rate of the defect by performing the autofocus routine and updates the POI coordinates. This ensures any thermal drift of the piezoelectric stage is negated, such that optimal defect fluorescence is always detected.

4.2.5 Sample preparation

Owing to the nature of achievable optical resolution, the surface of the sample needs to be prepared in order to reduce the background from fluorescence of biological matter. In holding the sample in such a way that a surface reflection of ambient lighting can be seen across the sample, a dirty surface usually shows streaks or small opaque spots.

The surface is very carefully cleaned by rubbing a lens tissue saturated with a solvent, such as acetone ($(CH_3)_2CO$), across the surface. This is repeated several times, until the surface reflection becomes free of streaks or spots. Before mounting, the surface is wiped with a fresh piece of lens tissue, wetted with one drop of deionised water, to remove any final residue from the acetone wash.

On occasions where samples did not become clean by this process, acid cleaning is employed. The diamond sample is placed in supersaturation of potassium nitrate in sulphuric acid, then heated to 250 °C for 60 minutes. After this, the sample is rinsed with deionised water, and then placed back into a beaker of sulphuric acid and heated for 60 minutes to remove any further potassium nitrate. A final wash with deionised water afterwards yields a diamond with a pristine surface.

References

1. B. G. Breeze, PhD thesis, University of Warwick, 2016.
2. G. R. Eaton et al., *Quantitative EPR* (SpringerWienNewYork, New York, NY, 2010).
3. B. L. Cann, PhD thesis, University of Warwick, 2009.
4. W. V. Smith et al., *Physical Review* **115**, 1546–1552 (1959).
5. M. W. Dale, PhD thesis, University of Warwick, 2015.
6. C. M. Welbourn, M. Cooper, P. M. Spear, *Gems & Gemology* **32**, 156–169 (1996).
7. D. Twitchen et al., *Diamond and Related Materials* **8**, 1572–1575 (1999).
8. J. Koike, D. M. Parkin, T. E. Mitchell, *Applied Physics Letters* **60**, 1450–1452 (1992).
9. B. Campbell, A. Mainwood, *physica status solidi (a)* **181**, 99–107 (2000).
10. O. Lehtinen et al., *Physical Review B - Condensed Matter and Materials Physics* **93**, 1–7 (2016).
11. G. Balasubramanian et al., *Nature materials* **8**, 383–7 (2009).
12. C. Schreyvogel et al., *Scientific Reports* **5**, 12160 (2015).
13. J. M. Binder et al., *SoftwareX* **6**, 85–90 (2017).

5

Multilayered B/N doped CVD Diamond

Boron is carbon's neighbour on the periodic table, which means it can do a passable carbon impression and wriggle its way into the matrix of a diamond.

- Sam Kean

5.1 Background

Diamond containing detectable boron is classified as type IIb diamond according to the presence of absorption features at 2802 cm^{-1}, 2457 cm^{-1} and 1290 cm^{-1} in IR spectroscopy [1]. However there is very little known about point defects which exhibit photoluminescence (PL) within boron doped diamond.

Since the neutral substitutional boron (B_S^0) acts as an electron acceptor in the diamond matrix, it is typically included during growth (also known as doping) in low concentrations as a way to produce other point defects in either the neutral or positive charge state. For example, recently there has been a push to investigate the neutral silicon vacancy defect for its potential role in the quantum processing arena as it is a NIR single photon source, where stable emission of this defect is observed due to the boron environment and significant silicon incorporation [2, 3].

Green demonstrated that irradiation damage in type IIb diamond produces a defect centre at 648.2 nm (1.913 eV) which was thought to be related to boron interstitials [4]. A thorough characterisation process resulted in showing the defect

to be of $\mathscr{C}_{1h}$ symmetry with absorption and emission dipoles orientated along $\langle 1\,1\,1 \rangle$ and $\langle 5\,5\,3 \rangle$ respectively, and has a LVM at 178.2 meV.

Steeds and Kohn also noticed that in electron irradiated diamond, containing NV centres and boron, a new centre was produced with a ZPL at 517.6 nm (2.395 eV) [5]. From this, it was tentatively ascribed to the positive charge state of NV (NV^+). On the other hand, it is not clear if this is the case since electrically biasing NV^0 centres into a 'dark' state and back would imply the conversion to NV^+, however in doing so there is no detectable PL. Despite this, NV^+ appears useful as a route to extending the lifetime of a quantum memory [6].

Several efforts have also been published on the theoretical study of boron related point defects. Goss *et al* investigated various configurations of boron complexes through density functional theory (DFT) and in particular boron-vacancy complexes, with and without hydrogen [7]. Here it was found that there would be no stable configuration with hydrogen, where the defects were passive (from hydrogen tunnelling), possessed deep energy levels, or were thermally unstable. Conversely, the negative boron vacancy defect (BV^-) could show similarities to NV^- [7]. In a later study, Goss and Briddon concluded that the neutral charge state (BV^0) should be optically active with transitions around 2 eV (619.9 nm) [8]. Kunisaki *et al*, in agreement with Goss, suggests that BV^- should be a stable defect with $\mathscr{C}_{3v}$ symmetry, and may show potential as a sensing defect due to the triplet ground and excited state [9].

This chapter focusses on a synthetic diamond grown by CVD, containing very distinct regions of boron doping. The aim therefore is to understand point defect incorporation, which may provide some insight into boron-doped CVD growth.

5.2 Material characterisation

5.2.1 The synthetic diamond

The research sample of interest for this chapter was grown by Element Six Ltd (E6), via the MPCVD technique, where homoepitaxial growth occurred on top of

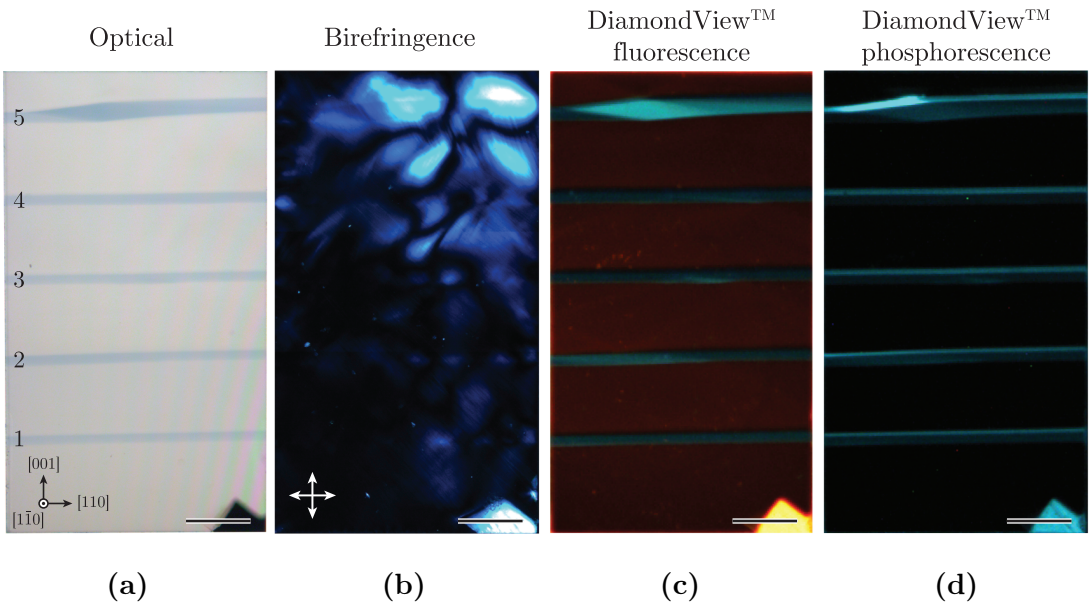

Figure 5-1 (a) Optical, (b) birefringence (with the orientation of cross polarisation marked), (c) DiamondView™ fluorescence and, (d) DiamondView™ , with 0.1 s delay, phosphorescence imaging of the study sample grown by MPCVD. The numbering of the boron layers in (a) dictates the growth direction along (0 0 1). Scale bar = 0.5 mm.

a {0 0 1} orientated HPHT diamond substrate. Growth was reported to be in line with the E6 standard optical grade recipe, where at specific intervals, the nitrogen in the gas phase was replaced with a boron dopant [10]. This sample was supplied as a 0.5 mm thick plate, where the main two parallel faces were polished to a {0 1 1} plane. Finally, the sample was laser sawn in-house to provide two pieces, A and B, where the former has the type Ib growth substrate removed as required for EPR measurements.

Shown in figure 5-1a, is the optical image of piece A showing the repeating layers of boron doping as blue lines, where the growth direction is from the bottom of the figure to the top. The layers between the boron doped regions are optically transparent. It can be inferred from the optical imaging that the boron regions are contained to distinct 60 ± 10 µm layers throughout, whilst the transparent regions between are 540 ± 20 µm.

Birefringence imaging (figure 5-1b) shows some strain around the interface regions of the boron layers. Towards the top of the sample (at boron layer 5) the amount of birefringence is significant and may indicate that the growth of the crystal was

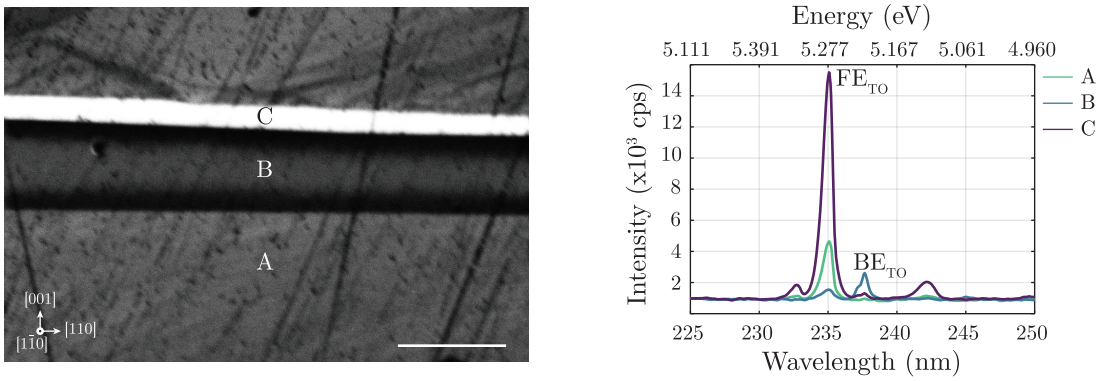

(a) **(b)**

Figure 5-2 (a) Free exciton image taken with an accelerating voltage of 15 keV across boron region 2 at 77 K. The dark diagonal lines are indicative of clatter tracks caused by polishing. (b) representative spectra taken at the marked locations where the free exciton (FE_{TO}) and boron bound exciton (BE_{TO}) peaks are indicated. Scale bar = 100 µm.

not as well controlled. This is further evidenced by the changing thickness of boron layer 5.

DiamondView^{TM} of this sample revealed three repeated layers throughout the growth (figure 5-1c and 5-1d). One repeated region very clearly coincides with the length scale of the optically transparent regions and contains orange fluorescence characteristic of $NV^{0/-}$ emission. A second repeated region coincides with the length scale of the boron doped growth. However a third repeated region is not readily recognisable in the optical or birefringence image, but exhibits no fluorescence whilst displaying long lasting phosphorescence.

Upon free exciton imaging by the SEM-CL system (figure 5-2), this third region contains free exciton emission which is higher than that of both the boron doped and optically transparent regions. From this, it can be concluded that this third region is free of significant quantities of either dopant and is assigned to be *high purity* diamond. Therefore, the layers will now be denoted as either being nitrogen-containing, boron-containing or high purity.

By stepping out the delay time of capture vs exposure time during DiamondView^{TM} imaging, the phosphorescence decay can be extracted from the pixel intensity for both the boron-containing and high purity regions. The boron-containing region,

although noisy due to the low phosphorescence intensity, can be fitted with a single term exponential where the decay lifetime is 0.11 ± 0.08 s. The high purity region requires a two term exponential fit where the lifetimes are determined as 0.24 ± 0.03 s and 2.30 ± 0.31 s.

5.2.2 Dopant concentrations

5.2.2.1 Nitrogen ($N_S^{0/+}$, $NV:H^-$)

As outlined in chapter 4, the nitrogen concentration is determined by RP-EPR. In order to obtain a value for $[N_S^0]$ for the diamond, RP-EPR was conducted on piece A so that nitrogen from the HPHT substrate did not influence the final value.

The charge state of N_S^0 can be manipulated according to

$$N_S^0 + X^0 \underset{UV}{\overset{Heat}{\rightleftharpoons}} N_S^+ + X^- \tag{5-1}$$

where $[N_S^0]$ is maximised after exposure to a UV source, and X can be any other point defect. Hence, before RP-EPR, the sample was exposed to a UV source within a DiamondView^{TM} for 5 minutes. In this state, the maximum $[N_S^0]$ is determined to be 133 ± 10 ppb.

Following this, the sample was then heated in the dark to 550 °C for 30 minutes. In retrieving the diamond it was placed into an opaque container to stop any further charge transfer due to ambient light, and the RP-EPR conducted again. Here, the $[N_S^0]$ was found to be 13 ± 2 ppb. Furthermore, by a standard CW-EPR experiment, it was possible to observe a signal for the negative nitrogen vacancy decorated with a hydrogen ($NV:H^-$), where $[NV:H^-] = 15 \pm 2$ ppb.

In both charge transfer cases, the positive charge state of substitutional nitrogen (N_S^+), and the neutral nitrogen vacancy decorated with a hydrogen ($NV:H^0$) were below the detection limits of FTIR spectroscopy.

Working with the upper limit on $[N_S^0]$, and assuming the incorporation of nitrogen follows a ratio of $[(N_S^0) + (N_S^+)] : [NV:H^-] : [NV^-] = 300 : 30 : 1$ [11], this would translate to a concentration of NV^- centres at approximately 0.44 ± 0.1 ppb. At this

concentration, in a confocal window of 100 µm^3 there would be close to 7700 NV$^-$ centres. The density of NV can also be inferred by the orange fluorescence seen in DiamondView^{TM} fluorescence imaging (figure 5-1c), hence the nitrogen-containing regions are therefore excluded from single defect studies.

5.2.2.2 Boron

Of interest in this sample is the uptake of boron. It is known that unintentional doping with boron can occur in a CVD reaction chamber, which can be mitigated against by introducing oxygen to the chamber [12–15].

The boron concentration is determined by three methods:

- Secondary ion mass spectrometry (SIMS) where the data was provided by E6. This method shows the total boron content in diamond at the cost of being a destructive technique. Data points were taken every 10 µm.
- CL spectroscopic measurements from an SEM to determine the ratio of BE_{TO}/FE_{TO}. Technique thought to provide total boron concentration in a non-destructive way. Data points were taken every 5 µm with the diamond held at 77 K.
- FTIR measurements on a Bruker Hyperion 2000 FTIR microscope, where the diffraction limit is on the order of 10 µm. Data points were taken every 5 µm with the diamond at room temperature.

For all these techniques, a line scan was taken across boron region 2 as a representative quantification of boron. The results are summarised in figure 5-3 and table 5-1. The data also agrees well with the optical imaging, where the boron region is localised to a region of 66 ± 12 µm. The discrepancy between the FTIR boron concentration compared to SIMS and SEM-CL will be discussed later.

5.2.3 Dislocations

XRT of the study sample was conducted at ESRF (§ 4.1.2.3), where the film micrographs are shown in figure 5-4. Clearly this diamond contains a high density

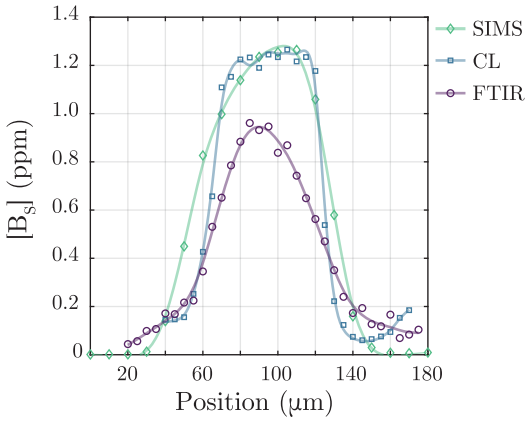

Figure 5-3 The profile of the boron concentration across region 2 for the three characterisation techniques. The spline between points has been added to guide the eye.

Technique	$[B_S]_{max}$ (ppm)	FWHM (µm)
SIMS	1.26	74 ± 10
SEM-CL	1.26	62 ± 5
FTIR	0.96†	61 ± 5

Table 5-1 The maximum substitutional boron concentration ($[B_S]_{max}$) in ppm and the full-width half-maximum (FWHM) of the distribution as determined by visual inspection. † uncompensated boron $[B_S^0]$ only.

of dislocations which propagate in the direction of growth, which is typical of CVD growth from a HPHT type Ib (0 0 1) substrate [16]. Furthermore, there is a higher density of dislocations close to the substrate before these annihilate and reduce the density.

On closer inspection it is possible to see deviations in the dislocations at the location of the boron regions. It is known that the incorporation of boron changes the growth surface morphology [17–19]. Therefore it is understandable that the dislocation direction alters as the diamond becomes intentionally boron doped.

Martineau *et al* demonstrated that under a step-flow growth mechanism, diamonds prepared with {0 0 1} faces exhibit dislocations that deviate, and proposed this was due to risers moving in a ⟨1 1 0⟩ direction [20]. As the diamond studied here is prepared with the major faces as {1 1 0} crystallographic planes (figure 5-1), this effect is not so clear, however in some of the nitrogen-containing regions the

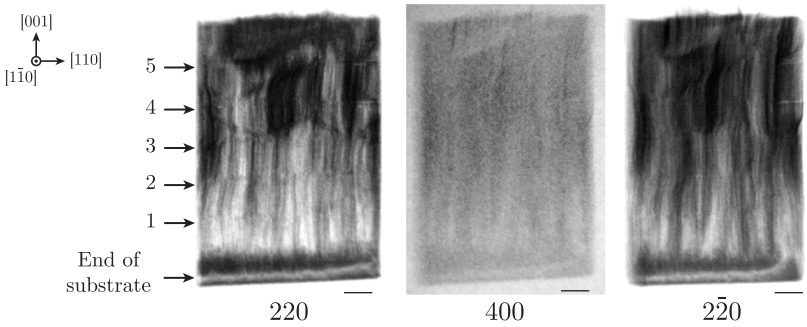

Figure 5-4 Film micrographs of X-ray topography (XRT) on piece B. The diffraction vector is included under the micrograph and locations of boron regions indicated. Scale bar = 0.5 mm.

dislocations do appear to deviate which is in agreement with Martineau *et al.*

Tallaire *et al* found that during stop/start CVD growth and high microwave power densities, the pre-existing diamond surface etches slightly when growth is resumed [12]. As such this introduces etch pits and can therefore generate an increased number of dislocations as the next layers grow. Furthermore, it was found that as the surface roughness increased, so did the uptake in boron, despite growth not being intentionally doped with boron.

Those conclusions agree with this study sample. After each boron layer has grown, the density of dislocations increases which implies the growing surface is etched during and after the high purity region is grown. Equally, in the CL measurements there is a slight increase in the visibility of the BE_{TO} peak in the subsequent nitrogen-containing region and would imply unintentional boron doping due to the increased surface roughness. This fact is missed by the SIMS measurement due to the lower sensitivity limit.

5.2.4 Widefield PL

Given the distinct orange fluorescence in DiamondView^{TM} imaging (figure 5-1c), PL with 514 nm excitation confirmed significant emission from both NV^0 and NV^- within the nitrogen-containing regions. A line scan across boron region 2 showed emission from NV significantly dropped across the boron-containing region (figure 5-5a).

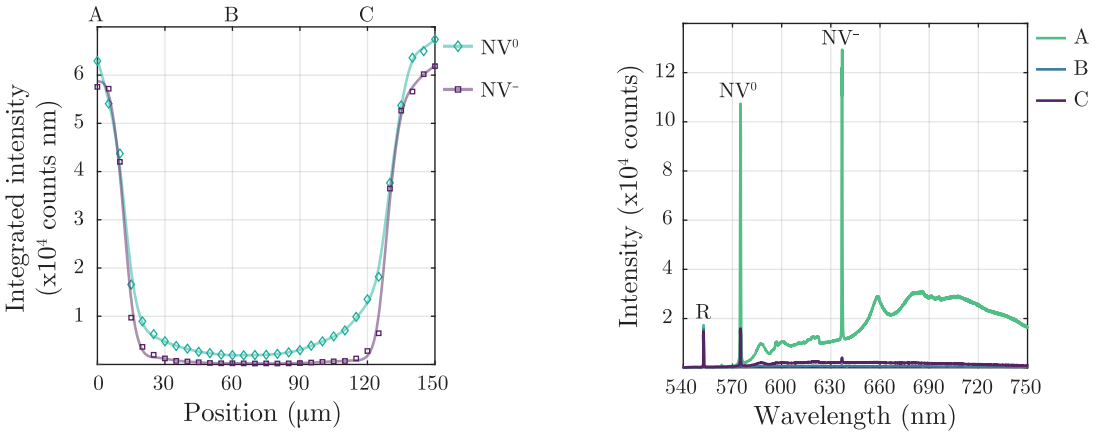

(a) **(b)**

Figure 5-5 (a) Integrated intensities of NV^0 and NV^- ZPLs as a function of position across boron region 2. A spline between data points has been added to guide the eye. (b) Representative PL spectra from the positions marked in (a). PL data was taken at 77 K with 514 nm excitation and a 50× long working distance objective (NA = 0.50), and normalised to the first order Raman (R) line at 552.4 nm.

Boron has acted as the electron acceptor by the virtue of the decrease in $NV^{0/-}$ at the boron interface. As the low temperature PL measurement was taken on a widefield microscope with a low NA objective, caution should be advised about the detection of NV^0 in the boron containing region (figure 5-5b). However, if NV^0 is indeed present with a negligible amount of NV^- in the boron doped region, this logically implies NV^+ has been produced as $[B_S] \gg [N_S]$.

The boron-containing region was also subjected to PL measurements with the suite of excitation sources available (§ 4.1.5) all at 77 K. As a result, and with the exception of $NV^{0/-}$, the region was inert over the excitation and detection range, and therefore indicates a lack of additional optically active point defects in significant concentration.

5.3 Confocal imaging and spectroscopy

5.3.1 Incorporation of single point defects

Under 532 nm excitation, care was taken to avoid damaging the sensitive SPCMs on the confocal microscope due to the $NV^{0/-}$ fluorescence intensity by setting the laser to 1 mW (at source). With the 633 nm longpass filter in place (NV^- target defect), very clearly defined striations can be observed in the nitrogen-containing regions (figure 5-6a), as is expected from the step-flow growth mechanism [16].

In order to further reduce the fluorescence intensity at the SPCMs, the NV^- target filter was changed for the 600 ± 26 nm bandpass filter (NV^0 target defect). In doing so, it became apparent that point defects could be seen in the boron-containing regions. Shown in figure 5-6b is a typical XY confocal scan of a boron-containing and high purity region interfaced with the nitrogen-containing regions, 15 µm below the diamond surface. Plotting the intensity on a logarithmic scale reveals discrete pixels with an intensity higher than the background, associated with point defect emission. These defects appear to be incorporated in straight lines (either vertical or inclined), as indicated by the arrows in figure 5-6c.

The structured manner of incorporation of these point defects is common to all five boron-containing regions in this material, where vertical and inclined lines are seen. The high purity region (area above dotted line in figure 5-6b) contains a higher concentration of luminescent point defects. Here, however, the distribution tended to be random and no linear features are apparent. Spectroscopic studies indicate that the majority of defects were NV^0, and will not be further discussed in this chapter.

By focussing in on the luminescent centres observed along the lines, the fluorescence intensity was not stable in about 50% of the defects. A high resolution confocal scan on just one such centre shows the fluorescence to *blink* (figure 5-7a). As the fluorescence sent to the confocal SPCMs is split by a 50:50 beamsplitter in free space, it was possible to move the location of the fluorescence filters such that one detector was covered by the NV^0 filter and the other by the NV^- filter. When the

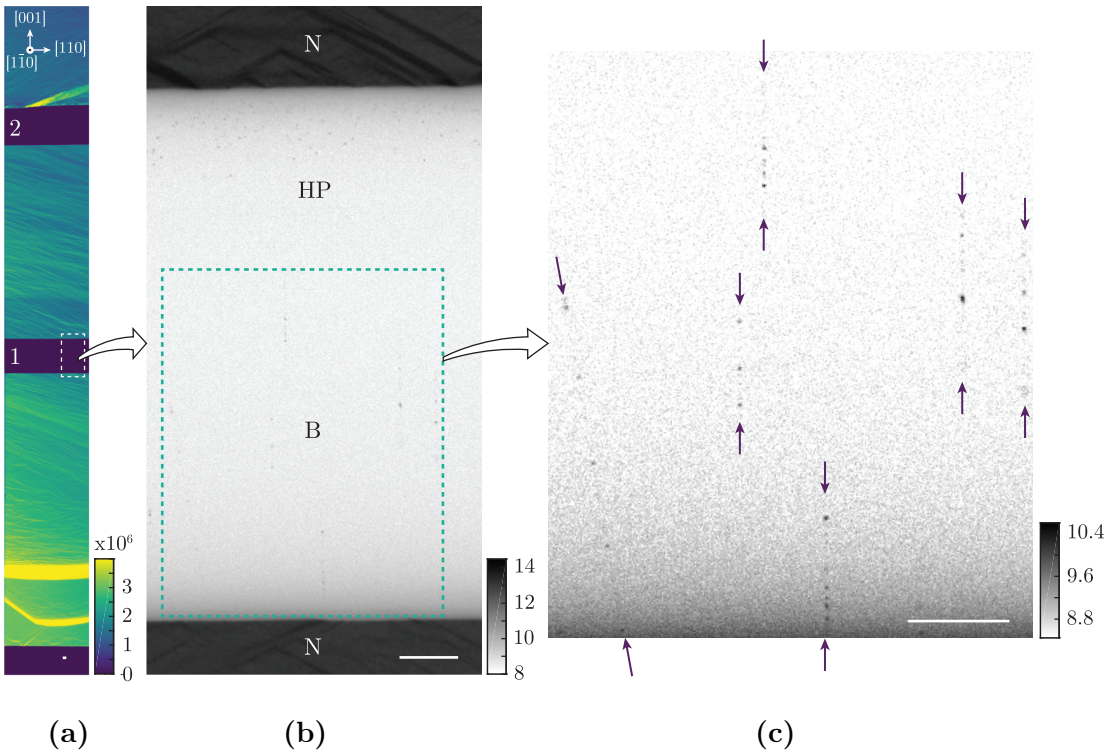

Figure 5-6 Confocal maps taken with 532 nm excitation where (a) is a montage of scans with two of the boron-containing regions (imaged with NV^- target filter), (b) Representative high resolution image of one of the boron-containing regions where the intensity is plotted in a log scale (imaged with NV^0 target filter), and (c) a high resolution snip highlighting point defects in the boron-containing region which follow a linear structure. Maps in (b) and (c) are plotted in a reverse grayscale to help distinguish features to the reader, where N, B, and HP denote the nitrogen containing, boron containing and high purity regions respectively. Scale bar = 10 µm. Photoluminescence intensity scale bar represents the photon count rate per second (cps).

fluorescence was not visible in the NV^0 channel, there was not an increase in the NV^- channel, but a slight decrease, as shown in figure 5-7b, likely due to defect fluorescence leakage into the 633 nm longpass filter.

Where fluorescence blinked stochastically, it was not possible to obtain an adequate second-order correlation function ($g^{(2)}(\tau)$). On the other hand, for the defects that were stable, this was possible as will be presented in the next section.

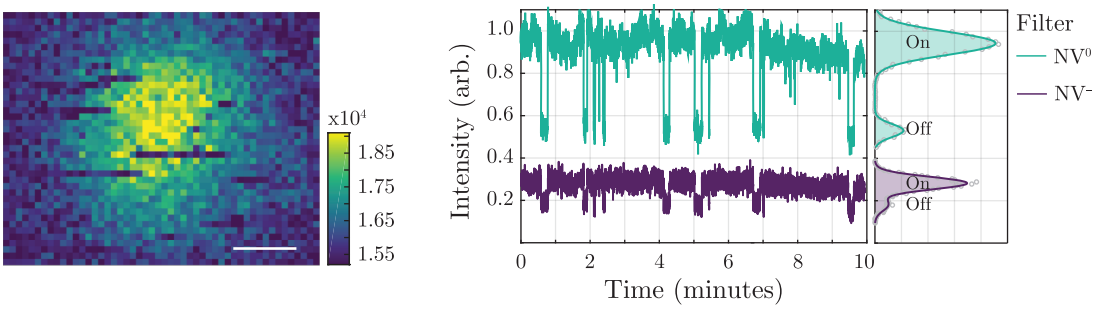

(a) **(b)**

Figure 5-7 (a) Confocal image of one isolated point defect in the boron-containing region (no $g^{(2)}(\tau)$ recorded) where the dark lines during the acquisition over the feature indicate a drop in PL intensity. (b) the PL intensity of the point defect recorded over 10 minutes, where the NV^0 target filter (600 ± 26 nm bandpass) covers one SPCM and the NV^- target filter (633 nm longpass) covers the other. Scale bar = 0.2 µm. Photoluminescence intensity scale bar represents the photon count rate per second (cps).

5.3.2 Spectroscopy, polarisation and fluorescence lifetimes

Despite point defects showing up prominently with the NV^0 target filter within the boron-containing region, it should not be assumed that the defects are NV^0 without knowing their spectral identity.

A total of 122 centres were individually characterised in terms of their spectroscopic features, polarisation behaviour, and where possible, the fluorescence lifetime was determined by the extracted fit from the $g^{(2)}(\tau)$ measurement. The PL intensity of the defect was maximised, and in all cases this proved to be with the excitation being linearly polarised, where the electric field component of the excitation source, $\boldsymbol{E}$, was parallel to the growth direction ($\boldsymbol{E}_{\parallel} = [0\,0\,1]$).

In all cases, the defect observed did not contain any characteristic emission pertaining to either NV^0 or NV^-. The majority of spectra show a sharp ZPL (at room temperature), with a Debye-Waller factor > 0.1, and with one or two LVM peaks at an energy separation between 180 meV and 200 meV from the ZPL. Figure 5-8 shows a representative set of data for commonly obtained spectral information.

Figure 5-9 shows the histogram of distribution in the ZPLs observed along with the spread in LVM. There appears to be a distinct separation of the ZPL in to

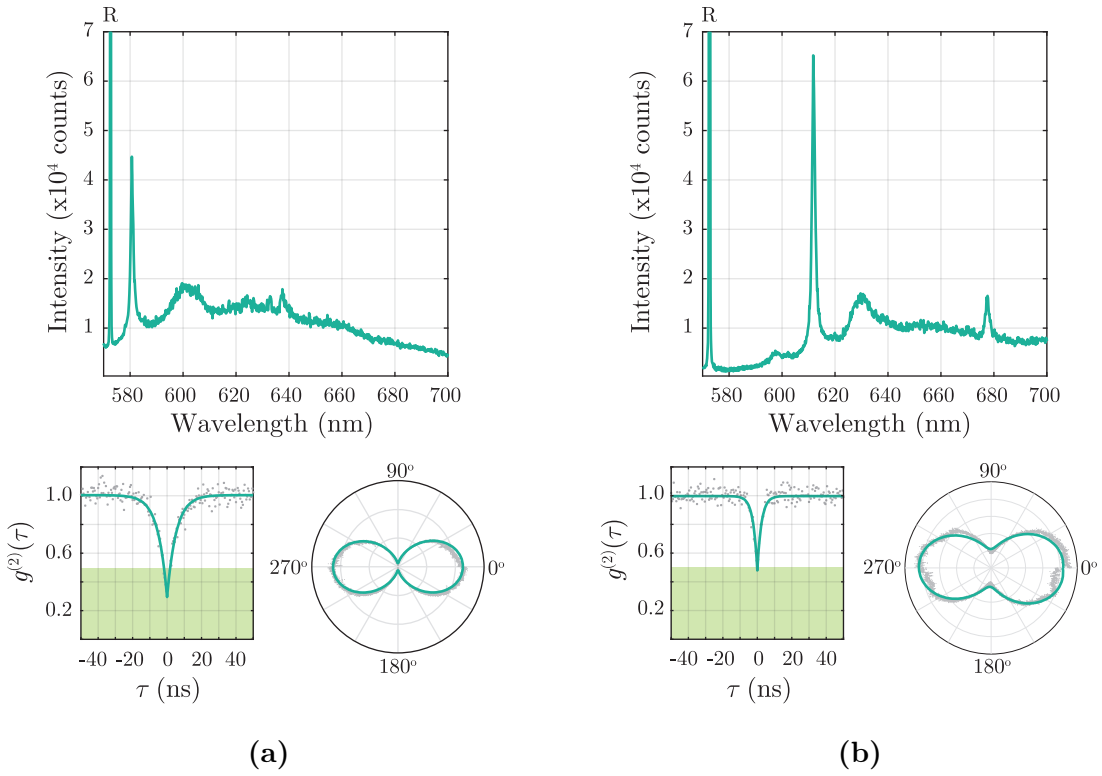

Figure 5-8 Two exemplar, background-corrected, spectra taken from the study of 122 point defects where (a) has a ZPL at 580.7 nm, and (b) has a ZPL at 611.8 nm. R denotes the first order Raman line at 572.6 nm. Fluorescence lifetimes of (a) and (b) as extracted from the fit are 5.3 ± 0.4 ns and 2.4 ± 0.3 ns respectively. Polarisation contrast for (a) and (b) are 95% and 74% respectively.

two classes, a series of defects whose ZPL is located at 580 ± 10 nm, and the other series where the ZPL is located at 612 ± 18 nm. The LVM distribution shows less of a distribution, where a single Gaussian shows the LVM to be located at 189 ± 10 meV.

Whilst 65 out of the 122 defects were able to provide a $g^{(2)}(\tau)$ measurement, in the majority of data the noise is on the order of ± 0.1, and so the $g^{(2)}(0)$ minima are classified here such that ≤ 0.4 is a single centre, $0.4 < g^{(2)}(0) \leq 0.6$ is two centres and $g^{(2)}(0) > 0.6$ corresponds to three or more centres. Hence by the recorded $g^{(2)}(0)$ values, 32% of defects are single centres, 37% are two centres, and the remaining 31% are three centres or more per PL spot. For the non-single centre defects, the spectral data tended to show only either the 580 nm ZPL or the 612 nm ZPL present, only 12% of the these exhibited both ZPLs in the spectral information.

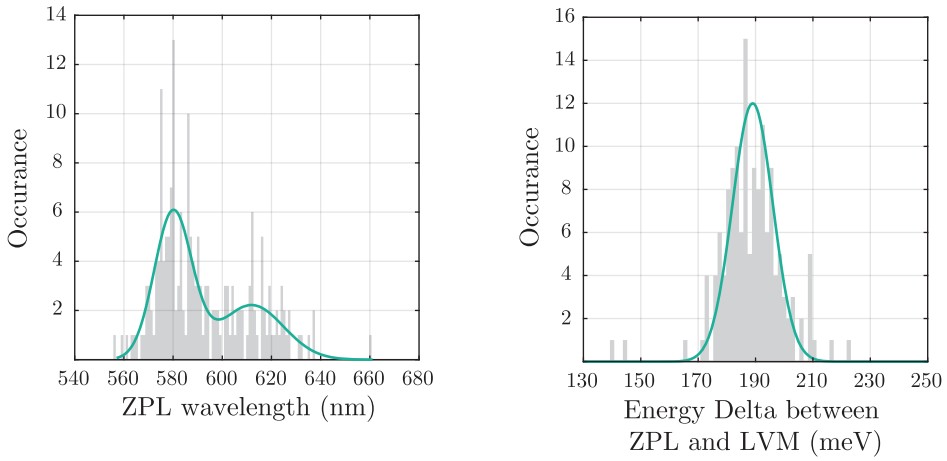

(a) **(b)**

Figure 5-9 Distributions of (a) ZPL position where the double Gaussian fit is centred on 580 nm and 612 nm, and (b) LVM position where the single Gaussian fit is centred on 189 meV.

From equation (3-52a), by fitting a two level system the mean extracted fluorescence lifetimes are given as 3.7 ± 1.7 ns and 1.8 ± 0.7 ns for the 580 and 612 nm defect groups respectively.

The absorption polarisation was measured on the fluorescent defect, with only the laser rejection filter in place, by the 360° rotation of the **E** field. The fluorescence intensity on the SPCMs was then simultaneously recorded. After this, the stage was moved to collect fluorescence only from the first-order Raman background and the same polarisation measurement repeated. On subtraction of the background response from the defect fluorescence a high degree of extinction can be seen, where in most measurements this is $> 90\%$. A lower degree of contrast is observed for defects that blink (figure 5-8b) which is likely due to fluorescence switching occurring faster than the detection time. Placing a linear polariser on the detection arm confirmed that both absorption and emission dipole of these defects are orientated along $\langle 0\,0\,1 \rangle$. For some of the defects, spectra were recorded as a function of excitation polarisation orientation where it was found that both the ZPL and LVM peaks behave in the same way.

After investigating the excitation polarisation of these 122 defects, it was noted that for an orthogonal polarisation ($\boldsymbol{E}_{\perp}$ to growth direction) additional point defects

were seen when rescanning the boron-containing region. From this, a further 10 defects were spectrally characterised. Here, the defects appeared to be less stable than the defects excited with the original polarisation. Figure 5-10a shows the typical spectrum of the point defects, where no discernible features can be seen other than a broad emission over the detection window.

Furthermore, out of these 10 defects, three showed a completely different polarisation behaviour where the maxima and minima of fluorescence intensity due to the polarisation are 54° ± 4° out of phase (figure 5-10b). These defects also show a spectrum with two strong ZPLs. Finally, these three defects with two ZPLs yield a $g^{(2)}(\tau)$ function with a three-level system compared to the rest of the defects measured which always showed a two-level system.

5.3.3 Defect spectral stability

Given that most of the defects studied exhibited fluorescence blinking, all of the spectral acquisition was completed with the Andor spectrometer set to a kinetic acquisition, such that one spectrum is typically acquired with a 0.3 s exposure time, and repeated at least 1000 times. In the cases where the fluorescence blinking is directly on/off, the frames without defect fluorescence were discarded. The complete spectrum of the defect is thereby given as the sum of all frames which show photoluminescence.

One of the defects which showed the fluorescence blinking behaviour was subject to a study on the excitation power. This defect had a ZPL at 577.0 nm, $g^{(2)}(0) = 0.63$ and a fluorescence lifetime of 5.4 ± 0.4 ns. Here, the PL intensity was recorded on the SPCMs over 120 s, as a function of laser power from 1 mW to 10 mW at the source. In analysing the durations of the on and off times as a function of laser power, it is possible to deduce the switching rates as per the switching rate analysis of NV^- in nanodiamonds [21].

Figure 5-11a shows the switching rate behaviour as a function of laser power at the source. By histogramming the time trace and counting the time the defect spent in the on and off states it was possible to see the trend caused by increasing the laser

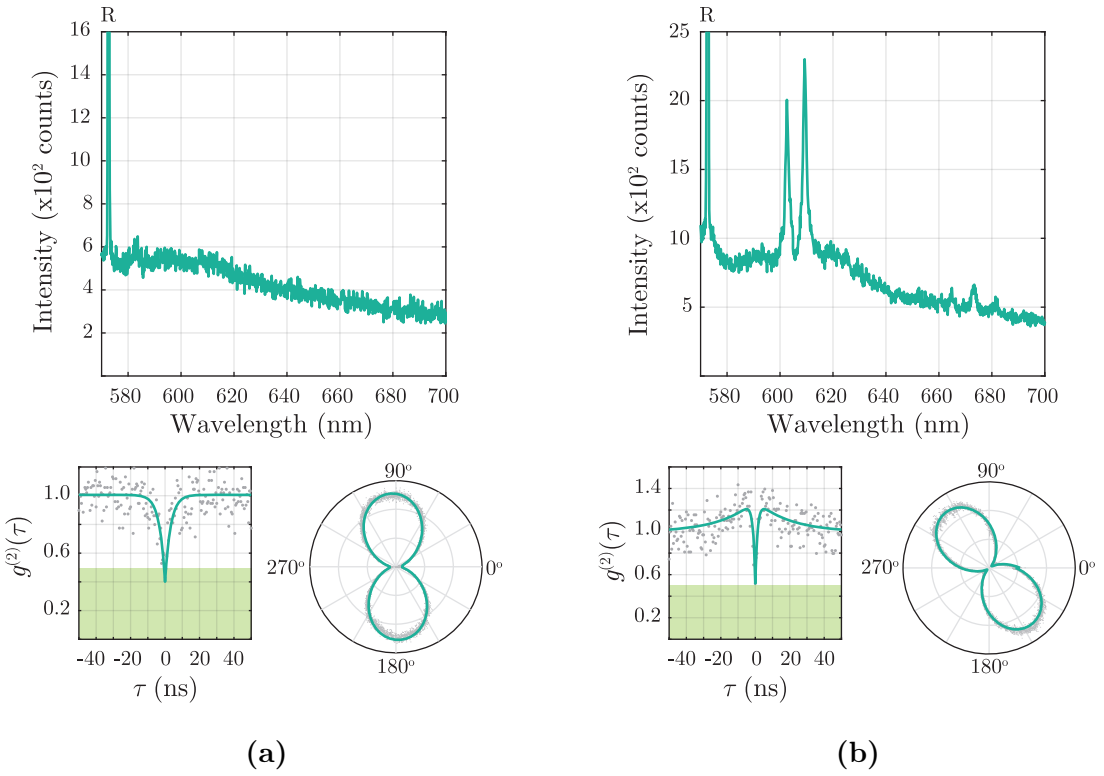

Figure 5-10 (a) When $\boldsymbol{E}_{\perp}$ to growth direction, the spectra do not contain any obvious features despite the defect being bright during confocal imaging. R indicates the first-order Raman line at 572.6 nm. A fit of the $g^{(2)}(\tau)$ data implies a fluorescence lifetime of 3.3 ± 0.3 ns. The polarisation behaviour is 90° out of phase with both 580 nm and 612 nm defects with a 92% contrast. (b) 3 out of 10 additional defects imaged revealed a spectrum with two sharp ZPLs at 602.6 nm and 609.3 nm, which may be two centres as judged by the autocorrelation measurement. The fluorescence lifetime is extracted as 1.3 ± 0.4 ns with a shelving state lifetime of 20 ± 6.2 ns. Polarisation data shows the absorption dipole to be 54° ± 4° out of phase from the 580 nm and 612 nm defects, with 96% contrast.

power, as seen in figures figures 5-11b and 5-11c. Here it is shown that as the laser power increases, the switching rate increases whilst the decay lifetime spent in both the on and off states exponentially decreases. This is perhaps not unreasonable if the increased laser power facilitates a two-photon absorption process to ionise the defect to remove fluorescence, as can be seen in the case of the NV centre [22].

Aside from fluorescence blinking, by manual inspection of all the spectral data sets during acquisition, it was noted that in some cases defects behaved in unexpected ways, namely by spectral diffusion and splitting.

Figure 5-12a shows an example case of a ZPL randomly moving throughout the

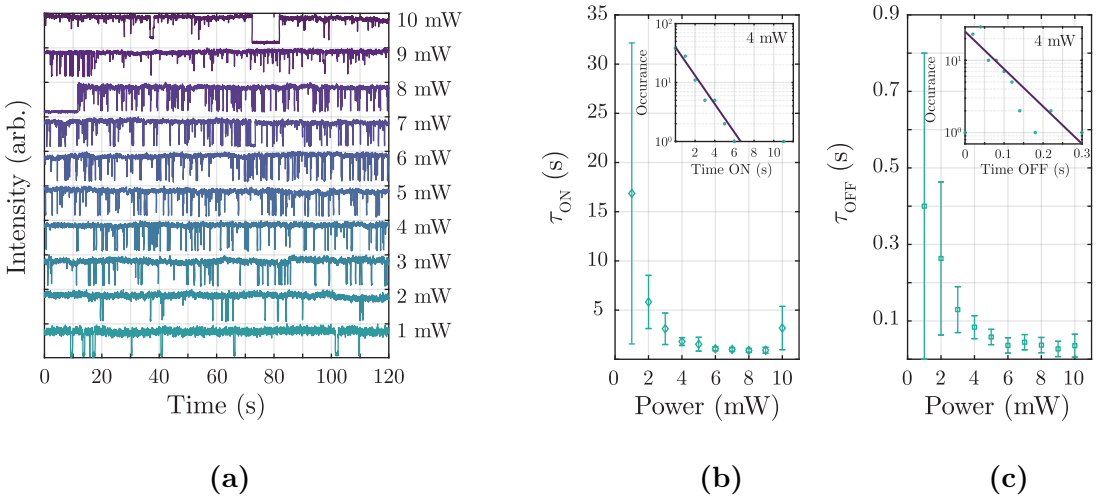

Figure 5-11 Fluorescence blinking behaviour as a function of laser power where (a) shows the trace of fluorescence over 120 seconds (where each laser power has been offset for clarity), (b) the trend of time spent ON, and (c) the trend of time spent OFF. Inset to (b) and (c) are examples of the fit at 4 mW for the histogrammed time intervals where the occurrence is plotted on a logarithmic scale.

kinetic series. From state 1, the 573.8 nm (2.161 eV) ZPL moves to state 2 where the ZPL is located at 575.4 nm (2.155 eV). This represents a spectral diffusion energy of 6 meV, where the two LVMs in state 1 also shift with the same energy. An excerpt of the ZPL motion is captured in figure 5-12c.

Alternatively, the ZPL can be shown to split in some instances (figure 5-12b). In this example, state 1 shows as a ZPL at 580.0 nm (2.138 eV) will change to two peaks at 580.2 nm (2.137 eV) and 582.4 nm (2.129 eV). When a defect undergoes a spectral split in the ZPL, the new state is less stable than the original state as shown by the trace in figure 5-12d. It is unclear whether the peak at 582.4 nm is a new feature that has started to produce PL since there is only a 0.2 nm difference between the ZPL in state 1 and the left most peak in state 2, which is on the order of the instrument noise. Nevertheless, an autocorrelation measurement was obtained on this centre, whilst undergoing spectral splitting, and resulted in a $g^{(2)}(0)$ value of 0.24 with a fluorescence lifetime of 4.7 ± 0.3 ns.

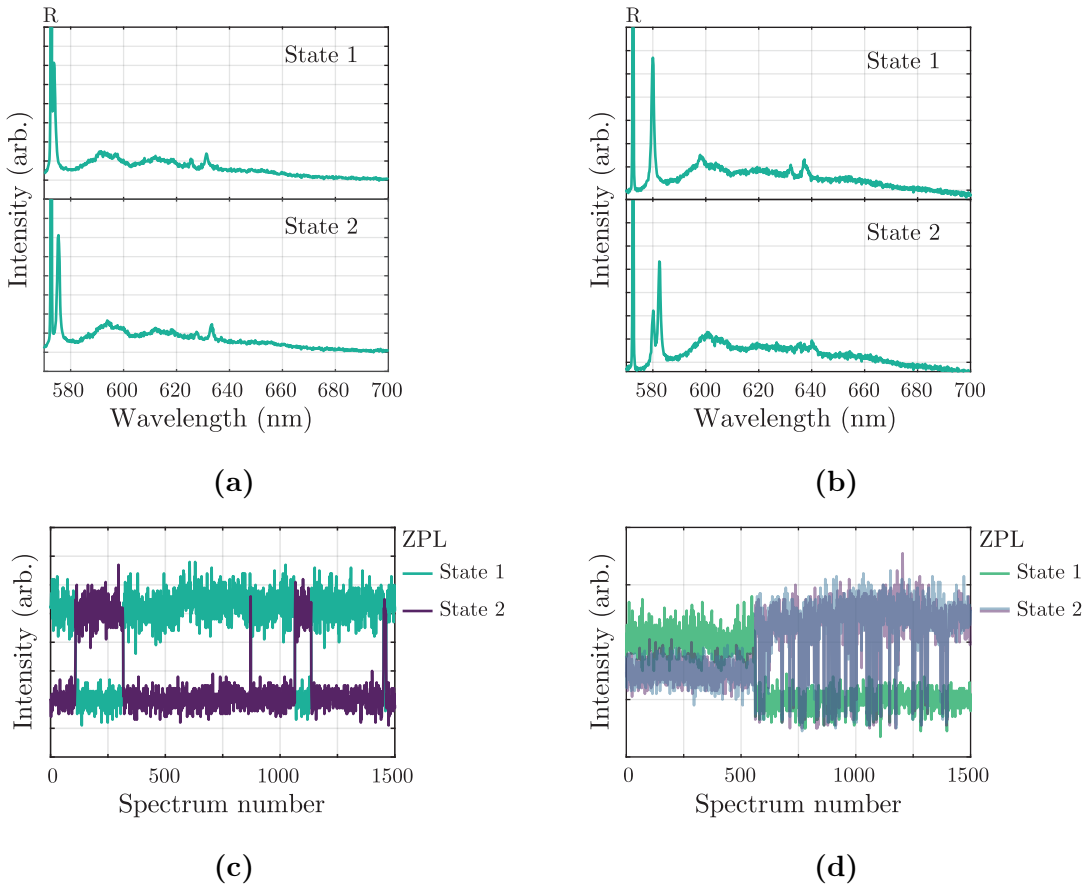

Figure 5-12 (a) Spectral diffusion whereby a single centre ($g^{(2)}(0) = 0.23$) with a ZPL at 573.8 nm jumps to 575.4 nm and back (b) Spectral splitting whereby a single centre ($g^{(2)}(0) = 0.24$) with a ZPL at 580.0 suddenly splits to become 580.2 nm and 582.4 nm. Time traces of the motion is shown in (c) and (d) whereby the acquisition time per frame is 0.1 s and 0.3 s respectively.

5.4 Discussion

5.4.1 Boron concentration discrepancy

In figure 5-3, it is noted that the boron concentration as determined by FTIR spectroscopy is approximately 200 ppb lower than both the concentration values obtained from SIMS and CL spectroscopy. The reason for this is perhaps not so clear, however it is reasonable to speculate as to the cause of this.

The optical resolution of the FTIR microscope used within this study will be limited by the diffraction limit of light. With a low magnification objective and large detector pixel size, the spatial resolution is likely to be on the order of 10 µm.

Hence the data collection is oversampled relative to the spatial resolution. From this, it can be assumed that there is sampling of non-boron doped material whilst collecting the IR spectrum, and could imply that the spatial resolution is slightly greater than 10 µm.

Furthermore, the FTIR value may be lower since it is only a measure of uncompensated B_S^0. From conducting Hall effect measurements, Wedephol was able to demonstrate that the intensity of 2454 cm^{-1} and 2800 cm^{-1} peaks as seen in IR spectroscopy were directly related to the number of neutral acceptor concentrations [23]. From this Collins and Williams devised a calibration constant relating the integrated area intensity of the 2800 cm^{-1} peak to the number of neutral acceptors [24]. Later Collins refined this, and produced calibrations constants for the 2454 cm^{-1} and 2800 cm^{-1} using a baselined peak height, as well as including a calibration to the one-phonon peak at 1290 cm^{-1} [1]. However, it is noted that Collins has also suggested that there are difficulties in interpreting the Hall data relative to the boron concentration, as there is no adequate theoretical description of the processes [25]. Therefore, it is not clear yet whether IR spectroscopy provides a reliable route to accurate knowledge about the substitutional boron content.

Equally, it should be highlighted that the agreement between SIMS and CL spectroscopy is encouraging, and perhaps not surprising. Kawarada *et al*, and then later Barjon *et al*, related the boron concentration from SIMS to the ratio of BE_{TO}/FE_{TO} as seen in low temperature CL spectroscopy, such that a suitable calibration constant could be given [26, 27]. In addition, Barjon claimed that the BE_{TO}/FE_{TO} ratio should be proportional to the total shallow acceptor (or donor) concentration, and independent of the compensation state since all shallow impurities are neutralised under an electron beam [28]. On the other hand, Omnes *et al* argues that CL spectroscopy would not yield a true measure of the boron content since boron-hydrogen (BH) pairs would dissociate under the electron beam, and boron vacancy complexes would not be electrically active [29]. In this study however, there is a very clear agreement between the SIMS and CL maximum values, with a difference less than 5 ppb between them. Therefore, CL spectroscopy is a powerful technique to realise the boron content without causing damage to

the diamond.

Despite all of this, the visual inspection of the FWHM for the boron doped layer from all three characterisation techniques are in agreement with each other, and clearly show very well defined regions of boron doping.

5.4.2 Defect orientation and incorporation mechanism

Clear from this study is the identification of PL emission from unknown defects, which are incorporated in very low concentrations. However, data from the polarisation study suggests possible symmetries by group theory considerations. Figure 5-13 models the polarisation dependence of an absorption dipole for either $\langle 0\,0\,1\rangle$, $\langle 0\,1\,1\rangle$ or $\langle 1\,1\,1\rangle$ orientations, where the $\boldsymbol{E}$-field of excitation is rotated about $[1\,\bar{1}\,0]$. Here, it is clear to see that the defects observed show the same dependence as a defect with either $\mathscr{D}_{2\mathrm{d}}$ or $\mathscr{C}_{2\mathrm{v}}$ symmetry. What's more, in relating the relative intensities of both dipole orientations, the experimental data favours the defect to be an electronic transition between a ground A state and an excited A state (c.f figures 5-13a and 5-13b).

The curious nature of incorporation is suggestive of these defects being incorporated with assistance from an extended defect, such as a dislocation. Gaukroger *et al* used XRT to study a CVD grown sample and saw dislocations tended to have a line direction along $\langle 0\,0\,1\rangle$ [30]. If one imagines isolating one of these dislocation bundles, and viewing it down the $\langle 0\,1\,1\rangle$ direction, it becomes possible to imagine seeing dislocations which have a line direction in and out of the plane, but also running at diagonals in the plane (figure 5-14). It is noted from this figure that the inclined lines in the image plane make an angle of $12^\circ \pm 2^\circ$ from $[0\,0\,1]$. Therefore, it is not unreasonable to link the incorporation of these points defects as a decoration of dislocations that are propagating between the nitrogen-containing regions. Upon careful inspection, it does appear that these lines point from the end of one striation to the start of another striation from the nitrogen sections.

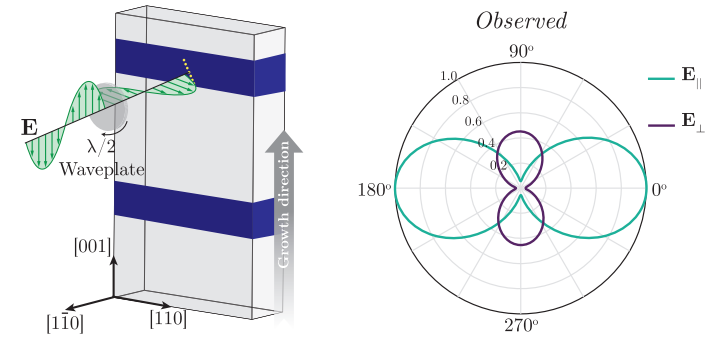

(a)

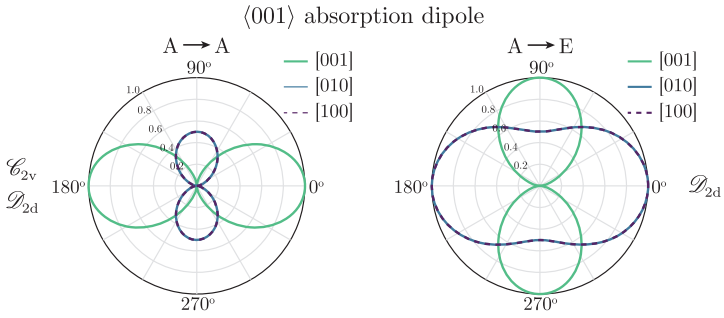

(b)

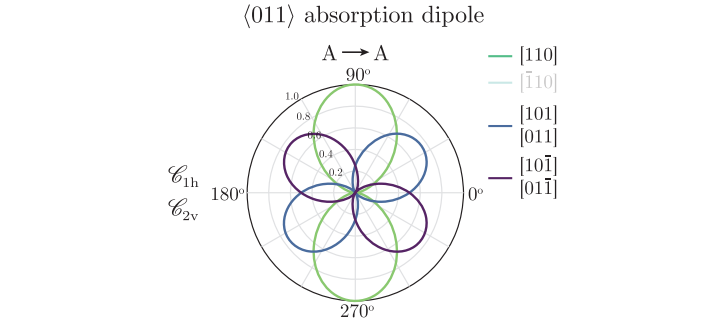

(c)

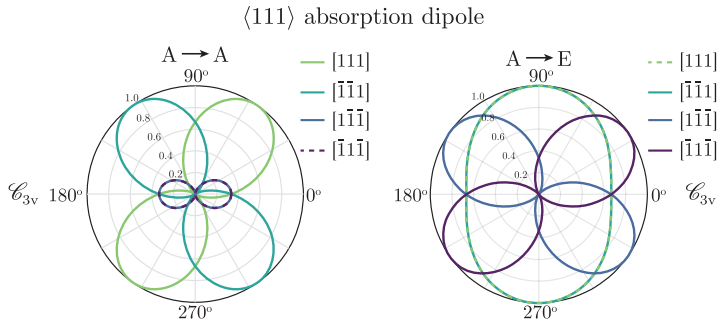

(d)

Figure 5-13 (a) A schematic of the ***E***-field from the excitation source being rotated about the sample viewing direction and the fitted lines from the absorption polarisation measurements. Polar plots of the absorption dipoles orientated along (b) ⟨0 0 1⟩ (c) ⟨0 1 1⟩, and (d) ⟨1 1 1⟩, where the possible symmetries are given on the left or right of the plot. Note with this orientation of sample, the [1 $\bar{1}$ 0] absorption dipole would be invisible during measurement.

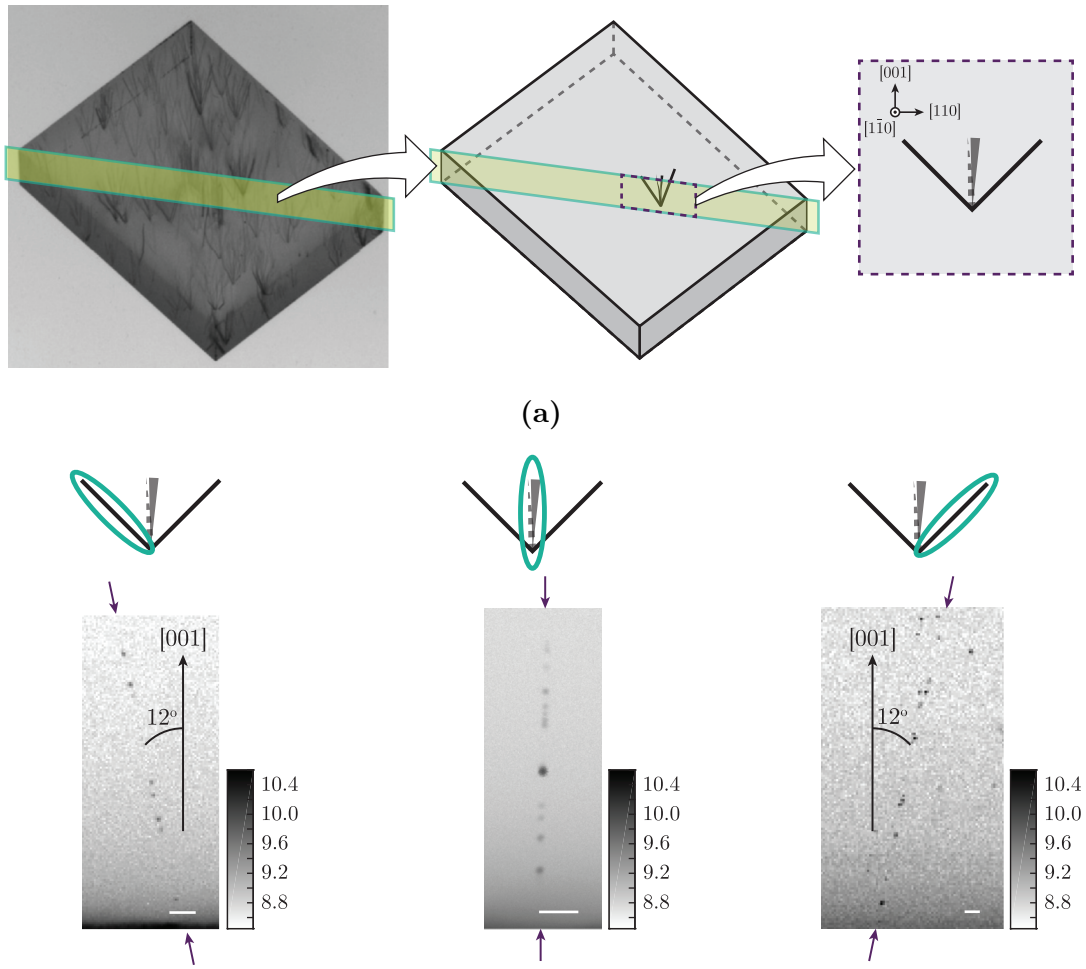

Figure 5-14 (a) XRT image from [30] where dislocation bundles are seen with ⟨0 0 1⟩ directions, if one bundle could be isolated and viewed down the ⟨0 1 1⟩ direction a series of diagonal and vertical lines would be seen. (b) examples of diagonal and vertical lines in the boron containing region showing point defect incorporation where the inclined lines are 12° ± 2° from [0 0 1]. Scale bar = 2 µm. Photoluminescence intensity scale bar represents the log of the photon count rate per second (cps).

5.4.3 Comparison to published work

Spectral diffusion is often considered in quantum dot research, including hexagonal boron nitride (hBN) and single-walled carbon nanotubes (SWCNT) material. Here, spectral diffusion is readily attributed to mobile charge carriers [31] and the absorption of emitted phonons at a localised exciton in order to create a ZPL replica at a lower energy [32]. However, with regards to the spectral diffusion in diamond, the effect is not as widely reported. It has previously been demonstrated

for the NV^- centre during photoluminescence excitation (PLE) measurements, and is mitigated by removing unwanted charge carriers [33, 34]. The spectral instability of the defects observed here is perhaps unsurprising, owning to the local boron content.

Very little literature has been published on point defects which show similar characteristics. Perhaps the most relatable of those is the study by John *et al*, whereby 27 amu[a] ions were implanted into electronic grade CVD material [35]. In doing so, it was found that two new types of point defect were created and designated as L1 and L2 with ZPL positions at 580 nm and 550 nm respectively. In the latter case, it was argued that L2 shows similarities to another defect, ST1, which is also formed by implantation and shows a positive ODMR response [35, 36].

Pertinent to this study though is the spectral characterisation of the L1 defect. Whilst the location of the L1 ZPL, and to some extent its distribution, agree with this data set, there are too many significant differences. L1 displays LVMs of two or three peaks which are situated 190 - 210 meV from the ZPL, whilst this data set shows the 580 nm defect to have either one or two LVM peaks < 200 meV. From the autocorrelation measurement, L1 is shown to be a 3-level system with a lifetime of 2 ns, whilst in this study defects were measured to be a 2-level system with a mean fluorescence lifetime of 3.7 ns. The polarisation data also signifies that L1 has a $\langle 1\,1\,0 \rangle$ absorption dipole, whereas here the defects observed show definitely a $\langle 0\,0\,1 \rangle$ orientated absorption dipole.

Evidently then, the defects observed in this boron-containing CVD material are not the same L1 defect. It should be noted that John *et al* state that the implantation could have been contaminated by the cathode used for implantation [35]. As such it is impossible to rule out that either boron, carbon, nitrogen, oxygen, or all four ion species were implanted to their diamond.

Wang *et al* were able to also observe a defect centred on 580 nm in type IIa diamond after electron irradiation, although it is not clear whether this defect was generated as a consequence of irradiation [37]. In this study, the 580 nm line is

[a] atomic mass units

stated to have two LVMs associated with it, however these appear at 198 meV and 237 meV which is not consistent with the mean value found in this study. Finally, Wang *et al*, and later Zaitsev *et al* [38] speculate that the 580 nm defect may be a negatively charged self-interstitial. In contrast, it is not certain that the 580 nm defect found in this study would be negatively charged, due to the local boron concentration since $[B_S] \gg [N_S]$.

Re-evaluating the theoretical study by Goss, it is claimed that BV^0 would be optically active with a transition at approximately 2.0 eV (620 nm) [8]. This is relatively close to 612 nm emission (2.02 ± 0.06 eV), however the symmetry of the defects here do not agree with that of BV which should be $\mathscr{C}_{3v}$, thus making BV unlikely for the 612 nm defects. This does however raise an interesting notion that three defects (with a ZPL around 606 nm (2.04 eV)) were observed with an absorption dipole 54° from [0 0 1], and would be consistent with a defect being of $\mathscr{C}_{3v}$ symmetry (figure 5-13). More defect statistics from this sample, or other boron doped CVD would be needed to aid Goss' prediction for BV.

In the same paper, Goss also considers boron substitutional-interstitial pairs and concludes there are stable configurations with $\mathscr{D}_{2d}$ and $\mathscr{C}_{2v}$ symmetries. Of these, the lowest energy configuration would be the [0 1 1]-orientated self interstitial with two substitutional boron atoms and $\mathscr{C}_{2v}$ symmetry. However, it is not clear if this complex would be optically active.

Since 648.2 nm PL emission was not found in the boron-containing region, it is not clear if these point defects in this layered material originate from a boron interstitial alone. Furthermore, the absorption dipole orientation disagrees with Green [4], again suggesting these defects are not the same.

5.5 Conclusion

A synthetic diamond grown by MPCVD, and containing localised regions of boron doping where $[B_S] \gg [N_S]$, was extensively studied by room temperature confocal PL microscopy. It was found that in the boron-containing regions, with 532 nm excitation where the $\boldsymbol{E}$-field of the laser was linearly polarised along [0 0 1], single

point defects could be identified. Furthermore, this incorporation of these defects appeared to follow inclined lines which either moved in or out of the image plane, or at 12° ± 2° in the image plane. Subsequent spectroscopy revealed the PL to be unrelated to NV centres, and instead exhibited a sharp ZPL centred either on 580 ± 10 nm or 612 ± 18 nm with an absorption dipole orientated along ⟨0 0 1⟩. Cross-referencing the XRT of the diamond with the incorporation of defects suggests a decoration of a dislocation running between the nitrogen-containing regions.

To the author's knowledge, these point defects have not been previously reported in literature, despite various accounts of ZPL emission at 580 nm. Consequently, these defects are currently an undetermined species, however the hypothesis of dislocation decoration may favour a complex involving interstitials of both boron and carbon atoms. Future work should focus on obtaining more spectral characterisation of the point defects across more of the boron-containing regions. In addition, an electron-irradiation and annealing study should help to identify this species of defect as well as the potential characterisation of newly created point defects.

References

1. A. T. Collins, presented at the De Beers 61st Diamond Conference.
2. B. L. Green et al., *Physical Review Letters* **119**, 096402 (2017).
3. B. C. Rose et al., *Science* **361**, 60–63 (2018).
4. B. L. Green, PhD thesis, University of Warwick, 2013.
5. J. Steeds, S. Kohn, *Diamond and Related Materials* **50**, 110–122 (2014).
6. M. Pfender et al., *Nano Letters* **17**, 5931–5937 (2017).
7. J. P. Goss et al., *Physical Review B* **69**, 165215 (2004).
8. J. P. Goss, P. R. Briddon, *Physical Review B - Condensed Matter and Materials Physics* **73**, 1–8 (2006).
9. A. Kunisaki et al., *Japanese Journal of Applied Physics* **56**, 04CK02 (2017).
10. D. J. Twitchen, *Private Communication*, 2016.
11. A. M. Edmonds et al., *Physical Review B* **86**, 035201 (2012).
12. A. Tallaire et al., *Diamond and Related Materials* **20**, 875–881 (2011).
13. M. Vanecek et al., *Diamond and Related Materials* **12**, 521–525 (2003).
14. I. Sakaguchi et al., *Diamond and Related Materials* **7**, 1144–1147 (1998).
15. M. Tsigkourakos et al., *physica status solidi (a)* **212**, 2595–2599 (2015).
16. P. M. Martineau et al., *Gems & Gemology* **40**, 2–25 (2004).
17. Z. M. Shah, A. Mainwood, *Diamond and Related Materials* **17**, 1307–1310 (2008).
18. J. Achard et al., *Diamond and Related Materials* **20**, 145–152 (2011).
19. A. Tallaire et al., *Comptes Rendus Physique* **14**, 169–184 (2013).
20. P. M. Martineau et al., *physica status solidi (c)* **6**, 1953–1957 (2009).
21. C. Bradac et al., *Nature Nanotechnology* **5**, 345–349 (2010).
22. N. Aslam et al., *New Journal of Physics* **15**, 013064 (2013).
23. P. T. Wedepohl, *Proceedings of the Physical Society. Section B* **70**, 177–185 (1957).
24. A. T. Collins, A. W. S. Williams, *Journal of Physics C: Solid State Physics* **4**, 1789–1800 (1971).
25. A. T. Collins, *Philosophical Transactions of the Royal Society of London. Series A: Physical and Engineering Sciences* **342**, 233–244 (1993).

26. H. Kawarada et al., *Physical Review B* **47**, 3633–3637 (1993).
27. J. Barjon et al., *Physical Review B* **83**, 073201 (2011).
28. J. Barjon, *Physica Status Solidi (A) Applications and Materials Science* **1700402**, 1–10 (2017).
29. F. Omnès et al., *Diamond and Related Materials* **20**, 912–916 (2011).
30. M. Gaukroger et al., *Diamond and Related Materials* **17**, 262–269 (2008).
31. X. Li et al., *ACS Nano* **11**, 6652–6660 (2017).
32. A. Jeantet et al., *Nanoscale* **10**, 683–689 (2018).
33. J. Wolters et al., *Physical Review Letters* **110**, 027401 (2013).
34. Y. Chu et al., *Nano Letters* **14**, 1982–1986 (2014).
35. R. John et al., *New Journal of Physics* **19**, 053008 (2017).
36. S.-Y. Lee et al., *Nature Nanotechnology* **8**, 487–492 (2013).
37. K. Wang, J. Steeds, Z. Li, *Diamond and Related Materials* **25**, 29–33 (2012).
38. A. Zaitsev, K. Moe, W. Wang, *Diamond and Related Materials* **71**, 38–52 (2017).

6

Understanding HPHT growth by single defect detection

You certainly usually find something, if you look, but it is not always quite the something you were after.

- *The Hobbit*, J. R. R. Tolkien

6.1 Background

Covered in chapter 2 are the two main methods to synthesise single crystal diamond, namely CVD and HPHT. Historically, diamond grown by HPHT tends to contain a high concentration of point defects and metallic inclusions. For applications of diamond that required high purity this naturally led to the further development of CVD processes to provide extreme control of point defect incorporation.

As research into HPHT synthesis advanced, new growth recipes were developed to mitigate against total defect incorporation, and to increase the size and quality of the crystal. For instance, nitrogen has a high solubility in diamond which can lead to growth rate changes and influences the final crystal morphology [1, 2]. To minimise this, a nitrogen *getter*, such as titanium, zirconium or aluminium, is added to the metal solvent to form stable nitrides, thus reducing nitrogen incorporation within the diamond lattice [3]. Typically then, boron tends to win out as the dominant impurity species where its source resides either in the HPHT growth capsule, the solvent/catalyst mixture or even from the carbon source [4]. Non-

traditional growth systems have also been demonstrated as a way to grow diamond with a low point defect incorporation [5].

The morphology of the crystal is affected by several parameters including pressure, temperature and impurity incorporation. Conventional pressures and temperatures usually result in a crystal morphology largely governed by the development of {0 0 1} and {1 1 1} growth sectors, producing a cubo-octahedral crystal [6]. With nitrogen and/or boron incorporation sectors such as {0 1 1}, {1 1 3}, and {1 1 5} can be present, where the uptake of impurity follows the growth sector dependence described by the modified Kanda diagram [3, 7, 8].

Now, it is possible to synthesise HPHT diamond of high quality both in terms of crystalline perfection and diminished impurity uptake [4, 9]. Furthermore, low dislocation concentrations over a large area is an attractive prospect for the enablement of several technological areas [4, 9–12]. Consequently it can be argued that HPHT should be the better route for creating a perfect diamond, as CVD growth still remains a challenge to produce high purity *and* high crystalline quality material. On the other hand, it is still difficult to produce HPHT diamond where the concentration of nitrogen and boron impurities are less than 50 ppb.

Partially responsible for the drive in furthering the understanding of diamond synthesis is clearly within the technology market. NV^- has already been discussed in this thesis as a viable quantum system for sensitive detection of many physical properties and quantum computation [13–15]. Equally, it should be noted that improved knowledge in HPHT synthesis can also yield larger material for the gemmological market, where 15 ct. polished gems have already been demonstrated [16].

Therefore, there is a desire to understand the point defect incorporation down to the single centre level in high purity and high quality HPHT diamond. This chapter considers two single crystal type II HPHT diamond samples from two different manufacturers in order to reveal further knowledge on the growth mechanisms.

6.2 HPHT samples and their bulk characterisation

Two manufacturers of HPHT synthetic diamond used in this study are; New Diamond Technology (NDT) and Element Six Ltd (E6). For the purpose of this study, a representative diamond sample from each company is characterised, where the NDT diamond will be considered as the primary research item and the E6 diamond used as a comparator. The NDT sample was reported to be synthesised in a cubic HPHT press, from a Co-Fe-C system using a proprietary nitrogen getter. Furthermore, this sample was received free of any post growth treatment (i.e. electron irradiation and annealing). Equally, the E6 sample was grown in a Co-Fe-C, nitrogen gettered system.

Before confocal imaging and spectroscopy, the material quality and dopant incorporation is assessed in line with the techniques already presented.

6.2.1 Material quality

Strain and extended defects are shown by means of birefringence microscopy and white beam X-ray topography (XRT) respectively.

The NDT sample exhibits a small fracture and metallic inclusion highlighted as A and B respectively in figure 6-1a. Aside from this, the material shows very low internal strain. XRT reveals an average dislocation density below 10^3 cm^{-2} where virtually zero dislocations are seen in the (0 0 1) growth sector, and stacking faults are seen in the {1 1 1} growth sectors. The E6 sample has a higher degree of strain and density of dislocations than the NDT sample, and also harbours an inclusion (figure 6-1b).

6.2.2 Morphology

Shown in figure 6-2a is a model of a perfect cubo-octahedral crystal from the as-grown state, and how an excised (0 0 1) slice would appear. The NDT sample exhibits an almost textbook growth sector pattern consistent with a (0 0 1) slice in

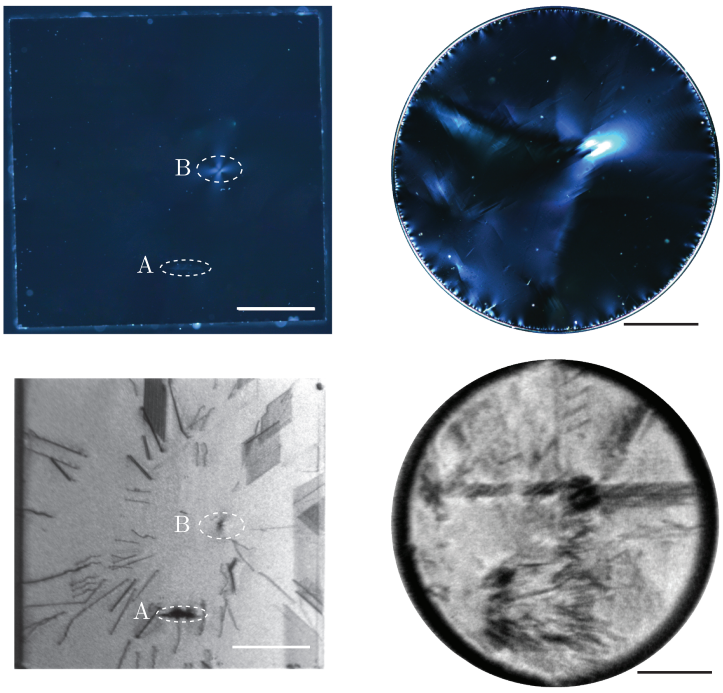

Figure 6-1 Top: Birefringence imaging, Bottom: 400 diffraction vector of XRT for (a) the NDT sample, and (b) the E6 sample. XRT of the 220 diffraction vector are omitted due to poor contrast. Scale bar = 1 mm.

cathodoluminescence (CL) visible imaging (figure 6-2b), whilst the E6 sample is less intuitive (figure 6-2c). Both samples are confirmed by Laue X-ray diffraction to be within a 2° cut of the (0 0 1) plane. Long lasting phosphorescence is seen from DiamondView™ in the {1 1 1} sectors, typical for the presence of nitrogen and boron.

6.2.3 Nitrogen and boron incorporation

EPR spectroscopy indicated that the average $[N_S^0]$ concentration in the NDT sample is 6.5 ± 1 ppb, whilst the E6 sample measured 34 ± 5 ppb. For both samples, NV^- could not be seen in in CW-EPR, and the positively charged substitutional nitrogen (N_S^+) was below the detection limit of IR spectroscopy. This result therefore implies that for certain growth sectors the substitutional boron concentration must be below that of substitutional nitrogen, where the charge balance is given by:

$$N_S^0 + B_S^0 \rightleftharpoons N_S^+ + B_S^-. \tag{6-1}$$

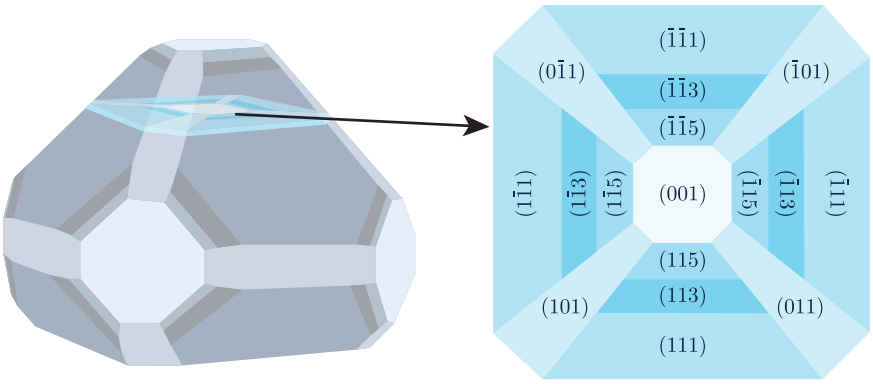

Figure 6-2 (a) A model of perfect cubo-octahedral growth via HPHT. The low temperature (77 K) SEM-CL visible images of (b) the NDT sample, and (c) the E6 sample. Growth sectors have been drawn next to the CL image for clarity. Scale bar = 200 µm.

	Growth sector [B_S] (ppb)				
	{0 0 1}	{0 1 1}	{1 1 5}	{1 1 3}	{1 1 1}
NDT	< 1	19 ± 3	2 ± 1	9 ± 2	84 ± 10
E6	< 1	†	†	8 ± 2	49 ± 9

Table 6-1 The mean substitutional boron concentration ([B_S]) in ppb per growth sector as determined by CL spectroscopy. † Value not obtained.

CL spectroscopic measurements at 77 K were taken on the SEM-CL system to evaluate the boron concentration according to equation (3-21b). Choosing this non-destructive method also resulted in being able to determine the boron concentration per growth sector, which is outlined in table 6-1. The boron bound exciton was detectable in both samples, in all growth sectors except {0 0 1}. Due to the E6 morphology, no {1 1 5} sectors are present and there is ambiguity in determining the {0 1 1} boron concentration and hence, these values are omitted.

6.3 Confocal imaging and microscopy

As the NDT sample is the primary research sample for this chapter, confocal images and spectral data will only be presented from this diamond within this section. Where applicable, data from the E6 material will be commented on with respect to the NDT diamond.

6.3.1 The decoration of growth sector boundaries

On imaging the central (0 0 1) growth sector of the NDT diamond no point defect emission could be seen when excited with both 488 nm and 532 nm lasers. Given the detection limit of the confocal microscope is on the order of 1 ppt, the lack of point defect emission implies there are essentially no (or fewer than 1 ppt) defects such as N_2V^0, NV^0, and NV^- within this growth sector. This was also true of the {0 0 1} growth sectors in the E6 material.

As the (0 0 1) sector of the NDT diamond is virtually central to the sample the

manual stage enabled a lateral translation of a known distance towards one of the edges. Images were taken at locations within the {1 1 5} and {1 1 3} growth sectors where, again, no point defect emission could be observed with either laser.

However, as the sample was translated towards the {1 1 1} growth sectors, it was possible to observe point defect emission. With the NV^- filter on the detection arm, a locally-high concentration of defects was seen with a linear structure. By translating the sample and following the structure it was clear that the incorporation of defects evolved throughout the material.

Figure 6-3 highlights one corner of the sample, with a comparison between the visible CL image and confocal PL imaging. At this corner, a confocal image of 300×300 µm contained {0 1 1}, {1 1 1}, {1 1 3}, and {1 1 5} growth sectors. Here it is clear to see that there is strong point defect emission at the interface between the {1 1 3} and {1 1 1} growth sectors. Furthermore, this decoration is not the same at each interface (figure 6-3). From the visible CL image, a small region of different contrast can be seen between the {1 1 3} and {1 1 1} growth sectors and directly correlates to the width of decoration seen in confocal PL imaging.

To confirm the interface of decoration, a 3D volume was sampled over 15 µm in depth to produce a series of XZ slices as shown in figure 6-4. By inspection, the lines of decoration between the growth sectors and [0 0 1] follows as 55° ± 5° and 30° ± 5°. By solving the dot product for angles made between crystallographic planes, these values agree with the angles made between {1 1 3} and {1 1 1}. Furthermore, the point defect incorporation in the {1 1 1} sectors can be used as a way to confirm the other sector interface as being {0 1 1} where angles 0° ± 5° and 19° ± 10° are observed.

In studying the E6 material, it was also noted that the {1 1 3}-{1 1 1} growth sector boundaries were also decorated by point defect emission, where taking a 3D volume confirmed the sectors.

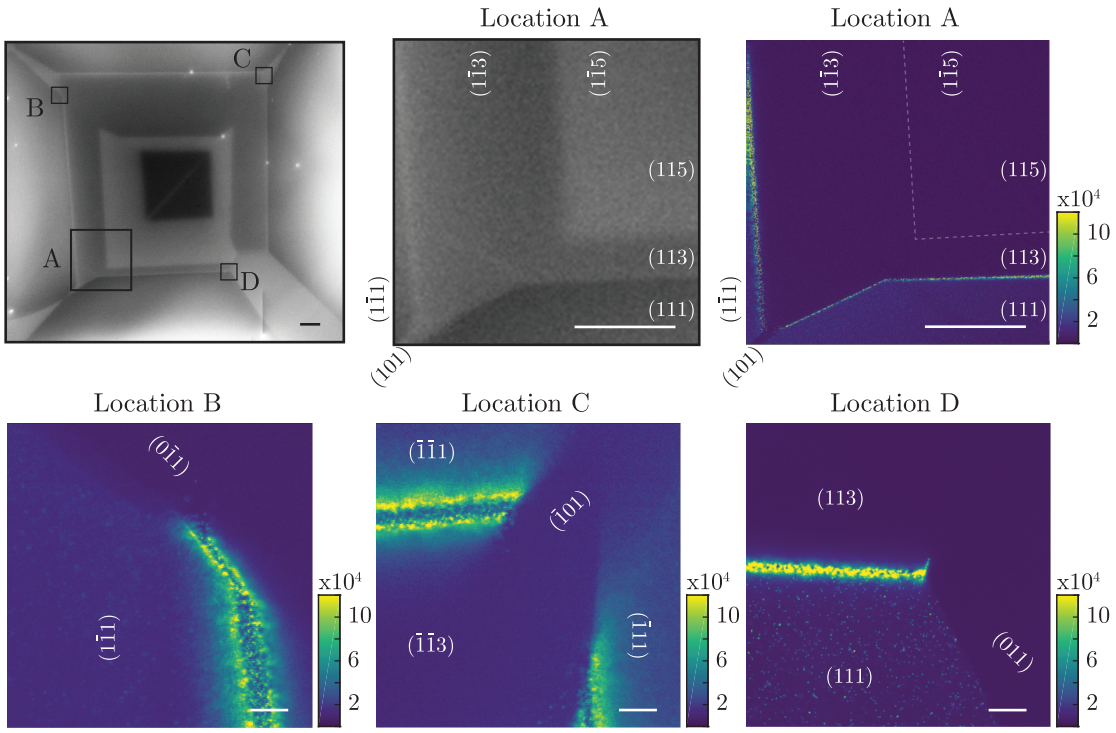

Figure 6-3 Top: Visible CL image compared to a 300 × 300 µm confocal image taken at a growth sector interface where decoration is only seen on the {1 1 3} to {1 1 1} transition. The dotted lines indicate the locations of the {1 1 5} to {1 1 3} transitions. Scale bar = 100 µm. Bottom: Defect incorporation at the positions marked in the visible CL image (top) for {1 1 1}, {0 1 1}, {1 1 3} intersections. Scale bar = 10 µm. Photoluminescence intensity scale bar represents the photon count rate per second (cps).

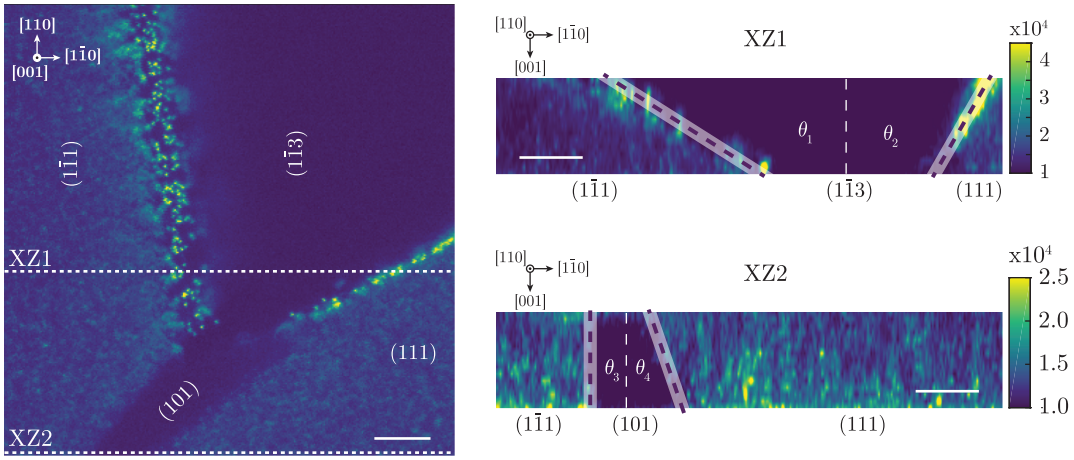

Figure 6-4 An example 80 × 80 µm XY confocal image, at location A, from a series of 15 taken at 1 µm depth separation to provide two XZ slices, XZ1 and XZ2, showing the interfaces between {1 1 3} and {1 1 1} and {0 1 1} and {1 1 1} respectively. Here four angle are determined as $\theta_1 = 55° \pm 5°$, $\theta_2 = 30° \pm 5°$, $\theta_3 = 0° \pm 5°$, and $\theta_4 = 19° \pm 10°$. Scale bar = 10 µm. Photoluminescence intensity scale bar represents the photon count rate per second (cps).

6.3.2 Identification and distribution of defects

Spectra were collected in a variety of locations across the NDT sample. Under 532 nm excitation, only three distinct emissions could be observed and were dependent on their location. At the {1 1 3}-{1 1 1} growth sector interface, only NV^- could be observed. In addition, NV^- could be seen in the {1 1 1} growth sector but at a very low concentration. On the other hand, within the {1 1 1} sectors, SiV^- and PL emission centred on 884 nm only were witnessed in higher concentrations. The PL at 884 nm is attributed to a nickel-related defect, and is often referred to in literature as the 1.40 eV defect or NIRIM-2 [17–19]. This defect is known to be of trigonal $\mathscr{C}_{3v}$ symmetry and paramagnetic (S = 1/2) [20, 21]. Research efforts have not yet conclusively identified the atomic constituents of the defect, and here it will be referred to as the 1.40 eV defect.

Repeating PL measurements for the E6 sample revealed NV^- at the {1 1 3}-{1 1 1} growth sector interface, and emission from both NV^- and SiV^- within the bulk {1 1 1} growth sectors. No evidence of the 1.40 eV defect was observed and will be discussed later.

Given the known defect PL emission, the spectral filters were employed to the imaging system to investigate the distribution of these defects (figure 6-5). Consequently it is seen that the incorporation of defects is indeed inhomogeneous. At the growth interface between {1 1 3} and {1 1 1}, the decoration only consisted of NV^-. Furthermore, it was confirmed only SiV^- and the 1.40 eV defect were seen in the bulk {1 1 1} growth sectors, as expected [18, 22], with very occasional NV^0 emission. On the other hand, it should also be noted that the filters do not completely discriminate against each defect, such that the SiV^- filter will also pass approximately 10% of the PL emission from the PSB of NV^- (c.f figure 4-7a).

Given the stated optical resolution of the confocal microscope, the number of defects within the diffraction-limited optical volume directly relates to their concentration (equation (3-36)). For the NV^- incorporation at the growth sector interfaces, the second-order autocorrelation measurement showed $g^{(2)}(0) < 0.5$ when the width of decoration is wider than 3 µm. For interfaces with a smaller width, $g^{(2)}(0)$

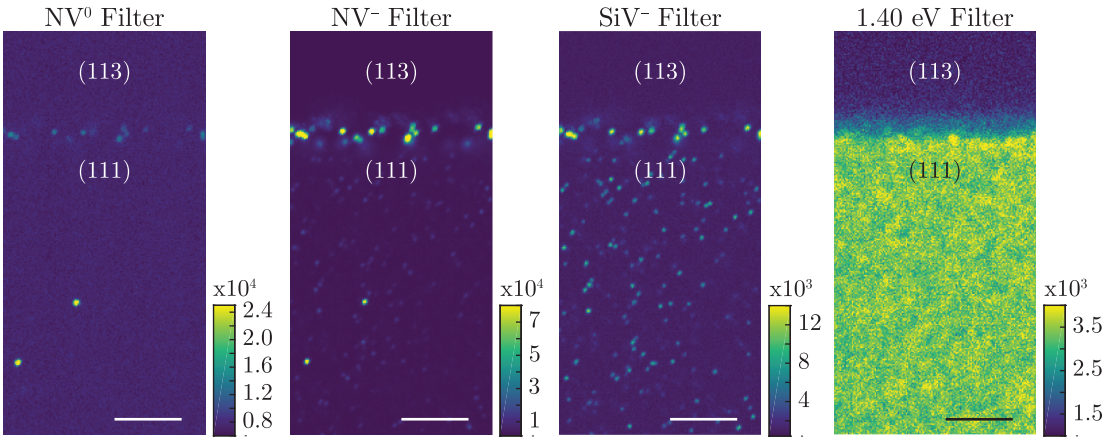

Figure 6-5 The distribution of defects as determined by spectral filtering in the NDT sample. A small amount of NV^0 signal is seen at the interface of {1 1 3} to {1 1 1} due to photoionisation, where as occasional NV^0 defects are incorporated into the {1 1 1} growth sectors. To excite the 1.40 eV defect with 532 nm, the excitation power was increased to 100 mW at the source (power = 5 mW at source for the rest). Scale bar = 5 µm. Photoluminescence intensity scale bar represents the photon count rate per second (cps).

was always above 0.5. Performing the $g^{(2)}(\tau)$ measurement on SiV^- defects in the {1 1 1} growth sectors gave an average $g^{(2)}(0)$ of 0.56 ± 0.1. Due to the poor excitation of the 1.40 eV defect, a measurement of $g^{(2)}(\tau)$ produced a flat line.

Hence by counting the defects within a typical confocal PL image, it is possible to put a lower limit on the concentration of defects, as summarised in table 6-2. Caution is advised since the distribution of defects will undoubtedly be inhomogeneous across the crystal. Defect counting has also been conducted over a very small volume, and so for these reasons the quoted numbers can only ever be the lowest limit.

Defect	Concentration (ppb)
NV^-	0.001
SiV^-	0.01
1.40 eV	> 0.1

Table 6-2 A lower limit on defect concentration by counting defects within a typical confocal PL image.

6.3.3 Orientation of incorporated defects

The orientation of defects incorporated into the diamond was studied in order to understand if any preferential alignment existed.

Shown in figure 6-6a is the interface of $(1\,\bar{1}\,3)$ to $(1\,\bar{1}\,1)$. Here 157 defects were classified based on their $g^{(2)}(\tau)$ minima where 78% of the defects were found to be single centres (figure 6-6b). Of this, 100 single NV^- centres were chosen for room temperature ODMR. A randomly orientated external magnetic field was applied to lift the ground state degeneracy of the $m_s = \pm 1$ state, and the location of the resonances recorded. As the NV^- can be aligned along any of the four $\langle 1\,1\,1 \rangle$ directions, by recording an equal probability distribution in the ODMR spectra, this revealed no preferential alignment (figure 6-6c).

It is not possible to conduct room temperature ODMR on neither SiV^- or 1.40 eV defects, and so the dependence of the PL intensity from the excitation polarisation provided further clues, as previously discussed in this thesis. Both defects are trigonal in symmetry, with the ZPL of the former being an optical transition between E $\leftrightarrow$ E states [23], and the latter arising from an A $\leftrightarrow$ E transition [21].

Here, the horizontal polarisation is defined as the electric field vector being parallel

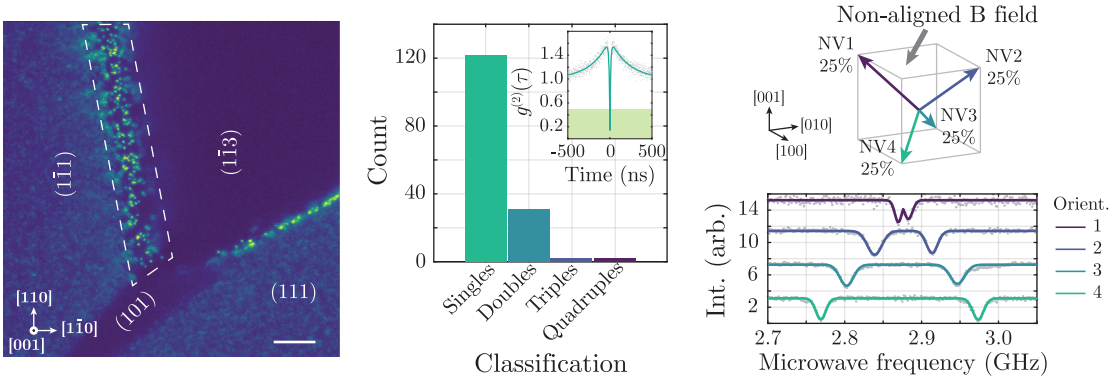

(a) **(b)** **(c)**

Figure 6-6 (a) Highlighted region where NV^- centres were investigated. Scale bar = 10 µm. (b) Classification of NV^- centres based on their value at $g^{(2)}(0)$, where the results of room temperature ODMR on 100 single NV^- centres are shown in (c) as identifying no preferential orientation by the equal probability of encountering all four possible alignments.

to $[1\,\bar{1}\,0]$, and vertical polarisation parallel to $[1\,1\,0]$. Using the appropriate filter, an image of SiV^- defects was taken across two $\{1\,1\,1\}$ growth sectors with both polarisation orientations. This same area was then imaged with the 1.40 eV filter in place, again for both laser polarisations. Subtracting the horizontal polarisation from the vertical revealed the difference in contrast for the defects. Here, an equal change in SiV^- is observed for both $\{1\,1\,1\}$ sectors, whilst the 1.40 eV defects show a uniform positive response in one sector verses a uniform negative response in the other, as shown in figure 6-7. Therefore, by the equal change in SiV^- contrast, there is no preferential alignment of this defect, whilst the 1.40 eV defect is preferentially orientated with respect to the $\langle 1\,1\,1\rangle$ growth direction.

The same investigation was conducted on the E6 diamond, where NV^- at the sector interface and in the bulk $\{1\,1\,1\}$ did not show any preferential orientation. Equally, the polarisation dependence on SiV^- also revealed these defects were not grown in preferentially orientated in any $\{1\,1\,1\}$ growth sector.

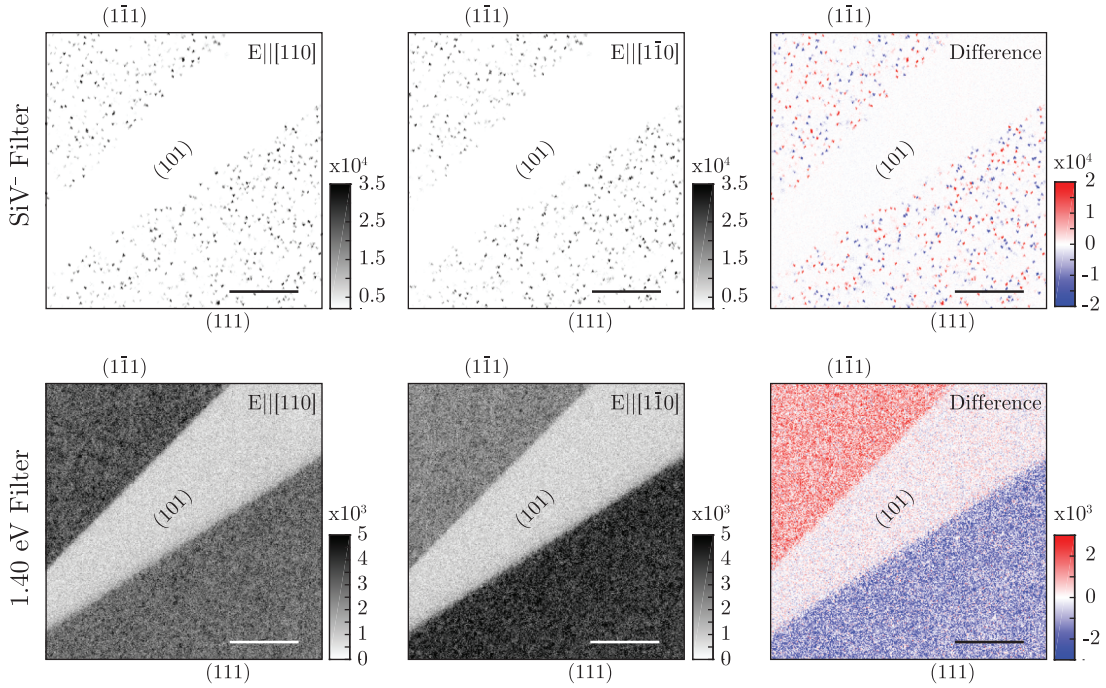

Figure 6-7 The polarisation dependence of both the SiV^- and 1.40 eV defects for a vertical (E ∥ $[1\,1\,0]$) and horizontal (E ∥ $[1\,\bar{1}\,0]$) polarisation of the 532 nm laser source. Maps are produced in greyscale for clarity. In subtracting horizontal from vertical, the nature of incorporation is revealed where SiV^- is not preferentially orientated whilst the 1.40 eV defect is. Scale bar = 10 µm. Photoluminescence intensity scale bar represents the photon count rate per second (cps).

6.4 Discussion

6.4.1 Growth sectors and the nitrogen and boron incorporation

During HPHT synthesis, the diamond crystal will consist of growth sectors that are grown in directions as defined by the normal of the crystal face involved. The final morphology is therefore governed by those faces which have low growth velocities since higher growth rate sectors will become extinct. It is well known that the incorporation of impurities, and in particular nitrogen and boron, varies between growth sectors and the actual uptake is influenced by the specifics of the growth conditions at each growth interface of the crystal [8]. The growth sector boundaries are internal surfaces to which the edges of neighbouring sectors pass during growth [24]. In addition, the local direction of that boundary depends upon the relative growth velocity of neighbouring faces. Hence, if the relative velocity between two faces is constant, the boundary is planar, and irregular if not.

HPHT diamond with fast growing {0 1 1} sectors often exhibit irregular surfaces with slower growing neighbouring {0 0 1} and {1 1 1} sectors [3]. These growth sector boundaries, and the surrounding regions, may be indistinguishable from the bulk growth sectors with regards to the defect and impurity incorporation. However this does not exclude the possibility of increased local impurity incorporation when growth layers on neighbouring faces meet.

Table 6-1 highlights that the boron concentration within the {0 0 1} sector of both samples is below 1 ppb. Equally, the variation in boron concentration is consistent with published literature [8, 25, 26], and in order of decreasing boron concentration follows:

$$\{1\,1\,1\} > \{0\,1\,1\} > \{1\,1\,3\} > \{1\,1\,5\} > \{0\,0\,1\} \tag{6-2}$$

These results, and the findings from Klepikov *et al* [25], suggest that the boron concentration for HPHT is lowest in the {0 0 1} growth sector, and significantly lower (> ×100) than the {1 1 1} growth sector.

The use of EPR to determine the concentration of N_S^0 is only valid for a homogeneous distribution throughout the entire volume of the diamond. Clearly then, it is difficult to speculate the relative nitrogen concentrations in the growth sectors, since this too will also be sector dependent. Furthermore, the measured N_S^0 concentration from EPR would be below the detection limit of SIMS.

With that said, it is reasonable to contemplate the relative incorporation based on what is known about the boron uptake. As the modified Kanda diagram outlines the growth sector dependence of nitrogen [8], to reach the sample average value of $[N_S^0]$ for the NDT material, and the area occupied by each growth sector, it is speculated that the N_S^0 concentration in the $\{0\,0\,1\}$ growth sector is almost 7x higher than the $\{1\,1\,1\}$ growth sector, as 46 ppb and 7 ppb respectively. This point will be discussed further in chapter 7.

Any further speculation is not necessary, other than to comment on the suitability of this material to the quantum market. This study has revealed that, at least in the $\{0\,0\,1\}$ growth sectors, the boron concentrations in HPHT diamond can be reduced to less than 1 ppb. Even if the N_S^0 concentration was as high as 100 ppb, the spin decoherence of any introduced point defects should still remain limited by the interaction with the local natural abundance ^{13}C environment. This should provide an alternative route to produce laser written NV^- centres, with attractive properties [27], in material with an extremely low concentration of extended defects. Lastly, if the N_S^0 impurity could be greatly reduced in the $\{0\,0\,1\}$ growth sector (< 1 ppb), then perhaps this material would outperform quantum grade CVD diamond in certain applications.

6.4.2 Significance of the NV decoration

As stated above, the growth sector boundary is dependent upon the relative growth velocities of neighbouring crystallographic faces. If the growth sector boundary is visible, and the growth direction of the adjacent faces can be identified, then it is possible to determine the relative growth rate [24]. For the region identified in figure 6-4, growth has proceeded in several different directions making analysis complicated. However, by assuming a linear growth rate in both $\langle 1\,1\,1\rangle$ and $\langle 1\,1\,3\rangle$

directions under HPHT synthesis at 1500 °C of 50 µm h^{-1}, the linear nature of decoration implies a stable growth rate over tens of minutes.

Taking a cross product of vectors normal to the intersecting planes results in a vector that is in the plane of the growth sector boundary, where the direction of travel is determined from the growth velocities of the adjacent planes. Understanding this allows the identification of the plane in which the growth sector boundary occupies. For location A of figure 6-3, where the diamond is viewed along [0 0 1], the boundaries between {1 1 3} - {1 1 1} and {1 $\bar{1}$ 3} - {1 $\bar{1}$ 1} growth sectors are independent of the relative growth velocities and are thus orientated along [1 $\bar{1}$ 0] and [1 1 0] directions respectively.

Figure 6-8 schematically shows two adjacent growth sector boundaries, where the relative growth rate velocity can be determined as [24]:

$$\frac{v_{h_1k_1l_1}}{v_{h_2k_2l_2}} = \frac{\cos(\beta_1)}{\cos(\beta_2)} \tag{6-3}$$

where $h_1k_1l_1$ and $h_2k_2l_2$ are the Miller indices of the crystallographic plane, and β_1 and β_2 are the angles made between the respective growth direction of the crystallographic plane and the growth sector boundary.

Therefore, from the angles presented in figures 6-3 and 6-4, the decorated interface

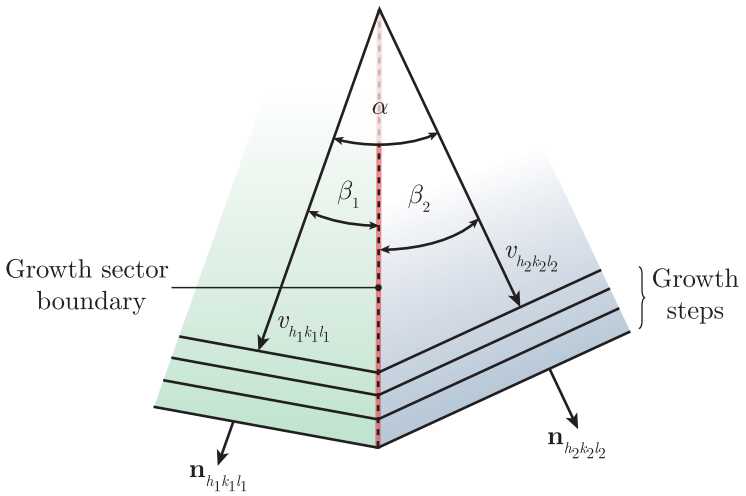

Figure 6-8 For two adjacent growth sectors with growth velocities $v_{h_1k_1l_1}$ and $v_{h_2k_2l_2}$, the growth directions $\mathbf{n}_{h_1k_1l_1}$ and $\mathbf{n}_{h_2k_2l_2}$ are separated by an angle α. Additionally, the angle between the growth direction and growth sector boundary (denoted by the dashed line) is given by β_1 and β_2 respectively, where $\beta_1 + \beta_2 = \alpha$. Figure adapted from [24].

between $\{1\,\bar{1}\,3\}$ - $\{1\,1\,1\}$ results in $v_{(1\bar{1}3)}/v_{(1\,1\,1)} \approx 1.13$. The angle between this decorated interface and $[0\,0\,1]$ suggests that $v_{(1\bar{1}3)}/v_{(1\bar{1}1)} \approx 0.87$ and $v_{(1\bar{1}3)}/v_{(1\,1\,1)} \approx 1.14$, with the latter value in good agreement with the observation. Additionally, whilst the interfaces made with $(1\,0\,1)$ are not decorated, the sector dependent defect incorporation allows for an estimation where $v_{(1\,0\,1)}/v_{(1\bar{1}1)} \approx 1.2$ and $v_{(1\,0\,1)}/v_{(1\,1\,1)} \approx 0.94$. However for the latter, the uncertainty is very large.

There is no knowledge of where the NDT plate was cut relative to the rough crystal, or the final morphology. Hence, further analysis on the growth sector decoration relative to the growth is not possible, as the sampled volume only represents a very small temporal window of synthesis.

Finally, the very nature of only the $\{1\,1\,3\}$ to $\{1\,1\,1\}$ growth sector boundaries being decorated with NV^- defects should not be overlooked. This growth sector boundary is very clearly visible in the CL images as a small region of higher emission relative to the two growth sectors. The confocal maps also correlate the width of the CL transition with the width of NV^- decoration. Table 6-3 outlines the minimum change in angle that can occur between two neighbouring growth sectors. Therefore, it could be possible that it is not energetically favourable for the crystal to grow with a direct transition from $\{1\,1\,3\}$ to $\{1\,1\,1\}$, and must hence do so via small steps with higher order crystallographic planes. Consequently, these steps could lead to the increased incorporation of nitrogen, and thus the NV^- defects at the growth sector boundary. On the other hand, kinetic and impurity absorption effects will likely have a role to play in the growth sector transition, and will require further work to determine why only $\{1\,1\,3\}$ - $\{1\,1\,1\}$ interfaces are decorated with NV^-, when $\{1\,1\,1\}$ - $\{0\,1\,1\}$ shows a larger minimum angle change.

Growth sector boundary			
$\{1\,1\,1\}$ - $\{1\,1\,3\}$	$\{1\,1\,1\}$ - $\{0\,1\,1\}$	$\{1\,1\,3\}$ - $\{1\,1\,5\}$	$\{1\,1\,5\}$ - $\{0\,0\,1\}$
29.5°	35.3°	9.4°	15.8°

Table 6-3 The minimum angle change between two neighbouring growth sectors.

6.4.3 The lack of NV preferential orientation

For both CVD and HPHT synthesis of diamond, preferential orientation of grown-in defects has been observed [28–31], and the surface kinetics, and chemistry, required to produce preferential orientation has been theoretically investigated [32]. Specifically, for $NV^{0/-}$ defects, preferential orientation has been observed for CVD growth on $\langle 0\,1\,1\rangle$, $\langle 1\,1\,3\rangle$ and $\langle 1\,1\,1\rangle$ orientated substrates [28, 33, 34]. The destruction of preferential alignment has also been shown possible by high temperature annealing [35].

Here, there are two plausible hypotheses as to the lack of preferential orientation of the NV^- defects:

1. NV^- did not grow in as a unit but formed by the migration of vacancies to substitutional nitrogen to produce all four possible alignments.

2. Preferential orientation did occur during growth, but was removed due to the HPHT growth temperature which was high enough to enable a reorientation of the defect, without completely annealing out the defect.

Clearly, by the virtue of synthesis, the diamond will have spent time at elevated temperatures within the growth capsule. A typical temperature range for solvent/catalyst HPHT synthesis is 1350 - 1600 °C [26].

By utilising first-order chemical kinetics, it is possible to estimate the degree to which a defect may undergo reorientation. With an activation energy, E_A = 4.0 eV and an attempt frequency $\nu = 10^{11}$ s^{-1} for NV [36], no appreciable preferential orientation remains after only a few minutes at 1350 °C, and after seconds at 1500 °C. Thus, it is likely that any initial preferential orientation of NV^- would have reorientated back to equilibrium populations during the time the sample was held at elevated temperatures, even if this sample came from material grown towards the end of the growth run. Using the activation energy and attempt frequency published by Pinto *et al* [37], NV^- would reorientate in under 1 minute at 1500 °C.

Therefore, the lack of preferential orientation of NV^- is consistent with our under-

standing of thermal reorientation. There is, however, one report of preferentially aligned NV^- defects produced in {1 1 1} growth sectors in an as-grown HPHT diamond [23], which is directly in disagreement with this conclusion.

Finally, the NV defect will undergo reorientation locally before undergoing dissociation and migration. The migration of NV is well understood, where the annealing out of NV produces the di-nitrogen vacancy defect, N_2V, presumably produced by the reaction:

$$NV + N_S \rightarrow N_2V \tag{6-4}$$

N_2V^0 gives rise to the H3 absorption and emission ZPL at 503 nm [36, 38], and N_2V^- produces the H2 ZPL at 982 nm with a characteristic EPR spectrum [39]. As no H3 emission could be seen in either sample under 488 nm excitation, this suggests an upper limit on the synthesis temperature at 1500 °C, since this is the approximate temperature at which H3 can be produced [36].

6.4.4 Preferential orientation of SiV^- and the 1.40 eV defect

The absence of preferential alignment for SiV^- is unexpected. From first principle calculations and experimental observations in CVD diamond, SiV^- is expected to grow in as a unit and therefore preferentially orientated [23, 29, 40]. Little is known about the reorientation mechanics of SiV^-, however even at temperatures as high as 1900 °C, the fluorescence intensity of SiV^- does not significantly reduce [41]. Furthermore, with a 2000 °C annealed CVD diamond, preferential orientation of SiV^0 persisted [29]. With this, it is expected that the activation energy for reorientation is very high and thus could imply silicon is incorporated as a substitutional impurity, where a mobile vacancy is then caught from a random direction.

Whilst the SiV^- centres studied in both HPHT samples do not exhibit preferential orientation, there has been one previous report where a [1 1 1] orientation was missing in the HPHT diamond studied [23]. Consequently, further studies are warranted on the incorporation mechanism of SiV^- in to {1 1 1} growth sectors from HPHT synthesis.

It has been previously reported that the 1.40 eV defect does grow in to {1 1 1}

growth sectors preferentially orientated [35, 42]. From the polarisation study, the sector-dependent contrast follows an approximate 3:1 intensity ratio contrast. This result is expected for a 100% preferential alignment of the symmetry axis of a trigonal defect aligned along the growth direction where the optical transition is between A and E states.

Whilst both samples were synthesised in a Co-Fe-C melt, the observation of the 1.40 eV defect in the NDT sample is perhaps a little surprising and indicates the growth system contained a source of nickel contamination. As the detection limit of the confocal system is very low, it is highlighted that even at a concentration of 0.1 ppb there would be approximately 20 defects in the confocal excitation volume. Therefore, if nickel is readily incorporated into the diamond matrix, then the contamination could be at trace amounts.

6.5 Conclusions

Two HPHT grown diamonds from different manufacturers were studied. Bulk characterisation show them both to be type IIa. The NDT grown sample exhibits very low strain and dislocation densities. Furthermore, the uptake of nitrogen and boron, whilst shown to be sector dependent, is relatively low. By confocal PL imaging and spectroscopy, three species of point defects were identified: NV^-, SiV^- and a nickel related defect with emission centred on 884 nm (here termed the 1.40 eV defect).

Confocal PL imaging revealed the growth sector boundaries between {1 1 3} and {1 1 1} are always decorated by NV^- defects. Consequently this can allow for a determination of the relative growth rates for neighbouring {1 1 3} and {1 1 1} growth sectors. Preferential orientation of NV^- and SiV^- was not seen in either HPHT diamond, whilst the 1.40 eV defect was observed to always be parallel to the growth direction, in agreement with published literature. It is thought that NV^- will rapidly reorientate at the HPHT growth temperature, and so preferential alignment of this defect is not expected. However, a further understanding on the incorporation of SiV^- is required as it is not clear from published annealing studies

to why no preferential orientation is seen here, if the defect grew in as a unit.

Evidently, the high crystalline quality of HPHT diamond coupled with the high purity and low point defect incorporation, reflects the recent strides made in HPHT synthesis methods. The following chapters therefore investigate the distribution of nitrogen and the suitability of the material for quantum processing.

References

1. J. Achard et al., *Diamond and Related Materials* **16**, 685–689 (2007).
2. Y. N. Palyanov et al., *Crystal Growth & Design* **10**, 3169–3175 (2010).
3. R. C. Burns et al., *Journal of Physics: Condensed Matter* **21**, 364224 (2009).
4. U. F. D'Haenens-Johansson et al., *Gems & Gemology* **51**, 260–279 (2015).
5. Y. N. Palyanov et al., *CrystEngComm* **17**, 4928–4936 (2015).
6. Y. N. Palyanov et al., in *Handbook of Crystal Growth* (Elsevier, 2015), pp. 671–713.
7. M.-L. T. Rooney, *Journal of Crystal Growth* **116**, 15–21 (1992).
8. R. Burns et al., *Journal of Crystal Growth* **104**, 257–279 (1990).
9. H. Sumiya, K. Harano, K. Tamasaku, *Diamond and Related Materials* **58**, 221–225 (2015).
10. S. Stoupin et al., *Journal of Synchrotron Radiation* **23**, 1118–1123 (2016).
11. A. Tallaire et al., *Diamond and Related Materials* **77**, 146–152 (2017).
12. B. Deljanin et al., *Contributions to Gemology* **15**, 1–7 (2015).
13. M. W. Doherty et al., *Physics Reports* **528**, 1–45 (2013).
14. I. Aharonovich et al., *Reports on Progress in Physics* **74**, 076501 (2011).
15. M. Markham et al., *Diamond and Related Materials* **20**, 134–139 (2011).
16. T. Ardon, S. Eaton-Magaña, *Gems and Gemology* **54**, 217–218 (2018).
17. A. M. Zaitsev, *Optical Properties of Diamond* (Springer Berlin Heidelberg, Berlin, Heidelberg, 2001).
18. A. T. Collins, H. Kanda, R. C. Burns, *Philosophical Magazine Part B* **61**, 797–810 (1990).
19. J. P. Goss et al., *Journal of Physics: Condensed Matter* **16**, 4567–4578 (2004).
20. J. Isoya, H. Kanda, Y. Uchida, *Physical Review B* **42**, 9843–9852 (1990).
21. M. H. Nazaré, A. J. Neves, G. Davies, *Physical Review B* **43**, 14196–14205 (1991).
22. P. Johnson, E. Myagkaya, *HPHT Synthetic Diamond with Intense Green Color*, 2017.
23. L. J. Rogers et al., *Physical Review B* **89**, 235101 (2014).

24. H. Klapper, in *Springer Handbook of Crystal Growth* (Springer Berlin Heidelberg, Berlin, Heidelberg, 2010), pp. 93–132.
25. I. V. Klepikov, A. V. Koliadin, E. A. Vasilev, *IOP Conference Series: Materials Science and Engineering* **286**, 012035 (2017).
26. R. Burns et al., *Diamond and Related Materials* **8**, 1433–1437 (1999).
27. C. J. Stephen et al., *arXiv:1807.03643*, 2–9 (2018).
28. A. M. Edmonds et al., *Physical Review B* **86**, 035201 (2012).
29. U. F. S. D'Haenens-Johansson et al., *Physical Review B* **84**, 245208 (2011).
30. A. T. Collins, *Journal of Physics: Condensed Matter* **1**, 439–450 (1999).
31. K. Iakoubovskii, *Physical Review B* **70**, 205211 (2004).
32. T. Miyazaki et al., *Applied Physics Letters* **105**, arXiv: 1409.2573 (2014).
33. J. Michl et al., *Applied Physics Letters* **104**, 102407 (2014).
34. M. Lesik et al., *Diamond and Related Materials* **56**, 47–53 (2015).
35. K. Iakoubovskii, A. T. Collins, *Journal of Physics: Condensed Matter* **16**, 6897–6906 (2004).
36. M. W. Dale, PhD thesis, University of Warwick, 2015.
37. H. Pinto et al., *physica status solidi (a)* **209**, 1765–1768 (2012).
38. A. T. Collins, *Journal of Physics C: Solid State Physics* **13**, 2641–2650 (1980).
39. B. L. Green et al., *Physical Review B* **92**, 165204 (2015).
40. Y. Guo, Y. Feng, L. Zhang, *Diamond and Related Materials* **61**, 91–96 (2016).
41. A. Zaitsev, K. Moe, W. Wang, *Diamond and Related Materials* **71**, 38–52 (2017).
42. A. R. Lang, G. M. Meaden, *Journal of Crystal Growth* **108**, 53–62 (1991).

7

Defect assay following electron irradiation of HPHT diamond

This looks like the end of the story; but it isn't.

- *The Tale of Squirrel Nutkin*, Beatrix Potter

7.1 Motivation

The irradiation of diamond by high energy particles causes the displacement of carbon atoms from their lattice site. In doing so, interstitial defects with nearby vacancy sites are formed - as discussed in chapter 2.

It has long been established that electron irradiation of type IIa diamond produces a strong absorption, and PL emission, with a ZPL at 741.1 nm (1.673 eV) and is attributed to the neutral vacancy, V^0 [1]. This arises from an optical transition between ^1E and $^1T_2$ states, with a further, yet weaker, optical absorption at 750.1 nm (1.653 eV) [2, 3]. The negatively charged vacancy (V^-) is also known to yield an absorption (and PL) ZPL at 393.6 nm (3.150 eV) [4]. Through the quantification of vacancy concentrations, an inference of the damage rate can be gained. However, literature has shown that this damage rate can vary depending upon impurities and defects within the diamond [5, 6].

The migration energy of the vacancy is understood by previous annealing studies. From isothermal annealing experiments, this migration energy is determined as 2.3 eV and has also been reported that a small concentration of V^0 is lost when the

self-interstitial becomes mobile at about 400 °C [7]. At 800 °C, the vacancy becomes highly mobile and caught by nearby traps - typically substitutional nitrogen or nitrogen aggregated defects such as the A centre (N_S-N_S) or the B centre (4 N_S surrounding a vacancy). Thus, it is at this temperature that NV centres are found to most strongly anneal in for diamond containing substitutional nitrogen [8].

Whilst the vacancy is just one type of defect, irradiation damage can produce many other defects [9]. Of these, the simpliest is the $\langle 0\,0\,1\rangle$-split self-interstitial ($C_{I_{001}}$), sometimes referred to in literature as the R2 defect. This particular defect is $\mathscr{D}_{2d}$ in symmetry [6, 10] and is associated with optical transitions at 735.8 nm (1.685 eV) and 666.9 nm (1.859 eV) where the latter is thought to be a forbidden transition by state mixing with the former [11, 12]. The production rate of this defect is said to increase when the temperature of the sample during irradiation is held below 100 K [13], and is reported to migrate at a temperature above 700 K [6], with activation energy of 1.6 eV [14], later updated by Breeze to be 2.0 eV [15]

In addition, other noteworthy irradiation related defects are the TR12 and 3H defects. The naming convention for 3H is unfortunate, since it has a ZPL at 503.5 nm (2.463 eV) [16], whereas N_2V^0 gives rise to a ZPL at 503.2 nm (2.464 eV) which is historically known as the H3 defect. TR12 comprises of several strong lines, where the ZPL is located at 470.2 nm (2.637 eV) and associated LVM at 508.8 nm (2.437 eV) [11, 17].

In both cases, there has been no definitive conclusion with regards to the constituents of 3H and TR12. It is suggested that the 3H configuration is the di-$\langle 0\,0\,1\rangle$-split self interstitial / Humble defect [13, 18], and TR12 is from a complex involving the self interstitial [17, 19]. Interestingly, TR12 was generated on carbon ion implantation and was shown to be a stable single photon source [20]. The annealing behaviour of both systems are different, where 3H is annealed out after a 400 °C anneal [16], whilst TR12 begins to anneal out after 800 °C [11]. Equally, both behave in the opposite fashion when excited with blue light as 3H exhibits photobleaching and TR12 shows an increase in intensity [21].

In the previous chapter, it was shown that more information about the synthesis of high purity HPHT diamond can be gained by considering the inclusion of point

defects at low concentrations. Particularly, the quality of this material could lend itself to incorporation into emerging quantum applications of diamond.

This chapter therefore builds upon the previous chapter and considers an assay of defects following an electron irradiation and targeted annealing temperatures. In particular, there is a motivation to understand the growth sector dependence of the nitrogen incorporation. Since the nitrogen concentration, as determined by EPR, falls below the detection limit of SIMS, it is necessary to alter the point defect incorporation. Here this will be done by performing electron irradiation to generate vacancies and then targeted annealing to produce additional defects. Thus, by seeking the creation of NV defects, it will be possible to infer the relative nitrogen concentrations within the different growth sectors. Hence, the same HPHT diamonds from chapter 6 (NDT and E6) are the focus of this study.

7.2 Material characterisation

7.2.1 Electron irradiation and annealing

Both samples were electron irradiated at an energy of 4.5 MeV for a total time of 30 minutes. The samples were placed in direct contact with a water cooled table, in an ambient atmosphere. From the Monte Carlo simulations, 4.5 MeV electrons should have a penetration depth greater than the thickness of either diamond sample, resulting in a uniform vacancy generation [22]. After irradiation, the samples were cleaned only with acetone, and then deionised water, to provide clean surfaces for characterisation and to avoid any further heating.

Once the initial characterisation across the various techniques were completed in the "as irradiated" state, both samples were acid cleaned in preparation for the first of two annealing stages. It is known that at 400 °C, carbon interstitials become mobile [8], and so this temperature is a suitable annealing temperature to target. The diamond was placed into an alumina boat, and placed into the centre of the furnace heated to 400 °C. The sample was removed after four hours, and acid cleaned to remove any graphitic conversion which may have occurred. The suite of

characterisation techniques were then repeated on both samples.

At 800 °C, the vacancies become mobile [8], and hence is a suitable temperature target for annealing. Again, the diamond was acid cleaned in preparation for the final annealing stage. The diamond was then placed into an alumina boat, buried in sacrificial diamond grit, and positioned into the centre of the furnace heated to 800 °C. The sample was removed after four hours, and acid cleaned to remove any graphitic conversion which may have occurred. Repeated characterisation measurements were conducted for a final time.

7.2.2 Quantitative EPR

As irradiated

To avoid any thermal defect migration and charge state dynamics, RP-EPR was conducted in the as-irradiated state without being heat treated or UV illuminated. Here then, measurements on the NDT sample indicated N_S^0 was below the detection limit of the system (<1 ppb), as no signal could be gained after 1000 scans. However, for the E6 sample, a signal from N_S^0 could be detected and was determined to be 15.2 ± 2 ppb. In both samples, it is possible to observe a signal from the negatively charged vacancy, V^-, however it is not possible to accurately quantify V^- during rapid-passage measurements.

400 °C anneal

Similar to the as-irradiated state, RP-EPR measurements were done following the anneal (and acid clean) without subjecting to UV illumination first, to avoid driving charge. Thus, it was possible to detect a very weak signal in the NDT sample where $[N_S^0] = 1.5 \pm 0.5$ ppb. Equally, the E6 sample also exhibited a weak signal where $[N_S^0] = 2.5 \pm 0.5$ ppb. Again in both cases, a signal from V^- could be detected but not quantified.

800 °C anneal

RP-EPR remained a challenge for the NDT sample with a very weak N_S^0 signal being detected. A fit of the signal revealed $[N_S^0] = 1 \pm 1$ ppb. For the E6 sample, a fit of the data resulted in $[N_S^0] = 15.9 \pm 2$ ppb. The signal from V^- was again present in both RP-EPR scans, however the intensity was reduced as is expected from the trapping and loss of vacancies.

7.2.3 UV-Vis absorption

As irradiated

Shown in figure 7-1 is the UV-Vis absorption at 77 K where a strong, sharp V^0 absorption ZPL is seen for both samples. The concentration of V^0 (equation (4-3)) in the NDT and E6 samples was determined as 423 ± 20 ppb and 408 ± 18 ppb respectively. It was not possible to observe the ZPL relating to V^-. Both sets of UV-Vis absorption spectra also reveal peaks at 310.6 nm, 429.4 nm, and 666.8 nm, with these being stronger in the NDT sample. Here it is noted that the presence of the peak at 666.8 nm relates to a significant concentration of $C_{I_{001}}$ defects. Using the correlation factor listed by Newton *et al* [23], along with the integrated intensity of the 666.8 nm peak, the concentration of $C_{I_{001}}$ was given as 401 ± 40 ppb and 391 ± 45 ppb in the NDT and E6 material respectively.

400 °C anneal

The V^0 concentration was recalculated by a UV-Vis absorption measurement at 77 K, where this was determined to be 369 ± 18 ppb and 378 ± 17 ppb in the NDT and E6 samples respectively. This corresponds to a loss of 10% ± 3% from the 400 °C anneal, and is in line with the data presented by Davies *et al* [7]. Since the UV-Vis absorption measurement does not discriminate against the growth sectors, it is unclear whether the relative concentration change in V^0 is homogeneous across the diamond. A small absorption at 503.5 nm was present in both samples, indicating the presence of 3H. Peaks at 310.6 nm, 429.4 nm and 666.8 nm remained

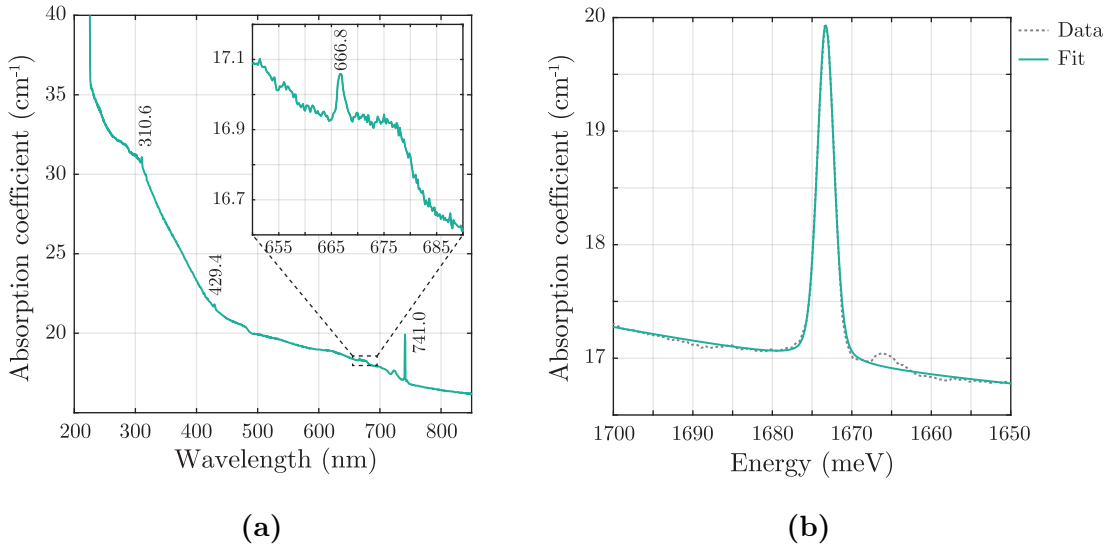

Figure 7-1 (a) The UV-Vis absorption spectra at 77 K in the as-irradiated state for the NDT sample. Four main peaks are present at 310.6 nm, 429.4 nm, 666.8 nm ($C_{I_{001}}$, inset) and V^0 at 741.0 nm. (b) Fit of V^0 ZPL to calculate the concentration.

after the 400 °C anneal. Here the intensity of 666.8 nm had reduced, such that the concentration of $C_{I_{001}}$ was now seen to be 252 ± 50 ppb in the NDT sample and 328 ± 35 ppb in the E6 sample.

800 °C anneal

The presence of V^0 could still be obtained in the UV-Vis absorption measurements, although significantly reduced. The concentration of the defect was now found to be 104 ± 10 ppb and 101 ± 10 ppb for the NDT and E6 sample respectively, representing a 75% ± 3% loss in vacancy concentration from the original value. On this annealing step, 310.6 nm, 503.5 nm, and 666.8 nm peaks were no longer visible in the spectra. The peak at 429.4 nm had reduced in intensity, and a new peak at 362.0 nm could be seen in both samples. It was not possible to observe any absorption due to $NV^{0/-}$.

7.2.4 FTIR absorption spectroscopy

Owing to the thickness of the E6 sample (0.25 mm), significant etaloning was present in all FTIR spectra. In performing a FFT to remove the frequency, too much of the signal was removed and hence not possible to investigate through FTIR. Hence only the NDT sample could be investigated with FTIR. For the NDT sample in the as grown state, the uncompensated B_S^0 concentration was previously found to be 10 ± 2 ppb by fitting the electronic transition at 2802 cm^{-1}.

As irradiated

By placing the NDT sample on to a 0.5 mm aperture within the FTIR spectrometer, an approximate position of the {1 1 1} and {0 0 1} growth sectors could be measured. In doing so, the spectra for revealed no features other than the characteristic intrinsic type IIa absorption.

400 °C anneal

Employing the same aperturing process as before, the FTIR absorption spectra predominately resembled the same intrinsic IIa absorption. On closer inspection, the NDT sample exhibits two very weak peaks at 2848 cm^{-1} and 2917 cm^{-1}.

800 °C anneal

Again, in FTIR spectroscopy, only the intrinsic IIa absorption spectrum could be seen. The weak peaks that were present in the 400 °C anneal of the NDT sample were no longer observed at this annealing stage.

7.2.5 Room temperature widefield PL mapping

As irradiated

Room temperature PL spectroscopy was conducted on the Horiba Raman microscope with 660 nm excitation to map the V^0 spatial variation. This revealed a growth sector dependence on the PL intensity, as shown in figure 7-2. No signficant broadening was observed in the width of the V^0 ZPL, and the position was located at 742.2 ± 0.1 nm. Consequently it can be seen that the PL intensity of V^0 decreases depending on the following growth sector ordering:

$$\{0\,1\,1\} \geq \{1\,1\,5\} > \{1\,1\,3\} > \{1\,1\,1\} > \{0\,0\,1\}.$$

With 488 nm excitation, no further PL features could be identified in any of the

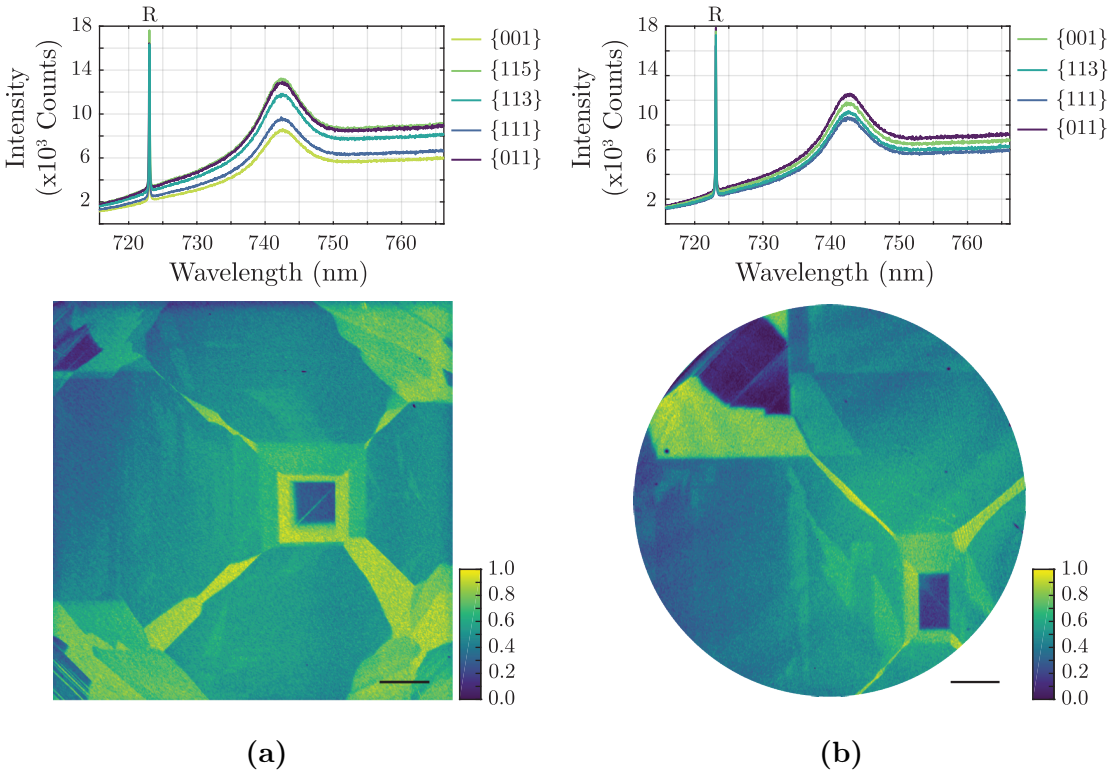

Figure 7-2 Top: representative V^0 spectra for each growth sector at room temperature in the as-irradiated state, using 660 nm excitation. Bottom: the integrated intensity of V^0 over the whole sample for (a) NDT and (b) E6 HPHT material respectively. NB: PL intensity is normalised to the maximum value in the series. Scale bar = 0.5 mm. Photoluminescence intensity scale bar represents the normalised photon count rate per second.

growth sectors of either material.

400 °C anneal

The variation in V^0 was mapped again on the Horiba PL system with the 660 nm excitation source, under the same acquisition parameters as previous. Whilst the growth sector dependence followed the same as before for the PL intensity of V^0, a slight increase in the integrated ZPL area was observed. Table 7-1 shows the average ratio for the integrated area of the V^0 ZPL against the first order Raman signal. Thus, the V^0 signal increased slightly at this stage, and could be attributed to some charge transfer following heat treatment and subsequent absorption measurements before PL.

Stage	{0 0 1}	{0 1 1}	{1 1 5}	{1 1 3}	{1 1 1}
As irradiated	4.3 ± 0.2	6.8 ± 0.2	6.9 ± 0.3	6.1 ± 0.2	5.0 ± 0.03
400 °C	7.5 ± 0.3	10.5 ± 0.4	12.4 ± 0.5	11.3 ± 0.3	6.5 ± 0.3

Table 7-1 Variation in the average ratio of V^0/Raman integrated areas for all growth sectors in the as electron irradiated state, and after the 400 °C anneal in the NDT sample. The increase in V^0 intensity in the latter stage may be due to charge dynamics.

Furthermore, both samples were investigated with the 488 nm excitation source with regards to PL from NV^0. In both samples, no discernible PL signal from NV^0 could be detected in any sector. However, there was a strong ZPL emission at 504.1 nm, which is attributed to the 3H defect as mentioned in section 7.1. Whilst 3H is known to be at 503.5 nm at low temperature, as was seen in the UV-Vis absorption measurement, the line broadens slightly with temperature such that the PL maxima is slightly redshifted[a]. From mapping the distribution of 3H across all growth sectors (figure 7-3), it can be seen that this defect also has a growth sector dependence where the PL intensity decreases in the following order:

$$\{0\,1\,1\} > \{1\,1\,1\} > \{1\,1\,5\} > \{1\,1\,3\} \geq \{0\,0\,1\}.$$

[a]This was tested on a different electron irradiated and annealed diamond sample within the research group, where at 77 K 3H is shown with a ZPL at 503.5 nm, and at room temperature at 504.1 nm.

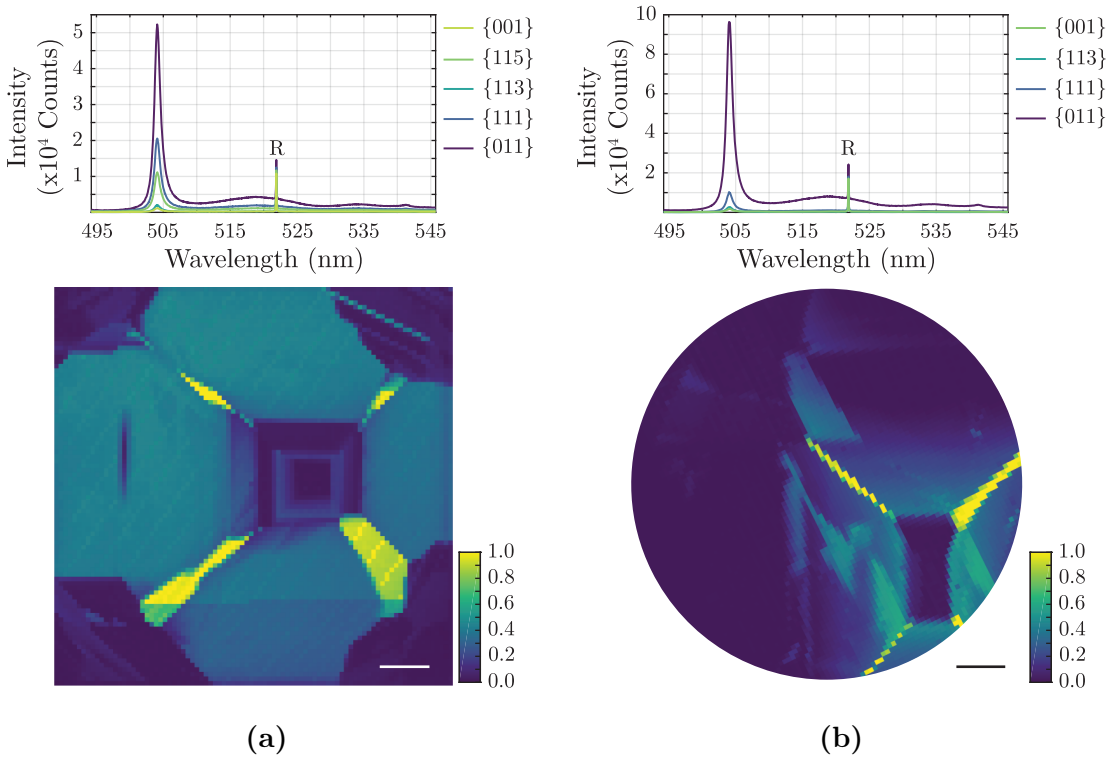

Figure 7-3 Top: representative 3H spectra for each growth sector at room temperature (using 488 nm excitation) for the 400 °C annealing stage. Bottom: the integrated intensity of 3H over the whole sample for (a) NDT and (b) E6 HPHT material respectively. NB: PL intensity is normalised to the maximum value in the series. Scale bar = 0.5 mm. Photoluminescence intensity scale bar represents the normalised photon count rate per second.

In addition to the 3H ZPL observed, a further strong peak was seen at 553.1 nm. From the plotted integrated intensity of this peak, the sector dependence follows that of the 3H ZPL, where emission of the peak is strongest in the {0 1 1} growth sectors and weakest in both {1 1 3} and {0 0 1} growth sectors. Walker shows that in the first recorded PL spectrum of 3H, there are strong features associated with the defect, where a strong luminescence peak is observed close to 220 meV from the ZPL [11]. Furthermore, Steeds and Kohn investigate the local vibrational mode (LVM) structure of 3H at low temperature, and also find a strong peak at 552.4 nm [24], 218 meV from the 3H ZPL. As the 553.1 nm peak measured here is located at 218 meV from the 3H ZPL, and that it follows the same growth sector dependence, it is likely this feature is a LVM to 3H.

800 °C anneal

From the 800 °C anneal, the PL intensity of V^0 greatly decreased. It is still clear to see where {0 0 1}, {0 1 1}, and {1 1 5} growth sectors are, however the distinction between {1 1 1} and {1 1 3} is now not as distinct as it once was. In the former case, the average V^0/Raman ratio is 0.7 ± 0.3, 1.8 ± 0.2, and 1.5 ± 0.2 respectively, and for the latter the ratio is 1.5 ± 0.3. Thus, the V^0 concentration has greatly reduced in the {0 0 1} growth sector compared to the 400 °C anneal stage.

The intensity of 3H has changed from annealing, and it is still clear to see the growth sector dependence. Table 7-2 shows the integrated intensity of the 3H ZPL against the first order Raman line at the 400 °C and 800 °C annealing stages. Thus in {0 1 1},{1 1 5} and {1 1 1} growth sectors, 3H has decreased in intensity relative to the Raman intensity. Conversely, in the {0 0 1} and {1 1 3} growth sectors, the relative intensity of 3H had increased significantly. This increase and decrease behaviour of the 3H ZPL intensity was also evident in the E6 material.

Stage	{0 0 1}	{0 1 1}	{1 1 5}	{1 1 3}	{1 1 1}
400 °C	2.2 ± 0.3	82.8 ± 0.5	17.1 ± 0.5	2.5 ± 0.3	37.8 ± 0.4
800 °C	27.2 ± 0.6	6.8 ± 0.3	3.1 ± 0.2	17.5 ± 0.4	17.8 ± 0.5

Table 7-2 Variation in the average ratio of 3H/Raman integrated areas for all growth sectors in the two annealing stages for the NDT sample. The same trend was also observed in the E6 sample.

As expected, this annealing temperature has created a significant concentration of NV defects. Owing to the ionising nature of the 488 nm excitation, only the ZPL relating to NV^0 was mapped as can be seen in figure 7-4. Clearly the {0 0 1} sectors contain the highest concentration of NV, where the detector has saturated in the {0 0 1} growth sector of the E6 sample. Shown in the inset spectra to figure 7-4a, the NV^0 ZPL can be seen in both {0 1 1} and {1 1 5} growth sectors. However, as the second order Raman lines can be seen (denoted 2R in the figure), this implies the concentration is very low within these sectors. Clearly then, the generation of NV^0 at this annealing temperature follows as

$$\{0\,0\,1\} > \{1\,1\,1\} > \{1\,1\,3\} > \{0\,1\,1\} > \{1\,1\,5\}.$$

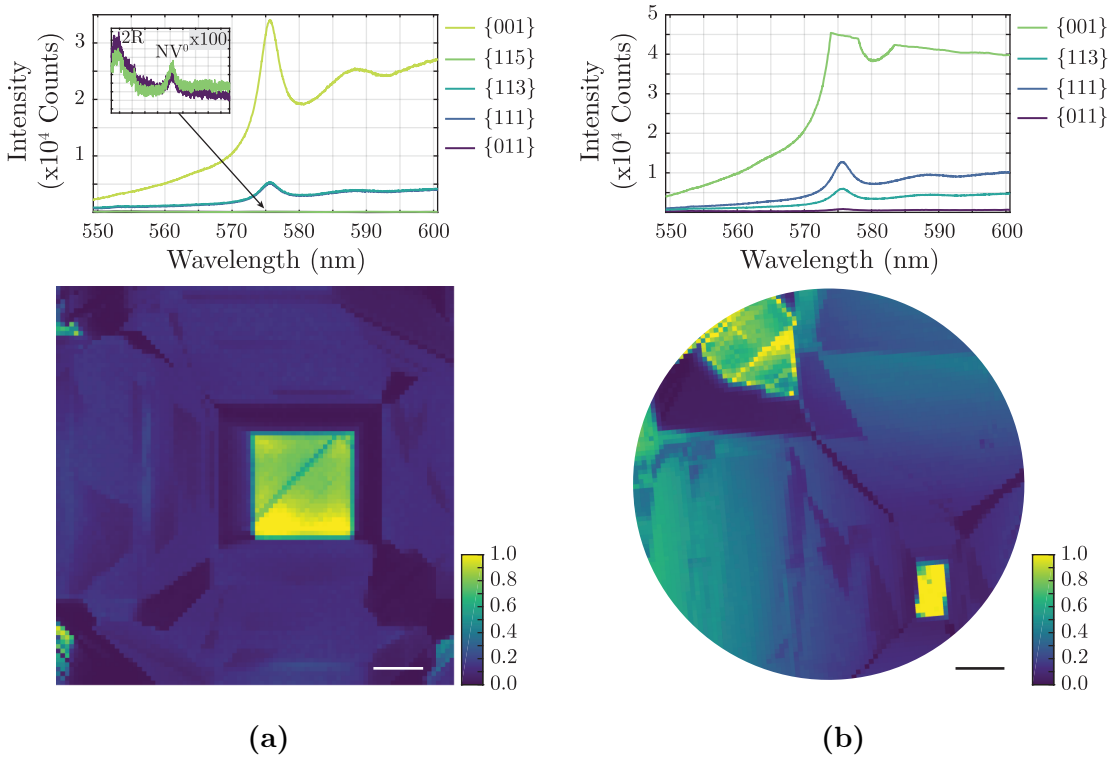

Figure 7-4 Top: representative NV^0 spectra for each growth sector taken on the Horiba PL system with 488 nm excitation at room temperature at the 800 °C annealing stage. Bottom: the integrated intensity of NV^0 over the whole sample for (a) NDT and (b) E6 HPHT material respectively. Inset spectra to (a) is a close up of NV^0 of {0 1 1} and {1 1 5} growth sectors where the second order Raman (2R) can be seen. NB: PL intensity is normalised to the maximum value in the series. Scale bar = 0.5 mm. Photoluminescence intensity scale bar represents the normalised photon count rate per second.

7.2.6 DiamondView™ imaging

As irradiated

Subsequent DiamondView™ fluorescence imaging revealed extremely weak green fluorescence in both samples, with no detection of phosphorescence. From the weak fluorescence it was not possible to resolve the different growth sectors. The lack of phosphorescence is consistent with the fact that the donor-acceptor recombination mechanism is now compensated.

400 °C anneal

Following the 400 °C anneal stage, the fluorescence image from DiamondView™ showed a stronger green fluorescence where growth sectors in both samples could be readily identified. It should be noted that DiamondView™ imaging in this instance was carried out after the SEM-CL spectroscopy. In this instance, it was possible to see regions of higher fluorescence which correlated to the locations investigated during SEM. In the {0 0 1} growth sector, some of the SEM-induced regions show red fluorescence as shown in figure 7-5c. The origin of this fluorescence resulted from NV^- centres, as will be shown in section 7.2.8. Once more, both samples did not exhibit any phosphorescence.

800 °C anneal

Following this annealing step, it was clear to see in DiamondView™ fluorescence imaging bright orange sectors with the most intense being the {0 0 1} growth sector of both samples (figure 7-6). It is perhaps interesting to note the {0 0 1} as the brightest sector in relation to the nitrogen growth sector order provided by the modified Kanda diagram, and will be discussed later. Finally, both samples remained

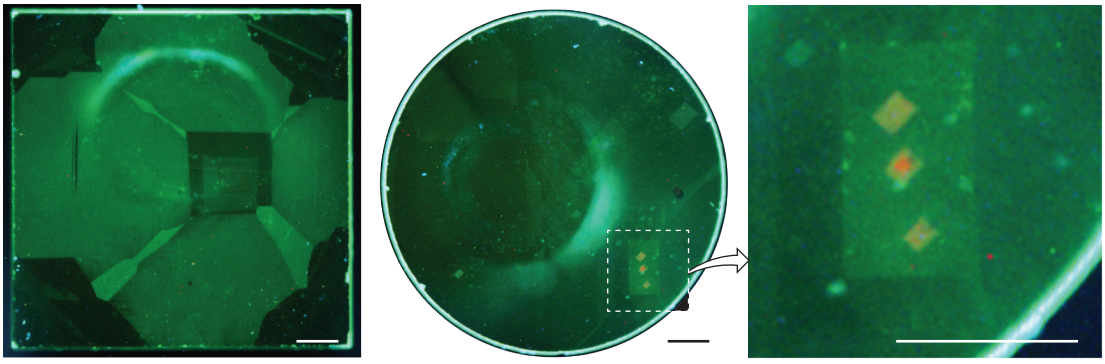

(a) **(b)** **(c)**

Figure 7-5 DiamondView™ fluorescence images for the NDT sample (a), and E6 sample (b), where (c) is a close up of the {0 0 1} growth sector of the E6 sample. In this, it is possible to see regions of higher fluorescence, in some instances red rather than green, following CL spectroscopy. These regions were later confirmed to contain a higher density of NV defects than the surrounding material. NB: the image brightness has been enhanced to aid the reader. Scale bar = 0.5 mm

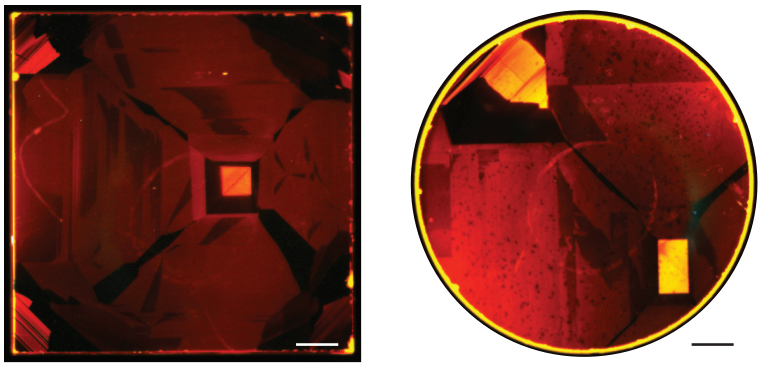

(a) (b)

Figure 7-6 DiamondView^{TM} fluorescence images for the NDT sample (a), and E6 sample (b). The brightest sector is {0 0 1} in both samples, where the colour of fluorescence agrees with a sufficient concentration of NV defects. NB: the image brightness has been enhanced to aid the reader. Scale bar = 0.5 mm

devoid of any phosphorescence, indicating the donor and acceptor recombination was still non-existent.

7.2.7 CL spectroscopy

As irradiated

CL spectroscopy was conducted to re-evaluate the substitutional boron concentration, [B_S]. Here, the growth sector dependence is once again seen, and follows the same distribution as given in the previous chapter for both samples. Furthermore, there appeared to be no significant change in [B_S] across all the growth sectors for the NDT sample, where the maximum concentration is measured in the {1 1 1} growth sectors as 80 ± 10 ppb. Conversely, in the E6 material, only the {1 1 1} growth sector appears to have a reduced value at 33 ± 9 ppb (c.f. 49 ± 9 ppb previously). It should be noted that the spatial homogeneity of the boron distribution is not accurately known in both samples within each growth sector, and hence the change in boron concentration of the E6 {1 1 1} growth sector may be a consequence of this.

400 °C anneal

Repeated measurements were taken by SEM-CL spectroscopy at 77 K, where $[B_S]$ once again obeys the same growth sector dependence. However, the maximum value of the NDT {1 1 1} growth sectors appeared to decrease by approximately 40%, such that $[B_S]_{max} = 48 \pm 10$ ppb, whilst the other growth sectors in this material did not change outside the limits of experimental error. On the other hand, the maximum boron concentration was not seen to significantly decrease in the {1 1 1} growth sectors of the E6 sample compared to the value obtained in the as irradiated state.

800 °C anneal

A final set of SEM-CL spectroscopy measurements were carried out, again at 77 K. For the NDT material, $[B_S]$ did not alter in the {1 1 5} growth sectors, however a reduction was seen for the remaining growth sectors. Here, the maximum boron concentration remained in the {1 1 1} growth sectors at 22 ± 6 ppb, a reduction of 54% from the 400 °C anneal stage. The concentration of boron in the {0 1 1} and {1 1 3} growth sectors had also decreased by 60% and 38% respectively.

The E6 sample also exhibited a decrease in the boron concentration for all growth sectors. Whilst it was not possible to obtain a suitable spectrum in the {1 1 3} growth sectors at this time, the {1 1 1} growth sector had reduced to 15 ± 6 ppb and {0 1 1} growth sector reduced to 6 ± 3 ppb, representing a reduction of 53% and 57% reduction in boron concentration respectively from the 400 °C anneal stage.

From the summary of boron concentration shown in table 7-3, this then indicates that the boron concentration is influenced by annealing following electron irradiation, where theses changes will be discussed in the next section.

Sample	Stage	Growth sector [B_S] (ppb) {0 0 1}	{0 1 1}	{1 1 5}	{1 1 3}	{1 1 1}
NDT	As received	< 1	19 ± 3	2 ± 1	9 ± 2	84 ± 10
	As irradiated	< 1	14 ± 5	3 ± 2	8 ± 2	80 ± 10
	400 °C	< 1	15 ± 3	3 ± 2	8 ± 2	48 ± 10
	800 °C	< 1	6 ± 3	2 ± 1	5 ± 3	22 ± 6
E6	As received	< 1	†	†	8 ± 2	49 ± 9
	As irradiated	< 1	15 ± 4	†	6 ± 2	33 ± 9
	400 °C	< 1	14 ± 2	†	4 ± 2	32 ± 5
	800 °C	< 1	6 ± 3	†	†	15 ± 6

Table 7-3 The mean substitutional boron concentration ([B_S]) in ppb per growth sector as determined by CL spectroscopy for each stage of the sample history. † Value not obtained.

7.2.8 Room temperature confocal imaging

As irradiated

With prior knowledge of the defect generation from PL mapping on the Horiba Raman microscope, confocal microscopy was employed to understand if other defects had been generated in a lower concentration.

Since the emission of V^0 was very strong in both samples, this acted as a guide to know which sector was being imaged. However, due to the intense nature of this emission, a 715 nm shortpass filter (Semrock FF01-715/SP-25) was employed to reject fluorescence. Consequently, it became possible to resolve individual centres throughout both diamond samples.

Shown in figure 7-7 is an exemplar image taken of the {1 1 3} to {1 1 1} growth sector decoration, as observed in chapter 6 (c.f. figure 6-3, Location A). On inspection, it is clear to see that individual centres can now be resolved in the {1 1 3} growth sector, whilst no resolvable centers can be seen in either the {1 1 5} or {0 1 1} growth sectors.

Spectroscopy showed the resolvable emission was due to NV^0 within {1 1 1} and {1 1 3} growth sectors, and at the interface between them (figure 7-7c). Again, due

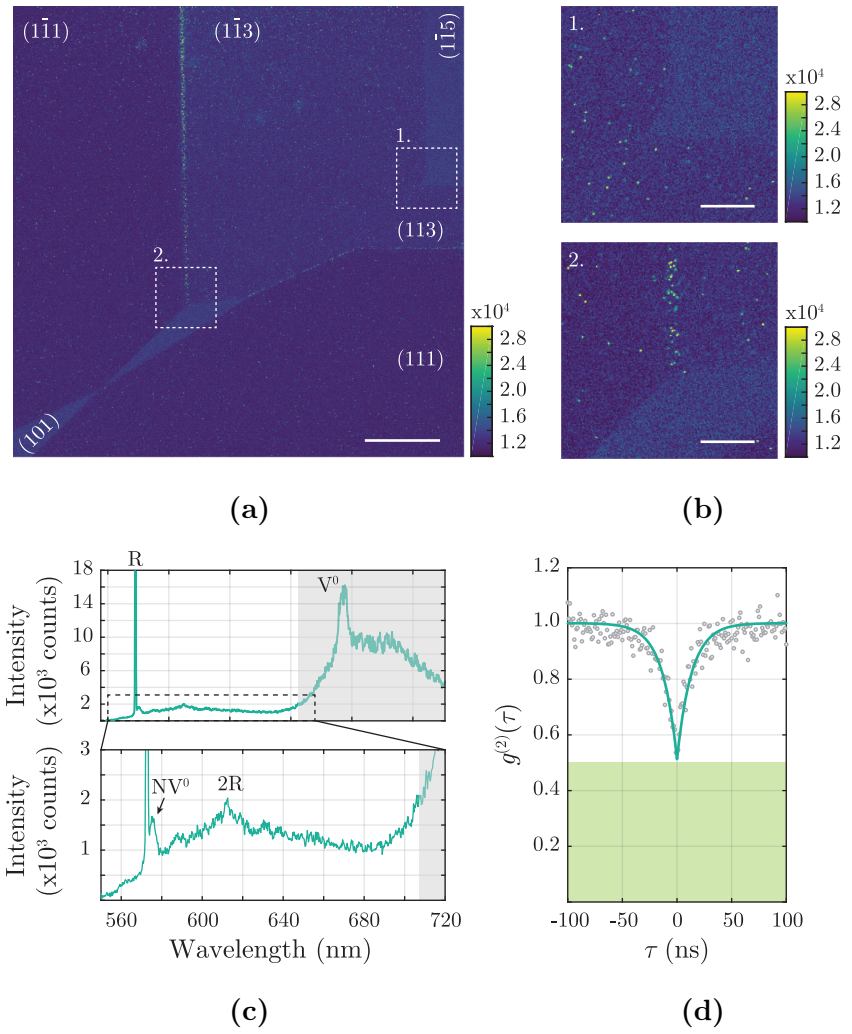

Figure 7-7 (a) A 300 × 300 µm room temperature confocal image in the as-irradiated state. A 715 nm shortpass filter was employed on detection to eliminate signal from V^0. Growth sector labelling as per the previous chapter. Scale bar = 50 µm. (b) Closer views of locations 1 and 2 showing localised and resolvable NV^0 centres in {1 1 1}, and {1 1 3} growth sectors. Scale bar = 10 µm. (c) Example spectrum of a resolvable feature from (1 1 3), where the ZPL relating to NV^0 can be seen. Note that the grey box highlights the spectral region rejected by the 715 nm shortpass filter. (d) Example second-order autocorrelation measurement from the {1 1 3} growth sector, with $g^{(2)}(0) = 0.51 \pm 0.1$ and fluorescence lifetime of 13.9 ± 1 ns. Photoluminescence intensity scale bar represents the photon count rate per second (cps).

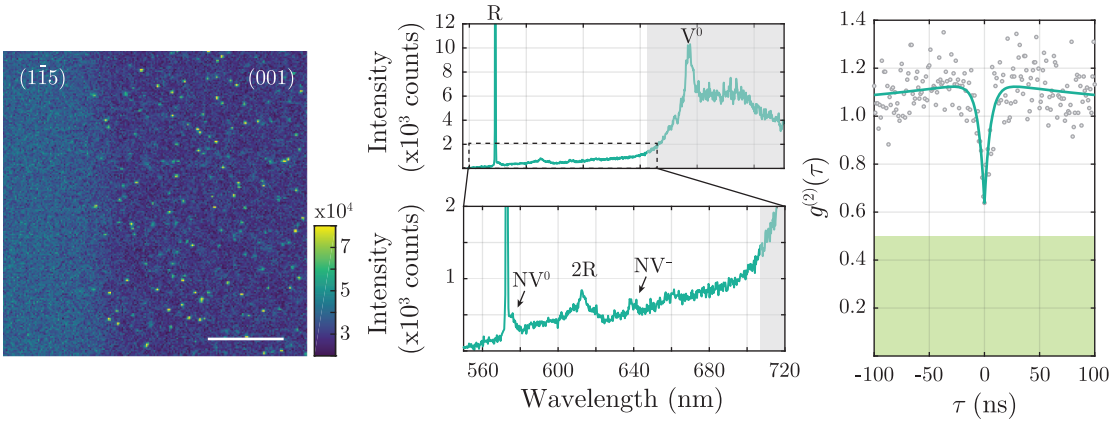

(a) **(b)** **(c)**

Figure 7-8 (a) A 40 × 40 µm room temperature confocal image with a 715 nm shortpass filter employed on detection to eliminate signal from V^0, where it is possible to see localised and resolvable defects. Growth sector labelling as per the previous chapter. Scale bar = 10 µm. (b) Example spectrum of a resolvable feature from (0 0 1), where it is possible to see ZPLs relating to NV^0 and NV^-. Note that the grey box highlights the spectral region rejected by the 715 nm shortpass filter. (c) Example second-order autocorrelation measurement from the {0 0 1} growth sector, with $g^{(2)}(0) = 0.64 \pm 0.1$ and fluorescence lifetime of 6 ± 1 ns. Photoluminescence intensity scale bar represents the photon count rate per second (cps).

to the intense nature of V^0, it was not possible to confirm the presence of SiV^-, or the 1.40 eV nickel defect. Second order autocorrelation ($g^{(2)}(\tau)$) measurements demonstrated the majority of centres to contain at least two emitters, with an average fluorescence lifetime of 16 ± 3 ns (figure 7-7d).

The sample was then translated to look at the {0 0 1} growth sector. Here, the density of resolvable defects was slightly higher than was seen in the {1 1 1} and {1 1 3} growth sectors. However, it was possible to resolve localised centres, as shown in figure 7-8a. Spectroscopic measurements revealed both NV^0 and NV^- could be detected, and the $g^{(2)}(\tau)$ measurement showed the majority of the centres to be two emitters, although the resultant data required fitting with the three level function due to the NV^- contribution (figures 7-8b and 7-8c).

By counting the number of resolvable NV^0 centres in figures 7-7 and 7-8, the concentration of NV^0 is on the order of 1 ppt in the {1 1 1}, {1 1 3}, and {0 0 1} growth sectors combined.

400 °C anneal

The same procedure was followed for confocal imaging with the use of the 715 nm shortpass to reject emission from V^0.

Here, NV^0 centres could once more be seen in the {1 1 1}, {1 1 3}, and {0 0 1} growth sectors for both samples. The relative concentration of these defects did not appear to increase substantially as the defects could still be spatially resolved. The minima of the $g^{(2)}(\tau)$ measurement did not drop below 0.55 ± 0.1 in all centres measured in any growth sector, indicating most spatially resolved centres comprised of two or more emitters, with the characteristic fluorescence lifetime of NV^0 in the {1 1 1} and {1 1 3} growth sectors and NV^- in the {0 0 1} growth sector.

Furthermore, it was now possible to spatially resolve centres in the {0 1 1} and {1 1 5} growth sectors. Here, the density of resolvable centres in the {0 1 1} growth sector is slightly higher than that of the {1 1 5} (figures 7-9a and 7-9b). In addition, the photostability of centres in both these growth sectors were poor, and as a result no spectral information or $g^{(2)}(\tau)$ measurement with an adequate signal to noise ratio could be obtained. Therefore it is presumed these defects are NV^0, based on the 715 nm shortpass filter employed.

Whilst Semrock specify the 715 nm shortpass filter to have 0% transmission at 711 nm, the leading edge to the V^0 ZPL appears to begin at approximately 680 nm at room temperature (figure 7-9c). Hence a higher background was seen in the confocal images at this stage, which is commensurate with a higher fluorescence intensity of V^0 by an increased leading edge intensity, and in agreement with the earlier widefield PL maps taken.

For this annealing stage, SEM-CL spectroscopy was conducted prior to confocal imaging with an electron accelerating voltage of 15 kV, and probe current of 150 nA. It is noted that in the E6 sample, from the DiamondView™ image, that there are regions of higher fluorescence intensity which correlate to the regions of interest from SEM-CL (figure 7-5c). With the 715 nm shortpass filter still in place, these regions were picked up during confocal microscopy, and were especially bright in the {0 0 1} growth sector as shown in figure 7-10a.

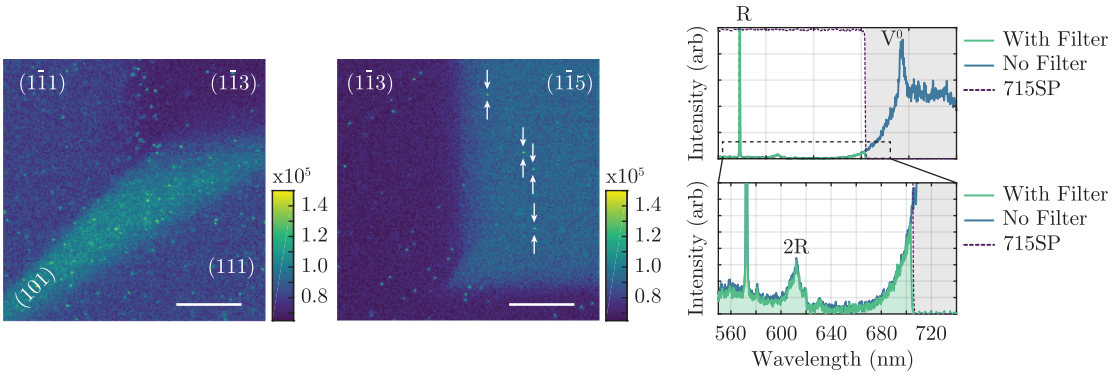

(a) **(b)** **(c)**

Figure 7-9 A 40 × 40 µm example of (a) the {0 1 1} and (b) the {1 1 5} growth sectors after the 400 °C anneal. Note centres in the {1 1 5} region are highlighted for clarity. Scale bar = 10 µm. (c) Example spectrum from the {0 1 1} growth sector showing the leading edge of V^0 is captured with the 715 nm shortpass filter (715SP). Photoluminescence intensity scale bar represents the photon count rate per second (cps).

Spectroscopic measurements in this region revealed emission from NV^0 and NV^-, as well as the V^0 background (figure 7-10b). By taking a depth profile across one of the bright regions, it is clear to see that the strong fluorescence is contained within 2.8 ± 0.5 µm of the surface of the diamond as seen in figures 7-10c and 7-10d. No resolvable centres could be seen within this region at the surface, whilst it was possible to pick up a higher fluorescence background up to 6 µm below the surface.

800 °C anneal

As evident from both the widefield PL mapping and DiamondView™ imaging, the intensity of NV^0 and NV^- emission in both plates was very high, and no spatially resolved centres could be found in the growth sectors of {0 0 1}, {1 1 3} or {1 1 1}. On the other hand, it was still possible to spatially resolve centres in both the {0 1 1} (figure 7-11a) and {1 1 5} growth sectors. However, the photostability of centres in the {0 1 1} growth sector was better than that of the {1 1 5} growth sector. Once more, spectroscopic measurements of these centres revealed NV^0, and the $g^{(2)}(\tau)$ measurement shows more than two centres per spot with a fluorescence lifetime typical of NV^0 at 16 ± 3 ns [25–27]. The relative density of centres is comparable between both sectors.

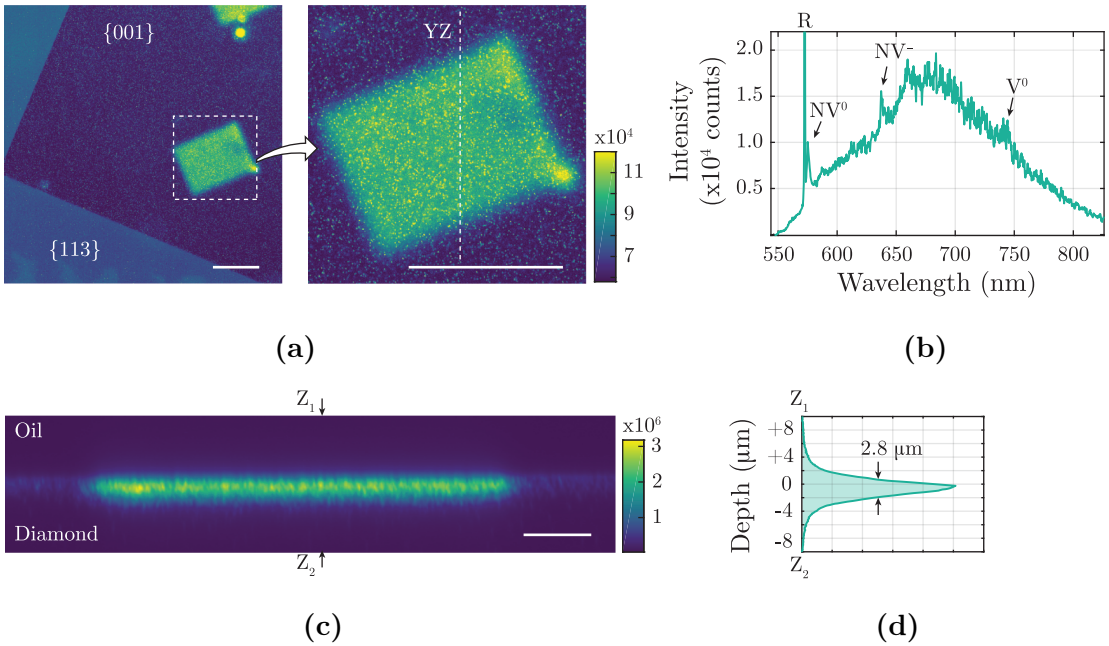

Figure 7-10 (a) {0 0 1} growth sector of the E6 sample showing a region of higher fluorescence intensity approximately 4 µm below the surface as caused by the SEM. Scale bar = 50 µm. (b) Spectroscopy of the region shows significant emission from NV^0 and NV^- with the ZPL of V^0 just visible. (c) Depth scan of the region showing fluorescence is localised to the surface of the diamond. Scale bar = 10 µm. (d) Profile of emission where the FWHM is 2.8 ± 0.5 µm. Photoluminescence intensity scale bar represents the photon count rate per second (cps).

Since the NV^- emission is bright within the {1 1 1} growth sectors, it was not possible to confocally image any emission from SiV^- in both samples or the 1.40 eV defect in the NDT sample. Thus, the fate of these defects remain unknown.

7.3 Discussion

7.3.1 Nitrogen and boron concentration changes

7.3.1.1 Nitrogen

From the original RP-EPR measurements, the sample average of N_S^0 was known for both samples in their as-grown states as 6.5 ± 1 ppb and 34 ± 5 ppb in the NDT and E6 material respectively. A very simplistic assumption can be applied from

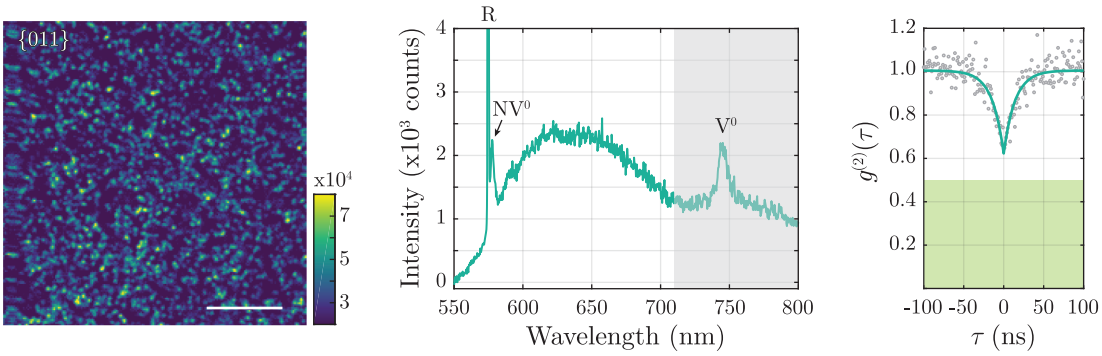

Figure 7-11 (a) 20 × 20 µm room temperature confocal image of the {0 1 1} growth sector with the 715 nm shortpass filter. Scale bar = 5 µm. (b) Example spectrum of one spatially resolved feature showing NV^0 and V^0 ZPLs. (c) Second-order autocorrelation measurement of one feature with the 715 nm filter in place, where $g^{(2)}(0) = 0.62 \pm 0.1$ with a fluorescence lifetime of 15.8 ± 1.7 ns. Photoluminescence intensity scale bar represents the photon count rate per second (cps).

the experimental results of Burns *et al* [28], where the ratio of nitrogen was found to be 100:50:10:1 for growth sector ordering {1 1 1} > {0 0 1} > {1 1 3} > {0 1 1} in type Ib synthetic HPHT diamond. If one assumes the area occupied by the growth sectors in SEM-CL imaging constitutes a uniform volume throughout the sample, and N_S^0 can be compensated by B_S^0, then table 7-4 outlines the approximate starting $[N_S^0]$ in each sector to yield the sample average EPR number. Consequently, it is perhaps fortuitous that the starting nitrogen content is similar for both samples, and hence the main difference in the measured EPR concentration is only due to the different starting boron concentration.

If one entertains the nitrogen growth sector dependence remains constant upon electron irradiation and annealing to 800 °C, then at the final stage this would constitute a reduction of $[N_S^0]$ to 23 ± 1 ppb and 32 ± 1 ppb in the NDT and E6 {1 1 1} growth sectors respectively. This model is included in table 7-5. However, this relationship is likely to break down due to interstitial formation and migration between the various steps [29, 30], as well as competing effects of charge balance.

In a nitrogen assay of neutron irradiated Ib diamond, Dale [8] deduced that the interstitial migration mechanism becomes important for nitrogen, where at approximately 400 °C, the single nitrogen interstitial (N_I) would form before

Sample	Sector	Area occupied	$[B_S]$ (ppb)	Estimation $[N_S^0]$ (ppb)	$[N_S^0] - [B_S]$ (ppb)	EPR (ppb)
NDT	{0 1 1}	0.04	19	0.91	-18.09	0
	{1 1 3}	0.24	9	9.15	0.15	0.04
	{0 0 1}	0.03	0	45.75	45.75	1.37
	{1 1 1}	0.69	84	91.5	7.50	5.18
					Total:	**6.6**
E6	{0 1 1}	0.01	15	0.87	-14.14	0
	{1 1 3}	0.09	8	8.65	0.65	0.06
	{0 0 1}	0.05	0	43.25	43.25	2.16
	{1 1 1}	0.85	49	86.5	37.5	31.88
					Total:	**34**

Table 7-4 An estimation on the starting $[N_S^0]$ using the relationship seen experimentally by Burns *et al* [28]. The EPR column is then the growth sector area multiplied by the uncompensated N_S^0 contribution, where the total is given to two significant figures.

Sample	Sector	Area occupied	$[B_S]$ (ppb)	Estimation $[N_S^0]$ (ppb)	$[N_S^0] - [B_S]$ (ppb)	EPR (ppb)
NDT	{0 1 1}	0.04	6	0.23	-5.77	0
	{1 1 3}	0.24	5	2.3	-2.7	0
	{0 0 1}	0.03	0	11.5	11.5	0.35
	{1 1 1}	0.69	22	23	1	0.69
					Total:	**1.0**
E6	{0 1 1}	0.01	6	0.32	-5.68	0
	{1 1 3}	0.09	2†	3.2	1.2	0.11
	{0 0 1}	0.05	0	16	16	0.80
	{1 1 1}	0.85	15	32	17	14.45
					Total:	**15**

Table 7-5 An estimation of the final $[N_S^0]$ following the 800 °C anneal, assuming the relationship by Burns *et al* [28] still holds true. The EPR column is then the growth sector area multiplied by the uncompensated N_S^0 contribution, where the total is given to two significant figures. † = estimated concentration as value not obtained.

annealing out at approximately 800 °C, at which temperature the di-nitrogen-interstitial (N_{2I}) would then be created. Hence the determination of $[N_S^0]$ becomes non-trivial as soon as the material has any form of treatment applied.

That said, the final sample average $[N_S^0]$ value for both samples is known, and does lend itself to speculation on the root cause for the observed reduction. On annealing at 800 °C there was a significant increase in the concentration of $NV^{0/-}$ defect. A crude estimation can be made of the NV defect concentration from the confocal microscopy, where the observed count rate is compared to that of a single NV^- under the same experimental conditions. Hence, the growth sector dependence of this can be found in table 7-6. It should be emphasised that this can only ever be a lower limit on the concentration, where the count rate for a single NV^- is judged to be similar to that of a single NV^0 defect. Furthermore, this assumption does not include any polarisation effects in the ensemble measurement.

In the {1 1 1} growth sector therefore, the generation of NV defects has not been as high as the concentration found in the {0 0 1} growth sector. This is despite the modified Kanda diagram suggesting the {1 1 1} growth sector as being the highest nitrogen containing sector. One likely explanation for this is the presence of boron, where it is below detection limits in the {0 0 1} growth sector, and consequently may imply a dark form of NV in the {1 1 1} growth sectors, such as NV^+. This is further affirmed by the stronger presence of NV^- in the {0 0 1} compared to {1 1 1}, implying a ready supply of electron donors.

Given the annealing temperature did not go above 800 °C, it is not expected

Sample	{0 0 1} (ppb)	{0 1 1} (ppb)	{1 1 5} (ppb)	{1 1 3} (ppb)	{1 1 1} (ppb)
NDT	21 ± 1.5	0.02 ± 0.005	0.01 ± 0.005	5.8 ± 1.3	3.2 ± 1.2
E6	27 ± 1.4	0.01 ± 0.005	†	2.2 ± 1.1	2.9 ± 1.3

Table 7-6 A lower limit on the NV concentration, in ppb, due to the fluorescence count rate in confocal microscopy, or where possible by counting the defects per growth sector. † = not obtained

that substitutional nitrogen has undergone aggregation to form A centres (N_S-N_S). Equally it is unknown if any A-centres were present in the as-grown material. No H3 defects (N_2V^0) were observed in any growth sector (chapter 6), which could imply a concentration of A-centres below detection limits. Furthermore, $[N_S^0]$ did not increase above the starting value at any point, also signifying no other aggregation states of nitrogen have broken up. Thus, the drop in $[N_S^0]$ is likely due to the creation of NV centres and nitrogen interstitial related defects.

7.3.1.2 Boron

The picture is further complicated by the addition of boron in the material. During the irradiation and annealing sequence, it was seen that the boron concentration only started to decrease upon the 400 °C anneal and then significantly (71% ± 2%) upon the 800 °C anneal. In absolute terms, this corresponds to a loss of 62 ppb and 34 ppb in the NDT and E6 material respectively from the as grown state.

It is not well reported in literature with regards to the fate of boron upon electron irradiation and annealing. Green [31] reported the generation of the 648 nm (1.913 eV) ZPL due to electron irradiation IIb material and annealing to 600 °C. Furthermore, it is seen that this defect anneals in at 400 °C and out by 800 °C, and hence would not have been observed during this work. However, from the deduced symmetry of the defect it was implied this defect may be derived of a boron interstitial, and that the annealing out at 800 °C coincides with the mobility of vacancies leading to its destruction.

Goss and Briddon [32] consider the aggregation states of boron from first principle calculations, where it was given that boron interstitial (B_I) pairs would not act as shallow acceptors unlike a complex such as B_S-N_S-B_S. It is also predicted that a self interstitial can become trapped as B_S sites, where the activation energy for migration of this complex would be 2.1 eV.

Throughout the work in this thesis, the calibration factor from Kawarada *et al* [33] and Barjon *et al* [34] has been used to non-destructively assess the substitutional boron concentration. In a later paper by Barjon, it is claimed the limit of sensitivity

for SEM-CL is approximately 0.05 ppb for the boron concentration [35]. Furthermore, we assume the electron beam neutralises any charge state. Hence there is no reason to suspect a breakdown in quantifying boron at low concentrations.

Thus, if boron becomes complexed such that it produces a deep level in the bandgap, this undoubtedly would reduce the intensity of the bound exciton seen in SEM-CL spectroscopy. Therefore, it could be possible that the slight reduction seen at 400 °C is the capture of the self interstitial at B_S sites, and the significant reduction of boron at 800 °C is facilitated by the formation of a boron complex located deeper in the bandgap, such as B_I pairs.

Finally, evident from table 7-3 is the non-uniform reduction of boron across all growth sectors. This may imply the reduction involves another point defect which itself has a growth sector dependence. It is unclear whether the generation of vacancies and interstitials themselves are growth sector dependent, where this study only shows the relative neutral charge state distribution of vacancies. Hence, a likely candidate is nitrogen. Table 7-7 shows the relative decrease in substitutional nitrogen and boron concentrations per growth sector, again with the proviso of Burns' relationship [28], where comparable differences of the two dopants are similar. Conversely, this would be at odds with the absolute reduction in boron of the {0 1 1} growth sector, where the starting nitrogen concentration is speculated to be below 1 ppb. Any further inference becomes non-trivial with this data set, and would warrant further in depth investigations from a wider sample set.

	{0 0 1}		{0 1 1}		{1 1 3}		{1 1 1}	
	$[N_S^0]$ (ppb)	$[B_S]$ (ppb)	$[N_S^0]$ (ppb)	$[B_S]$ (ppb)	$[N_S^0]$ (ppb)	$[B_S]$ (ppb)	$[N_S^0]$ (ppb)	$[B_S]$ (ppb)
Start	45.8	0	0.9	19.0	9.1	9.0	91.5	84.0
End	11.5	0	0.2	6.0	2.3	5.0	23	22.0
Δ	-34.3	0	-0.7	-13.0	-6.8	-4.0	-68.5	-62.0

Table 7-7 Relative growth sector changes of nitrogen and boron for the NDT sample, where it is assummed the relationship found by Burns *et al* [28] holds true at the 800 °C annealing stage for N_S^0.

7.3.1.3 Adding detail to the Kanda diagram

Despite the changes to both nitrogen and boron from the annealing stages in this chapter, it is perhaps beneficial to update the Kanda diagram once more with the findings of the previous two chapters, with the assumption this relationship holds true from low to high defect concentrations.

The version presented by Burns *et al* [28] does not discriminate for boron acceptors in {0 0 1} and {1 1 3} growth sectors. Additionally, the existing Kanda diagram does not consider higher order crystallographic planes, such as {1 1 5} which can form due to the presence of boron [36]. Therefore, figure 7-12, provides an up to date modification of the Kanda diagram with the afore mentioned distinctions.

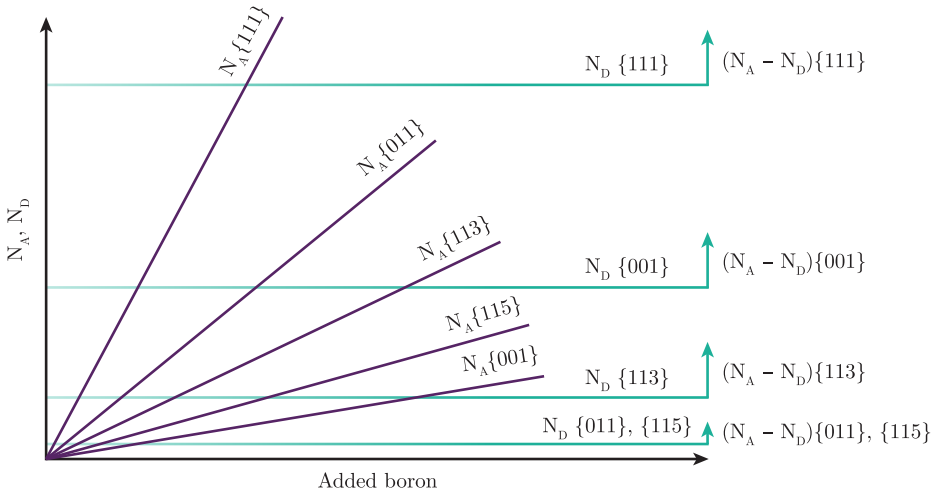

Figure 7-12 An update to the Kanda diagram with the results from this study, which builds upon the version modified in the work by Burns *et al* [28]. N_D, and N_A represent the concentrations of nitrogen (donor) and boron (acceptor) respectively.

7.3.2 SEM induced nitrogen implantation

Becker *et al* recently reported the creation of single and ensemble NV^- centres in electronic grade CVD diamond via nitrogen implantation, as facilitated by SEM [37]. In their work, a low energy electron beam (0.7 keV) was left to raster the diamond over 100 hours, and then the sample was annealed at 800 °C where it is known to generate NV defects. It was hypothesised that nitrogen atoms in the

purge gas become positively charged due to the interaction with the electron beam, and as a build up of negative charge occurs at the surface of the diamond the nitrogen ion is accelerated into the diamond by electrostatic forces (figure 7-13). To confirm this, Becker *et al* swapped the purge gas for isotopically enriched ^{15}N gas, and the experiment repeated. ODMR spectra on the subsequently generated NV^- defects revealed a hyperfine interaction consistent with a nuclear spin of $I = 1/2$, therefore confirming nitrogen implantation by SEM.

As seen in the DiamondView^{TM} image in section 7.2.6, the SEM-CL investigation on the 400 °C anneal occurred before confocal microscopy, creating regions of higher fluorescence intensity in the E6 sample. Confocal microscopy then confirmed this region to contain a higher amount of NV emission than the rest of the material. The sample was not annealed between SEM-CL measurements and confocal imaging. Since the samples already contained a substantial amount of vacancies from the initial electron irradiation, it is presumed the NV generation was enabled by the implantation of nitrogen at a vacancy position. Furthermore, the implantation of nitrogen will act to create vacancies, which themselves may be situated at neighbouring nitrogen atoms.

Based upon the maximum count rate of the NV emission within this region, and comparing with the known count rate of a single NV^- centre on the system, it is

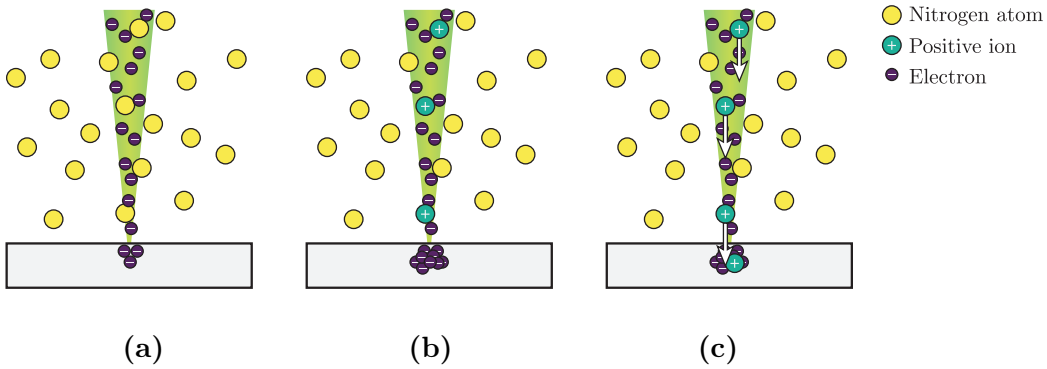

Figure 7-13 Schematic of ion implantation in diamond using SEM. (a) initial conditions whereby a electrons start to build at the diamond surface, (b) nitrogen atoms become positively charged due to interactions with the focussed electron beam whilst negative charge continues to build in the sample, (c) positive nitrogen ions are then accelerated into the surface of the diamond by electrostatic forces. Figure adapted from Becker *et al* [37]

not unreasonable to assume an average of 30 NV^- defects in the excitation volume. Therefore, a very tentative estimate can be made on the concentration within the localised region at 3 ppb. However, as the observed count rate is likely to be below the combined saturation power, and assuming the defects will be randomly orientated, the concentration is likely much higher than this.

During the SEM-CL measurement, the EHT voltage was set to 15 keV, thereby implying a maximum implantation energy of 15 keV. By modelling this energy in SRIM, this would correspond to a theoretical implantation depth of 21 ± 7 nm. The fluorescence intensity as a function of depth was investigated with the oil objective on the confocal microscope, where the axial resolution limit is 0.8 µm. Since the FWHM of the fluorescence intensity was measured to be 2.8 µm, one can speculate that secondary damage from the implantation occurred, whereby additional NV defects were created from N_S^0 in the $\{0\,0\,1\}$ growth sector at a depth greater than implantation stopping range.

7.3.3 3H growth sector dependence

3H is seen in electron irradiated and annealed diamond, where the current understanding on the defect configuration is the di-$\langle 0\,0\,1\rangle$-split self interstitial (Humble defect) [18]. Additionally, it is thought to be negatively charged where the generation occurs strongly in nitrogen containing diamond [38]. The annealing behaviour is reported such that it can be generated directly upon electron irradiation, and anneals out at approximately 400 °C [16, 39]. Finally, 3H has been reported to be a poor photostable defect with exhibited photochromic behaviour [39].

These facts are mainly in agreement with the findings reported here, however there are some subtle differences which can be picked up. In the as irradiated state, 3H was not detected in UV-Vis absorption, nor was it picked up in the widefield PL mapping. Subsequently, it could be seen following the 400 °C anneal.

It is interesting to note the DiamondView™ image in figure 7-5 where both samples exhibited green fluorescence. Furthermore, it is clear to see the growth sector dependence which follows that seen for 3H during the PL map. It is also

worth recalling that no TR12 absorption or emission could be identified in these diamonds. Since the DiamondView™ fluorescence image for both samples showed virtually no green fluorescence, this also agrees with the lack of 3H signal seen during UV-Vis absorption and is evidential for 3H not being present in the as-irradiated state. Therefore, the green fluorescence seen in DiamondView™ at the 400 °C stage could be caused by the 3H defect. This is perhaps at odds with the photobleaching behaviour of 3H seen during laser excitation [21], but may imply that the UV excitation source of DiamondView™ has a significantly lower power density incident upon the sample than would be caused by laser excitation removing any two-photon ionisation processes.

The distinction here is hard to ascertain as to whether the defect configuration has annealed in, or there has been movement of charge within the diamond to put the already existing di-⟨0 0 1⟩-split self interstitial complex into the negative charge state to generate the 3H fluorescence. Furthermore, the annealing behaviour in this work is perhaps surprising. At 400°C, the ratio of 3H ZPL against the Raman signal followed as:

$$\{0\,1\,1\} > \{1\,1\,1\} > \{1\,1\,5\} > \{1\,1\,3\} > \{0\,0\,1\}$$

whilst for the 800 °C anneal stage, this ratio followed as:

$$\{0\,0\,1\} > \{1\,1\,1\} \geq \{1\,1\,3\} > \{0\,1\,1\} > \{1\,1\,5\}$$

Evidently, upon the 400 °C anneal, 3H was strongest in the {0 1 1} growth sector, and weakest in {0 0 1}. This is at odds with the assignment of the negative charge state since the {0 1 1} growth sector does contain considerably more boron than the {0 0 1} growth sector. The direct reversal of this dependence was seen at the 800 °C annealing stage, and as such would tend to agree with the negative charge state, since the intensity loosely follows the expectation of nitrogen incorporation. However, if one considers the {1 1 3} growth sector, this understanding breaks down since the 3H/Raman ratio increased in this sector upon the 800 °C anneal, and is known to contain an appreciable amount of boron.

Again, the distinction between charge transfer and defect migration is not clear, and is further complicated by the presence of both substitutional boron and nitrogen,

especially in the {1 1 1} growth sector. If we consider the final substitutional boron concentration in the {1 1 1} growth sector of both samples, it is not too dissimilar to the boron concentration in the {0 1 1} growth sector during the 400 °C stage. However the 3H/Raman ratio is much weaker for {1 1 1} compared to {0 1 1} given the equivalent boron concentrations. This may imply an argument to 3H production which cannot be explained by charge dynamics alone, but instead becomes a many body problem.

Twitchen *et al* [40] investigated the annealing study of the R1 EPR centre (di-⟨1 0 0⟩-split self interstitial) and saw that a reduction in R1 correlated to a loss in 3H. However, it was also commented that from the annealing curve, complex processes were likely to be involved. Thus, to further this work, an investigation into the photochromism of the defect should be considered and if the relative strengths per growth sector can be directly influenced purely on a charge consideration.

7.4 Conclusion

Here, two previously studied high purity HPHT diamonds (NDT and E6) were subjected to electron irradiation, and then annealed at two targeted temperatures (400 °C and 800 °C) as way to learn more about the relative nitrogen incorporation.

Following a 30 minute irradiation with 4.5 MeV electrons, the neutral vacancy (V^0) defect was readily quantified by UV-Vis absorption (at 77 K) as 423 ± 20 ppb and 408 ± 18 ppb for the NDT and E6 material respectively. The relative intensity of the V^0 ZPL at room temperature decreased, based on the following growth sector ordering:

$$\{0\,1\,1\} > \{1\,1\,5\} > \{1\,1\,3\} > \{1\,1\,1\} > \{0\,0\,1\}.$$

Quantification of boron per growth sector was carried out at each stage, and was seen to decrease significantly upon annealing at 800 °C, and followed the growth sector dependence as described by the modified Kanda diagram. The concentration of the neutrally charged substitutional nitrogen (N_S^0) was monitored by EPR, where the sample average also reduced significantly.

Confocal imaging with 532 nm excitation and a 715 nm shortpass filter revealed neutral nitrogen vacancy (NV^0) defects were directly generated on irradiation, at a concentration on the order of 1 ppt, visible only in {1 1 1}, {1 1 3} and {0 0 1} growth sectors. Annealing at 400 °C generated resolvable NV^0 defects in the {0 1 1} and {1 1 5} growth sectors. As expected, annealing at 800 °C vastly increased the nitrogen vacancy emission due to the capture of vacancies at N_S sites. The fluorescence intensity decreased based on the following growth sector ordering:

$$\{0\,0\,1\} > \{1\,1\,1\} > \{1\,1\,3\} > \{0\,1\,1\} \geq \{1\,1\,5\}$$

where the intensity follows the uptake of nitrogen as described by the modified Kanda diagram. Here the {0 0 1} appears brigher than {1 1 1} and could be a consequence of the local boron environment quenching emission.

Finally, electron irradiation and subsequent annealing at 400 °C generated the 3H defect, which is thought to be the di-⟨0 0 1⟩-split self interstitial (Humble defect) in the negative charge state. The green fluorescence seen in DiamondView™ image correlated to the relative intensity of the 3H ZPL during room temperature PL mapping. The growth sector dependence is not well understood, and is seen to drastically change upon annealing at 800 °C, where the relative intensity increases in certain growth sectors, whilst decreasing in the rest. Whilst charge transfer can provide some light with regards to the changes, it is not clear if additional mechanisms are at play where 3H could be generated due to interstitial migration.

Further work should include investigating the growth sector dependence of defects at higher temperatures, as well as investigating a wider range of HPHT material. Equally, a suite of CVD diamonds of different growth chemistries may allow for better control of the donor and acceptor defects with regards to understanding the annealing behaviour of 3H.

References

1. C. D. Clark, R. W. Ditchburn, H. B. Dyer, *Proceedings of the Royal Society A: Mathematical, Physical and Engineering Sciences* **234**, 363–381 (1956).
2. C. D. Clark, J. Walker, *Proceedings of the Royal Society A: Mathematical, Physical and Engineering Sciences* **334**, 241–257 (1973).
3. C. A. Coulson, M. J. Kearsley, *Proceedings of the Royal Society A: Mathematical, Physical and Engineering Sciences* **241**, 433–454 (1957).
4. G. Davies, *Nature* **269**, 498–500 (1977).
5. D. Twitchen et al., *Diamond and Related Materials* **8**, 1572–1575 (1999).
6. D. C. Hunt et al., *Physical Review B* **61**, 3863–3876 (2000).
7. G. Davies et al., *Physical Review B* **46**, 13157–13170 (1992).
8. M. W. Dale, PhD thesis, University of Warwick, 2015.
9. A. M. Zaitsev, *Optical Properties of Diamond* (Springer Berlin Heidelberg, Berlin, Heidelberg, 2001).
10. E. A. Faulkner, J. N. Lomer, *Philosophical Magazine* **7**, 1995–2002 (1962).
11. J. Walker, *Journal of Physics C: Solid State Physics* **10**, 3031–3037 (1977).
12. G. Davies, H. Smith, H. Kanda, *Physical Review B* **62**, 1528–1531 (2000).
13. D. J. Twitchen et al., *Physica B* **273-274**, 628–631 (1999).
14. L. Allers, A. T. Collins, J. Hiscock, *Diamond and Related Materials* **7**, 228–232 (1998).
15. B. G. Breeze, PhD thesis, University of Warwick, 2016.
16. G. Davies, *Proceedings of the Royal Society A: Mathematical, Physical and Engineering Sciences* **336**, 507–523 (1974).
17. G. Davies, C. Foy, K. O'Donnell, *Journal of Physics C: Solid State Physics* **14**, 4153–4165 (1981).
18. J. P. Goss et al., *Physical Review B - Condensed Matter and Materials Physics* **63** (2001).
19. A. Mainwood, A. T. Collins, P. Woad, *Materials Science Forum* **143-147**, 29–34 (1993).
20. B. Naydenov et al., *Applied Physics Letters* **95**, 181109 (2009).

21. I. Vlasov, V. Ralchenko, E. Goovaerts, *physica status solidi (a)* **193**, 489–493 (2002).
22. B. Campbell, A. Mainwood, *physica status solidi (a)* **181**, 99–107 (2000).
23. M. Newton et al., *Diamond and Related Materials* **11**, 618–622 (2002).
24. J. Steeds, S. Kohn, *Diamond and Related Materials* **50**, 110–122 (2014).
25. N. Mizuochi et al., *Nature Photonics* **6**, 299–303 (2012).
26. G. Liaugaudas et al., *Journal of Physics: Condensed Matter* **24**, 435503 (2012).
27. E. Fraczek et al., *Optical Materials Express* **7**, 2571 (2017).
28. R. Burns et al., *Journal of Crystal Growth* **104**, 257–279 (1990).
29. I. Kiflawi, H. Kanda, A. Mainwood, *Diamond and Related Materials* **7**, 327–332 (1998).
30. R. Jones et al., *Diamond and Related Materials* **53**, 35–39 (2015).
31. B. L. Green, PhD thesis, University of Warwick, 2013.
32. J. P. Goss, P. R. Briddon, *Physical Review B - Condensed Matter and Materials Physics* **73**, 1–8 (2006).
33. H. Kawarada et al., *Physical Review B* **47**, 3633–3637 (1993).
34. J. Barjon et al., *Physical Review B* **83**, 073201 (2011).
35. J. Barjon, *Physica Status Solidi (A) Applications and Materials Science* **1700402**, 1–10 (2017).
36. M.-L. T. Rooney, *Journal of Crystal Growth* **116**, 15–21 (1992).
37. S. Becker et al., *Scientific Reports* **8**, 32 (2018).
38. A. Wotherspoon et al., *Diamond and Related Materials* **11**, 692–696 (2002).
39. K. Iakoubovskii et al., *Physica B: Condensed Matter* **340-342**, 67–75 (2003).
40. D. J. Twitchen et al., *Journal of Physics: Condensed Matter* **13**, 2045–2051 (2001).

8

The spin decoherence lifetime of NV^- in HPHT material

There's plenty of room at the bottom

- Richard P. Feynman

8.1 Defects in diamond for quantum applications

Quantum mechanics describes the world in which we cannot readily observe with our eyes, yet we have the ability to experimentally interrogate the fundamentals of this branch of physics. The theoretical physicist Richard P. Feynman is often cited as forecasting the progression of technology based on quantum mechanical principles in his 1959 lecture titled *There's plenty of room at the bottom* [1]. Today, innovations such as the global position system (GPS), magnetic resonance imaging (MRI), or the internal workings of the Apple MacBook Pro used to write this thesis would not exist without the development of this field. One may then ask, what does diamond have to do with quantum technologies?

It has already been discussed at length in this thesis, that diamond is known to harbour many exciting and extreme properties. In particular, many point defects in diamond are considered to be essentially well-confined quantum systems with the ability to be manipulated for quantum information processing or sensing applications [2, 3]. Thus, in tandem with the material properties, diamond is carving out a reputation as being one of the key foundation materials for future

quantum based technologies.

Recently, research on point defects in diamond which emit in the near infrared, has gained momentum to unveil the photo- and spin-physics of single photon sources. Such examples are the neutral silicon vacancy defect (SiV^0, ZPL at 946 nm) [4–6] or nickel related defects (NE8, ZPL at 793 nm) [7]. A plausible motivation for this is the inclusion into already existing telecom infrastructures, where fibres permit optical transmission at 1550 nm, such that quantum communication could become viable to the mass market.

However, historically the NV^- defect in diamond has shown the most promise for quantum processing. As a spin $S = 1$ system, this defect can be initialised into a specific spin state, manipulated by microwaves, and then read out by an all optical process [8]. Quantum enabled demonstrations often come from diamond synthesised by the CVD route since the growth can be precisely controlled, and then specific defects introduced at deterministic locations [9–12].

There are many outstanding articles which demonstrate the capability of NV^- to perform quantum-based operations. For example, Hensen *et al* entangled two remote single NV^- centres over a distance of 1.3 km to experimentally prove a loophole-free violation of the Bell inequality [13], unequivocally rejecting any local-realist theories. Additionally, deterministic entanglement was shown possible between two remote NV^- centres by Humphreys *et al* [14], a requirement for establishing a quantum network. Equally, Glenn *et al* demonstrated that ensemble NV^- defects enabled nuclear magnetic resonance (NMR), via synchronised readout, for the sensing of external spins where a spectral resolution approached 1 Hertz; a crucial step towards biological NMR spectroscopy of single cells [15].

This short chapter therefore focuses on the NV^- defect within HPHT diamond, and how the local environment impacts on the spin properties of the defect. The figure of merit used in this work is the spin-spin relaxation time which will henceforth be referred to as the spin decoherence lifetime, T_2. NV^- defects in as-grown material (hereinafter termed native NV defects), will be assessed from the same material presented in chapter 6. Additionally, to assess the viability of HPHT material with respect to various growth sectors, a third HPHT plate will be investigated whereby

nitrogen ions are implanted at a low energy, and the sample subsequently annealed to generate NV^- defects. All T_2 lifetime measurements will be conducted at room temperature.

8.2 T_2 for native NV defects

For the characterisation of native NV defects, the same two samples from chapter 6 (NDT and E6) were investigated, before the annealing study of chapter 7. Hence only native NV defects at the growth sector boundary of {1 1 1}-{1 1 3} were studied for the NDT sample since none were located in the {1 1 1} growth sectors. For the E6 material, native NV defects were investigated at both the growth sector interface and bulk {1 1 1} growth sectors.

To conduct ODMR measurements, the samples were independently mounted onto a co-planar waveguide, where a 20 µm wire was stretched across the surface and soldered to the centre line for microwave delivery (see figure 4-9). For both samples, the wire was located in an arbitrary position as no growth sector definition is visible under white light illumination. Once mounted on to the stage of the confocal microscope, the sample is positioned such that the 20 µm wire is situated in the middle of the piezoelectric stage range.

The alignment of the external magnetic field was aided by ODMR on four, single NV^- centres which all showed different resonance frequencies under a static randomly orientated magnetic field. An alignment to the ⟨1 1 1⟩ crystallographic direction was therefore achieved when the four NV^- defects showed resonance frequencies with a 1:3:3:1 relationship. Once aligned, the position of the resonances were cross-checked with the simulated resonances for a given field strength, and found to be in very good agreement. Spin manipulation was therefore conducted on NV^- centres with the greatest separation in resonances, since this corresponds to the defect being aligned parallel to the orientation of the magnetic field. Hence the field strength was determined as 26.4 ± 1.0 mT for both samples.

All spin operations were conducted on the low-field resonance only and on single NV^- centres at a distance ≤ 10 µm from the microwave wire. A Rabi oscillation

measurement was first conducted on the native NV to discover the timescale required to move the system around the Bloch sphere, where the typical Rabi oscillation period was < 80 ns.

The Hahn echo sequence was employed to obtain T_2 values at room temperature, and repeated twice per measurement. Here, the first sequence projects the spin back into the bright $|0\rangle$ state at the end by a final $\pi/2$ pulse (phase 1), whilst the second sequence projects back into the darker $|-1\rangle$ state by a final $3\pi/2$ pulse (phase 2). Subtracting phase 2 from phase 1 gives an improvement in the baseline. The resultant decay is then fitted by equation 8-1, where A is the initial decay amplitude, T_2 is the spin decoherence time, and n is the stretched component.

$$I(\tau) = Ae^{(-\tau/T_2)^n} \tag{8-1}$$

The Hahn echo pulse sequence is given in figure 8-1a, along with exemplar Hahn echo measurements from both NDT and E6 materials in figure 8-1b. As the studied material was not isotopically enriched, the separation time between microwave pulses was chosen to coincide with the revival frequency of ^{13}C, which was determined by conducting a shorter Hahn echo measurement. The measured revival frequency was in good agreement with the published values for the Larmor frequency of ^{13}C, which has a dependence of 10.71 kHz mT^{-1} [16].

Thus, at the growth sector interface, the mean T_2 lifetime of native NVs were < 40 µs in the NDT material. On the other hand, for the E6 material the mean T_2 lifetime was 579 ± 35 µs for both growth sector interface and bulk {1 1 1} growth sector locations, with no discernible difference between the two locations. There is a stark difference in observed fluorescence during the Hahn echo measurement between the NDT and E6 material, such that the behaviour of native NV defects in the NDT material was unexpected, and will be discussed later in this chapter.

In performing the Hahn echo sequence without the microwave source turned on, figure 8-2 shows the mean fluorescence intensity for readout and initialisation stages for all laser pulses. It is clear to see that the nature of behaviour for native NVs in the NDT material is very different to that of the E6 material. The gradual rise seen in the NDT NV trace was fitted with a single exponential yielding 337 ± 7 ns,

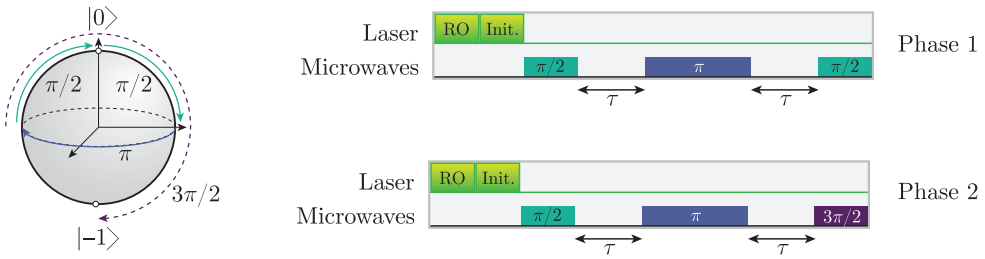

(a)

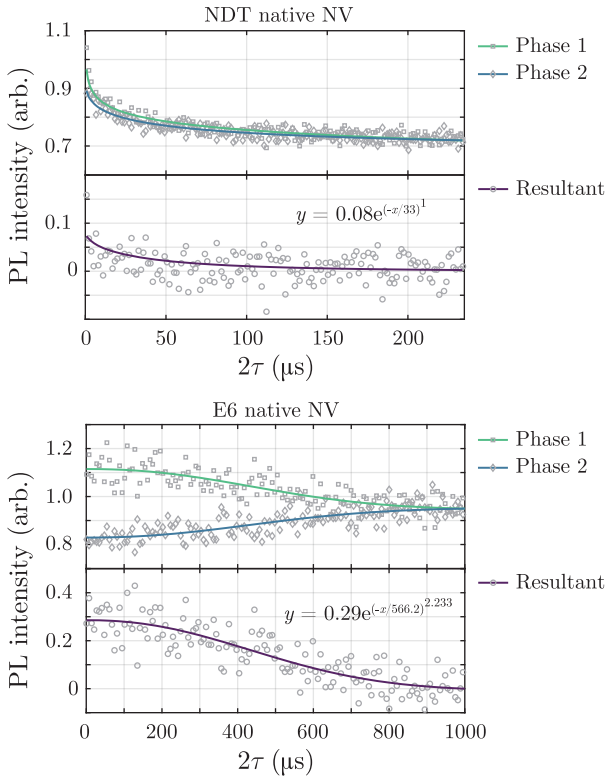

(b)

Figure 8-1 (a) Hahn echo pulse sequence for the two phase measurement, where the microwave pulse is represented on the Bloch sphere. (b) Exemplar T_2 measurements, taken at room temperature, from native NV defects in the NDT (top) and E6 (bottom) material with characteristic lifetimes of 36 ± 10 μs and 566 ± 40 μs respectively.

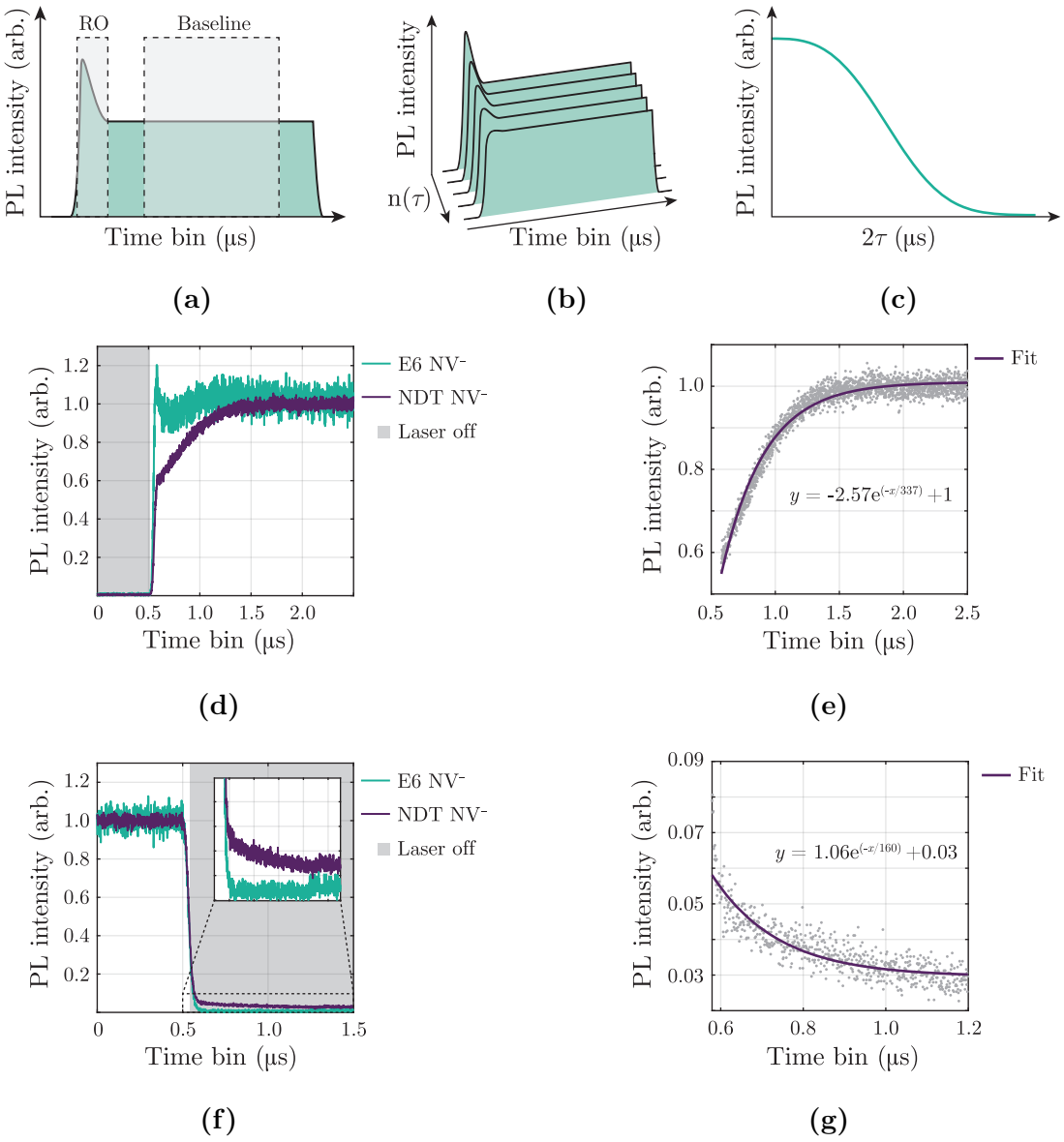

Figure 8-2 During the laser pulses of the Hahn echo the PL intensity is recorded, where the readout (RO) integration window and baseline integration window are shown schematically in (a) for phase 1. These are then recorded as a function of microwave delay time (b), such that the T_2 lifetime is given as the decay observed in the RO integration window (c). The mean PL intensity is shown in (d) and (f) for the periods where the laser is turned on and off respectively. Here it can be seen that the native NV within the NDT material did not behave as expected, where the rising and decay profiles are shown in (e) and (g) with the fitting of a single exponential giving lifetimes of 337 ± 7 ns and 160 ± 20 ns respectively.

whilst the long lived fluorescence/phosphorescence shown for the same defect when the laser is switched off decays with a lifetime of 160 ± 20 ns. Again, this result is unexpected and will be discussed later.

8.3 Characterisation of NV^- produced by ion implantation

8.3.1 Sample choice and implantation

To understand the growth sector dependence of T_2, an additional HPHT plate was sourced, also grown by New Diamond Technology (NDT). As shown in figure 8-3 this plate is of a similar morphology to the previous NDT sample, whilst XRT shows this sample to contain a similar dislocation density, although with slightly more stacking faults. RP-EPR was used to quantify $[N_S^0]$, where the sample average was found to be 17 ± 3 ppb. Initial confocal imaging revealed the same growth sector boundary decoration between {1 1 1} and {1 1 3} growth sectors, and no single NV^- defects in any growth sector. Therefore to investigate the growth sector dependence of the spin decoherence time, the sample required nitrogen implantation and annealing.

Here, implantation and annealing was conducted in a similar fashion to the investigation carried out by Chu *et al*, which showed it was possible to generate coherent and stable optical transitions of NV^- defects following sample preparation, ion implantation and stepped annealing [11].

Hence, this sample was first prepared with a reactive ion etch using Ar/Cl_2 and O_2 to remove the surface layer. Consequently it was found that this etch produced many etch pits at the surface and is likely to be due to an initial poor polish and extended defects within the crystal. After this, a low energy (20 keV) and low dose rate (1×10^9 cm^{-2}) nitrogen-14 ion implantation was carried out at the Surrey Ion Beam Centre. The diamond was then annealed in three, sequential stages:

- 400 °C for 4 hours

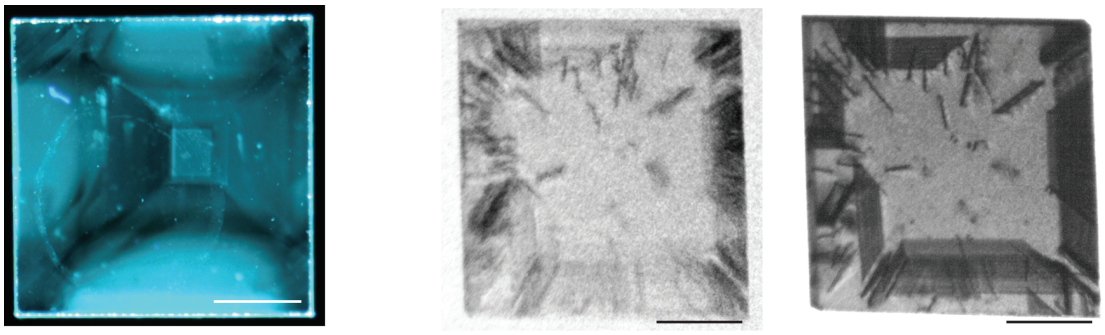

(a) **(b)**

Figure 8-3 (a) DiamondView™ image of the chosen sample for ion implantation showing a cubo-octahedral morphology typical of a plate cut parallel to the (0 0 1) crystallographic plane. (b) XRT images of the 220 and 400 diffraction vector showing dislocations and stacking faults in the material. Scale bar = 1 mm.

- 800 °C for 2 hours
- 1200 °C for 2 hours

Acid cleaning provided a clean surface for confocal microscopy, where again the sample was mounted in the same way as described in the previous section.

8.3.2 Spin decoherence measurements

Whilst the placement of the wire was arbitrary again for the sample, care was taken to ensure the location was central to increase the probability of good coverage of the (0 0 1) growth sector.

With an implantation energy of 20 keV, the stopping range of the nitrogen ion was calculated to be 28 ± 9 nm. Therefore all generated NV centres were effectively observed to be localised close to the surface, due to the axial resolution of the confocal microscope. From this, the initial observation was that the generation of NV appeared to be sector dependent, with the central (0 0 1) growth sector containing a higher density of NV defects than anywhere else. An example of the (0 0 1) to {1 1 3} region is shown in figure 8-4, along with a higher resolution scan of the transition. Also evident in figure 8-4 is the appearance of the etch pits at the surface, where there is an uneven distribution in NV⁻ fluorescence, both laterally

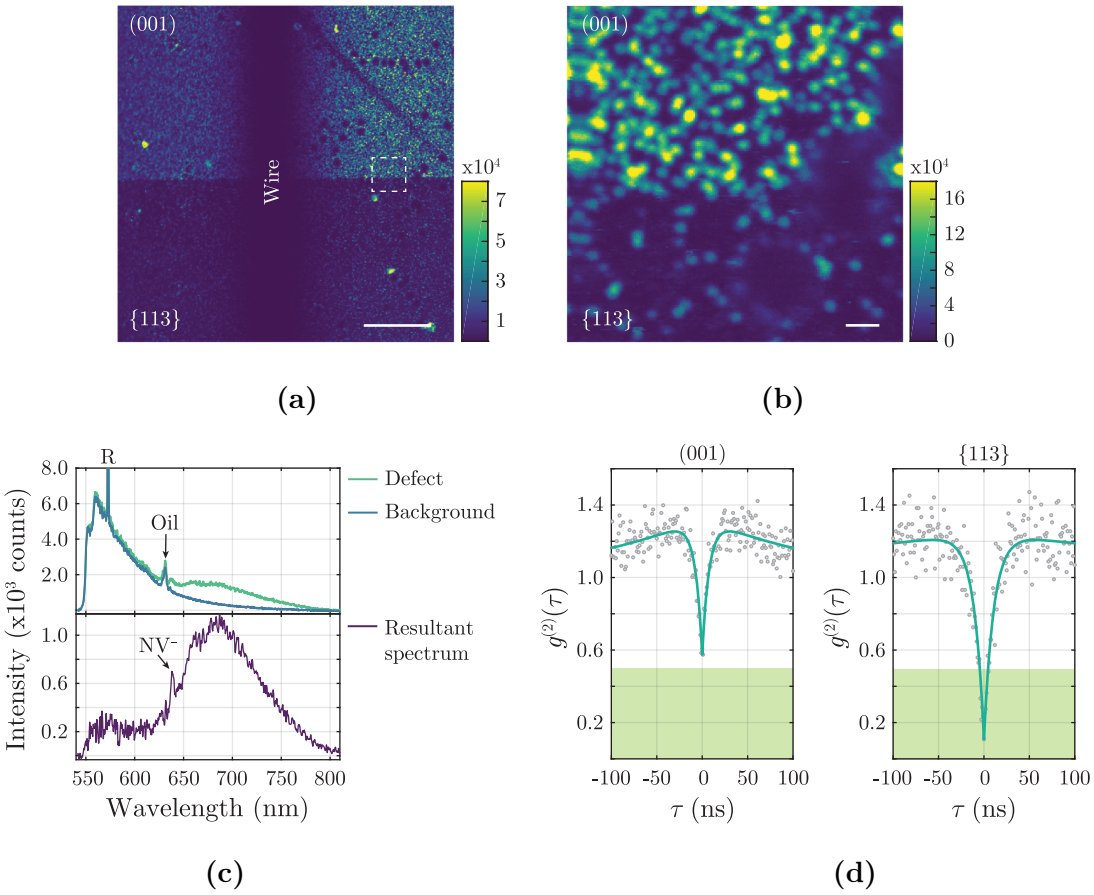

Figure 8-4 (a) Room temperature confocal image with 532 nm excitation and 633 nm longpass filter, showing the change in density between (0 0 1) and {1 1 3} growth sectors. The vertical dark region indicates the position of the 20 µm wire. Scale bar = 20 µm. (b) Close up of the interface between the two growth sectors as highlighted in (a). Scale bar = 1 µm. (c) example spectrum of a defect where the top shows the spectrum due to the fluorescence of the immersion oil used. Subtracting both sets of spectra reveal the 637 nm ZPL belonging to NV⁻. (d) Representative $g^{(2)}(\tau)$ measurements where no single emitters could be seen in (0 0 1), whilst all defects in {1 1 3} were single centres. Photoluminescence intensity scale bar represents the photon count rate per second (cps).

and axially, and may imply some etch pits are deeper than others.

Due to the higher NV fluorescence in the (0 0 1) growth sector, it was not possible to resolve single centres. However, in the {1 1 1} and {1 1 3} growth sectors, it was possible to resolve single centres as confirmed by their $g^{(2)}(\tau)$ measurement.

The alignment of the external magnetic field was this time facilitated by an NV⁻ centre of 4 emitters in the (0 0 1) growth sector, such that an ensemble ODMR measurement could be made. Hence, the applied magnetic field in this instance

was 22 ± 1 mT. Thus, it was possible to conduct Hahn echo measurements on a range of generated NV defects in the (0 0 1), {1 1 3}. However, for NV defects in the {1 1 1} growth sectors, the spectral stability was poor and as such became challenging to produce a Hahn echo with an adequate signal-to-noise ratio.

Exemplar measurements are shown in figure 8-5, and the mean decoherence time per growth sector is given in table 8-1. In addition, it was possible to conduct Hahn echo measurements on native NV defects at the growth sector boundary of {1 1 1}-{1 1 3} where the mean T_2 lifetime was found to be 610 ± 100 µs.

	{0 0 1}	{1 1 3}	{1 1 1}
T_2 (µs)	562 ± 170	438 ± 60	< 100

Table 8-1 Room temperature mean T_2 values, in µs, per growth sector, for generated NV defects following implantation.

8.4 Discussion

8.4.1 Native NV variation

As stated earlier, care was taken to align the field to the ⟨1 1 1⟩ crystallographic direction by monitoring the resonance positions of four NV defects, and cross-checked with simulations. Maze *et al* [17] demonstrated the effect of T_2 lifetime as a function of both magnetic field strength and misalignment from ⟨1 1 1⟩. Here an applied field strength of approximately 4 mT, aligned perfectly along ⟨1 1 1⟩ will yield a T_2 lifetime on the order of 600 µs, and then decrease to 200 µs for a 45° misalignment. Therefore the variation in T_2 lifetimes between the material cannot be attributed to a substantial misalignment in field orientation or significantly different field strengths.

As shown earlier in figure 8-2, the NV⁻ defects did not behave as expected during the Hahn echo sequence for the NDT material. The trace shown in the figure is the mean of all laser pulses. By turning the laser on, the defect should populate the bright state on relaxation, as per the E6 NV⁻ time trace. However, the NDT

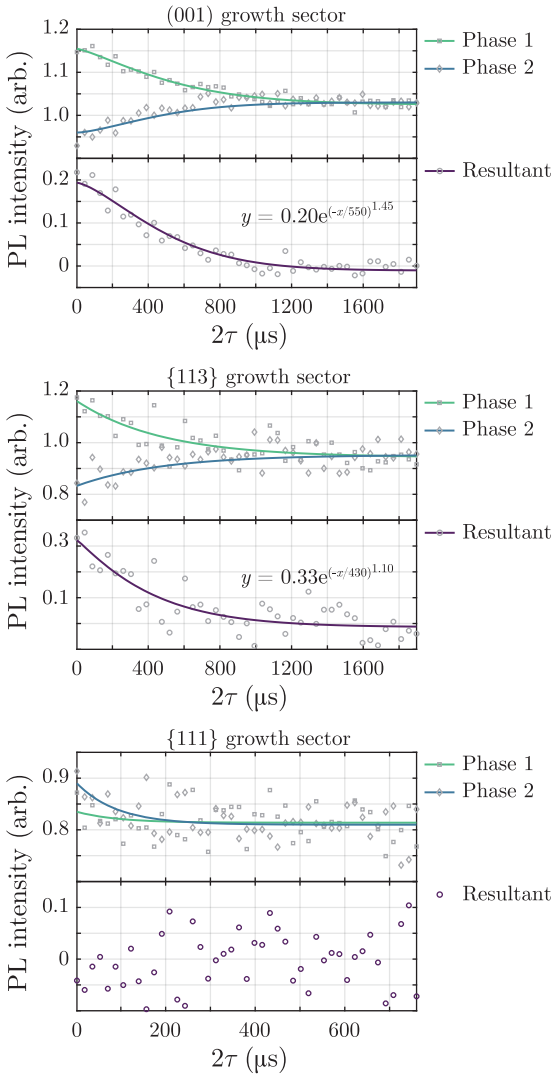

Figure 8-5 Exemplar T_2 measurements on NV defects in (0 0 1), {1 1 3}, and {1 1 1} growth sectors where the T_2 lifetime here are 580 ± 100 µs, 470 ± 70 µs, and < 100 µs respectively.

NV^- time trace shows a slow increase up to the equilibrium value. A plausible explanation for this is charge state switching, where the increase is due to laser driven charge transfer from NV^0 to NV^-. A similar effect was seen by Doi *et al* [18], where electrical biases were applied to investigate the charge dynamics of NV, and it was found the recovery of NV^0 to NV^- occurred on a longer timescale than the switch from NV^- to NV^0.

Furthermore, when the laser is turned off, the NDT native NV exhibited long lived fluorescence which decayed, suggesting a possible phosphorescence mechanism. To explain this, it is hypothesised that NV^- converts to the excited state of NV^0,

which then emits a photon as it relaxes to the ground state. As the 633 nm longpass fluorescence filter will allow a proportion of the vibronic band of NV^0 to be detected, it is this emission which is seen to decay over time. Given the unusual behaviour, it is perhaps not surprising the effective T_2 lifetimes are short for the NDT material since the defect is responding to charge state dynamics.

By studying near surface NV^- defects, Kim *et al* found that the T_2 lifetime decreased due to electrical noise from a liquid coating on the surface of high dielectric constant [19]. Myers *et al* later observed the same effect in isotopically enriched ^{12}C diamond with near surface NV^- centres [20]. Furthermore, from a nitrogen ion implantation study, de Oliveira *et al* found that the T_2 lifetime of NV^- decreased based on the environmental noise generated by di-vacancy defects [21].

Evidently there is a significant variation in the spin properties for native NV defects between material grown by different manufacturers, where the main contrast between material is the relative concentrations of boron. From chapter 6, it was shown that the maximum concentration of boron in the {1 1 1} growth sectors was 84 ± 10 ppb and 49 ± 9 ppb in the NDT and E6 material respectively. Furthermore, in chapter 7, it was proposed that the starting nitrogen concentrations in both material were very similar (< 100 ppb in the {1 1 1} growth sector). Thus, the short mean T_2 lifetime of < 40 µs in the NDT material, and the unusual behaviour during the Hahn echo, strongly suggests boron has a detrimental effect.

From fitting a stretched exponential to the Hahn echo decay curve, one can assess whether the decoherence lifetime has become limited by the spin bath presented by the natural abundance ^{13}C. de Lange *et al*, and later Wang *et al*, explain that for a slowly fluctuating spin bath, the T_2 lifetime decays with a cubic stretched exponential [22, 23]. Here, it is noted the stretched exponent obtained for the E6 native NVs averaged at n = 2.3 ± 0.3 implying the ^{13}C limit has not quite been reached, but is approaching the limit.

Finally, it is interesting to compare the native NV defects in the original NDT material from chapter 6, verses the native NV measured at the growth sector boundary in the additional NDT sample chosen for ion implantation. In this second NDT material, the measured mean value of T_2 was found to be 650 ± 100 µs,

an order of magnitude longer than the other NDT material, and with a stretched exponent of 2.5 ± 0.3. In this sample chosen for implantation, the average value for $[N_S^0]$ was found to be higher and may therefore imply a lower overall boron concentration, particularly in the {1 1 1} growth sectors. This would then fit with the native T_2 lifetime approaching the ^{13}C limit, just like the native NV measured in the E6 material. Further characterisation work on the sample chosen for implantation would therefore be warranted to understand the variation in boron.

8.4.2 Implant generated NV

From the XRT, the sample chosen for the implantation study does contain an appreciable amount of extended defects, namely stacking faults and dislocations predominately within the {1 1 1} and {1 1 3} growth sectors. This is then reflected in the surface quality following the plasma etch, where a significant number of etch pits were formed. Whilst these have not impacted on the results obtained, it does however highlight the importance of material quality and sample preparation.

Implantation of nitrogen ions into the high purity HPHT material has also revealed the sector dependence of the already-incorporated nitrogen concentration. Furthermore, the T_2 lifetimes observed per growth sector correlates with the distribution in boron, which is likely to be highest in the {1 1 1} growth sector, and here proved difficult to obtain a meaningful Hahn echo measurement. In addition, it did appear that the T_2 lifetime in the {1 1 3} growth sector were shorter than that found in the {0 0 1} growth sector, again good supporting evidence for the presence of a (smaller) local concentration of boron in that growth sector. However, it was shown in the native NV defects of the E6 material that the spin decoherence can still be ^{13}C limited, despite a local boron concentration of 50 ppb. Thus, the shorter lifetime from implantation into the {1 1 3} growth sector may indicate there are other factors influencing the result, such as the proximity to the surface of the diamond where electrical noise may be present [19, 20].

To further investigate the spin properties of the implanted NV^- defects within the {1 1 1} growth sectors, it may be useful to consider dynamic decoupling techniques.

For instance, the Carr-Purcell-Meiboom-Gill (CPMG) sequence is considered an extension to the Hahn echo sequence by using multiple π-pulses between the initial and final $\pi/2$-pulses, such that slow fluctuating components are suppressed, leading to a factor of 6 improvement in the T_2 lifetime [24, 25]. By applying such a sequence here, it may become possible to interrogate the spin dynamics of the NV^- defect and reconfirm the charge state dynamic. Alternatively, it may be possible to perform double electron-electron resonance (DEER) with a small modification to the microwave delivery system to understand if the NV^- defects are strongly coupled to any nearby paramagnetic defects, providing it is possible to obtain a suitable Hahn echo measurement in the first instance [26, 27].

Given that the nature of implantation will likely generate knock-on effects causing secondary damage [28, 29], it is not unreasonable to reconcile this with the higher density of NV defects in the $\{0\,0\,1\}$ growth sector compared to the rest of the material. This would therefore imply a significant concentration of N_S in the $\{0\,0\,1\}$ growth sector, a result already discussed in chapter 7. Hence, this study would benefit from one of two modifications:

- The use of nitrogen-15 implantation to discriminate against NV generated directly from implantation ($^{15}NV^-$) verses NV generated due to secondary damage ($^{14}NV^-$) by their respective ODMR measurements.
- Laser writing of vacancies in the material and then annealed, either by furnace or locally, to generate single NV defects at known locations and without generating secondary damage [30, 31].

8.4.3 Viability of HPHT material for NV-based quantum applications

Table 8-2 compares the published values of T_2 lifetimes against those observed here, as well as detailing the relative concentrations of nitrogen, NV^-, and boron. Thus, it can be said that high purity HPHT material can compete with that of quantum grade CVD material, where this study has shown the T_2 lifetime is limited seemingly by the ^{13}C environment for low, local, concentrations of boron.

Genesis	$[N_S^0]$ (ppb)	$[NV^-]$ (ppb) {0 0 1}	$[NV^-]$ (ppb) {1 1 1} / {1 1 3}	$[B_S]$ (ppb)	T_2 (µs)	Reference
CVD	<1	<0.001	-	<1	600	[10]
CVD	<1	<0.001	-	<1	1800$^{\triangledown}$	[32]
CVD	6	0.2	-	<1	600	[33]
HPHT	6.5*	<0.001	0.001	84	40	This work†
HPHT	34*	<0.001	0.003	49	580	This work†
HPHT	17*	0.001	0.001	<1$^{\diamond}$	560	This work‡

Table 8-2 Compilation of T_2 lifetimes (to two significant figures) and point defect concentrations for material of varying genesis of synthetic diamond. $\star$ = average value across all growth sectors as determined by RP-EPR, $\diamond$ = assumed boron value in {0 0 1} growth sector, $\triangledown$ = ^{12}C isotopically enriched diamond, † = native NV defect at {1 1 1}-{1 1 3} growth sector boundary, ‡ = implant generated NV in {0 0 1} growth sector,

Not only this, but it should be remembered that the crystalline quality of HPHT synthesised diamond is generally better than that of CVD synthesised diamond [34, 35]. Here, the quantity of dislocations in the studied HPHT material has been lower than that of quantum / electronic grade CVD [36]. Furthermore, the boron content within the {0 0 1} growth sectors is considered to be negligible (< 1 ppb) whilst showing T_2 lifetimes that are approaching the ^{13}C limit. Comparing this with the work of Balasubramanian, where CVD was grown isotopically enriched with ^{12}C [32], it becomes possible to envisage that isotopically enriched ^{12}C high purity HPHT material could be processed to provide NV defects with a T_2 lifetime longer than 1 ms, in virtually dislocation free material.

8.5 Conclusions

In this short chapter, an investigation to the spin decoherence lifetime (T_2) of single NV^- defects was carried on high purity HPHT diamond. Three samples were investigated where the first two are the NDT and E6 sample in their as-grown state, as characterised in chapter 6. The third sample was an additional NDT grown sample where single NV^- defects were generated by nitrogen-14 ion implantation

and subsequent annealing (referred to as implanted NDT sample).

It was found for the as-grown (native) NV^- defects, the mean T_2 lifetime as measured by the Hahn echo sequence exhibited a fundamental difference between the two types of diamond samples, observed as < 40 µs and 579 ± 35 µs in the NDT and E6 material respectively. It is proposed that the difference is a consequence of the local boron concentration.

For the implanted NDT sample, a growth sector dependence of the T_2 time was established. The mean T_2 lifetimes were measured to be 562 ± 170 µs, 438 ± 60 µs, and < 100 µs in the {0 0 1}, {1 1 3}, and {1 1 1} growth sectors respectively. In the latter case, the local concentration of boron, and proximity to the surface of the diamond, resulted in difficulties obtaining reliable Hahn echo measurements.

Furthermore, it was possible to observe a growth sector dependence on the generation of NV^- defects, which is in agreement with the relative nitrogen distribution as discussed from chapter 7. Therefore further work would be warranted on additional, and similar material, where the implant species of nitrogen is nitrogen-15. ODMR on created defects would then establish whether the defect formed from the implanted nitrogen, or through subsequent damage from implantation. Alternatively, laser writing of vacancies and subsequent annealing to generate NV^- would minimise secondary damage, and hence the relative concentration of the defect.

Nevertheless, it is clear to see that the T_2 lifetime of single NV^- defects in the {0 0 1} growth sector approaches the ^{13}C limit. Thus, it is plausible that {0 0 1} growth sectors of high purity HPHT diamond would be complementary to quantum grade CVD, whilst benefiting from higher material quality afforded from the HPHT synthesis process. High purity, ^{12}C isotopically enriched HPHT diamond could therefore be considered as highly desirable material to further extend decoherence lifetimes of point defects.

References

1. R. P. Feynman, *Engineering and Science* **23**, 22–36 (1960).
2. L. Childress, R. Hanson, *MRS Bulletin* **38**, 134–138 (2013).
3. R. Schirhagl et al., *Physical Chemistry* **65**, 83–105 (2014).
4. B. L. Green et al., *Physical Review Letters* **119**, 096402 (2017).
5. B. C. Rose et al., *Science* **361**, 60–63 (2018).
6. B. L. Green et al., arXiv: `1804.09141` (2018).
7. I. Aharonovich, E. Neu, *Advanced Optical Materials* **2**, 911–928 (2014).
8. M. W. Doherty et al., *Physics Reports* **528**, 1–45 (2013).
9. J. Meijer et al., *Applied Physics Letters* **87**, 1–3 (2005).
10. M. Markham et al., *Diamond and Related Materials* **20**, 134–139 (2011).
11. Y. Chu et al., *Nano Letters* **14**, 1982–1986 (2014).
12. Y.-c. Chen et al., *Nature Photonics* **11**, 77–80 (2016).
13. B. Hensen et al., *Nature* **526**, 682–686 (2015).
14. P. C. Humphreys et al., *Nature* **558**, 268–273 (2018).
15. D. R. Glenn et al., *Nature* **555**, 351–354 (2018).
16. L. Childress et al., *Science* **314**, 281–285 (2006).
17. J. R. Maze, J. M. Taylor, M. D. Lukin, *Physical Review B* **78**, 094303 (2008).
18. Y. Doi et al., *Physical Review X* **011057**, 1–11 (2014).
19. M. Kim et al., *Physical Review Letters* **115**, 1–5 (2015).
20. B. A. Myers, A. Ariyaratne, A. C. B. Jayich, *Physical Review Letters* **118**, 197201 (2017).
21. F. Fávaro de Oliveira et al., *Nature Communications* **8**, 15409 (2017).
22. G. de Lange et al., *Science* **330**, 60–63 (2010).
23. Z.-H. Wang et al., *Physical Review B* **85**, 155204 (2012).
24. B. Naydenov et al., *Physical Review B* **83**, 081201 (2011).
25. N. Bar-Gill et al., *Nature Communications* **3**, 858 (2012).
26. B. Grotz et al., *New Journal of Physics* **13**, 55004 (2011).
27. H. J. Mamin, M. H. Sherwood, D. Rugar, *Physical Review B* **86**, 195422 (2012).
28. C. Santori et al., *Physical Review B* **79**, 125313 (2009).

29. S. Onoda et al., *physica status solidi (a)* **212**, 2641–2644 (2015).
30. C. J. Stephen et al., *arXiv:1807.03643*, 2–9 (2018).
31. Y.-C. Chen et al., *Optica* **6**, 662 (2019).
32. G. Balasubramanian et al., *Nature materials* **8**, 383–7 (2009).
33. P. L. Stanwix et al., *Physical Review B* **82**, 201201 (2010).
34. R. C. Burns et al., *Journal of Physics: Condensed Matter* **21**, 364224 (2009).
35. T. N. T. Thi et al., *Journal of Applied Crystallography* **50**, 561–569 (2017).
36. A. Tallaire et al., *Diamond and Related Materials* **77**, 146–152 (2017).

9

Summary

No one undertakes research in physics with the intention of winning a prize. It is the joy of discovering something no one knew before.

- Stephen Hawking

The work in this thesis has provided an insight into the recent advances made in diamond synthesised by both the chemical vapour deposition (CVD) and high pressure, high temperature (HPHT) techniques. Here, research into the material properties has been enabled by the development of a custom built scanning confocal photoluminescence (PL) microscope, where diffraction limited spatial resolution has been achieved. Optically detected magnetic resonance (ODMR) studies were also possible with this microscope, by the mounting of samples on to a co-planar waveguide which enabled microwave delivery, and a multi-axis translation of an external magnetic field.

Additional information about the diamond material has also been garnered, where nitrogen concentrations were obtained by rapid passage electron paramagnetic resonance (RP-EPR) measurements, an understanding of the boron incorporation and growth morphologies was gained non-destructively by cathodoluminescence (CL) spectroscopy and infrared absorption (IR), an insight to the extended defect content by X-ray topography (XRT), and point defect assays by widefield PL microscopy and absorption spectroscopies were performed.

9.1 Single point defects in boron doped diamond

In chapter 5, a unique synthetic diamond grown by CVD was provided by Element Six Ltd (E6) for study, where the diamond contained multiple distinct, and repeated, layers:

- **Layer type 1:** Large (540 ± 20 µm), optically transparent regions which presented orange fluorescence in DiamondView™ imaging, typical of $NV^{0/-}$ emission. This orange fluorescence contained bright striations, consistent with an increased uptake in $NV^{0/-}$, where step flow growth had occurred from nitrogen doping. RP-EPR determined the concentration of substitutional nitrogen to be 133 ± 10 ppb.
- **Layer type 2:** Discrete, localised boron doped layers within 60 ± 10 µm regions, as seen by the blue colour in white light microscopy. These regions were sandwiched between the nitrogen regions. The concentration of substitutional boron incorporation was determined by secondary ion mass spectrometry (SIMS) and CL to be 1.3 ± 0.1 ppm, with the uncompensated value ($[B_S^0]$) determined by IR absorption as 0.9 ± 0.1 ppm.
- **Layer type 3:** Small, distinct regions confined within 40 ± 10 µm which exhibited very high free exciton emission during CL imaging. This region was situated after the growth of layer 2 and before the next growth of layer 1. The bound exciton due to substitutional boron was below the detection limit (< 1 ppb), and the free exciton emission was higher here than the nitrogen doped regions. Hence this region is considered as high purity diamond.

Growth of the diamond followed this order where the sequence was repeated five times during synthesis. The fact this diamond exists shows extreme control over the growth conditions.

By confocal microscopy, localised and resolvable point defect emission could be seen in the boron doped regions. On investigation, these point defects were not randomly distributed throughout these regions, and instead appeared to follow lines either running along the $\langle 0\,0\,1 \rangle$ growth direction, or inclined at ±12° to this.

Confocal PL spectroscopy of these defects revealed two classes of a zero phonon line (ZPL), one at 580 ± 10 nm and the other at 612 ± 18 nm. Defect emission also exhibited local vibrational modes where the position is centred on 189 ± 10 meV from the ZPL. Second-order autocorrelation ($g^{(2)}(\tau)$) measurements showed that in roughly a third of the point defects, the fluorescence was due to single emitters. In addition, the $g^{(2)}(\tau)$ measurements established that the mean fluorescence lifetime was 3.7 ± 1.7 ns and 1.8 ± 0.7 ns for the 580 nm and 612 nm defect groups respectively.

Furthermore, it was shown through optical polarisation measurements that these defects are likely to be either $\mathscr{C}_{2v}$ or $\mathscr{D}_{2d}$ symmetry, with the absorption and emission dipole orientated along $\langle 0\,0\,1 \rangle$, where the optical emission is a result of an $A \rightarrow A$ transition.

Through a consideration of the point defect distribution, and dislocations in the material, it was hypothesised that the incorporation is a consequence of the decoration of a dislocation.

A previous study by John *et al* showed a new defect formed by ion implantation with a ZPL at 582 nm, which is referred to as the L1 defect, although the defect constituents were not made clear [1]. Whilst there are some spectral similarities, the L1 defect is not the same as the 580 nm defect reported in this thesis.

PL from boron doped diamond is rare, and it is not well documented in journal articles. Furthermore, to the author's knowledge, this is the first report of single point defects within boron doped diamond. Further work should therefore focus on obtaining more statistics on the spectral emission, and a subsequent annealing study to understand defect migration which may allow the possibility of working backwards to understand the origin and constituents of these defects.

9.2 The decoration of growth sector boundaries with single NV^- centres

The advances in HPHT growth are evident by the increasing sizes of polished gemstones, where the diamond has been synthesised by the HPHT technique [2–5]. Consequently there is a motivation to understand the growth of the material.

Two high purity type IIa HPHT diamonds were selected for study in chapter 6, one grown by the manufacturer New Diamond Technology (NDT) and the other by E6. Here, the NDT sample exhibited a very low level of birefringence when compared to the E6 sample. XRT showed the NDT material to contain stacking faults and a dislocation density below 10^3 cm^{-2}, whilst the E6 sample dislocation density was considerably higher. Both samples exhibited typical cubo-octahedral morphologies, consistent with a slice taken parallel to the $\{0\,0\,1\}$ crystallographic plane.

CL spectroscopy detailed the boron concentration per growth sector, which was in agreement with the modified Kanda diagram [6]. The greatest concentration was found in the $\{1\,1\,1\}$ growth sectors as 84 ± 10 ppb and 49 ± 9 ppb in the NDT and E6 material respectively. No boron was detectable in the $\{0\,0\,1\}$ growth sectors, indicating a concentration below the detection limit of 1 ppb.

Confocal microscopy showed no point defect emission in $\{1\,1\,3\}$, $\{0\,1\,1\}$ or $\{0\,0\,1\}$ growth sectors of either sample when using 488 nm or 532 nm laser excitation. Common to both however was the point defect decoration between $\{1\,1\,1\}$ and $\{1\,1\,3\}$ growth sectors. Spectroscopy revealed the defects to be the negatively charge nitrogen vacancy (NV^-) centre, and at the majority of interfaces resolvable NV^- centres were classified as single emitters by their $g^{(2)}(\tau)$ measurement.

ODMR with a randomly orientated external magnetic field exposed NV^-, at the $\{1\,1\,1\}$-$\{1\,1\,3\}$ growth sector boundary, to not be preferentially orientated. This is perhaps unsurprising since the growth temperature from synthesis is likely high enough to rapidly reorientate the NV^- defect, even if it has grown in preferentially.

By the decoration of the growth sector boundaries, angles were determined from the $\langle 0\,0\,1\rangle$ direction showing very good agreement with the expected angle between

{1 1 1} and {1 1 3} crystallographic planes, further confirming where the decoration is located. Equally, the relative linear growth velocity of the neighbouring growth sectors could be calculated.

A working hypothesis for the decoration was given where it is thought that the angle to change from the crystallographic {1 1 3} plane to the {1 1 1} plane must be large enough to be energetically unfavourable, and as a consequence growth must be facilitated by small steps on which the NV^- defect is incorporated. However, as kinetic and impurity absorption effects need to be considered, further work would be needed to determine why the {1 1 1} to {0 1 1} interface is not decorated despite a larger minimum angle change between planes.

Two further types of defect were seen in the {1 1 1} growth sectors, the negatively charged silicon vacancy (SiV^-) and a nickel related defect with PL emission centred on 884 nm, referred to in this study as the 1.40 eV defect. Here, a difference between the NDT and E6 material was seen, where only the former contained the 1.40 eV defect. As both were synthesised in a Co-Fe-C system, it does highlight variation between manufacturers where the incorporation of nickel is likely to be through contamination of the source and capsule materials.

Preferential orientation of these defects were investigated by their optical absorption. It was found that the 1.40 eV defect was preferentially aligned, in agreement with previously published work [7, 8], whilst SiV^- was not preferentially orientated in either sample. The lack of preferential orientation for SiV^- is not so well understood, and hence further work would be necessary across a range of high purity HPHT material to see whether this fact is true for all HPHT material.

9.3 Electron irradiation and targeted annealing of high purity HPHT diamond

To build upon the knowledge gained from the results presented in chapter 6, the two studied diamond samples were subjected to electron irradiation and annealing. By doing so, it would be possible to infer the relative nitrogen concentrations in

each growth sector from the eventual formation of NV centres.

Electron irradiation for both samples lasted 30 minutes, at an energy of 4.5 MeV. Low temperature UV-Vis absorption showed the average concentration of generated neutral vacancies (V^0) were 423 ± 20 ppb and 408 ± 18 ppb for the NDT and E6 material respectively. Room temperature widefield PL measurements showed the growth sector dependence of the V^0 ZPL intensity, with it being greatest in the {0 1 1} and {1 1 5} growth sectors. RP-EPR showed N_S^0 could no longer be detected in the NDT material, whilst the concentration had just over halved in the E6 material to 15.2 ± 2 ppb. No significant changes were observed in the concentration of substitutional boron in the different growth sectors.

Before annealing, both diamond samples were studied with confocal imaging. With the 532 nm excitation, single NV^0 defects could be observed in the {1 1 1}, {1 1 3} growth sectors when a 715 nm shortpass filter was placed in front of the detectors. In the {0 0 1} growth sector, resolvable centres could also be seen where the PL spectroscopy showed emission of both NV^0 and NV^-. Through a counting exercise it was stated that the lower limit to the concentration of NV^0 was on the order of 1 part per trillion (ppt), with NV^- being lower than this.

Two targeted annealing temperatures were chosen as 400 °C and 800 °C, where the former is said to be the temperature at which interstitials become mobile and the latter where vacancies become mobile [9, 10]. After each anneal, the two diamonds were subjected to the same suite of characterisation for comparison.

From the 400 °C anneal, the concentration of V^0 decreased slightly as expected from some recombination with interstitials. The growth sector dependence of PL emission for the V^0 ZPL remained, although the relative intensity was seen to increase in comparison to the as-irradiated state. Confocal imaging with 532 nm excitation and a 715 nm shortpass filter covering the detectors showed single NV^0 defects were now also visible in the {0 1 1} and {1 1 5} growth sectors. Resolvable $NV^{0/-}$ defects still remained in the {1 1 1}, {1 1 3} and {0 0 1} growth sectors.

After annealing at 800 °C, the overall concentration of V^0 had decreased to 75% of it's original value, and a significant amount of NV centres had been created.

Confocal imaging showed resolvable, single NV^0 centres remained in the {0 1 1} and {1 1 5} growth sectors. RP-EPR revealed the concentration of N_S^0 in the NDT material barely detectable at 1 ± 1 ppb, and 15.9 ± 2 ppb in the E6 material. Thus, convolved with the relative distribution of boron, the growth sector dependence of the fluorescence intensity for $NV^{0/-}$ implies the nitrogen distribution of both diamond samples also agree with the modified Kanda diagram [6]. The work presented in chapters 6 and 7 have both confirmed the modified Kanda diagram and facilitated a minor update to detail the dependence observed in {1 1 3} and {1 1 5} growth sectors.

During this study, three unusual results were also obtained. At all stages, the boron concentration was monitored, and was found that it significantly decreased upon the 800 °C anneal. The mechanism for this decrease is not clear. As the decrease was not uniform across all growth sectors, it does imply this decrease is dependent upon other point defects which themselves have a growth sector dependence - where the likely culprit is nitrogen. To understand this, it would be beneficial to consider a wider range of HPHT material containing nitrogen and boron through an irradiation and annealing study to see if the relative concentrations of the two dopants are linked.

In addition, curious throughout this study is the generation and changes in the 3H defect. This defect was observed at room temperature to have a ZPL at 504.1 nm and is thought to be the di-⟨0 0 1⟩-split self interstitial (Humble defect) [11]. 3H was generated at 400 °C with an apparent growth sector dependence. Upon annealing at 800 °C the defect persisted, despite some of the literature claiming that it anneals out at this temperature [12]. Furthermore, the growth sector dependence changed such that the relative intensity within the {0 0 1} growth sector strongly increased where it was weakest before. Again, this result is not well understood and may require further consideration.

Finally, at the 400 °C anneal stage, CL spectroscopy was conducted on both samples prior to any other measurement due to the availability of equipment. Consequently it was possible to observe in DiamondView™ imaging a region of higher fluorescence in the E6 material within the {0 0 1} growth sector. Confocal imaging

of this material then revealed this emission to be caused by NV^-, and localised to the surface of the diamond. By assessing the intensity of fluorescence against the known count rate for a single NV^- centre, a lower limit of the concentration was found to be 3 ppb. Becker *et al* reported in 2018 that it was possible to implant nitrogen during secondary electron microscopy (SEM) measurements due to the ionisation of nitrogen atoms in the chamber and electrostatic forces accelerating these ions into the diamond [13]. Here then, it is realised that SEM may be an alternative pathway to generate NV^- centres in diamond in a controllable way.

9.4 Spin properties of single NV^- defects in high purity HPHT diamond

In the final results chapter of this thesis, high purity HPHT diamond is further considered in its role for quantum based technologies. In particular, this work is aimed at understanding the material with regards to the spin decoherence lifetime (T_2) of NV^-, as measured by a Hahn echo sequence.

An opportunity was taken with the NDT and E6 material before subjecting them to electron irradiation to study the NV^- centres in their as-grown state, referred to here as native NV defects. For the NDT material only native NV defects at the {1 1 1}-{1 1 3} growth sector interface could be studied, whilst this boundary and native NVs in the {1 1 1} growth sector were studied in the E6 material. The mean T_2 lifetime was found to be < 40 µs and 579 ± 35 µs respectively.

The growth sector dependence of the T_2 lifetime was studied in an additional high purity HPHT plate grown by NDT. This sample exhibited a similar cubo-octahedral morphology, and a sample average N_S^0 concentration of 17 ± 3 ppb. The work of Chu *et al* was followed for sample preparation, and subsequent NV generation following ion implantation [14]. Subsequently, the mean T_2 lifetime was measured for {0 0 1}, {1 1 3} and {1 1 1} growth sectors as 562 ± 170 µs, 438 ± 60 µs, and < 100 µs respectively.

In non-isotopically enriched diamond, the T_2 lifetime is limited by the spin interac-

tion with carbon-13 (^{13}C), to ~600 µs [15]. This limit is therefore considered to be reached in the E6 material and of the implanted NDT material.

The local boron environment was considered as the likely cause of variation in T_2 lifetimes observed in this study. This subsequently supported by the investigation of the charge stability of NV^- during the Hahn echo measurement, where a laser driven charge conversion from NV^0 to NV^- was observed.

Thus, it can be concluded that despite some of the challenges presented here, high purity synthesis of diamond via the HPHT technique is viable to produce quantum grade diamond where the extended defect content is much reduced compared to that grown by CVD.

References

1. R. John et al., *New Journal of Physics* **19**, 053008 (2017).
2. U. F. D'Haenens-Johansson et al., *Gems & Gemology* **51**, 260–279 (2015).
3. B. Deljanin et al., *Contributions to Gemology* **15**, 1–7 (2015).
4. H. Sumiya, K. Harano, K. Tamasaku, *Diamond and Related Materials* **58**, 221–225 (2015).
5. T. Ardon, S. Eaton-Magaña, *Gems and Gemology* **54**, 217–218 (2018).
6. R. Burns et al., *Journal of Crystal Growth* **104**, 257–279 (1990).
7. K. Iakoubovskii, A. T. Collins, *Journal of Physics: Condensed Matter* **16**, 6897–6906 (2004).
8. A. R. Lang, G. M. Meaden, *Journal of Crystal Growth* **108**, 53–62 (1991).
9. G. Davies et al., *Physical Review B* **46**, 13157–13170 (1992).
10. M. W. Dale, PhD thesis, University of Warwick, 2015.
11. J. P. Goss et al., *Physical Review B - Condensed Matter and Materials Physics* **63** (2001).
12. G. Davies, *Proceedings of the Royal Society A: Mathematical, Physical and Engineering Sciences* **336**, 507–523 (1974).
13. S. Becker et al., *Scientific Reports* **8**, 32 (2018).
14. Y. Chu et al., *Nano Letters* **14**, 1982–1986 (2014).
15. M. Markham et al., *Diamond and Related Materials* **20**, 134–139 (2011).